# Aircraft-based in-situ aerosol mass spectrometry: Chemical characterization and source identification of submicron particulate matter in the free and upper troposphere and lower stratosphere

Dissertation zur Erlangung des Grades

„Doktor der Naturwissenschaften“

am Fachbereich Physik, Mathematik und Informatik

der Johannes Gutenberg-Universität in Mainz

vorgelegt von

Julia Yvonne Schmale

geboren in Bochum

Mainz, Juli 2011

Tag der mündlichen Prüfung: 11. November, 2011

## Abstract

The composition of the atmosphere is frequently perturbed by the emission of gaseous and particulate matter from natural as well as anthropogenic sources. While the impact of trace gases on the radiative forcing of the climate is relatively well understood the role of aerosol is far more uncertain. Therefore, the study of the vertical distribution of particulate matter in the atmosphere and its chemical composition contribute valuable information to bridge this gap of knowledge. The chemical composition of aerosol reveals information on properties such as radiative behavior and hygroscopicity and therefore cloud condensation or ice nucleus potential.

This thesis focuses on aerosol pollution plumes observed in 2008 during the POLARCAT (Polar Study using Aircraft, Remote Sensing, Surface Measurements and Models, of Climate, Chemistry, Aerosols, and Transport) campaign over Greenland in June/July and CONCERT (Contrail and Cirrus Experiment) campaign over Central and Western Europe in October/November. Measurements were performed with an Aerodyne compact time-of-flight aerosol mass spectrometer (AMS) capable of online size-resolved chemical characterization of non-refractory submicron particles. In addition, the origins of pollution plumes were determined by means of modeling tools. The characterized pollution episodes originated from a large variety of sources and were encountered at distinct altitudes. They included pure natural emissions from two volcanic eruptions in 2008. By the time of detection over Western Europe between 10 and 12 km altitude the plume was about 3 months old and composed to 71 % of particulate sulfate and 21 % of carbonaceous compounds. Also, biomass burning (BB) plumes were observed over Greenland between 4 and 7 km altitude (free troposphere) originating from Canada and East Siberia. The long-range transport took roughly one and two weeks, respectively. The aerosol was composed of 78 % organic matter and 22 % particulate sulfate. Some Canadian and all Siberian BB plumes were mixed with anthropogenic emissions from fossil fuel combustion (FF) in North America and East Asia. It was found that the contribution of particulate sulfate increased with growing influences from anthropogenic activity and Asia reaching up to 37 % after more than two weeks of transport time. The most exclusively anthropogenic emission source probed in the upper troposphere was engine exhaust from commercial aircraft liners over Germany. However, in-situ characterization of this aerosol type during aircraft chasing was not possible. All long-range transport aerosol was found to have an O:C ratio close to or greater than 1 implying that low-volatility oxygenated organic aerosol was present in each case despite the variety of origins and the large range in age from 3 to 100 days. This leads to the conclusion that organic particulate matter reaches a final and uniform state of oxygenation after at least 3 days in the free troposphere.

Except for aircraft exhaust all emission sources mentioned above are surface-bound and thus rely on different types of vertical transport mechanisms, such as direct high altitude injection in the case of a volcanic eruption, or severe BB, or uplift by convection, to reach higher altitudes where particles can travel long distances before removal mainly caused by cloud scavenging. A lifetime for North American mixed BB and FF aerosol of 7 to 11 days was derived. This in consequence means that emission from surface point sources, e.g. volcanoes, or regions, e.g. East Asia, do not only have a relevant impact on the immediate surroundings but rather on a hemispheric scale including such climate sensitive zones as the tropopause or the Arctic.

# Zusammenfassung

Die chemische Zusammensetzung der Atmosphäre wird oft durch die Emission von Gasen und Partikeln aufgrund natürlicher sowie anthropogener Prozesse gestört. Während die Rolle der Spurengase für den Strahlungsantrieb des Klimas relativ gut erforscht ist, ist der Einfluss von Aerosolen weit unsicherer. Deshalb kann die Untersuchung der vertikalen Verteilung von Partikeln in der Atmosphäre und deren Eigenschaften noch fehlende Informationen liefern. Insbesondere das Wissen über die chemische Zusammensetzung von Aerosolen gibt Aufschluss über deren Strahlungseigenschaften und Hygroskopizität und somit über die Wolkenkondensations- und Eiskeimfähigkeiten.

Diese Dissertation konzentriert sich auf die Beobachtung von Aerosolfahnen während der POLARCAT (Polar Study using Aircraft, Remote Sensing, Surface Measurements and Models, of Climate, Chemistry, Aerosols, and Transport) Kampagne über Grönland im Juni/Juli 2008 und der CONCERT (Contrail and Cirrus Experiment) Kampagne über Mittel- und Westeuropa im Oktober/November 2008. Die Messungen wurden mit einem Aerodyne compact time-of-flight Aerosol Massen Spektrometer (AMS) durchgeführt, welches in Echtzeit die größenaufgelöste chemische Zusammensetzung von nicht refraktären Partikeln, die kleiner als ein Mikrometer sind, liefert. Zusätzlich wurden die Quellen der Aerosolverschmutzung mit Hilfe von Modellen bestimmt. Die charakterisierten Verschmutzungsperioden sind auf eine große Bandbreite von Quellen zurückzuführen und wurden in unterschiedlichen Höhen gemessen. Sie resultierten teilweise aus zwei Vulkanausbrüchen im Jahr 2008. Zur Zeit der Detektion war die Aerosolschicht ca. 3 Monate alt und bestand zu 71 % aus Sulfat und zu 21 % aus organischen Verbindungen. Verschmutzung durch Waldbrände (BB) in Kanada und Ostsibirien wurde über Grönland in einer Höhe von 4 bis 7 km Höhe gemessen. Der Ferntransport dauerte ca. ein bis zwei Wochen, respektive. Das Aerosol war zu 78 % aus organischer Materie und zu 22 % aus Sulfat zusammengesetzt. Einige kanadische und alle sibirischen BB Verschmutzungsfahnen waren mit anthropogenen Emissionen aus der fossilen Brennstoffverbrennung (FF) in Nordamerika und Ostasien vermengt. Ein Trend, bei dem der Anteil von Sulfat mit wachsendem Einfluss von FF aus Ostasien auf bis zu 37 % nach zwei Wochen Transport anstieg, konnte nachgewiesen werden. Rein anthropogene Verschmutzung aus den Abgasen des Luftverkehrs wurde in der oberen Troposphäre gemessen. Jedoch war eine chemische in-situ Charakterisierung dieser Art von Atmosphärenverschmutzung nicht möglich. Jede Art von ferntransportiertem Aerosol unbeachtlich der Herkunft und des Alters (drei bis 100 Tage), wies ein O:C Verhältnis nahe bei eins oder sogar größer auf. Dies entspricht schwer volatilen oxygenierten organischen Verbindungen. Diese Beobachtung führt zu der Schlussfolgerung, dass organische Partikel nach ca. drei Tagen Aufenthalt in der freien Troposphäre eine endgültige und einheitliche Form der Oxygenierung erreichen können.

Alle hier erwähnten Emissionsquellen, bis auf die Abgase aus dem Luftverkehr, sind bodengebunden, weshalb verschiedene Arten vertikalen Transports nötig sind, um die Emissionen in der Atmosphäre zu verteilen. Diese sind u.a. direkte Injektion in große Höhen wie im Falle der Vulkanausbrüche, starke Waldbrände und Transport durch Konvektion. Sobald das Aerosol die freie Troposphäre erreicht hat, kann es über weite Strecken transportiert werden bevor es hauptsächlich durch Wolkenbildung und anschließenden Niederschlag aus der Luft entfernt wird. Eine Lebenszeit zwischen 7 und 11 Tagen wurde für BB und FF gemischtes nordamerikanisches Aerosol berechnet. Dies bedeutet, dass Emissionen aus Punktquellen, z.B. Vulkane, oder Regionen wie Ostasien, nicht nur Einfluss auf die nähere Umgebung, sondern auf die gesamte Hemisphäre und damit auch auf äußerst klima-sensible Regionen wie die Tropopause oder die Arktis ausüben.

# Table of Contents

# 1. Introduction

## *1.1 Motivation*

In contrast to the radiative forcing by long-lived greenhouse gases such as $CO_2$ $CH_4$, $N_2O$, and $O_3$, the radiative forcing caused by aerosol is still poorly understood (Forster et al., 2007). Therefore the investigation of airborne particulate matter requires further attention to quantify its role in climate change. Depending on the vertical distribution of the aerosol, impacts are different with altitude. Aerosol plays a crucial role in the upper troposphere and lower stratosphere (UTLS), because particles in this atmospheric regime affect the mixing ratios of water vapor and ozone due to heterogeneous (involving the gaseous and particulate phase) chemical reactions. Earth's radiative balance is especially sensitive to the abundance of these trace gases in this region (Lacis et al., 1990; Forster and Shine, 2002). Furthermore, aerosol lifetime is enhanced in these altitudes (Farina et al., 2010) so that their impact augments. However, detailed knowledge on these particles' properties is scarce because only few aircraft-based in-situ measurements have been conducted up to now in these altitudes (8 – 18 km). In the context of studying UTLS aerosol, several more aspects need to be considered: Little is still known about the sources of the UTLS aerosol, its transport pathways, chemical composition, photochemical state and mixing state. To understand these aspects and processes it is necessary to vertically resolve the analysis of atmospheric aerosol which implies equally focusing on free tropospheric particulate matter which ultimately might be uplifted to the UTLS. In the free troposphere, the impact of particles is dominated by their interaction with clouds through which they change not only the optical properties of clouds but also their precipitation behavior. In addition, air mass exchange between the LS and UT or vice versa influences the abundance and properties of UTLS aerosol. Up to now, this type of air mass movement has been studied almost exclusively by means of trace gases. Hence knowledge of respective aerosol characteristics is rare.

The field experiments conducted within the scope of this work contribute insights into the characteristics of free tropospheric and UTLS aerosol through measurements performed over Greenland during June/July 2008 and over Central and Western Europe in October/November 2008. The measurement of air masses on their way into and out of the Arctic bears an additional asset compared to the general interest in such data as mentioned above: Since the Arctic is one of the most sensitive environments to climate change (Lemke et al., 2007), investigating the properties of summertime aerosol is of greatest interest because understanding the role of short-lived pollutants as climate forcers is the key to promoting effective mitigation strategies. The objective of this thesis is to elaborate aerosol source-receptor relationships within the target regions of the two campaigns and to put the results into larger context via comparison with similar available data. More specifically, this includes the identification of aerosol and precursor gas emission source regions and types, their influence on the aerosol chemical composition, the identification of transport pathways and their effects on the measured particle chemical properties and potential significance for aerosol direct radiative effects or aerosol-cloud interactions.

## *1.2 Structure of the thesis*

This thesis encompasses a large variety of aspects associated with the study of submicron aerosol in the free troposphere and tropopause. On the one hand instrumental and measurement related challenges need to be overcome to obtain valuable data in environments where particle mass concentrations are near the detection limit and the aircraft flight speed requires high time resolution. On the other hand aerosol chemical data alone are not sufficient for a comprehensive analysis. Complementary tools such as trajectory and dispersion models, additional information from meteorological parameters and trace gas mixing ratios are necessary to establish links between emission sources and receptor regions, and aerosol properties in the atmosphere. Additionally, knowledge of particle characteristics related to their emission source type is indispensible for the correct interpretation of the data. The introduction shall answer the following questions to provide the reader with the background knowledge to follow the motivation and focus of the performed data analysis:

For what purpose and where were the data obtained?

What do we already know about aerosol from various emission source types that reach the free troposphere and tropopause?

What are common aerosol transport pathways?

What are potential effects?

What are the expected new contributions to this field of research through this work?

Additionally, definitions for relevant terms and concepts are given. Subsequently, this work is structured as follows: A brief history of mass spectrometric airborne aerosol measurements is presented followed by the instrument and data processing description (sections 1.7 to 2.7). Additional resources for the analysis of the aerosol mass spectrometric data are introduced before the final results are elaborated. Representative case studies are discussed in chapter 3. In the end, all data are combined and put into larger context (chapter 4) including the final conclusions and an outlook for further research needs (chapter 5).

## *1.3 Field experiments and their objectives*

This work is based on the data sets which I obtained through the deployment of the Aerodyne compact time-of-flight aerosol mass spectrometer (C-ToF-AMS or AMS) in two airborne field experiments in 2008. The main results have been published in Schmale et al. (2010) and (2011). The AMS measures the online size-resolved chemical composition of non-refractory submicron particles.

### *1.3.1 POLARCAT campaign*

The POLARCAT (Polar Study using Aircraft, Remote Sensing, Surface Measurements and Models, of Climate, Chemistry, Aerosols, and Transport) France summer campaign was carried out from 30 June to 14 July, 2008, as part of the International Polar Year (http://ipy.arcticportal.org/) initiatives. The Safire (Service des Avions Français Instrumentés pour la Recherche en Environnement) research aircraft ATR-42 was based in Kangerlussaq (67.0°N, 50.7°W), Greenland, from where all scientific flights were conducted between 60 to 71°N and 40 to 60°W (see green trace in Figure 1).

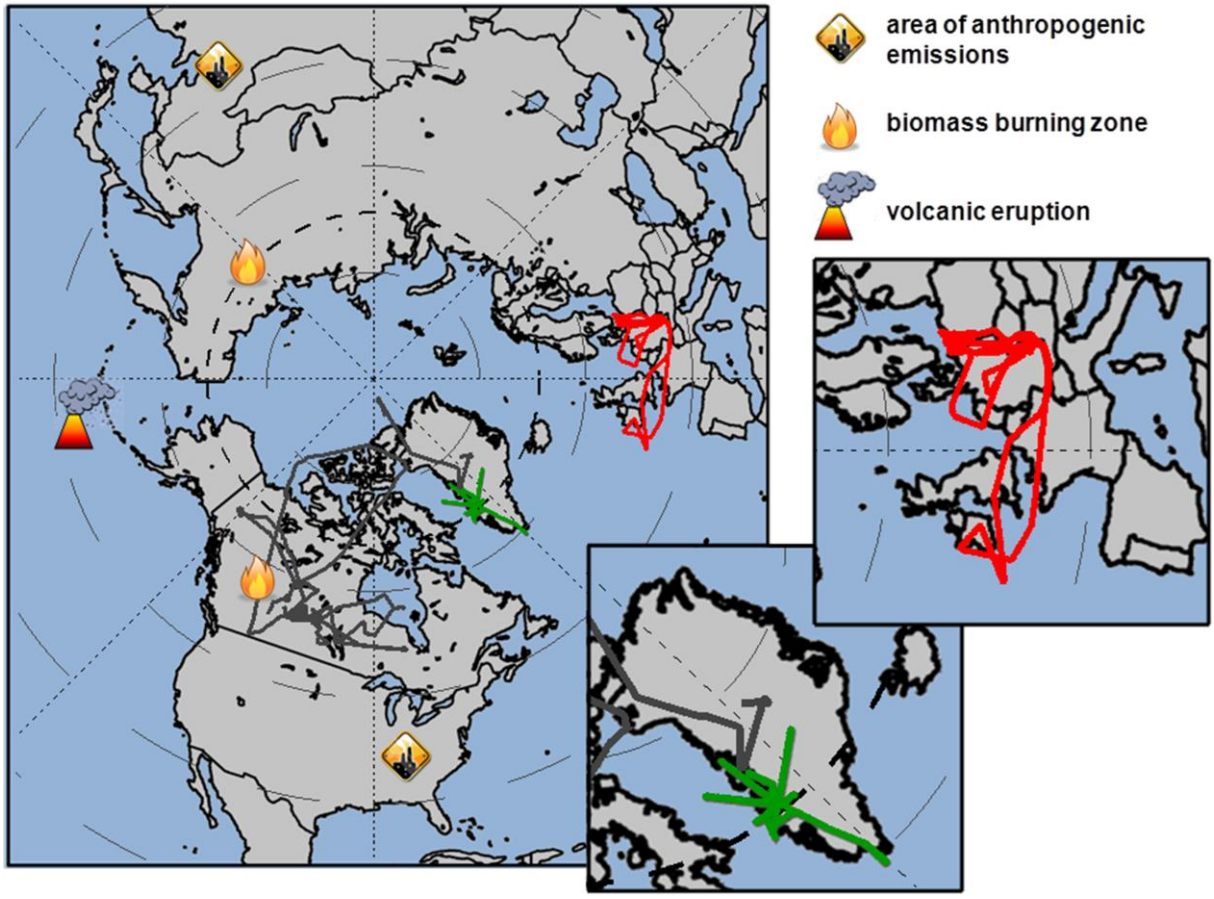


**Figure 1: Flight tracks of the POLARCAT (green), CONCERT (red) and ARCTAS (grey) campaigns, and relevant emission source regions and types of the characterized aerosol.**

The maximum altitude ceiling was 7.6 km, the speed 100 m $s^{-1}$ and the maximum flight duration three hours. Eight out of twelve flights the AMS operated successfully. The main purpose of the AMS deployment within the scope of the POLARCAT-France study was the identification and chemical characterization of particulate matter in long-range transport pollution plumes originating from

different source regions and emission sources. The relevant source regions (East Asia, Siberia, Canada, and eastern and mid-west USA) are indicated in Figure 1 by symbols for anthropogenic activity, corresponding primarily to fossil fuel combustion (FF), and biomass burning (BB) as having occurred in June/July 2008.

In the Arctic, numerous campaigns and continuous measurements of Arctic aerosol have been conducted previously (Rahn et al., 1977; Schnell, 1984; Shaw, 1995; Law and Stohl, 2007; Quinn et al., 2007). However, Arctic aerosol research has focused predominantly on winter/spring (Rahn and McCaffrey, 1980; Shaw, 1995; Stohl, 2006) while fewer measurements have been performed during summer when concentrations are generally lower (Law and Stohl, 2007). Most of the available in-situ measured aerosol data (optical, microphysical, and chemical) have been collected at the surface, whereas only very few summertime airborne studies of aerosol chemical composition have been carried out so far (Brock et al., 1989; Brock et al., 1990; Talbot et al., 1992; Franke et al., 1997; Dreiling and Friedrich, 1997). In this respect, results from the POLARCAT summer campaign contribute to the knowledge about aerosol on its way into and out of the Arctic and sub-Arctic.

### *1.3.2 CONCERT campaign*

From 27 October to 2 November, 2008, the CONCERT (CONtrail and Cirrus ExpeRimenT) Chemistry campaign was performed out of Oberpfaffenhofen (48.07° N, 11.27° E), Germany, (Voigt et al., 2010). Six flights were conducted mostly in altitudes between 8 and 12 km at a speed of roughly 200 m $s^{-1}$ over Central and Western Europe between longitudes of 15° E and 14° W and latitudes of 48° and 55° N (see red tracks in Figure 1). The intended primary goal of the AMS deployment was the measurement of submicron particles in the North Atlantic flight corridor and in condensation trails (here after contrails) produced by commercial airliners. However, when probing a tropopause fold on 28 and 31 October over the North Atlantic near the Netherlands and between France and Ireland, respectively, coincidentally a lower stratospheric volcanic aerosol plume was intercepted. This enabled us to investigate volcanic particles emitted by Mts. Okmok (53.40° N, 168.17° W) and Kasatochi (52.18° N, 175.51° W) that erupted on 12 July and 7 August, 2008, in the Aleutians (see volcano symbol in Figure 1). This was the first time on-line mass spectrometric data on volcanic aerosol in the UTLS were obtained from direct in-situ measurements.

### *1.3.3 ARCTAS campaign*

An additional set of AMS data, acquired by the Jimenez working group at CU Boulder during the ARCTAS (Arctic Research of the Composition of the Troposphere from Aircraft and Satellites) summer campaign flown out of Cold Lake, Canada (see grey trace in Figure 1), was used to complement results from the POLARCAT study. Specifically, pollution plumes originating from East Asia and Siberia detected in altitudes near the tropopause were investigated for this work since the adopted NASA research aircraft DC-8 reached much higher altitudes than the ATR-42.

## *1.4 Structure and dynamics of the tropopause region*

Vertical profiles of chemically resolved aerosol mass concentrations are an important aspect of this work. Therefore, relevant concepts and terminology describing the vertical structure of the atmosphere are introduced here. Figure 2 is the original graph published by Holton et al. (1995) including captions explaining the structure of the lower atmosphere as a function of pressure and altitude versus latitude. The dashed lines indicate ambient temperature while the solid contours denote the potential temperature. The potential temperature (theta, $\Theta$) is a measure of the temperature that an air parcel would have if it was moved dry-adiabatically to a pressure of 1000 hPa. Lines of constant $\Theta$ are isentropes. As long as the $\Theta$ of an air parcel is not changed by diabatic processes like radiative cooling or latent heat release, transport occurs along the isentropes. Based on this, potentially, air parcels at different locations can be linked while adjacent air masses can be distinguished based on their potential temperature as it may function as a measure of air mass origin as long as diabatic processes can be excluded in the history of the air mass. All air masses with a $\Theta$ below 300 K are per definition tropospheric, all with a $\Theta$ above 380 K are stratospheric. These two regimes are also called underworld and overworld, respectively. The middleworld, or lowermost stratosphere, is defined as the space between these two isentropes (grey shaded areas in Figure 2).

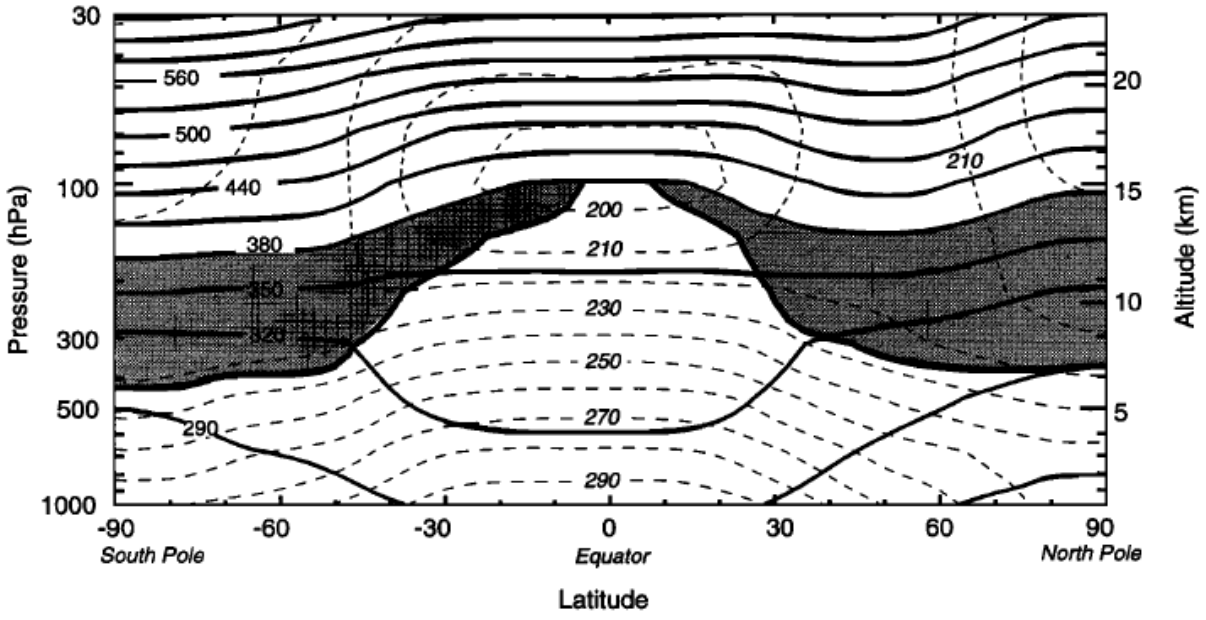


**Figure 1.** Latitude-altitude cross section for January 1993 showing longitudinally averaged potential temperature (solid contours) and temperature (dashed contours). The heavy solid contour (cut off at the 380-K isentrope) denotes the 2-PVU potential vorticity contour, which approximates the tropopause outside the tropics. Shaded areas denote the ''lowermost stratosphere,'' whose isentropic or potential temperature surfaces span the tropopause. Data are from UKMO analyses [*Swinbank and O'Neill*, 1994]. In these data the tropical tropopause occurs near $\theta \approx 380$ K, which is somewhat higher than the mean tropical tropopause potential temperature ($\theta \approx 370$ K) determined from radiosonde data by *Reid and Gage* [1981]. Polar tropopauses are far more variable and less well defined than might be suggested here. Figure courtesy of C. Appenzeller.

**Figure 2: Original figure with captions explaining the concept of the tropopause, upper troposphere and lower stratosphere as published in Holton et al. (1995).**

From Figure 2 it becomes clear that these regimes are a function of latitude. Near the tropics the middleworld disappears above 15 km altitude while it gains vertical extension towards the poles where it reaches down to roughly 8 km. The lower boundary of the lowermost stratosphere is indicated in the figure as the 2 potential vorticity unit (PVU in $10^{-6}$ $m^2$ $s^{-1}$ K $kg^{-1}$) isoline. Ertel's potential vorticity is a measure for the vertical stability of the atmosphere: the higher the PVU the more stable the layering of air masses and the more stratospheric the characteristics. This measure of stability describes a fundamental difference between the two regimes troposphere and stratosphere. Conventionally, 2 PVU are used as the threshold between the upper troposphere and lower stratosphere (UTLS) whereas values in literature range between 1 and > 3 (e.g. Bethan et al., 1996; Stohl et al., 2003a). Figure 2 shows that isentropes cross the 2 PVU isoline so that air mass transport from the troposphere to the stratosphere (TST) can happen polewards while exchange from the stratosphere to the troposphere (STT) happens towards the equator. For this work relevant details of TST and STT are elaborated later in this section.

The term UTLS was introduced in the literature to represent the immediate region above and below the 2 PVU isoline. This threshold is also described as tropopause. While the potential vorticity embodies a conservative dynamical tracer on the scale of a few days for the tropopause there are several other definitions referring to important differences between stratosphere and troposphere. According to the World Meteorological Organization's (WMO) temperature based definition the tropopause is reached once the vertical gradient of temperature with altitude (lapse rate) is equal to or smaller than -2 K/km ((WMO), 1986). In the troposphere temperature decreases with altitude while it stagnates near the tropopause at a (local) minimum and then increases in the stratosphere before it remains at a certain temperature again. The temperature interpretation of the tropopause, however, was not applied within the scope of this work. Next to the dynamic rather chemical definitions were used to determine the chemical composition of submicron aerosol relative to the tropopause. Chemical interpretations of the tropopause make use of the significantly different trace gas (and aerosol) composition of the two regimes.

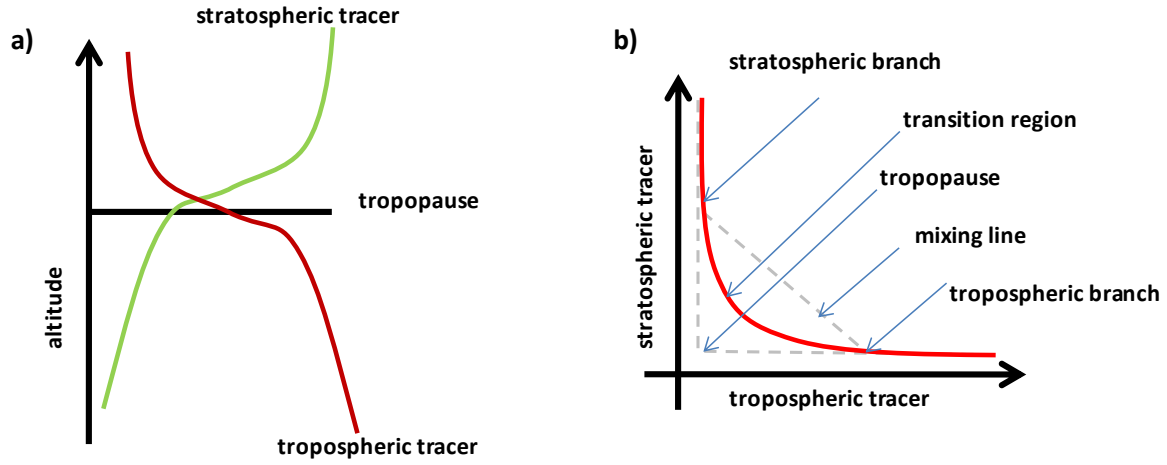


**Figure 3: Chemical definition of the tropopause. a) Schematic vertical profiles of tropospheric and stratospheric tracers. b) L-shaped profile resulting from relating the stratospheric to the tropospheric tracer. This figure is adapted from Pan et al. (2004).**

Figure 3 illustrates the chemical interpretation of the tropopause based on a stratospheric and tropospheric tracer as introduced in Pan et al. (2004). Panel a) shows the vertical profile of the two types of tracers. The stratospheric tracer, e.g. ozone, has a low concentration in the troposphere which increases gradually with altitude and steeply near the tropopause. The tropospheric tracer, e.g. carbon monoxide, shows the opposite behavior by decreasing slowly towards the tropopause and then abruptly above the threshold. When correlating the two tracers, as done in panel b), an L-shaped profile is obtained featuring distinct regimes. The upper vertical extending branch represents stratospheric characteristics while the lower horizontally directed branch indicates tropospheric properties. The tropopause is found where the two branches meet. If the interception resembles a right or slightly obtuse angle the transition from troposphere to stratosphere is sharp (compare grey dashed lines in Figure 3b). If the interception is curve-like (red line) a transition regime or mixing layer exists above the tropopause which exhibits stratospheric and tropospheric characteristics e.g. (Fischer et al., 2000; Hoor et al., 2004; Pan et al., 2004). Tracers might also fall along mixing lines (inclined grey dashed line) by means of which it can be estimated how strongly each regime influences the probed air mass. Instead of ozone and carbon monoxide other tracers such as water vapor and nitrous oxide ($N_2O$) can be used as tropospheric tracers, and $NO_y$ (relatively reactive total nitrogen gases $NO_y$ = N + NO + $NO_2$ + $ClONO_2$ + $NO_3$ + $N_2O_5$ + $BrONO_2$ + $HNO_3$ + other trace species (Solomon, 1999)) or even particulate matter as stratospheric tracers (e.g. Borrmann et al., 1995; Foltescu and Zahn, 1995; Fischer et al., 2000; Pan et al., 2004; Hoor et al., 2004; Hegglin et al., 2006; Strahan et al., 2007). When using onboard measured tracer correlations it has to be kept in mind that there are natural limitations inherent to in-situ measurements. The correlations cannot reflect the characteristics of a single vertical atmospheric column but rather represent properties along the entire flight track or the chosen segment.

Another way to determine the location of the chemical tropopause is based only on the ozone mixing ratio (Bethan et al., 1996) which by ozonesonde profiles has been observed to occur slightly below the thermal tropopause. As a result of 5 years long CARIBIC (Civil Aircraft for the Regular Investigation of the atmosphere Based on the Instrument Container) measurements between Germany and southern India and southern Africa Zahn and Brenninkmeijer (2003) introduced an empirical formula on how to derive the tropopause ozone mixing ratio. The formula (see Eq. 1) is a function of the day of the year due to seasonal variations of the UT ozone mixing ratio and is best applied in low polluted (little CO perturbations) regions which is between 35 and 45°N in their case.

$$O_3^{tropopause} = 97\ nmol\ mol^{-1} + 26\ nmol\ mol^{-1} * sin\left[\frac{2\pi(d_y - 30)}{365}\right] \quad \textbf{Eq. 1}$$

$O_3^{tropopause}$ denotes the ozone mixing ratio in nmol $mol^{-1}$ and $d_y$ is the day of year.

In this work not only the location of submicron aerosol with respect to the tropopause is determined but also the history of the air masses is discussed. This includes considerations on whether the air parcel has descended from the LS to the troposphere or vice versa. Chemically resolved measurements of particles during cross-tropopause exchange processes in the extra-tropics is of particular interest because this phenomenon has mainly been studied on a basis of trace gas measurements and model simulations (e.g. Shapiro, 1980; Holton et al., 1995; Sprenger and Wernli, 2003; Hoor et al., 2004;

Strahan et al., 2007). One major reason for this lack of data is the only recent development of aircraft-deployable aerosol mass spectrometers (see section 1.7) providing the needed time resolution and the limited number of aircraft and field experiments which are flown in the UTLS. In the following only a brief overview on the topic of UTLS air mass exchange is given with focus on the aspects most relevant for the observations reported in this work.

Generally, cross-tropopause exchange can occur in many ways, for example through large-scale and seasonal air mass movements between the potential temperature surfaces of 300 and 380 K, advection of air parcels along isentropes, intrusion associated to jet streams, tropopause folds (see Figure 32 b) and subsequent filamentation and small-scale diffusions (e.g. Shapiro, 1980; Holton et al., 1995; Appenzeller et al., 1996; Esler et al., 2001; Stohl et al., 2003c). Briefly, according to the WMO definition, jet streams are strong and narrow currents along a quasi-horizontal axis in the UTLS. They are characterized by high vertical and horizontal wind speeds with a defined minimum of 30 m $s^{-1}$. They can extent over several thousand kilometers in length encircling large parts of the globe, and several kilometers in width. Jet streams occur in the Southern and Northern Hemisphere (NH). In the NH there is a weaker subtropical jet near 30°N and a stronger polar jet stream by the polar front at high northern latitudes depending on the seasonal location. A tropopause cannot be defined within a jet stream. Tropopause folds can be associated with jet streams and described as stratospheric tongue-like intrusions into the troposphere. While the center of a fold exhibits stratospheric properties near the interface to the tropopause small scale mixing occurs (Holton et al., 1995). STE (stratosphere troposphere exchange, general term for STT and TST) can be subdivided in shallow and deep events where the deep events account only for 10 % of the air mass exchanges (James et al., 2003). Shallow events exhibit short residence times of stratospheric air masses in the troposphere or vice versa and mixing is likely to be reversible. Deep convective events intrude significantly into the stratosphere or troposphere and lead to irreversible air mass exchange (Stohl et al., 2003c). For the cases discussed in this work both types of STE apply, however not all events can be clearly categorized. Detailed discussions follow in sections 3 and 3.2. In the case of the Mts. Okmok and Kasatochi volcanic aerosol, deep intrusion into the stratosphere occurred through the ascending eruption column. When probing the plume, a tropopause fold was crossed with true stratospheric properties where mixing had not taken place. Only when flying very close to the modeled 2 PVU isosurface characteristics of a transition region could be observed (see section 3.1.3). Besides the sporadic volcanic deep TST more frequent intrusions occur by the entrance regions of the mid-latitude North Pacific and Atlantic storm tracks (Stohl et al., 2003c; Sprenger and Wernli, 2003) which are located over the Pacific east of Japan and over the Atlantic at the east coast of North America. These regions coincide with areas of intense anthropogenic activity and thus represent a potential source for emission transport into the lower stratosphere or upper troposphere (see sections 3 and 3.2). While this is generally true for all seasons, maximum air mass exchange occurs during winter. The strong and rapid (time scale of roughly 2 days) uplift of air masses occurs in so-called warm conveyor belts (WCB, Browning and Monk, 1982; Cooper et al., 2002; Eckhardt et al., 2004) associated with cold fronts in extratropical cyclones (low pressure systems). The warm and moist air mass ascends ahead of the cold front polewards in north or north-easterly flow and develops clouds as the humidity condenses in higher altitudes. These boundary layer air masses can well penetrate through the tropopause. Sprenger and Wernli (2003) found that TST is strongest near southern Greenland and the Aleutians. Another TST phenomenon is the so-

called pyroconvection in association with biomass burning triggered thunderstorm development (Fromm et al., 2005). This transport pathway is introduced in more detail in the context of biomass burning transport in section 1.5.2. Like TST, STT is less intense in summer than in winter. However, it is still significant over the Arctic and high northern latitudes and has been observed in individual cases described in section 3 and 3.2.

## *1.5 Sources, pathways, properties and effects of aerosol in the free troposphere and the UTLS*

Before going into details of source type specific aerosol properties, in the following subsections basic concepts that characterize atmospheric particles are discussed, based on the illustration in Figure 4. At the very bottom the terms for aerosol size modes are introduced.

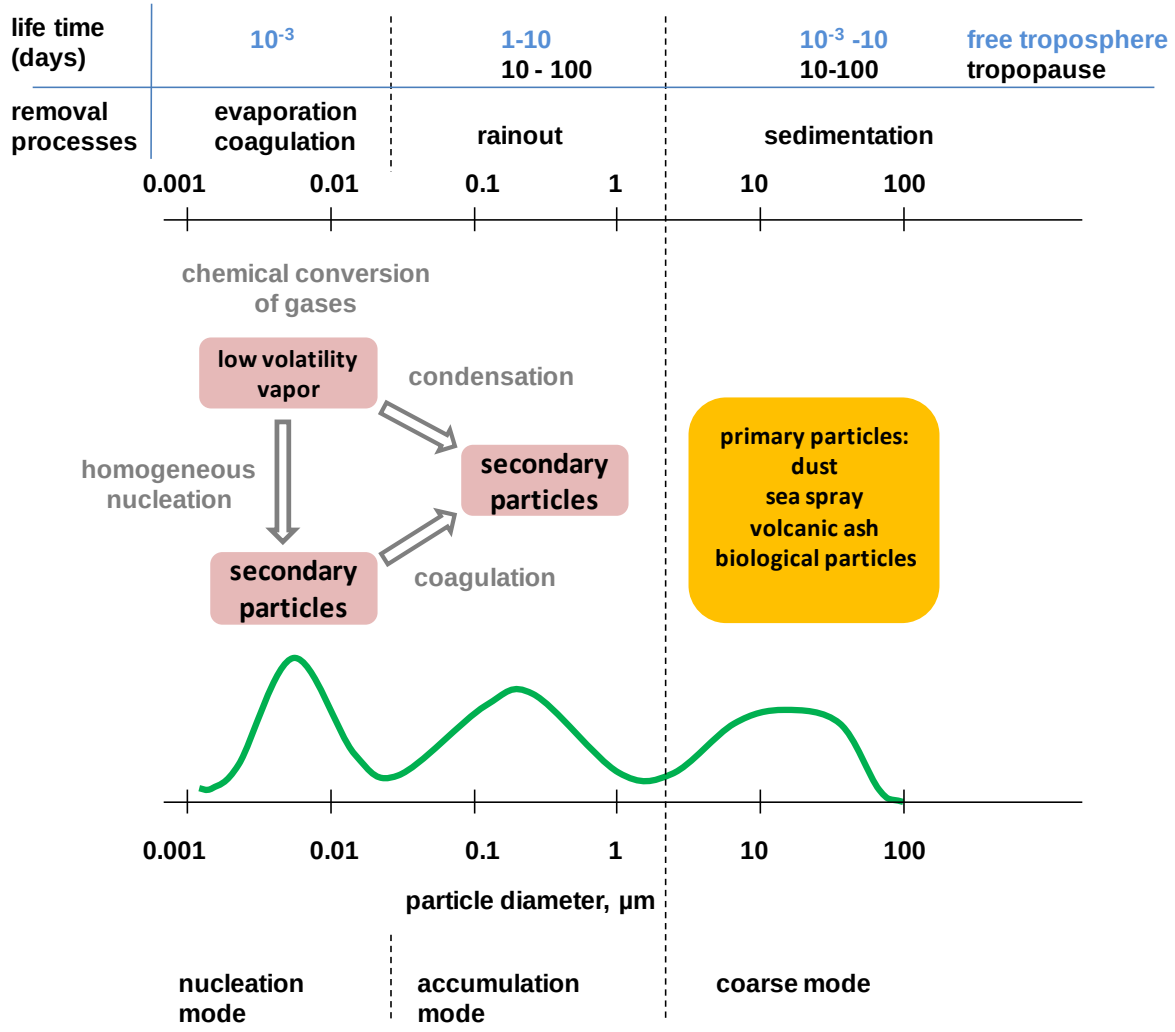


**Figure 4: Basic concept of atmospheric particle sources, size distributions, removal processes and lifetimes. This figure is adapted from Seinfeld and Pandis (2006) and Jaenicke (1988).**

Nucleation mode particles are in the order of 1 to 20 nanometers, particles in the size range of several 10 to several 100 nm are described by the accumulation mode while particles larger than 1 µm are attributed to the coarse mode (green curve). The smallest size category consists of secondary particles which were formed by homogeneous nucleation, i.e. low volatile vapors that cluster and subsequently form particles. The nucleation mode can grow to accumulation mode sizes by coagulation of particles. Another way of accumulation mode particle formation is the condensation of low volatile gases onto a pre-existing particle. In this way, different components which may originate from different sources, thus being constituted of different chemical substances, compose a single particle which is then called internally mixed. Externally mixed aerosol is composed of individual particles that consist of distinct

substances. Accumulation mode particles can serve as cloud condensation nuclei (CCN) or ice nuclei (IN) on which water vapor condenses or freezes thereby forming clouds and influencing the properties of clouds such as droplet number and size and therefore cloud lifetime and cloud emissivity. Many small drops lead to whiter clouds which reflect more sunlight. This is defined as the aerosol indirect effect. The aerosol direct effect refers to the particles' radiative properties. Black carbon, for example, absorbs strongly, while sulfate aerosol tends to scatter sunlight. Particles coated by condensed organic vapors adopt different optical properties. Since accumulation mode particles are involved in cloud formation processes they are removed primarily via precipitation from the atmosphere. Coarse particles are mainly emitted by primary processes and sediment quickly due to their relatively high mass. The removal processes influence aerosol lifetime which is denoted at the top of Figure 4. The most relevant size range for this work, the accumulation mode, has roughly a lifetime of 1 to 10 days in the free troposphere and up to several hundred days in the tropopause and stratosphere where wet removal cannot occur (see Figure 5). Nucleation mode particles have a short lifetime because they coagulate quickly to larger particles and coarse mode particles have such a high mass that they are deposited quickly by gravitational force.

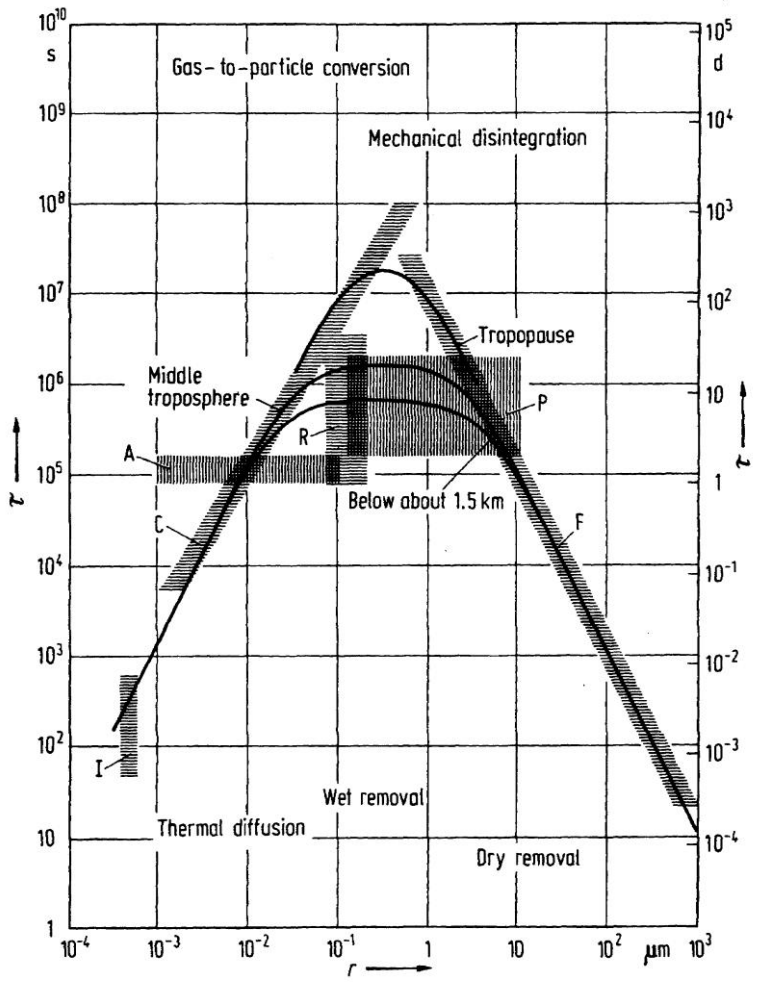


**Figure 5: Aerosol lifetime as a function of particle size from Jaenicke (1988). The bottom axis describes the radius of the particles while the vertical axes show their lifetime τ (left in seconds, right in days).**

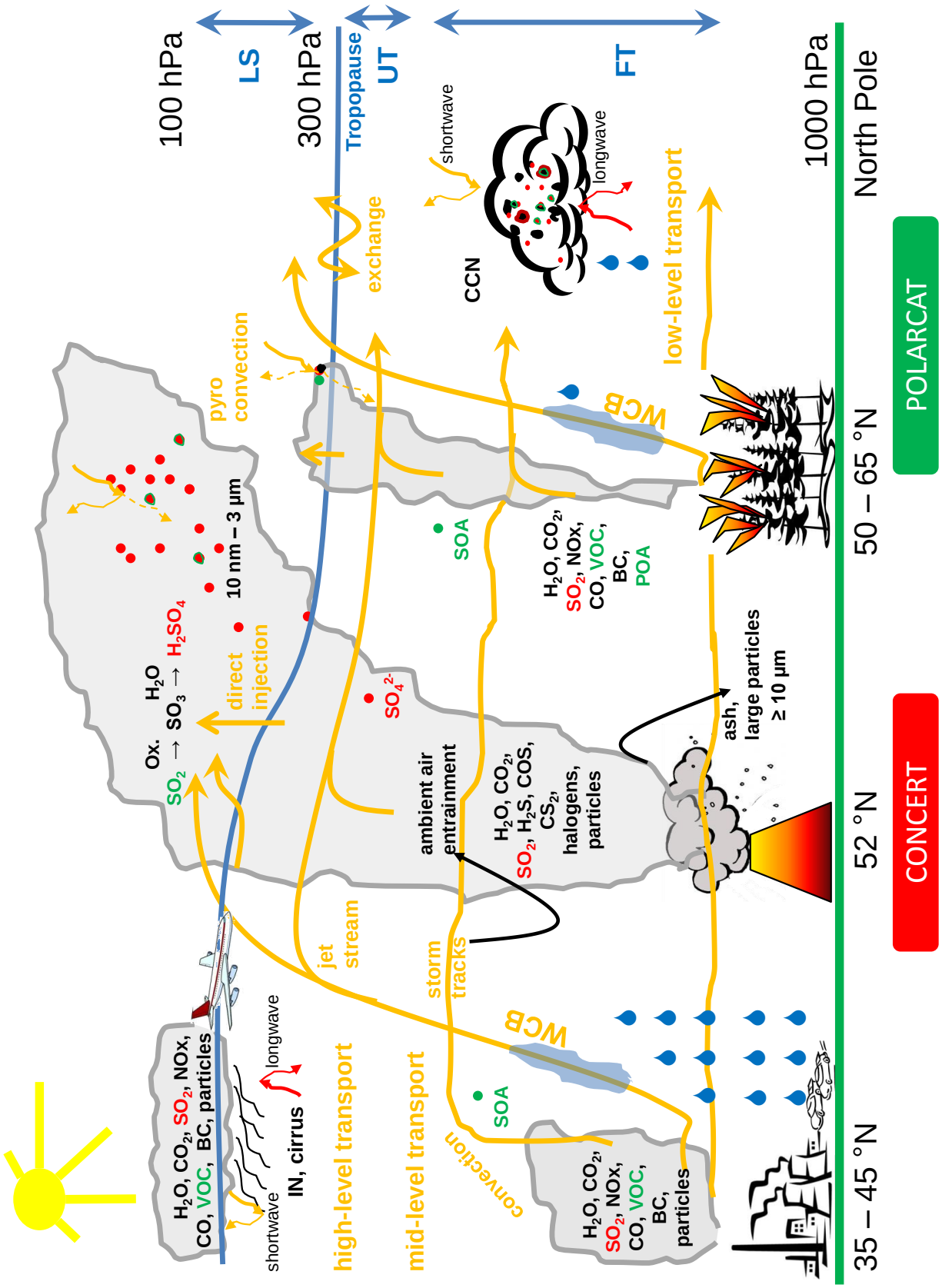


**Figure 6: Cartoon of the main emission sources, transport pathways and basic aerosol characteristics that were observed during POLARCAT and CONCERT campaigns.**

Figure 6 illustrates schematically the main emission sources which were probed during the POLARCAT and CONCERT campaigns and complemented by ARCATS data as a function of latitude. More specifically these are anthropogenic fossil fuel combustion (FF) between 35 and 45°N in East Asia and the United States, and air traffic above Central and Western Europe, boreal forest fires or biomass burning (BB) between 50 and 65°N in the Yakutsk region, Siberia, Saskatchewan, Canada, and less influential in Alaska, and two volcanic eruptions in the Aleutians at 52 and 53°N. BC stands for black carbon, VOC for volatile organic compounds, SOA for secondary organic aerosol, and POA for primary organic aerosol. The most relevant pathways are indicated (orange arrows) and show how emissions were transported away from their near surface sources and into higher regimes. On the right side the free troposphere (FT), upper troposphere (UT), tropopause (blue line) and lower stratosphere (LS) are marked. The transport patterns include low-level and free tropospheric transport, uplift by convection and in WCBs, advection in storm tracks and jet streams, and volcanic eruption or fire induced convection triggered direct injection into the UTLS. The receptor regions or sampling areas are indicated by the horizontal bars at the bottom saying CONCERT and POLARCAT. Also, the main emitted species and the basic $SO_2$ chemistry are indicated. Primary emitted and from precursor gases formed secondary particles interact with solar radiation through the aerosol direct effect. Depending on their properties they can also function as CCN or IN and thus significantly determine the characteristics of clouds and their emissivity. Clouds were drawn in prominent places for better readability of the figure but are not confined to these locations, as well as the associated precipitation. To indicate mechanisms of stratosphere troposphere exchange two orange rolling arrows cross the tropopause.

The following subsections provide more detailed information on aerosol properties and evolution, their transport pathways and potential effects classified according to the source type starting from pure natural emissions and ending at exclusively human induced pollution. [Large parts have been adapted from Schmale et al. (2010) and (2011).] Considerations on aerosol types which have not been observed during the respective field experiments, such as marine particles, mineral dust, primary and secondary organic aerosol from biogenic sources, e.g. forests, and biological aerosol etc. are excluded.

### *1.5.1 Volcanic eruptions*

Volcanoes are a purely natural, sporadic but important source of stratospheric aerosol and precursor gases. In Figure 6 an eruption column injecting chemical species into the stratosphere is shown. The emission of gaseous species and primary aerosol particles, which sediment quickly if too large, is depicted. Other particles like sulfuric acid droplets and trace gases are transported across the tropopause. Gaseous constituents, especially $SO_2$, undergo chemical oxidation and build up aerosol mass when forming new particles or condensing onto pre-existing ones. A more detailed description of the $SO_2$ chemistry is given in section 2.6.6. Also, chemical species in the free troposphere might be entrained into the eruption column and uplifted with it.

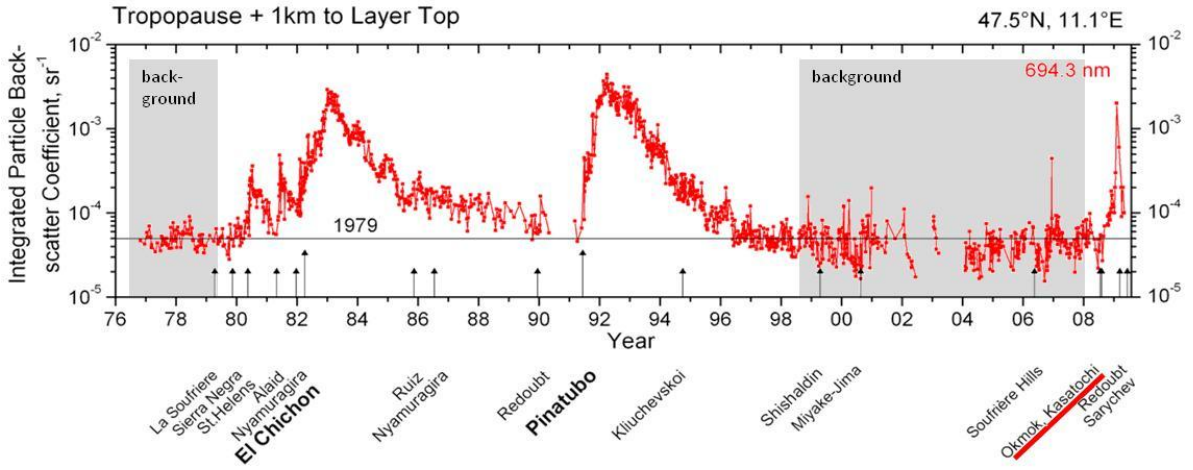


**Figure 7: Lidar observations (integrated particle backscatter coefficient, $sr^{-1}$) of stratospheric aerosol from 1976 to 2010 in Garmisch-Partenkirchen, Germany. Perturbations due to volcanic eruptions are indicated by arrows. This figure is adapted from (Trickl et al., 2010).**

Figure 7 provides an overview of stratospheric perturbations due to volcanic eruptions from 1976 to 2010 (Trickl et al., 2010). The measurements were performed by the lidar (light detection and ranging) at Garmisch-Partenkirchen and are shown as integrated particle backscatter coefficient ($sr^{-1}$) from 1 km above the tropopause to the layer top about 30 km (Jäger, 2005). Large eruptions like El Chichón (1982, Mexico) or Mt. Pinatubo (1991, Philippines) emitted approximately 8 and 20 Mt of sulfur dioxide, respectively, into the stratosphere (Krueger et al., 2008; von Glasow et al., 2009) that was eventually converted into sulfate (or sulfuric acid) aerosol and perturbed the stratosphere for half a decade (Thomas, 2003). Between these two eruptions stratospheric aerosol did not decline to background values. The grey columns in Figure 7 covering periods in the late 70's and from 98 – 2008 denote stratospheric aerosol background in volcanically quiescent times (Deshler, 2008; Borrmann et al., 2010) as does the horizontal grey line based on the average data from 1979. Only the eruption of Mts. Okmok and Kasatochi on 12 July and 7 August, 2008, terminated the latter period allowing for the first time to study stratospheric volcanic particles by means of airborne aerosol mass spectrometry. Previously only tropospheric mass spectrometric measurements of continuous volcanic sulfate emissions originating from Mts. Popocatépetl and Colima near Mexico City and Iceland have been reported by DeCarlo et al. (2008) and Ovadnevaite et al. (2009), respectively. In 2009 several more outbreaks contributed to the aerosol load in the stratosphere: Mt. Redoubt on 22 March and Mt. Sarychev on 13 June, and Mt. Shiveluch on 10 September, 2009, (Mattis et al., 2010). However, neither these plumes, nor the tropospheric plumes of Mt. Eyjafjalla in April and May 2010 (Schumann et al., 2011) were probed by airborne aerosol mass spectrometry.

Mt. Okmok (53.40° N, 168.17° W) became active between 12 July and 19 August, and Mt. Kasatochi (52.18° N, 175.51° W) on 7 and 8 August, 2008. Both plinian eruptions were strong enough to inject trace gases and aerosol particles into the stratosphere. The estimated altitude range for the multiple injections is between 8 and 20 km while the predominant receptor height was observed to be around 15.2 and 13.7 km for Mts. Okmok and Kasatochi, respectively (Karagulian et al., 2010; Bitar et al., 2010; Kristiansen et al., 2010). The enhanced trace gas and aerosol load in the lower stratosphere and tropopause has been observed by in-situ and remote sensing measurements, (e.g. Martinsson et al.,

2009; Theys et al., 2009; Mattis et al., 2010; Hoffmann et al., 2010; Jurkat et al., 2010). Based on these observations the estimated amount of $SO_2$ injected into the stratosphere is between 1.0 and 1.7 Tg for Mt. Kasatochi and 0.3 Tg for Mt. Okmok (Karagulian et al., 2010; Prata et al., 2010; Kristiansen et al., 2010). Compared to the amount of material which Mts. El Chichón and Pinatubo injected, these two eruptions are at least a factor 4 and 10 smaller, respectively. Model simulations revealed that their climatic effects were negligible mainly because of the reduced solar radiation by August and the fast decay of the aerosol layer so that it did not persist until the following spring (Kravitz et al., 2010). Based on satellite measurements stratospheric background conditions were reached again 7 months after the eruptions (Bourassa et al., 2010).

Unfortunately, this short episode of stratospheric perturbation did not allow for extensive in-situ aerosol and trace gas measurements which are indispensible for deducing chemical and microphysical properties, effects on heterogeneous chemistry, and climatic implications of volcanic plumes. Therefore, the main knowledge is based on intensive measurements performed after the Mt. Pinatubo eruption. In-situ aerosol data are available that quantify the additional particle surface area due to the volcanic aerosol, e.g. (Borrmann et al., 1993; Wilson et al., 1993; Jonsson et al., 1995). In addition to the effects of the volcanic aerosols on radiation and climate the particles offer surface and volume for heterogeneous reactions (Arnold et al., 1990; Fahey et al., 1993; Borrmann et al., 1997) and act as nuclei for the formation of polar stratospheric clouds (Thomason and Peter, 2006). Generally, polar stratospheric clouds form during winter as a result of adiabatic and diabatic air mass cooling which leads to condensation or freezing. In particular, for the layers directly in the vicinity of the mid-latitude tropopause heterogeneous effects of cirrus and volcanic aerosol enhancements may influence the ozone and water vapor abundance and thus the radiative budget (Lacis et al., 1990; Borrmann et al., 1996; Solomon et al., 1997; Forster and Shine, 2002; Voigt et al., 2006; Froyd et al., 2009a). For the descending aerosol layer after the 1991 Mt. Pinatubo eruption Keim et al. (1996) showed based on mid-latitude in-situ measurements that $NO_x$ can be reduced to almost zero near the thermal tropopause on account of heterogeneous processing. The influence of such chemistry on ozone is still under debate (Smith et al., 2001; von Hobe et al., 2011) and quantification of its magnitude and frequency of occurrence still remains open. The efficiency of heterogeneous reactions largely depends on the chemical composition and size of the aerosol particles involved (Cziczo et al., 2004; Froyd et al., 2009a). Reaction rates for e.g. $N_2O_5$ depend most significantly on aerosol particles when the surface area is between 2 and 5 $\mu m^2\ cm^{-3}$ (Fahey et al., 1993). Thus a small enhancement of reactive particles as provided by volcanic eruptions can increase the reaction rates efficiently in the upper troposphere and lower stratosphere (Sander et al., 2006; Griffiths et al., 2009). For these reasons direct in-situ measurements of the particulate chemical composition are of high value. This is in particular the case for the tropical UTLS where post eruption volcanic aerosols have been shown to contain significant amounts of volatile material (Borrmann et al., 2010) and where low temperatures enhance heterogeneous processing (Popp et al., 2007; Voigt et al., 2007). Comprehensive summaries of the issues in connection with volcanic aerosols are provided by SPARC und WMO Ozone assessments (WMO, 1999; Thomason and Peter, 2006) including extensive referencing and by von Glasow et al. (2009).

### *1.5.2 Biomass burning*

Biomass burning (BB) occurs ubiquitously all around the year and is a major source of atmospheric chemical composition perturbation. In the Northern Hemisphere around April and June to August wild fires are most frequent whereas inter-annual variations can be large (Bond et al., 2004; van der Werf et al., 2006). Most important for this work are fires which occur in the circumboreal between 50°N and the Arctic Circle that make up 4 % of global fires on average (Lavoue et al., 2000). Siberian boreal forest fires are estimated to contribute around 56 % of CO emissions from extratropical NH fires (van der Werf et al., 2006). In general, boreal biomass burning is ignited both naturally by lightning and by humans (Flannigan et al., 2009). However, while the number of human induced fires is greater, large fires are rather caused by lightning (Stocks et al., 2002).

BB is responsible for the emission of a vast number of different volatile, semi-volatile and particulate species that are primarily black carbon and of organic nature (Andreae and Merlet, 2001). According to the inventory by Bond et al. (2004) primary organic carbon aerosol emissions exceed black carbon release by a factor of 10 for forest and savanna fires. Reid et al. (2005) state that about 50 to 60 % of the emitted particle mass is composed of organic carbon and 5 to 10 % of BC. Roughly half of the organic matter is thought to be water soluble (Andreae and Rosenfeld, 2008). Focusing on gaseous precursor species, Table 1 lists the emission ratios of $SO_2$ and VOC (volatile organic compounds) to CO for fossil fuel combustion and biomass burning. FF characteristics are discussed in the following subsection. Both types of gaseous tracers, $SO_2$ and VOCs, will undergo chemical oxidation over time and transport and partition to the particle phase e.g. Hallquist et al. (2009), Donahue et al. (2009), Jimenez et al. (2009), and section 2.6.6 for $SO_2$ chemistry. Little $SO_2$ is released from wild fires with a ratio of below 1 %. Depending on the inventory the VOC emission of BB sources is in the same order magnitude as from FF emission (Streets et al., 2003) or roughly an order of magnitude smaller (Andreae and Merlet, 2001; Wiedinmyer et al., 2006; Yokelson et al., 2009; Neto et al., 2009). Even though it is suggested that BB events emit less VOCs than FF, the VOC/CO ratio is at least a factor 10 higher than the $SO_2$/CO ratio. Based on this and a recent estimation that secondary organic aerosol formed from BB emissions is responsible for roughly 5 % of the global organic aerosol (Cubison et al., 2011), a dominant particulate organics signature is expected in BB related aerosol. Yokelson et al. (2009) reported 67 times higher concentration of particulate carbon than sulfate measured by an AMS in relatively young BB plumes. Also Shinozuka et al. (2010) report on high ratios of organics to particulate sulfate for BB plumes measured by an AMS over Alaska during ACRTAS spring 2008. In aged plumes, however, the contribution of sulfate as a secondary species is expected to increase if sulfur sources are present along the transport pathway (Hudson et al., 2004). Young BB mass spectra can be identified by the ratio of certain markers for levoglucosan (*m/z* 60 and *m/z* 73, Schneider et al. (2006b) and Alfarra et al. (2007), which is a thermal decomposition product of cellulose (Simoneit et al., 1999). However, during long-range transport, especially in summer, particles might be photochemically processed to such high degree that levoglucosan is expected to be decomposed (Hennigan et al., 2010). Nevertheless, under special circumstances such as the spring Arctic atmosphere, which is characterized by cold temperatures and extreme dryness, *m/z* 60 has been observed even in mass spectra recorded out-of-plume in aged background air (Cubison et al., 2011).

**Table 1: Emission ratios of gaseous sulfur and gaseous organic compounds from fossil fuel (FF) and biomass burning (BB) based on several emission inventories and studies**

| Reference | Fossil fuel combustion | | Biomass burning | |
|---|---|---|---|---|
| | $SO_2$/CO | VOC/CO | $SO_2$/CO | VOC/CO |
| EDGAR 32FT2000 [1)] | 0.30-0.45 | - | - | - |
| Streets et al. (2003) [2)] | 0.16 | 0.19 | 0.007 | 0.18 |
| Lamarque et al. (2010) [3)] | 0.15 | 0.21 | 0.008 | 0.17 |
| Zhang et al. (2009) [4)] | 0.16 | 0.18 | - | - |
| Andreae and Merlet (2001) [5)] | - | - | 0.009 | 0.05 |
| Wiedinmyer et al. (2006) [6)] | - | - | 0.0004 | 0.004 |
| Yokelson et al. (2009) [7)] | - | - | - | 0.04 |
| Neto et al. (2009) [8)] | - | - | - | 0.05 |

[1)] for North America (Great Lakes, Ohio Valley, East Coast) and Asia (Beijing area, Korea, Japan)

[2)] Asia, values for FF correspond to combustion, values for BB to open burning, VOC = NMVOC

[3)] global for the year 2000

[4)] Asian anthropogenic emissions, VOC = NMVOC

[5)] extratropical forest, VOC = total VOC

[6)] average over all vegetation classes, VOC = NMHC

[7)] BB in the Yucatan, VOC = NMHC

[8)] deforestation in Brazil, VOC = NMHC

VOC = volatile organic compounds, NMVOC = non methane volatile organic compounds, NMHC = non methane hydrocarbons

Characterizing the size and chemical composition of BB particles is important to understand the effects on the radiative balance and climate. As for the aerosol direct effect, BC particles have a warming impact, while primary and secondary organic particles exhibit cooling properties (Maria et al., 2004). BC particles coated with organic matter are thought to absorb solar radiation even more than pure black carbon (Schwarz et al., 2008) and coating was observed to happen quickly (Shiraiwa et al., 2007). The organic aerosol (OA) indirect effect depends primarily on the cloud condensation nuclei characteristics. According to Reid et al. (2005) 80-90 % of the volume of biomass burning aerosol is found in accumulation mode which is coherent with more recent studies (e.g. Petzold et al., 2007). Generally, the size of an aerosol particle is more important for its CCN capability compared to the chemical composition: Larger particles are more effective than nucleation mode aerosol (Dusek et al., 2006). However, BB particles were found to be effective CCN even near the source still being relatively small and hydrophobic due to the large fraction of elemental carbon. In addition, during long-range transport, BC particles grow through coating by organic matter as organic acids form within BB plumes which become more hygroscopic during photochemical aging and thus enhance the

CCN capability (Reid et al., 2005: Andreae and Rosenfeld, 2008 and references therein). Consequently, BB particles have an impact on cloud formation processes, precipitation and radiation properties. In the context of Arctic clouds, Lance et al. (2011) found that BB aerosol leads to a decrease in precipitating ice particles in mixed-phased (containing ice particles and liquid droplets) clouds and an increase in cloud lifetime and emissivity.

Figure 8 provides a satellite view of MODIS (Moderate Resolution Imaging Spectroradiometer onboard NASA's Terra and Aqua satellites) observations of biomass burning between 29 June and 8 July, 2008. The orange circles highlight the fires in Yakutsk, Siberia, and Saskatchewan, Canada, from where BB aerosol long-range transport towards the Arctic happened. These emissions were intensively characterized during ARCTAS in Canada (e.g. Jacob et al., 2010; Singh et al., 2010), the YAK campaign in Russia (Paris et al., 2009) and POLARCAT in Greenland (Schmale et al., 2011; Quennehen et al., 2011), all in summer 2008.

BB aerosol is not only a local but also a hemispheric source for air pollution. Observed and modeled lifetimes range from 5 days for BC to up to 16 days for SOA near the tropopause (Koch and Hansen, 2005; Paris et al., 2009; Farina et al., 2010). Due to the elevated injection height of emissions compared to e.g. fossil fuel combustion, trace gases and particles frequently reach the free troposphere or even higher altitudes. Guan et al. (2010) investigated plume injection heights by means of satellite data and found that a large number of emissions reach altitudes higher than 5 km, especially over North America and Asia/Siberia. They also found an important number of events that reached the UTLS. Once the emissions enter the free troposphere they can be advected across long distances, thousands of kilometers, (Fromm and Servranckx, 2003; Jost et al., 2003; Mattis et al., 2003) including to the Arctic (Stohl et al., 2007; Hirdman et al., 2010). A rather recently discovered phenomenon is the fire started thunderstorm which is accompanied by strong convection facilitating fire emissions to reach the lower stratosphere (Fromm et al., 2008a; Fromm et al., 2008b). These incidents are also called pyro cumulonimbus or pyroCb. The presence of BB trace gases and particles in the LS has important implications on the characteristics of stratospheric aerosol which was formerly considered to originate primarily from volcanic eruptions (Fromm et al., 2010). According to Hudson et al. (2004) 7 % of submicron lower stratospheric particles exhibit BB signatures. PyroCb events were also observed in June / July 2008 during the ARCTAS summer campaign (personal communication, September, 2010[1]).

[1] The reference of this information is known by name to the author of this thesis.

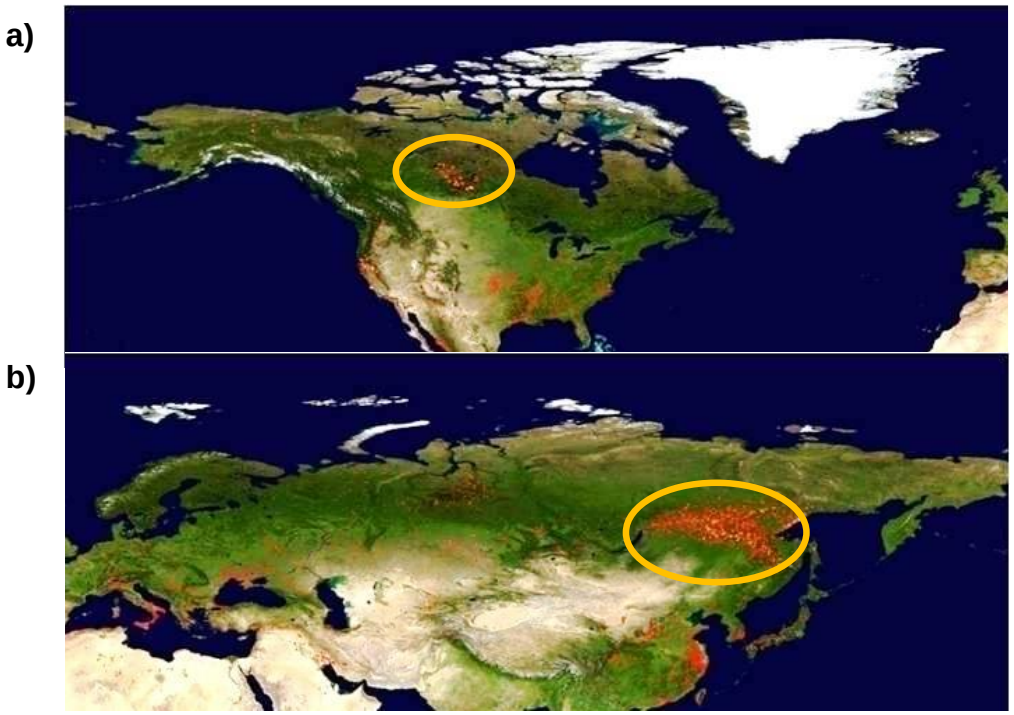


**Figure 8: Biomass burning in the Northern Hemisphere from 29 June to 8 July, 2008, recorded by MODIS (Moderate Resolution Imaging Spectroradiometer). The red dots denote fire events that were accounted for within the 10 day period. The orange circles indicate the relevant fire regions in Saskatchewan, Canada (a), and Yakutsk, Siberia (b). (downloaded from http://rapidfire.sci.gsfc.nasa.gov/firemaps/ on 14. April 2011)**

### *1.5.3 Fossil fuel combustion*

Our economies, industries and life styles including mobility are based on fossil fuel resources which we constantly burn to obtain energy. Thereby a multitude of trace gases and primary particles are emitted. The main activities contributing to FF emissions are power plants, industry, transport and domestic activities. Comparing global FF to BB emissions for the year 2000 based on an inventory by Lamarque et al. (2010) anthropogenic activities seem to be the larger emission source in terms of CO (608.3 vs 459.1 Tg $y^{-1}$), $SO_2$ (92.7 vs 3.8 Tg $y^{-1}$), VOCs (129.5 vs 78.3 Tg $y^{-1}$), and BC (5.0 vs 2.6 Tg $y^{-1}$), whereas the emission of primary organic aerosol is dominated by forest fires (23.3 vs 12.7 Tg $y^{-1}$). While the BB CO and $SO_2$ emissions increased by a factor of 1.4 between 1850 and 2000, mainly due to changing land use and associated fire clearing, FF sources released almost a factor 10 more CO and a factor 46 more $SO_2$. FF emissions are thus associated with a clear sulfate signature in the secondary formed aerosol (compare also Table 1). The $SO_2$ emission ratio for FF may vary largely due to the fuel sulfur content (FSC). While natural gas has a low FSC, bituminous coal might contain large fractions of sulfur of up to 2 % (Zhao et al., 2010). Historically, a first peak of $SO_2$ emissions has already been overcome after the 1990s when western industrialized countries introduced clean air acts thereby reducing emission of sulfur compounds. Recently, however, Asian development leads to increased emissions again (Asian Development Bank, 2008). Lu et al. (2010) report that the annual growth rate of $SO_2$ emissions from China was 7.3 % between 2000 and 2006. The main contribution came from Northern China power plants which almost doubled their $SO_2$ emissions in this period.

These historical changes of emission source areas and strengths are clearly reflected by particle deposition data from ice-cores from receptor regions like Greenland (McConnell et al., 2007). Figure 9 shows the satellite retrieved average $SO_2$ columns over the Northern Hemisphere for the year 2006 which reflects the situation in 2008 when the here discussed field campaigns were carried out. The enhancement over the Beijing area is clearly visible being currently the strongest emission sources on a global level. Additionally, the eastern United States, especially the Ohio Valley, strongly emit $SO_2$.

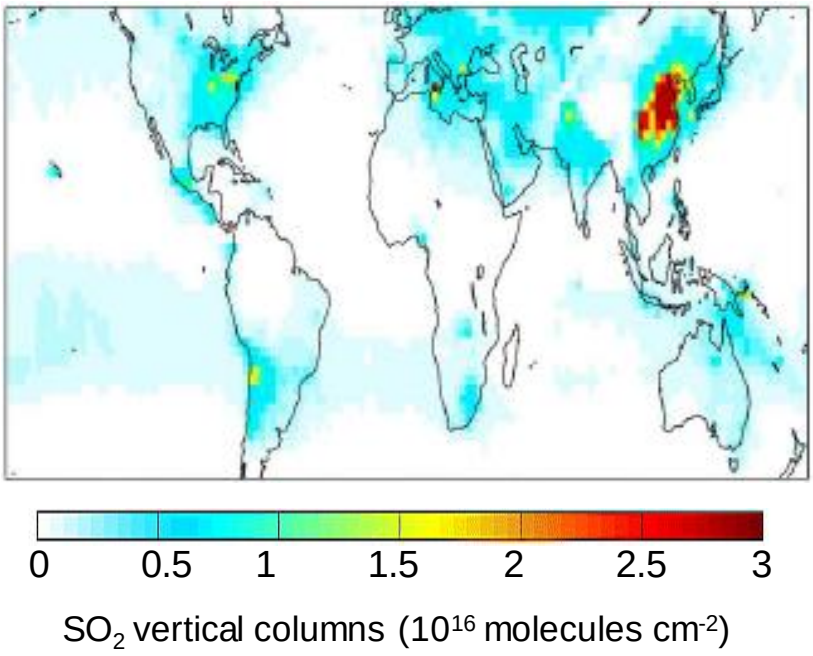


**Figure 9: SCIAMACHY annual mean $SO_2$ column for 2006, adapted from (Lee et al., 2011).**

Numerous field experiments involving AMS measurements to study the composition of primary and secondary anthropogenic aerosol, their evolution and effects were conducted at near-source surface sites in e.g. Pittsburgh (Zhang et al., 2005b), Mexico City (e.g. Aiken et al., 2009) or Beijing (Takegawa et al., 2009) or by airborne studies close to and distant from the source (e.g. Crosier et al., 2007; DeCarlo et al., 2008; Bahreini et al., 2009; Dunlea et al., 2009). Generally, near-source anthropogenic aerosol comprises organic matter, particulate sulfate, ammonium, nitrate and chloride, based on a multitude of AMS measurements (Zhang et al., 2007a), black carbon and other components. The contribution of each species depends strongly on the source type, the FSC and the $NO_x$ chemistry which is responsible for particulate nitrate. Aged outflow plumes exhibit a different composition with enhanced particulate sulfate and organics fractions, low particulate ammonium (below 10 %) associated to sulfate, and nitrate contributions near 1 % (Dunlea et al., 2009). The changed composition is due to several factors such as wet deposition of highly water soluble aerosol which is especially important for nitrate components, and the formation of secondary species such as particulate sulfate and secondary organic aerosol. It has been established that SOA forms roughly within one day downwind of the emission source (DeCarlo et al., 2008; Brock et al., 2008) while the exponential production time for sulfate is around 3 to 4 days in summer (Brock et al., 2008). In the absence of cloud processing this means that young (1-2 days) anthropogenic plumes are dominated by organic matter, while with increasing age sulfate will gain in importance. Much attention has been paid to the evolution of the organic aerosol component. Close to the emission source hydrocarbon-like

organic aerosol (HOA) from incomplete combustion is dominant while downwind oxygenated organic aerosol (OOA) is found. OA evolves during the atmospheric aging process over semi-volatile (SV-) to highly oxygenated organic aerosol, i.e. low-volatile (LV-) OOA (Jimenez et al., 2009). This is determined by a high fraction of the organic aerosol contribution to the *m/z* 44 in the AMS mass spectra (Zhang et al., 2005a). The contribution from chemically changed HOA to downwind or long-range transported OA was observed to be low. Rather the formation of SOA is responsible for the increase in OA mass (Zhang et al., 2007a). As particulate sulfate is equally a secondary species, OOA and particulate sulfate are often found to be positively correlated (Zhang et al., 2005a). For measurements conducted in the free troposphere and UTLS over Europe and Greenland, characteristics of the SV- and LV-OOA component are of higher interest than HOA as it was not detected in the pollution plumes due to the long distance from the source. Due to the extended time of one to two weeks the aerosol spent in the atmosphere before detection, some properties can be estimated to be quite similar despite the different emission origins. Most particles are found in the accumulation mode and are likely to have similar CCN capabilities due to the aging of the organic matter and thus chemical homogenization (Andreae, 2009; Jimenez et al., 2009; Roberts et al., 2010).

With regard to FF source regions relevant for POLARCAT, CONCERT and ARCTAS-summer campaigns mainly already characterized transport patterns of pollution outflow from East Asia, Siberia and North America were observed. Long-range transport from East Asia towards North America is strongly determined by cyclones, the westerly zonal winds and seasonal convection. Two important factors for efficient intercontinental transport are the uplifting of air masses from the boundary layer to the mid or upper troposphere and the strong winds (jet streams) in the upper troposphere which allow for rapid advection of short-lived pollution (Wuebbles et al., 2007). One of the most important lofting mechanisms is the warm conveyor belt (Wuebbles et al., 2007; Dickerson et al., 2007; Dunlea et al., 2009). As discussed in section 1.4 WCB are associated with precipitation events through which water soluble particles will be scavenged influencing strongly the composition of long-range transport aerosol. Based on the discussion above, secondary species (organic matter and particulate sulfate) are thus more likely to arrive at the receptor regions than other aerosol constituents (e.g. Dunlea et al., 2009). Hydrophobic particles were found to have a higher export efficiency than hygroscopic particles. The export efficiency from combustion related emissions is defined after Park et al. (2005) as the inverse of the emission ratio of species *X* to CO, times the ratio of the enhancements of *X* and CO over the background at a defined altitude. Park et al. report that the export efficiency of BC is at least 63 % in altitudes between 2 and 4 km and 27 % between 4 and 6 km over the Pacific whereas efficiencies for sulfur and nitrate species are lower. A similar study for BC export to the North American Arctic in summer 2008 based on ARCTAS data by Matsui et al. (2011) revealed that efficiencies are 4 % for Siberian BB and below 1 % for Asian FF due to the enhanced wash-out along the pathways. The importance and impact of East Asian aerosol outflow on regional meteorological patterns has been shown by Zhang et al. (2007b) who argue that due to aerosol-cloud interactions convection and precipitation over the Pacific is enhanced leading to intensified Pacific storm tracks. This phenomenon, however, occurs primarily during winter season.

Dickerson et al. (2007) argue that next to WCB lofting over the Pacific Ocean dry convection is the more important mechanism over the continent that feeds pollution into the westerly winds. In addition,

the second phase of the POLARCAT campaign was characterized by cross-polar transport of Asian and Siberian pollution towards Greenland (Sodemann et al., 2010; Roiger et al., 2011). Despite the different pathway the air mass uplifting occurred as well in WCBs as described in detail by Roiger et al. (2011) and as illustrated in Figure 50. Generally, for the POLARCAT and ARCTAS-summer campaigns Asian and Siberian pollution arrived primarily in the mid and upper troposphere and in several cases in the lower stratosphere.

Like for Asian pollution export WCBs and all associated aspects play a significant role over the West Atlantic of the east coast of the United States (Cooper et al., 2002) and were responsible for pollution plumes detected in the mid and upper troposphere above Greenland. Additionally, low-level transported outflow from the Ohio Valley region occurs regularly (Stohl et al., 2003b). In such cases air masses travel at low altitudes over the North Atlantic in north-easterly direction towards Greenland where they are uplifted due to the high elevation of the ice sheet and continue in the mid troposphere north of Iceland towards north-western Europe. This pathway was observed near the southern tip of Greenland at altitudes around 2 km and over Ireland in the mid troposphere.

A source of FF aerosol different from all discussed ones above is the exhaust from aircraft which was sampled during the CONCERT campaign. It is distinct in the sense that the emissions are released directly in the UTLS, in cruising altitude, and do not need to be uplifted and thus avoid potential wet removal. Aircraft engines emit a large variety of compounds among which water vapor, primary particles such as soot, and aerosol precursor gases are most relevant for the formation of contrails. When the hot and humid air mixes with the cold and dry ambient air, supersaturation with respect to ice and water can be reached and the water vapor condenses on the available particulate matter. It is assumed that condensation starts to form water or solution droplets first since higher supersaturation for ice crystal nucleation is necessary except for very low temperatures (Schumann, 1996). If ambient temperatures are below the freezing point or as the air cools further, the droplets become supercooled and can subsequently freeze and form ice crystals. If saturation conditions exist throughout longer periods, contrails may become persistent and evolve into cirrus clouds (ice clouds). The available particulate matter originates either from the combustion process or is entrained by mixing with ambient air. Also, secondary particulate matter can be formed through the oxidation of $SO_2$, whose amount is a function of the FSC, and VOCs and subsequent condensation (Kärcher et al., 2007). From the perspective of AMS detectable species, young contrails will probably contain little non-refractory aerosol in the size range which is transmitted through the inlet system. Soot particles are non-detectable, other primary non-refractory particles are too small, and the secondary formation of aerosol exceeds the timescale of several seconds to minutes as does the coagulation of particles (Kärcher et al., 2007). After a period of time in which aerosol might have formed and grown to detectable sizes dilution will be too strong as to distinguish the “plume” from UTLS background (see section 3.3). Nevertheless, from a climate perspective, the study of contrails is of greatest interest as the particles exhibit direct and indirect radiative effects. As for the latter, the net effect is estimated to be positive and accounts for roughly 5 % of anthropogenic radiative forcing. Contrails and contrail-induced cirrus reflect solar radiation thereby cooling but also reflect longwave terrestrial radiation thereby heating which is the more dominant effect (Lee et al., 2009). As aviation is still on the rise the impact is increasing. Aircraft exhaust does not only have implications through contrail formation but also

through the deposition of particles in the lower stratosphere. Forster et al. (2003) found by means of a modeling study that between 60 and 70 % of the emissions are directly released to the LS and have a mean residence time of 23 days. The impact of trace gas and particle injection into the stratosphere has already been discussed in section 1.5.1 by the example of volcanic eruptions.

## *1.6 Current knowledge of the atmospheric vertical distribution of aerosol chemical components and new contributions through this work*

Several chemical aerosol measurements have been performed in the past ten years providing a general perspective on the composition of particles in the atmosphere as a function of altitude. Even though techniques other than mass spectrometry, e.g. Lee et al. (2003) and Kline et al. (2004), have added to the current knowledge, this section focuses on contributions made by aerosol mass spectrometry. Knowing the vertical aerosol chemical distribution and particle mixing state is necessary to understand the atmospheric budget of aerosol, the associated light scattering (aerosol direct effect), the impact of aerosol size and chemistry on CCN capability (aerosol indirect effect) and the impact of particles on gas phase tracers through heterogeneous chemistry (Murphy et al., 2006; Solomon et al., 2007; Pratt and Prather, 2010). The latter is especially important in the UTLS where water vapor and ozone abundances are most climate-sensitive (Lacis et al., 1990; Forster and Shine, 2002). Furthermore, this type of information is indispensible for global modeling studies trying to estimate the role of aerosol radiative impact for climate change.

This paragraph briefly summarizes the current state of knowledge of aerosol chemical vertical distribution. In the planetary boundary layer, closer to emission sources, particles are constituted of a larger variety of chemical compounds including amongst other ammonium sulfate, ammonium nitrate, organic matter (e.g. Crosier et al., 2007; Morgan et al., 2010b) and black carbon. Especially ammonium nitrate and –sulfate containing particles have larger scattering properties than distinctly composed higher altitude aerosol (Morgan et al., 2010a). Next to the aerosol mass also the number of chemical superordinate species, i.e. particulate sulfate, organics, ammonium, nitrate, black carbon, dust, sea salt etc., declines with altitude in the free troposphere. The main reasons for lower particle concentrations are dilution and scavenging. Many studies found that the major free tropospheric aerosol constituents are particulate sulfate and carbonaceous and organic matter (e.g. Murphy et al., 2006; Schneider et al., 2006a; Pratt and Prather, 2010) which seem to be internally mixed (Pratt and Prather, 2010). Implications and effects have been discussed in the previous sections. In the upper troposphere and tropopause only few measurements have been conducted so far. For the tropical regions it was found that UT aerosol was composed mainly of highly oxygenated organic material, partly containing nitrate probably due to direct injection through convection (Froyd et al., 2009b). Above the local tropopause organic matter containing aerosol concentration decreases and sulfuric acid particles are most abundant (Murphy et al., 1998; Froyd et al., 2009b). However, organic material is still present and it was observed that sulfate particles formed in the stratosphere assimilated organic matter when descending to the tropopause (Murphy et al., 2007). Also the injection of BB particles directly into the LS has been observed (Fromm et al., 2010). Regarding trends of stratospheric aerosol, Hofmann et al. (2009) report of long-term lidar measurements on Mauna Loa, Hawaii, and Boulder, Colorado, where an increase in aerosol backscatter between 20 and 30 km altitude in the order of 4-7 % was found beginning in 2001. The authors attribute this enhancement to intensified coal burning in East Asia and the related $SO_2$ emissions of which 0.6 – 0.8 % reach the stratosphere. Considering this from the perspective of where relevant TST happens, it is likely that East Asian emissions enter the stratosphere via the North Pacific storm track east of Japan. However, Vernier et al. (2011) argue

that such large increase in stratospheric background aerosol cannot exclusively be attributed to anthropogenic activity. According to their observations, rather a number of medium explosive tropical volcanic eruptions after 2002 are responsible for the gradual increase in the aerosol optical thickness between 20 and 25 km altitude.

Results which I obtained during the POLARCAT and CONCERT campaigns can contribute to the current knowledge in several respects. Information regarding the vertical distribution of particulate matter in the Greenland troposphere is very scarce, hence the data will reveal how this remote region is impacted by long-range transport of short-lived aerosol in summer. Concentrations are usually too low to be characterized by means of satellite data but nevertheless significant with regard to their impacts in the sub-Arctic and Arctic environment as ice-core data show. Furthermore, there is almost no aerosol data available from regions this remote as such, so that especially the photochemical state of organic material is of high interest. Considering the outcome from the CONCERT campaign the chemical in-situ analysis of lower stratospheric volcanic aerosol is a novum which showed that opposed to the former belief volcanic particulate matter is not solely composed of binary sulfuric acid water droplets but also organic matter is present in the aerosol. At the same time this confirms observations as discussed above that suggested the presence of organic material in the LS imported from the troposphere.

## *1.7 Overview of on-line airborne mass spectrometric particle measurements*

To measure the aerosol chemical composition in the UTLS it is necessary to operate aerosol mass spectrometers on aircraft. However, airborne on-line size-resolved mass spectrometric measurements of submicron particles are still sparse since respective aircraft deployable instruments have only been developed since the late 1990s. The following technical challenges have to be overcome: A reduced physical size is required for installing the instruments in standard aircraft racks. The overall payload and energy supply are usually limited so the instruments need to be light-weight and power efficient. Moreover, since aircraft move at speeds between 100 and 200 m $s^{-1}$, propeller airliner and jet aircraft, respectively, fast data acquisition is indispensable as measurement conditions change quickly and aerosol composition might be highly variable. Slow response times would lead to undifferentiated data and inhibit detailed understanding of particle chemical composition in the atmosphere. Furthermore, away from sources the particle concentration can be very low, less than 1 µg $m^{-3}$ (Murphy, 2005) so high sensitivities and low detection limits are necessary. Furthermore, with on-line techniques sampling artifacts such as evaporation of volatile particle components (e.g. ammonium, organics) or condensation of gas-phase components onto the particles are mainly avoided. An alternative to aircraft-based mass spectrometer deployment, balloon borne experiments have been conducted to study the bulk composition of polar stratospheric aerosol (Arnold et al., 1998; Voigt et al., 2000; Schreiner et al., 2002). However, the aircraft deployment has several advantages over balloon missions such as better electrical power supply, the possibility that an operator can accompany the instrument and the flight track can be controlled and adapted if necessary.

Basically, there are two categories of mass spectrometric instruments which meet the requirements: the single particle and the particle ensemble mass spectrometers (MS). The first type of MS attributes the chemical composition and size to a single particle while the second type of MS chemically characterizes particles within a certain size range and measures their mass size distribution. The Aerodyne AMS, an ensemble instrument, is the only aircraft deployable one of its kind whereas there are several exemplars in the first category. They shall only be mentioned very briefly here. A more thorough discussion can be found in Brands (2009). The PALMS (Particle Analysis by Laser Mass Spectrometry, (Murphy and Thomson, 1995)) was the very first aerosol mass spectrometer to be operated during the WB-57 Aerosol Mission in 1998 (Murphy et al., 1998) and has been flown several times since. The (A)-ATOFMS (Aircraft Aerosol Time-of-Flight Mass Spectrometer (Pratt et al., 2009) was deployed first in 2007 on a C-130 aircraft during ICE-L (Ice in Clouds Experiment-Layer Clouds), and SPLAT II (Single Particle Laser Ablation Time-of-Flight Mass Spectrometer, (Zelenyuk et al., 2009) during ISDAC (Indirect and Semi-Direct Aerosol Campaign) in 2009. ALABAMA (Aircraft-based Laser Ablation Aerosol Mass Spectrometer, (Brands et al., 2011), the most recent development, measured boundary layer aerosol over Paris onboard the ATR-42 during MEGAPOLI (Megacities: Emissions, urban, regional and Global Atmospheric POLlution and climate effects, and Integrated tools for assessment and mitigation) in summer 2009.

In contrast to the AMS these instruments use laser desorption and ionization and detect either positive or negative ions with the time-of-flight MS in the case of the PALMS or both ion types for all other instruments. An important research focus for single particle MS is the characterization of ice particle

residuals in the context of cirrus cloud formation processes. Also, Murphy et al. (1998) reported on the chemical composition of UTLS aerosol and Hudson et al. (2004) focused on biomass burning particles. Moreover, these instruments have the ability to detect refractory particulate matter such as soot, mineral dust and metals which the AMS cannot measure.

While single particle MS were deployed first on aircraft, the airborne operation of AMS has also been established by now. The history of AMS aircraft deployments (see Table 2) starts in 2001 with a Q-AMS on a Twin Otter aircraft during ACE-Asia (Aerosol Characterization Experiment). Since then, AMS instruments were flown about 19 times until summer 2009 including the newer developments of the compact and the high resolution time-of-flight AMS. Details regarding the different versions of AMS instruments are discussed in chapter 2. Most campaigns with extensive AMS participation were conducted in 2004, 2006 and 2008. The research foci were manifold and included the general chemical composition of the atmosphere, aircraft exhaust characterization, distribution and chemical evolution of urban/anthropogenic aerosol, biomass burning aerosol, and detection and identification of long-range transport particulate pollution. Next to the evaluation of the size-resolved chemical data as such, AMS results are used to complement particle optical property and cloud condensation nuclei measurements for multi-dimensional aerosol characterization (e.g., Morgan et al., 2010a; Lance et al., 2011; McNaughton et al., 2011). The majority of campaigns took place in the proximity of highly polluted areas or near biomass burning sources so that aerosol concentration was usually well above detection limit. An exception are measurements conducted mainly in the free troposphere away from sources such as ICARTT-ITOP based in the Azores and as described in Morgan et al. (2009) and during CONCERT (Schmale et al., 2010). The campaign operated in the most remote region was POLARCAT in Greenland (Schmale et al., 2011). Altitudes ranged between near surface (boundary layer) to 12 km (UTLS). Most campaigns were flown in the lower and free troposphere, either due to the maximum altitude ceiling of the aircraft or due to the scientific objectives of the campaigns. Out of the aircraft fleet from Table 2 exclusively the two jet aircraft DC-8 (four engines) and Falcon (two engines) are able to reach the upper troposphere and lower stratosphere so that only four missions (PAZI, ARCTAS I & II and CONCERT) provide AMS data in these altitudes. Future AMS deployments aboard the DLR HALO (High Altitude LOng Range Research Aircraft) will contribute significantly to the available data.

**Table 2: History of AMS aircraft deployments**

| Year | Instrument | Aircraft | Location | Max. Altitude | Acronym | Focus | Publication |
|---|---|---|---|---|---|---|---|
| 2001 | Q-AMS | Twin Otter | East Asia | 3.7 km | ACE-Asia | East Asian outflow | Bahreini et al. (2003) |
| 2003 | Q-AMS | Falcon | Germany | 11 km | PAZI | Aircraft exhaust, tropospheric chemical composition | Schneider et al. (2006a) |
| 2004 | Q-AMS | WP-3D | US East Coast | 6.4 km | NEAQS-ITCT ICARTT | Air Quality and air mass chemical evolution over NE United States | Brock et al. (2008) |
| 2004 | Q-AMS | BAe-146 | Azores | 9 km | ITOP ICARTT | Long-range transport from North America | Fehsenfeld et al. (2006), Lewis et al. (2007) |
| 2004 | Q-AMS | Twin Otter | Cleveland, USA | FT | ICARTT Cloud-Aerosol Study | Aerosol Cloud interaction | Fountoukis et al. (2007) |
| 2004 | Q-AMS | BAe-146 | Po, Valley, Adriatic and Black Sea | 5 km | ADRIEX | Quantative analysis of internally/externally mixed aerosol | Crosier et al. (2007), Brooks et al. (2007) |
| 2005 / 2006 | Q-AMS | BAe-146 | UK, western Europe | 10.5 km | - | Tropospheric chemical composition | Morgan et al. (2009) |
| 2006 | C-ToF-AMS | WP-3D | Texas | 6.5 km | TexAQS II | Distribution and evolution of industrial/urban aerosol in the atmosphere | Bahreini et al. (2009) |
| 2006 | Q-AMS | Twin Otter | Texas | FT | TexAQS II | Aerosol and cloud properties in the free troposphere | Parrish et al. (2009) |
| 2006 | HR-ToF-AMS | C-130 | Washington, USA | 7.5 km | Intex-B | Asian long-range transport | Dunlea et al. (2009), Roberts et al. (2010) |
| 2006 | Q-AMS | Cessna | Whistler, Canada | 5 km | Intex-B | Asian long-range transport | Van Donkelaar et al. (2008) |
| 2006 | HR-ToF-AMS | C-130 | Mexico City, central Mexico | 2 km, 6 km | MILAGRO / MIRAGE | Megacity boundary layer aerosol, megacity outflow | DeCarlo et al. (2006; 2008; 2010) |
| 2008 | C-ToF-AMS | BAe-146 | Europe | 3 km (5 km) | LONGREX (EUCAARI) | Chemical composition and evolution of OA in the PBL | Morgan et al. (2010a; 2010b) |

| | | | | | | | |
|---|---|---|---|---|---|---|---|
| 2008 | HR-ToF-AMS | DC-8 | Alaska | 12 km | ARCTAS-I | Tropospheric composition of the Arctic | Jacob et al. (2010), Singh et al. (2010) |
| 2008 | C-ToF-AMS | WP-3D | Alaska | 7.4 km | ARCPAC | Aerosol, radiation and cloud processes affecting the Arctic Climate | Brock et al. (2010) |
| 2008 | C-ToF-AMS | ATR-42 | Rotterdam, North-Western Europe | 3 km | EUCAARI | Aerosol Cloud interactions and European Air Quality | Weigel et al., in prep. |
| 2008 | C-ToF-AMS | ATR-42 | Greenland | 7.6 km | POLARCAT | Long-range pollution transport to the Arctic | Schmale et al. (2011) |
| 2008 | HR-ToF-AMS | DC-8 | California, Canada | 12 km | ARCTAS-CARB, ARCTAS-II | Biomass Burning emissions, tropospheric composition of the Arctic | Jacob et al. (2010), Singh et al. (2010) |
| 2008 | C-ToF-AMS | Falcon | Central and Western Europe | 12 km | CONCERT | Aircraft exhaust, volcanic aerosol | Schmale et al. (2010) |
| 2009 | C-ToF-AMS | ATR-42 | Paris | 5 km | MEGAPOLI | Megacity boundary layer and outflow aerosol characterization and evolution | - |

# 2. The mass spectrometer, data analysis, complementary tools, air mass and plume classification

## *2.1 Description of the aerosol mass spectrometer*

In this section, the general set-up and functioning of the compact time-of-flight aerosol mass spectrometer (C-ToF-AMS) used for measurements discussed in this thesis are presented briefly. Aircraft deployment specific issues are highlighted. Thorough descriptions of the C-ToF-AMS can be found in Drewnick et al. (2005) and in the PhD thesis by Hings (2006).

### *2.1.1 Functioning of the AMS*

On both aircraft the same instrument was used to measure the chemical composition, mass concentration, and size distributions of non-refractory submicron particles (Drewnick et al., 2005; Canagaratna et al., 2007). The C-ToF-AMS is a unit resolution mass spectrometer.

Figure 10 shows a schematic set-up of the C-ToF-AMS (adapted from Drewnick et al. (2005) and Kimmel et al. (2008)) Typically, aerosol is sampled through a critical orifice (100 µm) at a flow rate of 1.4 $cm^3s^{-1}$ at sea level pressure upstream of an aerodynamic lens system (Liu et al., 2007; Liu et al., 1995a, b) which focuses the particles into a narrow beam before they enter the vacuum chamber. Generally, this system permits the detection of particles in the range of 30 – 1000 nm vacuum aerodynamic diameter ($d_{va}$) (Liu et al., 2007). The aerodynamic diameter is defined as:

$$d_{va} = d_{mob} * S * \frac{\rho_p}{\rho_0}$$

**Eq. 2**

with $d_{mob}$: mobility diameter, $S$: Jayne shape factor, $\rho_p$ particle density, and $\rho_0$ unit density (Jayne et al., 2000; DeCarlo et al., 2004). Details regarding the orifice, flow rate and actual detected particle size range are discussed in section 2.3. The chamber is pumped differentially with five turbo pumps in total which establish a vacuum of approximately $10^{-7}$ mbar at the rear side of the chamber. The entrance of the chamber is separated from the main body by a 1 mm inner diameter (ID) skimmer to further reduce the pressure. Behind the lens, the particles are thus concentrated and accelerated. The start point of the particle time-of-flight region is marked by a metal plate chopper which is operated at a rotational speed of typically 120 Hz. In the blocked position, it inhibits the particle beam from further entering the vacuum chamber. This way, the instrumental background concentrations from residual gases can be determined. In the open position, particles pass unhindered, while in the chopped position the beam is let through only 2 % of the time. This periodical "release" of the particle beam serves the purpose of recording the time-of-flight along a defined distance from the chopper to the vaporizer (long chamber 395 mm) which takes time in the order of milliseconds (approximately 2 - 5 ms at standard temperature and pressure (STP) according to Jayne et al. (2000)). The particle velocity can be converted into the $d_{va}$ by means of a previously recorded calibration curve. The minimum and maximum time thresholds for particle size recording can be set by the acquisition software (see further discussion in section 2.3). The time-of-flight region ends with the heater, an inverted tungsten cone

operated at 600 °C, upon which the particles impact and flash-vaporize (50 – 100 µs). This operational temperature implies that only non-refractory particle components can be detected. Mineral dust, metals and BC cannot be vaporized under these conditions. The generated gas molecules are ionized by electron impact (70 eV). The electrons are emitted by a tungsten filament with a 2 mA emission current. A set of lenses operated at different voltages extracts the ions into the time-of-flight mass spectrometer (Tofwerk, Thun, Switzerland) where an orthogonal extractor redirects the ions onto the c-shaped flight path (430 mm). The user can determine the number of points per recorded mass spectrum which is typically in the order of 10,000 points (covering a range from 10 to 300 *m/z*, 1 point representing 1 ns of ion flight time) and thus the range of mass to charge (*m/z*) ratios recorded. The ions are detected by a multi channel plate (MCP) which is operated between 1900 and 2500 V. The analog output is converted by a high speed acquisition card (ADC) into a digital signal which is stored by a custom written logging software.

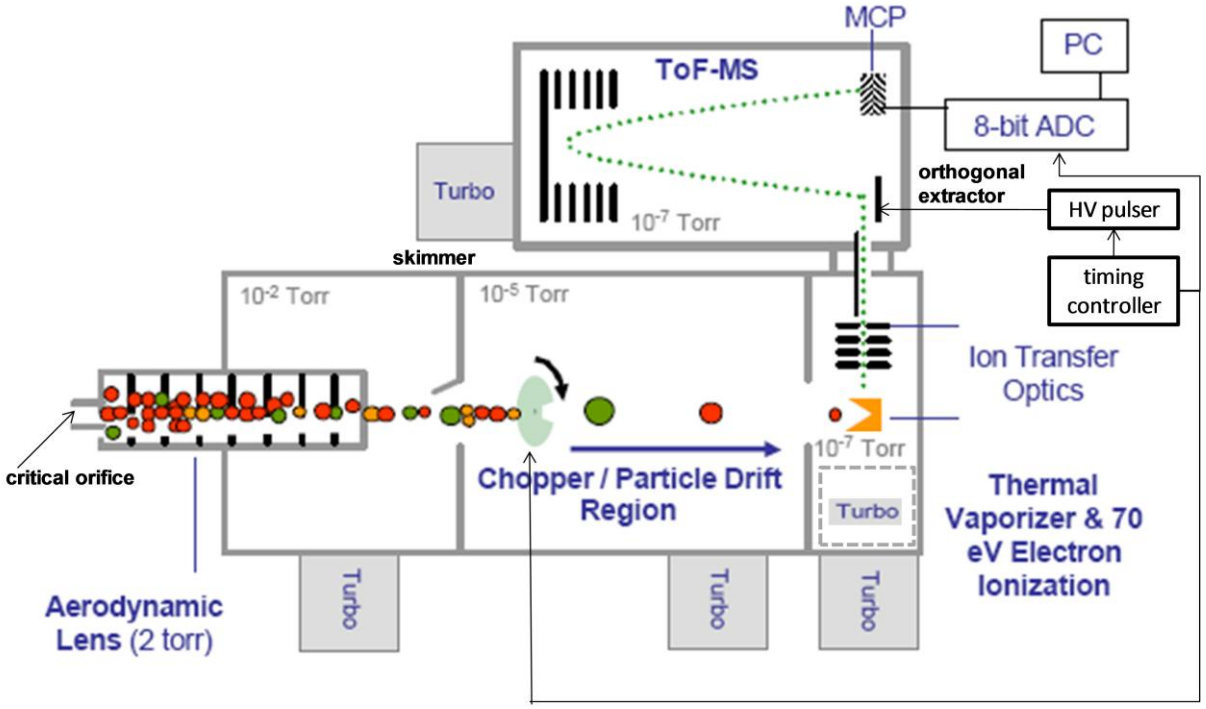


**Figure 10: Compact Time-of-Flight Aerosol Mass Spectrometer (C-ToF-AMS), adapted from (Drewnick et al., 2005; Kimmel et al., 2008).**

The standard AMS quantification procedure is described in Allan et al. (2003) and in Hings (2006). Very briefly, for the quantification the following measures are necessary: A calibration of the ion flight time has to be conducted to relate this parameter to the respective *m/z*. Typically, dominant peaks such as $N^+$, $N_2^+$, $O_2^+$, $Ar^+$ or $W^+$ (*m/z* 14.003, 28.006, 31.990, 39.962 and 183.951, respectively), are used. By means of the analysis software the user can decide how much of the area around a full *m/z* shall be integrated. This function is *m/z* dependent. The single ion intensity (*SI*) in bits*ns is determined by recording the signal of very small gas-phase background ions signals which are due to single ion events. Thus the signal per *m/z* can be converted into ion $s^{-1}$ based on the *SI* and the orthogonal extractor frequency. A duty cycle of the pulser needs to be applied as the ion velocity and thereby the efficiency of the extraction into the MS is *m/z* dependent. Through regularly conducted

ionization efficiency (*IE*) calibrations for nitrate, typically in the order of $10^{-7}$ ions/molecule (details see section 2.4.1), and relative ionization efficiencies for other species (*RIE*) the original amount of molecules per species can be deduced (Allan et al., 2003; Jimenez et al., 2003). A rough estimation of how many molecules could be obtained from1 µg $m^{-3}$ $NH_4NO_3$ yields a number of $2.3*10^{16}$ molecules. During the evaporation process in the AMS molecular fragments of $NH_4NO_3$ are formed, such as NH, $NH_2$, $NH_3$, $H_2O$, NO, and $NO_2$. Assuming that about 3 fragments result from each $NH_4NO_3$ molecule, based on the molecular mass, the above mentioned result is obtained. By means of an editable "fragmentation table" (Allan et al., 2004b) the recorded mass spectra can be attributed to determined chemical species (sulfate, nitrate, ammonium, organics, and chloride). Knowing the molecular weight of the species (e.g. nitrate, $NO_3$, 62 g $mol^{-1}$) and the volumetric flow rate at constant ambient pressure into the instrument the ambient mass concentration can be calculated. As the instrument's sensitivity to the species varies during sampling the recorded "air beam" (*m/z* 28, $N_2$, and 32, $O_2$) is used as a standard to correct for these variations. Finally, a collection efficiency (*CE*) factor accounting for bounce-off effects of particles on the vaporizer is applied to the mass loading.

### *2.1.2 Advantage of the compact time-of-flight AMS over other models for aircraft deployment*

Beside the C-ToF-AMS, there exists the quadrupole AMS (Q-AMS), a predecessor model (Jayne et al., 2000), and the successor, the high-resolution time-of-flight AMS (HR-ToF-AMS) (DeCarlo et al., 2006). The instruments are exactly the same until the ionization stage, only the type of mass spectrometer differs. In contrast to the C-ToF and HR-ToF-AMS which can acquire a complete mass spectrum every 12 µs, the Q-AMS needs to scan over the mass range of *m/z* 1 – 300 within 300 ms with only one *m/z* at a time (Hings et al., 2007). This gives the ToF-AMS types the advantage of more complete chemical information over the Q-AMS. For aircraft deployment this is important as aerosol populations and concentrations might change rapidly when intercepting air masses of different origins at speeds between 100 and 200 m $s^{-1}$.

The HR-ToF has two available modes, the high-resolution mode (W mode) with $R$ ~4300 at *m/z* 200 and a high-sensitivity mode (V mode) with $R$ ~2100 at *m/z* 200 (DeCarlo et al., 2006). $R$ is the ratio of *m/z* over $\Delta m/z$ (full width half maximum at a specific *m/z*). The C-ToF has an approximate resolution of $R$ ~640 at *m/z* 184 (data from CONCERT flight on 2 Nov. 2008). Thus, with the HR-ToF more detailed information on chemical composition of aerosol can be gained compared to the C-ToF. For example, organic fragments containing oxygen, nitrogen or both atoms can be distinguished from alkane chains and the O:C ratio (oxygen to carbon ratio) can be determined directly (Aiken et al., 2008).

Another aspect to consider is the detection limits, shown in Table 3 for one-minute average data. The Q-AMS and HR-ToF in W mode have the highest limits of detection (LOD), whereas the HR-ToF in V mode is almost as sensitive as the C-ToF for the surface measurements. Comparing the surface data to aircraft data from the CONCERT and POLARCAT campaign it becomes obvious that for airborne data acquisitions the LOD is between a factor 4 to 30 higher. This can be attributed to the operating conditions during aircraft campaigns. Powering up the instrument and thus establishing the vacuum is usually only possible four hours prior to take-off. Hence, instrumental background concentrations are

still elevated and increase the LOD whereas long pumping times can be assumed for ground-based experiments. More details are discussed in section 2.4.

**Table 3: One-minute detection limits of the three different versions of AMS, units in µg m$^{-3}$ (STP), and the highest mass resolving power *R* (*m/z*/Δ*m/z*) between *m/z* 10 and 200. Data from DeCarlo et al. (2006) are surface measurements, whereas POLARCAT and CONCERT data are aircraft-based.**

| Species | C-ToF-AMS | | HR-ToF-AMS (DeCarlo et al., 2006) | | | Q-AMS (DeCarlo et al., 2006) |
|---|---|---|---|---|---|---|
| Data in µg m$^{-3}$ (STP) | CONCERT | POLARCAT | DeCarlo et al. (2006) | W mode | V mode | |
| Particulate | | | | | | |
| Organics | 0.07 | 0.5 | 0.019 | 0.360 | 0.022 | 0.470 |
| Sulfate | 0.02 | 0.08 | 0.002 | 0.110 | 0.005 | 0.160 |
| Nitrate | 0.02 | 0.03 | 0.001 | 0.032 | 0.003 | 0.032 |
| Ammonium | 0.10 | 0.37 | 0.016 | 0.150 | 0.038 | 0.350 |
| Chloride | 0.02 | n. d. | 0.004 | 0.053 | 0.012 | 0.032 |
| *R* | ~640 | ~640 | ~800 | ~4300 | ~2100 | ~220 |

n. d. not defined

This comparison shows the advantage of a C-ToF-AMS aircraft deployment over a Q-AMS or HR-ToF-AMS in W mode. The high LODs during POLARCAT are still of the same order of magnitude or even lower than the surface LODs for the other two instrument types. Alternatively, a HR-ToF in V mode could be operated instead of a C-ToF-AMS with similar results. Considering especially the remoteness of the two campaigns POLARCAT (Greenland, long distance from sources) and CONCERT (tropopause) and the relatively low aerosol concentrations it is important to aim rather for a high sensitivity instrument than for high-resolution.

### *2.1.3 Acquisition modes*

For aircraft-based measurements three operational modes are relevant. The *mass spectrum mode* (MS mode) serves to quantify the aerosol mass concentration and composition via the difference of mass spectra recorded from ambient particles and instrumental background. Mass concentrations are given in µg m$^{-3}$ at standard temperature and pressure (STP). Details relevant to the measurements presented here are given in section 2.4.

Chemical composition can also be provided size-resolved in the particle time-of-flight mode (*PToF mode*) (Jayne et al., 2000; Allan et al., 2003). Above it was already described that the chopper cuts the particle beam to provide a starting point for the flight time measurement. The determination of mass concentration is exactly the same as for the *MS mod*e only that the data is acquired as a function of

particle flight time. To relate the particle time of flight to the vacuum aerodynamic size, calibrations need to be performed. Data is typically displayed as $dM/dlog(d_{va})$, with $dM$ is the aerosol mass concentration for the respective size interval, and $dlog(d_{va})$ is a notation for $log(d_{va\ i+1}/d_{va\ i})$. More information regarding the specific configuration and calibration of the C-ToF-AMS is discussed in section 2.3 and 2.4. The sequential recording of data in *MS* and *PToF mode* is called *general alternation* mode.

The third relevant acquisition mode is the fast mass spectrum mode (*FMS*) in which spectra can be obtained at rates greater than or equal to 1 Hz (Kimmel et al., 2008). The key to such fast acquisition is the onboard averaging of data in the ADC card before transfer to the computer, a time consuming step. In contrast to the *MS* and *PToF modes* a single data point does not comprise both, a particle (open) and a background (closed) spectrum, but either one of them. Therefore, the average of a certain number of closed spectra in a measurement cycle is subtracted from each open data point in the same cycle. The advantage of the *FMS* is that rapid changes in aerosol concentration and composition can be highly resolved. This is especially important for airborne measurements where data acquisition translates into spatial resolution and characteristics of single air masses with different origins can be described more accurately. Beside *FMS* application during CONCERT it was only used during the ARCTAS campaigns before. More details regarding the data analysis of *FMS* are given in section 2.4.

## 2.2 Technical modifications to the aircraft deployable C-ToF-AMS

Prior to mounting the C-ToF-AMS in either research aircraft, ATR-42 or Falcon, several technical modifications had to be realized.

### 2.2.1 Mechanical requirements

The instrument had already been placed into two standard 19" Falcon racks (see Figure 11) from an earlier campaign (PAZI) in 2003 (Schneider et al., 2006a). All components need to be fixed in the rack properly so they resist certain forces (multiples of gravitational acceleration g) in all six directions oriented in flight direction: forward 9 g, backward 1.5 g, upward 4.5 g, downward 7 g, and to either side 3 g. This is based on the European Joint Aviation Requirements JAR 23/25/27. The first rack (see also block diagram in Figure 12) contains the electronic equipment such as the computer (AMS 06, 11, 400, 401), two voltage converters (AMS 02, 22), the turbo pump controller (AMS 04), further electronic controllers for various other components like the chopper or the vaporizer (AMS 09), a BNC board (AMS 21), and an uninterruptable power supply (UPS, AMS 01). The second rack comprises the vacuum chamber (AMS 10) with the inlet system (AMS 24, 241-247) and diaphragm pumps (AMS 03, 23), the turbo pumps (AMS 101-106) and the actual mass spectrometer (AMS 10) with the control unit (AMS 18). Altogether this specific instrument weighs 168.4 kg including the racks (14.6 kg each). This already satisfies HALO requirements with an upper payload of 150 kg per rack. When installing all components into one HALO rack, potentially, weight can still be reduced by shortening cables and condensing the electronics into one box. Additionally, the required rack power distribution box can replace the voltage converters. A major weight contributor is the UPS (21.1 kg) which could be omitted if possible. However, in case of power failure the UPS provides extra time (20 min) for a controlled shut down avoiding stress for the MCP detector and turbo pumps. Additionally, switching power from the ground power unit to aircraft power supply is usually accompanied by a short power interruption which is bridged by the UPS.

### 2.2.2 Electrical requirements

For the AMS deployment on Falcon in October 2008, the main modifications to be realized concerned the electrical security. Currents of up to 10 A for the pumps are reached during the start-up of the instrument and voltages of up to 3 kV are reached during operation. The total electrical power consumption during data acquisition is about 0.7 kW. This C-ToF-AMS is equipped with a total of 79 cables. Adequate cable diameters for the expected currents, protection wrapping against fire and fuses need to assure save power distribution. An additional 7 A fuse box (AMS 300) was installed, as well as single fuses for turbo pump fans and the standard inlet diaphragm pump. Also, all power cables were replaced by Teflon mantled cables and power cable connectors had to be exchanged by certified Amphenol plugs which are screw-tied to the socket and cannot come lose during flight. Another major modification was the installation of an emergency shut-off switch (AMS 10S). In case power has to be cut from the scientific equipment, the UPS would continue to provide the AMS with power, so a simple switch to disconnect the UPS from the AMS was required.

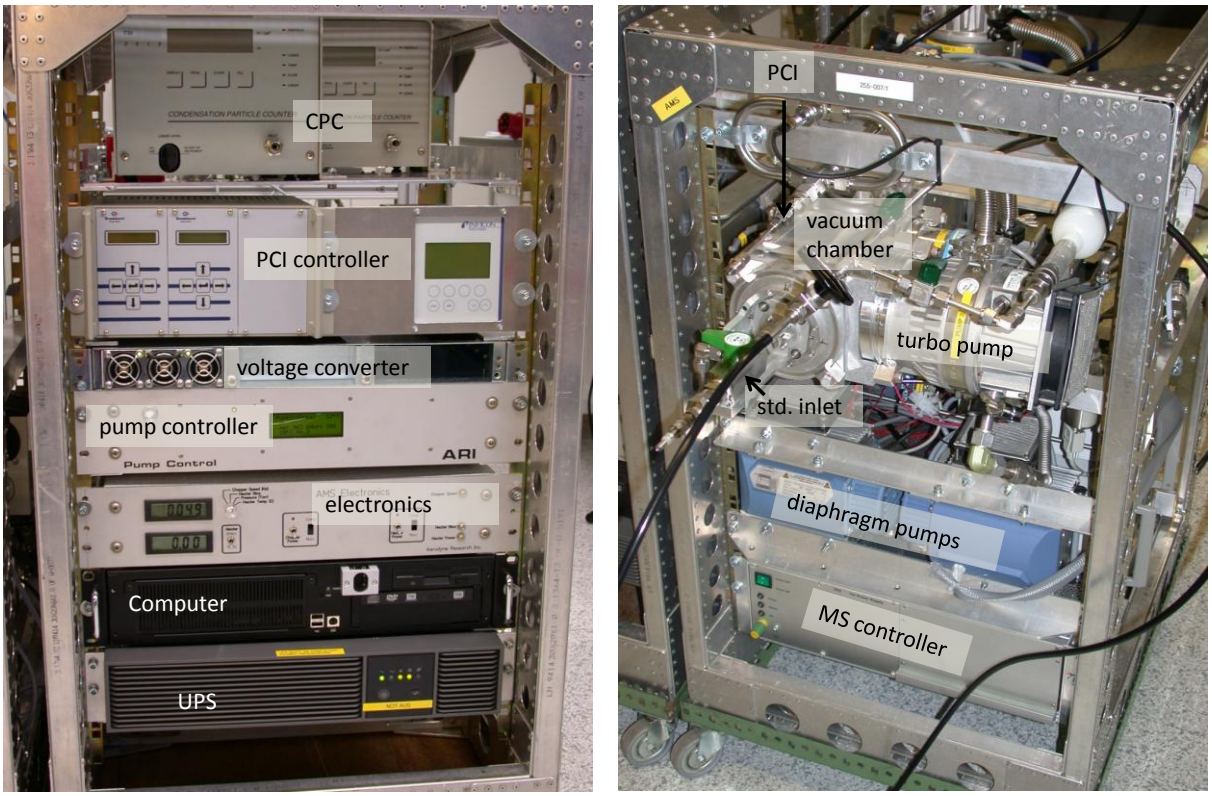


**Figure 11: C-ToF-AMS in two standard Falcon 19" racks. Left: electronics rack; right: mass spectrometer rack.**

### *2.2.3 Risk Assessment*

The minimization of operational risks for aircraft-based measurements is especially important since malfunctions during flights can lead to life threatening situations. The disconnection of the 3 kV supply cable to the MCP poses a threat which is reduced by screw-tied plugs on either side. The five turbo pumps operate at a rotational speed of 75,000 rpm but are sufficiently shielded by the casing in case of a dysfunction. A sudden increase of pressure in the vacuum chamber will be reflected in the performance of the turbo pumps. Therefore two interlocks connect the pump controller with the vaporizer and filament controller and the high voltage supply to the MCP to shut them down including the pumps. Another critical component is the UPS containing lead acid batteries which can only be operated within a certain temperature and pressure range (charge 0-40°C, discharge -20-50°C, minimum pressure equivalent to 2000 m altitude). Sufficient ventilation is provided to keep the temperature below 40°C and the minimum cabin pressure in the two respective research aircraft does not drop below a value equivalent to 1800 m.

Beside the risk the operation of the AMS poses to the installations and people in the aircraft there is also stress imposed onto the instrument during airborne science missions. Mechanical stress during take-off and landing and turbulences is reduced by the use of shock-mounts. Another environmental factor which can cause overheating of instrument components is the cabin temperature which can rise to approximately 40°C together with poor air circulation. Therefore, as much space and ventilation as possible is left around critical hardware such as the data acquisition card with a maximum temperature allowance of 60°C. It has been operated at roughly 55°C during flights.

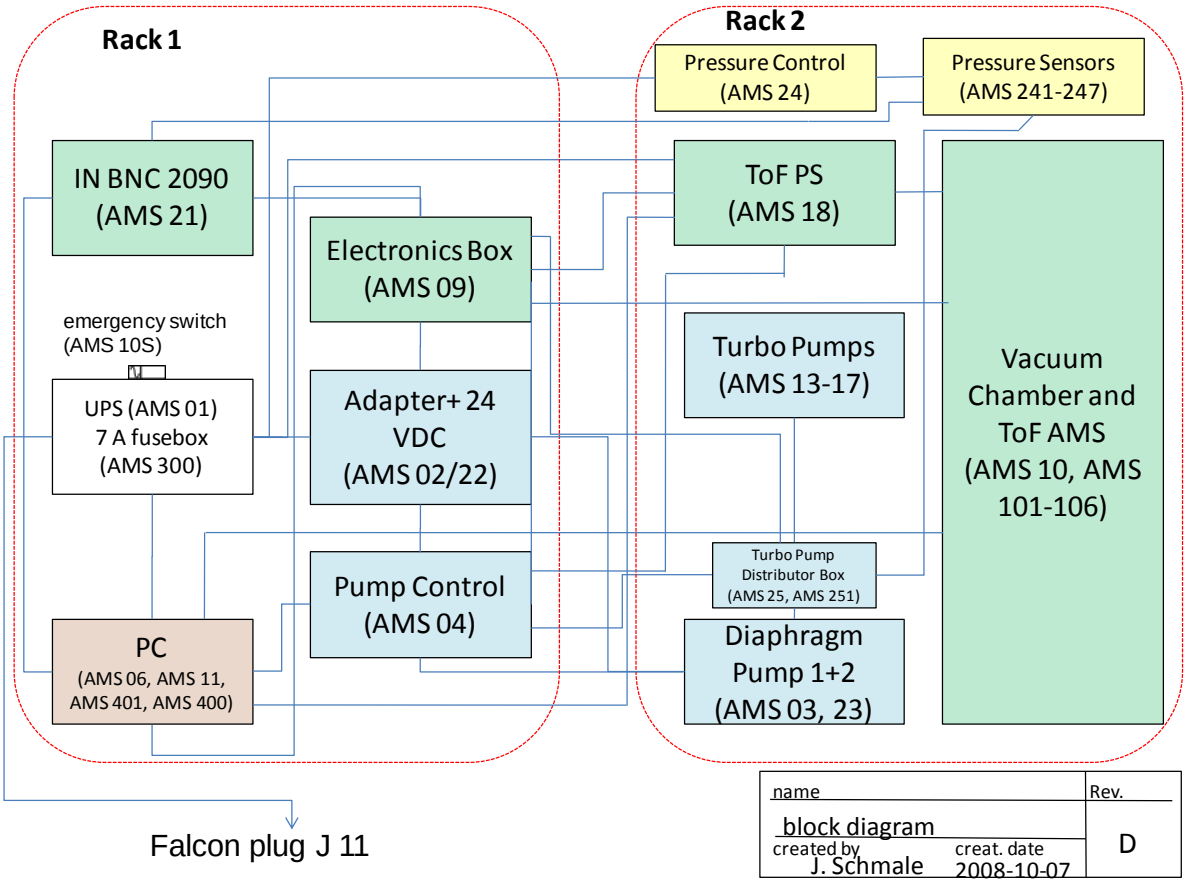


**Figure 12: Block diagram of electrical connections between individual AMS components.**

## 2.3 Scientific modifications to the AMS for aircraft deployment – pressure controlled inlet system (PCI)

In contrast to stationary surface measurements the changes in ambient pressure during airborne missions are significant and need special attention. Ambient pressure levels can range from roughly 1000 hPa to 200 hPa for a maximum altitude ceiling of 12 km. The critical orifice (*COr*) upstream the AMS lens keeps the volumetric flow rate constant. However, as ambient pressure changes, the mass flow rate changes with air density leading to fluctuations in lens pressures. This introduces changes in the lens transmission as function of the particle diameter. Liu et al. (2007) conducted transmission efficiency measurements and calculations with the FLUENT model for the standard AMS inlet at 1013 and 780 hPa. The results show that at lower pressures the size dependent transmission efficiency function favors smaller particle diameters. Also, changing pressures in the aerodynamic lens lead to varied particle velocities and acceleration within the lens and after leaving the nozzle (last stage of the lens). Thus, the flight time of a certain particle size is not constant which will lead to errors in determining the particle mass size distribution. In theory, these effects can be corrected during data post processing by means of laboratory calibrations. However, transmission effects can be large especially for larger particle sizes and thus are difficult to calibrate for. A pressure controlled inlet (PCI) can avoid these drawbacks by maintaining the pressure ($P_{PCI}$) in front of the *COr* and lens system at a constant level irrespective of changes in ambient pressure.

### 2.3.1 PCI design

The PCI design chosen for the C-ToF-AMS was originally introduced by Lee et al. (1993) as a pressure reducer and adapted for the AMS by Bahreini et al. (2008). The here applied PCI only differs from the Bahreini PCI in terms of dimensions and the selected critical orifice diameters. Figure 13 shows the PCI details in side (a) and top view (b) at a scale of 1:4 (units: mm). The ambient air is sampled at $P_{amb}$ (ambient pressure) with a certain isokinetic volumetric flow rate ($Q_o$) and velocity ($U_o$) upstream the first critical orifice ($COr_1$). Isokinetic sampling requires that the flow velocity inside the sampling tube is the same as outside in order to minimize particle losses and not to bias the sample towards larger or smaller particles. $Q_o$ is determined by the utilized aircraft aerosol inlet, hence the flow into the PCI has to be controlled accordingly. Details are given in section 2.3.3 which describes how aircraft inlets and the PCI were coupled. Subsequently, the sample enters the PCI chamber where the pressure ($P_{PCI}$) is kept at constant level. After a distance longer than the particle stopping distance ($L$) a subsample is drawn through a stainless steel tube which is inserted into the PCI chamber. Before entering the standard AMS inlet aerodynamic lens the sample air passes a second critical orifice ($COr_2$) which sets the lens pressure ($P_{Lens}$). $COr_2$ keeps the lens pressure constant so that due to the stable $P_{PCI}$ not only the volumetric but also the mass flow into the AMS is constant. To maintain $P_{PCI}$ constant it is continuously monitored and compared to the target value by means of a PID controller (proportional-integral-derivative). The target value is half the lowest expected ambient pressure for $COr_1$ to operate critically, i.e. maintaining a constant $Q_o$. The controller operates a valve which closes if $P_{PCI}$ is too low (high altitudes) or opens if $P_{PCI}$ is too high (low altitudes). The control valve response time is < 30 ms. Air is sucked through the valve by a diaphragm pump. This surplus air is withdrawn symmetrically to either side through a 180 ° bend 105.00 mm behind the actual sampling spot in the

intermediate chamber in order not to create any turbulence near the sampling point. The Reynolds numbers in the sampling line (inner diameter of 0.066" or 1.7 mm) in the PCI ranges between 334 and 477 depending on $P_{PCI}$ and $COr_2$, and between 21 and 74 within the tube from where the excess air is withdrawn through the PID valve (see Appendix A for details).

To keep particle losses at a minimum certain geometric restrictions need to be considered. To avoid deposition losses in front of $COr_1$ after Lee et al. (1993), the diameter of $COr_1$ ($d_1$) should be such that $\sqrt{St} < 1$, where the stokes number ($St$) is defined as follows:

$$St = \frac{\rho_p D_p^2 C_c U_o}{18 \mu d_1}$$

**Eq. 3**

with $\rho_p$: particle density, $D_p$: particle diameter, $C_c$: Cunningham slip correction, $U_o$: velocity upstream of $COr_1$, and $\mu$: dynamic air viscosity. All units are given in Appendix A. To minimize deposition losses at the walls of the intermediate chamber its inner diameter $D_t$ is chosen so that the modified stokes number ($\sqrt{St'}$) is < 1. $\sqrt{St'}$ is given by

$$\sqrt{St'} = \sqrt{\frac{\rho_p D_p^2 C_c U_s}{18 \mu d_1}} \left(\frac{d_1}{D_t}\right)^{0.58}$$

**Eq. 4**

with $U_s$: sound velocity at $COr_1$. For ammonium nitrate particles ($\rho_p$ = 1.72 g cm$^{-3}$) of 750 nm diameter at a $P_{amb}$ of 200 hPa $\sqrt{St}$ and $\sqrt{St'}$ are 0.15 and 0.36 for both 380 and 400 µm orifices as used during the POLARCAT and CONCERT campaigns. Details regarding the calculations are given in Appendix A. The values chosen here reflect on the one hand a density which is expected for aged and sulfate dominated aerosol (discussion see section 2.5.1) and on the other hand roughly the maximum particle diameter which is transmitted by the PCI. The larger the particle and the lower the ambient pressure, the larger become $\sqrt{St}$ and $\sqrt{St'}$, e.g. $\sqrt{St}$ is 0.02 at 1000 hPa for an 80 nm particle ($\sqrt{St'}$ is 0.05) while it reaches a maximum value of 0.15 at 200 hPa for a 750 nm particle ($\sqrt{St'}$ is 0.36), see Appendix A. As the maximum values are clearly below 1 the chosen design is able to keep particle losses at a minimum. Changing $COr_1$ to larger diameters at fixed $D_t$ reduces losses in front of the PCI while losses in the intermediate pressure region increase. Also, a larger orifice would require higher volume flow rates through the PID valve as $P_{PCI}$ would increase otherwise and reduce the maximum altitude at which the PCI can be operated. Increasing $D_t$ would result in reduced losses in the intermediate chamber and leave losses in front of the inlet unchanged. However, the volume flow through the PID valve would have to be increased, as well. Currently the valve facilitates a maximum gas flow of 5 slpm (standard liter per minute).

During the POLARCAT campaign this PCI design was modified by introducing a sampling line to a CPC (condensation particle counter, TSI 3010) in the intermediate chamber after the withdrawal of AMS sampling air (see Figure 13 a). The particle counter was used at the same time as the pump to operate the PCI so that the flow into the PCI was 1.74 l/min. $COr_1$ was 400 µm and $COr_2$ 160 µm. Both campaigns' PCIs included a relative humidity and temperature probe (see Figure 13 a).

For CONCERT the CPC was omitted, instead a bypass with a capacity of 1.3 l $min^{-1}$ upstream $COr_1$ had to be installed to achieve a total sample flow rate of 2.5 l $min^{-1}$ to guarantee isokinetic sampling conditions. As shown in Figure 14, a second manual valve (MV) regulated bypass with a particle filter in line was installed for both campaigns to facilitate filtered air measurements during flights for the edition of the "fragmentation table" for data analysis (see section 2.4). During CONCERT the combination of critical orifices was changed three times in order to best meet the flight specific requirements. $COr_1$ and $COr_2$ were 380 and 200 µm, 400 and 200 µm, and 380 and 250 µm. In Appendix A photographs of the PCI are shown.

This PCI design with the easily exchangeable critical orifices $COr_1$ and $COr_2$ satisfies the requirements of a broad range of aircraft types and hence a variety of operational conditions. While the ATR-42 is a propeller aircraft with an approximate speed of 100 m $s^{-1}$ and a maximum altitude of 8 km, the Falcon is a twin jet plane that reaches altitudes of 12 km at a speed of more than 200 m $s^{-1}$.

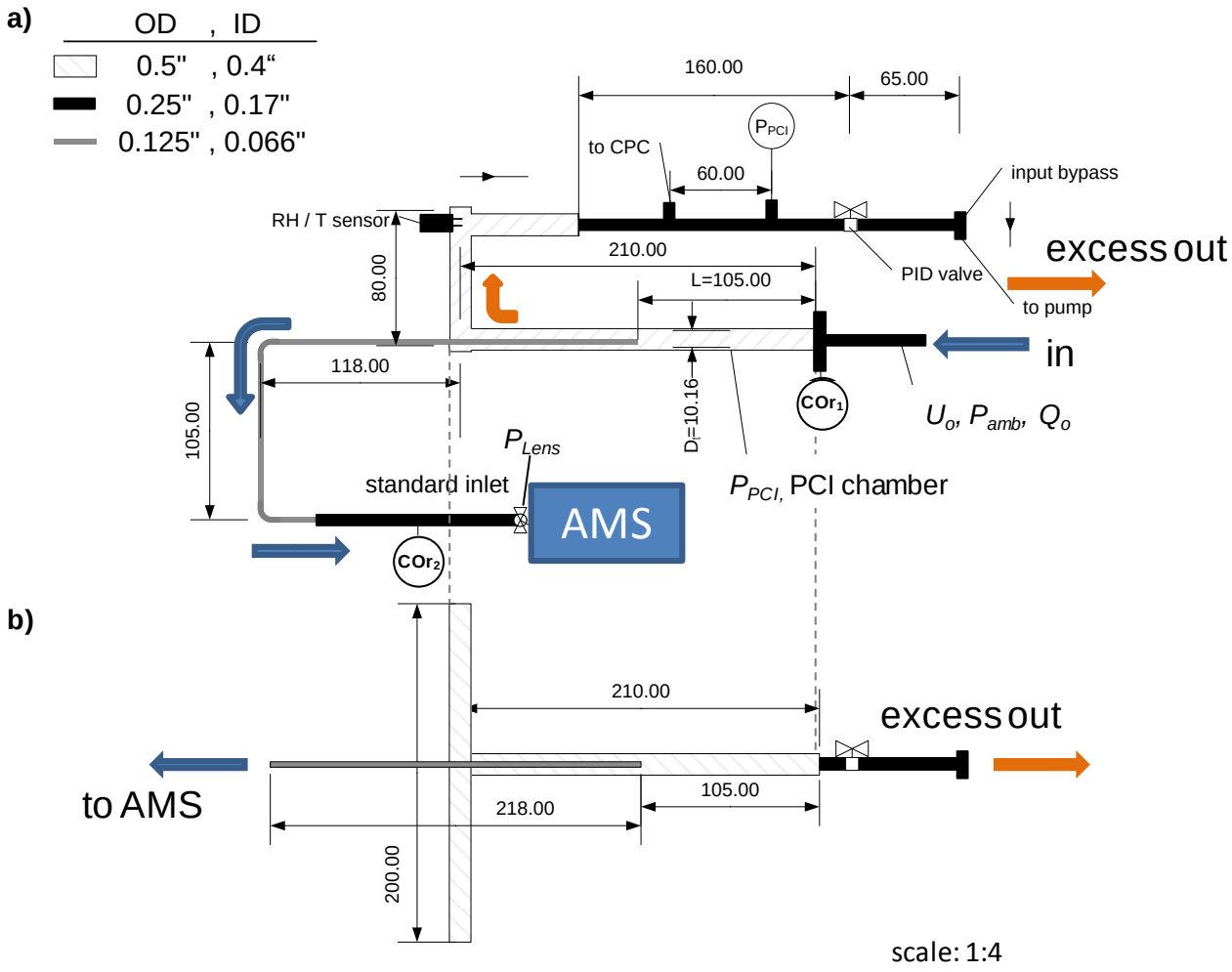


**Figure 13: Pressure controlled inlet design for the C-ToF-AMS.**

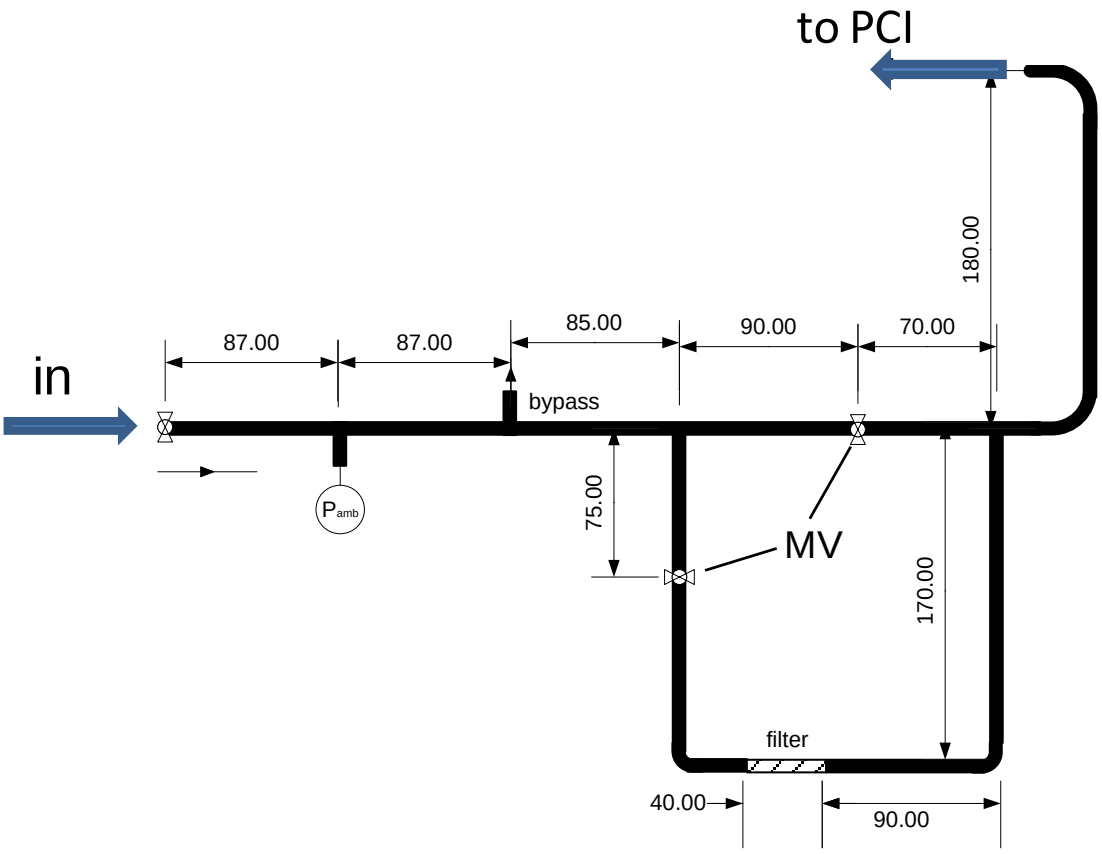


**Figure 14: Pre-PCI inlet system.**

### *2.3.2 PCI characterization*

In order to report AMS mass concentration measurements quantitatively and particle size distributions correctly the pressure controlled inlet needs to be characterized in two respects: The transmission as a function of particle size needs to be determined, and a size calibration has to be conducted. In total there were four PCIs to be characterized (see Table 4) plus the AMS standard inlet as reference.

Figure 15 shows the schematic set-up for the transmission efficiency measurements. A custom built atomizer was used to produce aerosol from polystyrene latex spheres (PSL, Nanosphere Size Standards, Duke Scientific Corporation) and an ammonium nitrate solution. Two diffusion dryers filled with silica gel (Riedel-de Haën) dried the aerosol before it entered a differential mobility analyzer (DMA, Model Nr. 5.5-900, Grimm Aerosol Technik GmbH & Co. KG) providing a monodisperse distribution of the generated particles. The sample flow was diluted by particle-free compressed air and split three-way to two CPCs (TSI 3010, Grimm 5.401) and the AMS (solid lines in Figure 15). The two CPCs where used to check the complete mixing of sample and dilution air, and to be able to correct for non-ideal mixing.

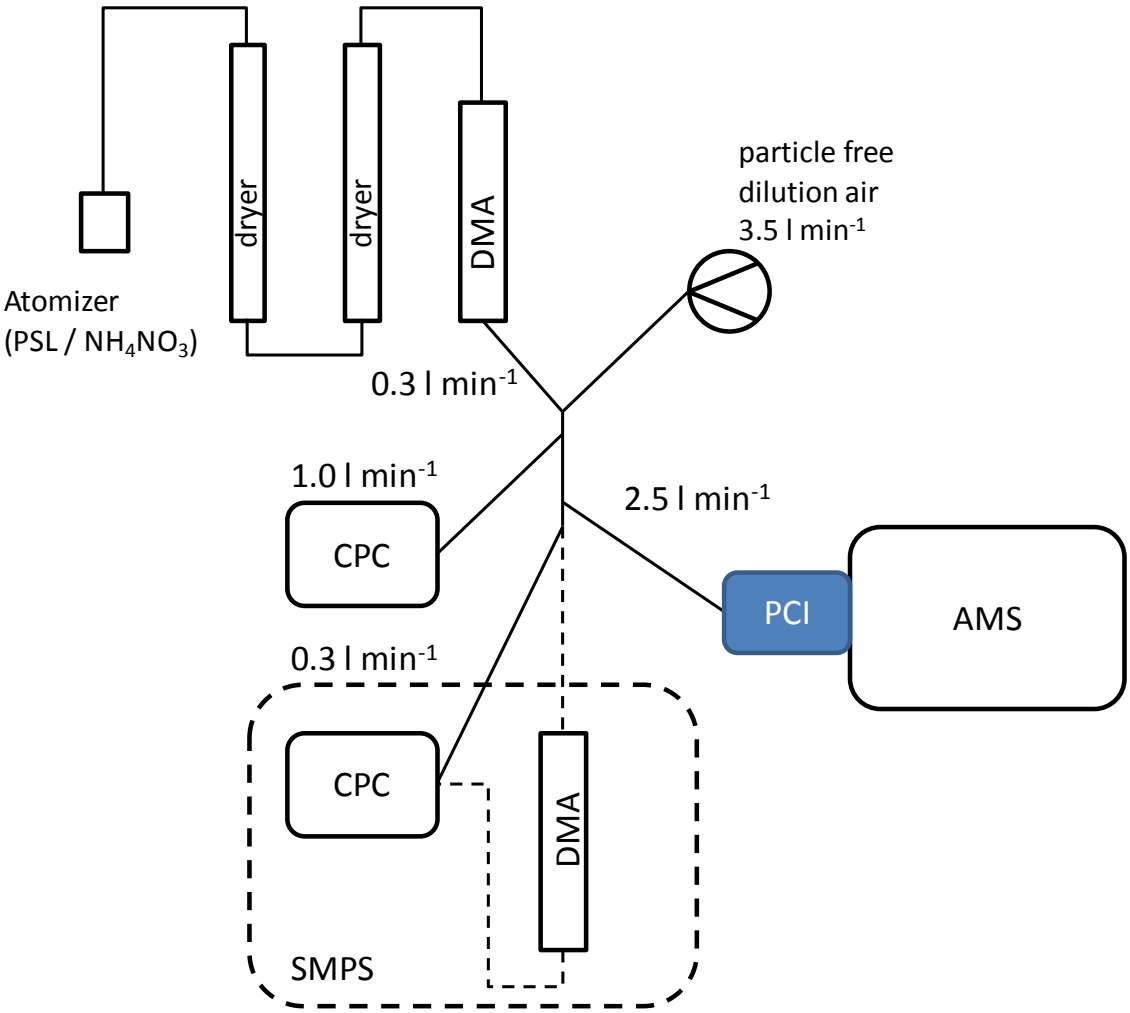


**Figure 15: Laboratory set-up for the characterization of the PCI transmission efficiency.**

Two methods were applied to determine the transmission efficiency: For particles from 80 to 400 nm vacuum aerodynamic diameter ($d_{va}$) the so-called mass method was applied (see description below). Beyond the upper end diameter errors become relatively large since it is difficult to generate enough monodisperse particles for an accurate mass determination with the AMS. Thus, a counting method was used for diameters from 420 to 1050 nm $d_{va}$. For the purpose of counting PSL particles the AMS was operated with a light scattering probe (LSP) (Cross et al., 2007). The probe consists of a diode pumped 405 nm continuous wave 50 mW laser, external mirrors for alignment of the light beam, an ellipsoidal mirror for scattered light collection, a razor blade beam stop, and a photomultiplier tube for scattered light detection. Due to the diverging laser beam through which all particles pass that are focused by the aerodynamic lens system, the number of particles entering the AMS after having passed the PCI can be counted and related to the number of particles detected by the CPCs. The minimum detectable physical particle size is 180 nm, the reason why the mass method had to be applied for smaller diameters. The transmission efficiency for the counting method is here defined as the number of particles having passed the PCI, detected by the AMS, over the number of particles having entered the PCI, as counted by the CPCs.

For the mass method, particles from an $NH_4NO_3$ solution were generated with the atomizer, dried by two diffusion dryers and size selected with a DMA (Grimm DMA 5.5-900). Again, the sample air was

diluted before the flow was split three-way to one CPC (Grimm Model 5.401), an SMPS system (TSI, Series 3080), and the AMS. The SMPS system (dashed box in Figure 15) was used to compensate for multiply charged particles by determining the probability distribution of non-singly charged particles in the actually applied DMA for every particle size used in the experiment.

Before particles with a certain electrical mobility diameter can be selected they pass a radioactive source (Am-241 in case of the Grimm DMA) which produces bipolar ions and thus applies an equilibrium charge distribution to the aerosol. The theoretical charge distribution can be calculated as given by the Boltzmann law and the number fraction of particles carrying a single charge and thus corresponding to a selected mobility diameter can be derived. The particle number fraction (*PP*) is the fraction of particles that actually had the selected diameter after passing the DMA. It was measured for the following sizes of ammonium nitrate particles: 58, 72, 145, 218, 290, and 327 nm $d_{mob}$. These diameters correspond to 80, 100, 200, 300, 400, and 450 nm $d_{va}$. As an example, Figure 16 a) presents the particle number fraction for a selected diameter of 218 nm. Figure 16 b) shows a comparison of the measured values with theoretical values from the TSI DMA manual. For singly charged particles theory and experimental values agree well, whereas for doubly charged particles the predicted trend is different from the actual behavior. The error bars denote the standard deviation from all scans during three repetitive experiments. The number of scans ranged between 6 and 13.

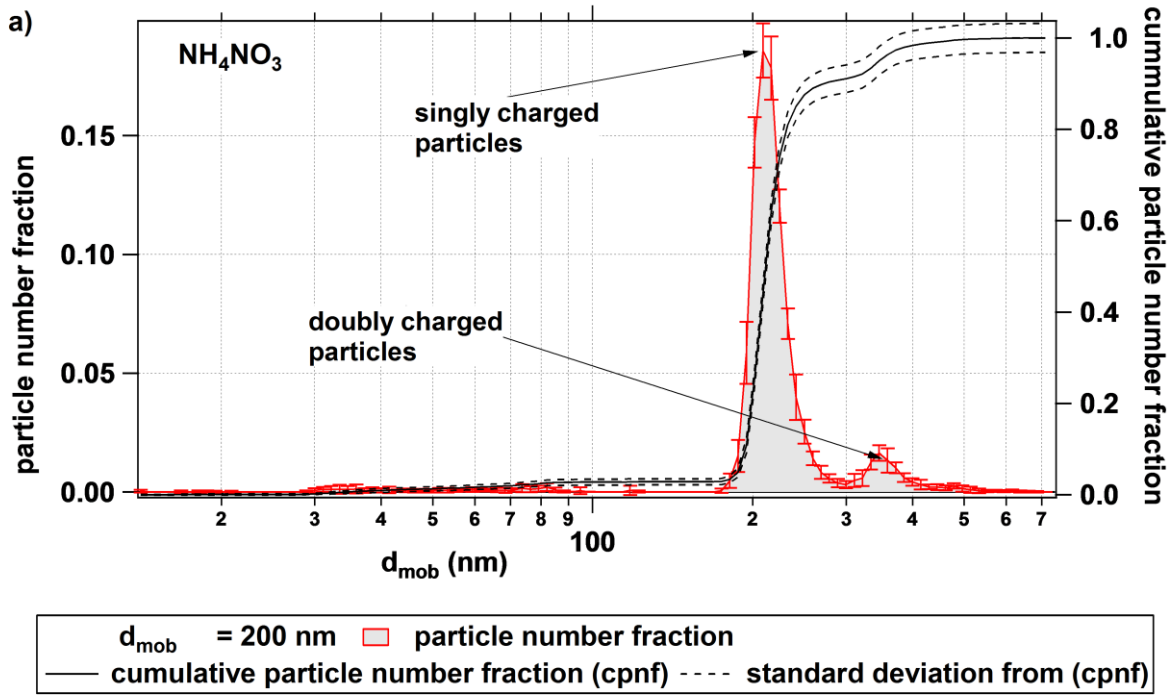

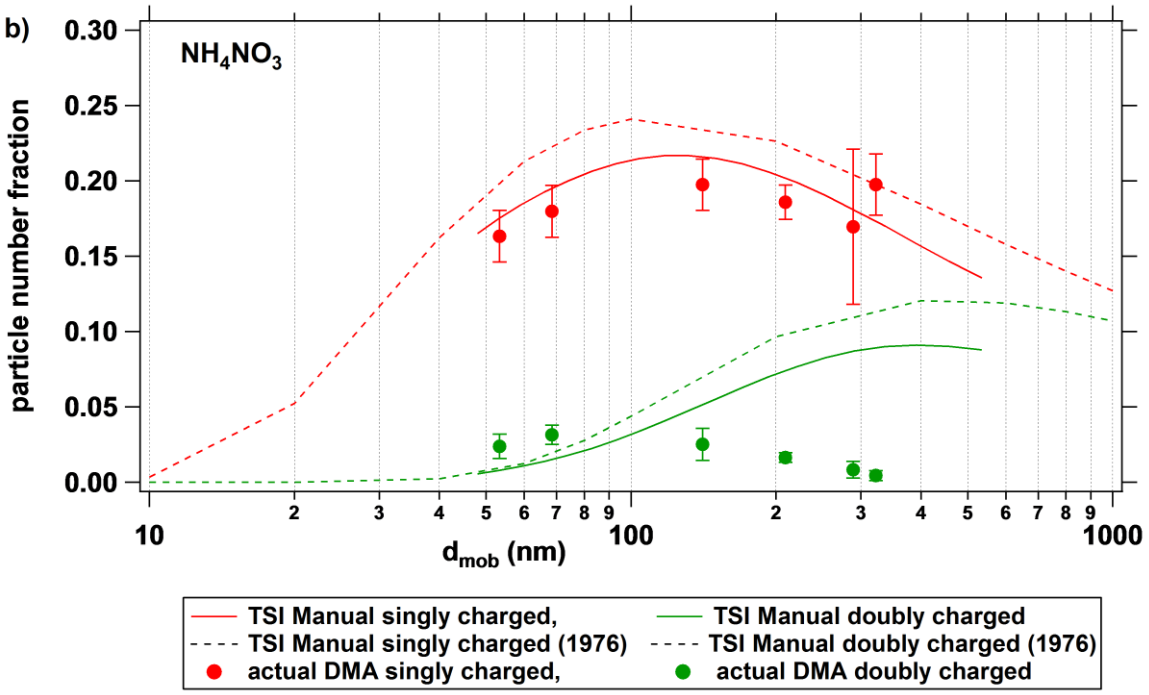


**Figure 16: a) Number fraction as a function of size after selection of 200 nm particles with the TSI DMA (the vertical bars denote the standard deviation from 9 scans), b) Comparison of particle number fractions from theory and the actually used TSI DMA.**

This result was considered in the quantification of mass of $NH_4NO_3$ by the AMS. For cases, where only a noisy signal was obtained by the SMPS system due to the sample flow dilution, the characterization of the monodisperse aerosol was conducted separately, assuming the same charge distribution. With the known diameter ($d_{mob}$), density ($\rho_p$, 1.72 g cm$^{-3}$) and the particles' Jayne shape factor *S* of 0.8 (Jayne et al., 2000) the particle number concentration as recorded by the CPC ($CPC_{avg}$) at a particular diameter was converted into mass concentration of $NH_4NO_3$.

$$M_{NH_4NO_3} = PP * CPC_{avg} * \rho_p * \frac{1}{6} * \pi * {d_{mob}}^3 * S$$

**Eq. 5**

For mass determination with the AMS only *m/z* related to $NO_3^+$ (30, 46) were taken into account. Thus, nitrate mass was derived and ammonium mass deduced stoichiometrically. The *PToF mode* was used to specify the fraction of mass that was contributed by the respective diameter to total $NH_4NO_3$ mass. The transmission efficiency is defined as mass detected by the AMS divided by the mass detected by the CPC.

The results are shown in Figure 17 and include the PCI deployed during POLARCAT, the three PCIs used during CONCERT (PCI 1 – 3), and the standard AMS inlet. The critical orifice combination for PCI 1 was 380, 200; for PCI 2 400, 200; for PCI 3 380, 250; and for PCI POLARCAT 400, 160 µm.

Additionally, the findings by Liu et al. (2007) at 760 torr are displayed. The error bars for the mass method points (solid symbols) include the standard deviation of the detected particle number by the CPC during the 20 min measuring interval and the standard deviation of the charge distribution of the monodisperse aerosol. The LSP derived data points (open symbols) have uncertainties comprising the

standard deviations from the mean particle numbers counted by the CPC and LSP. The calculations of errors for both methods are shown in Appendix A and an example is given.

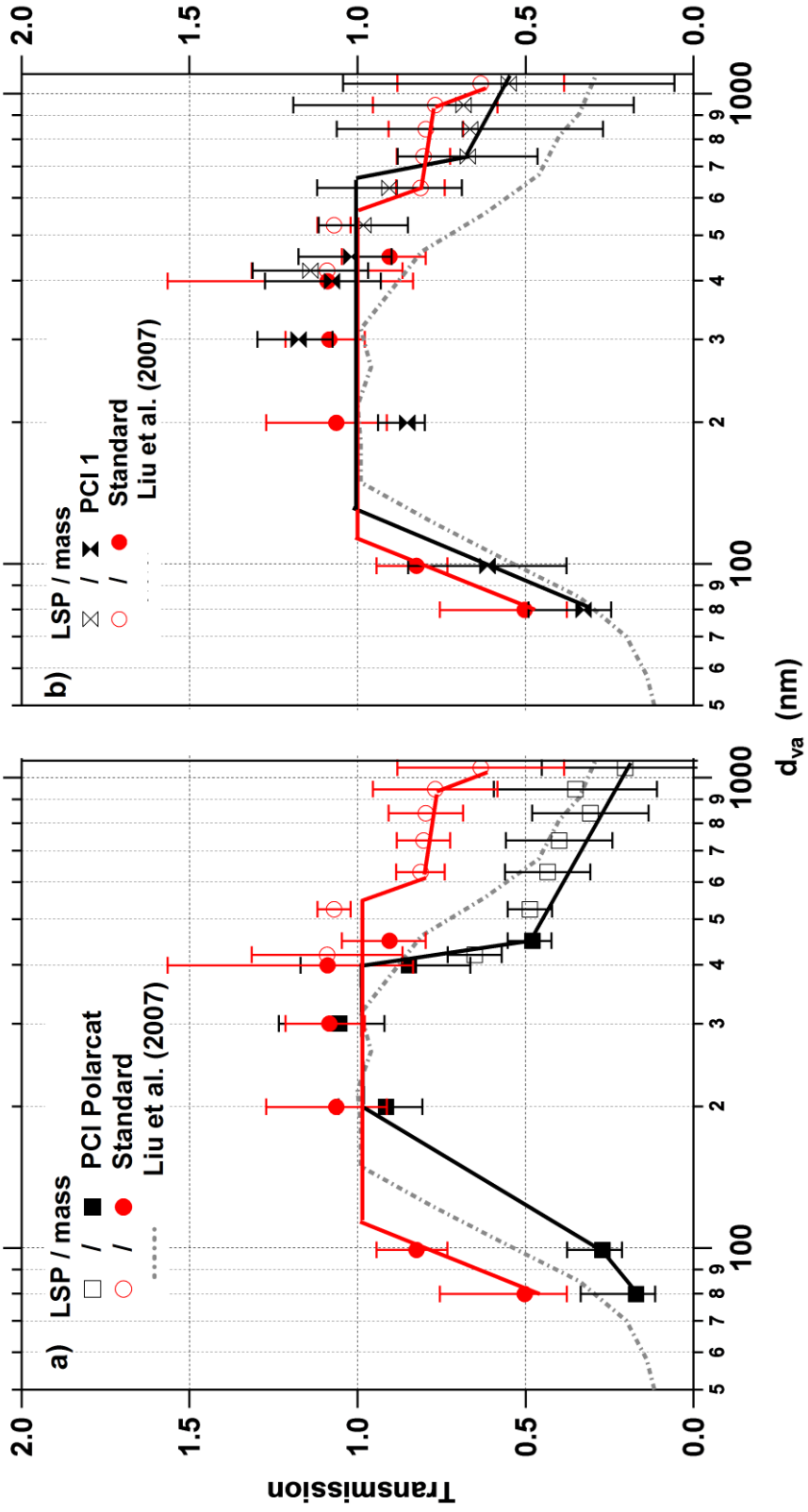

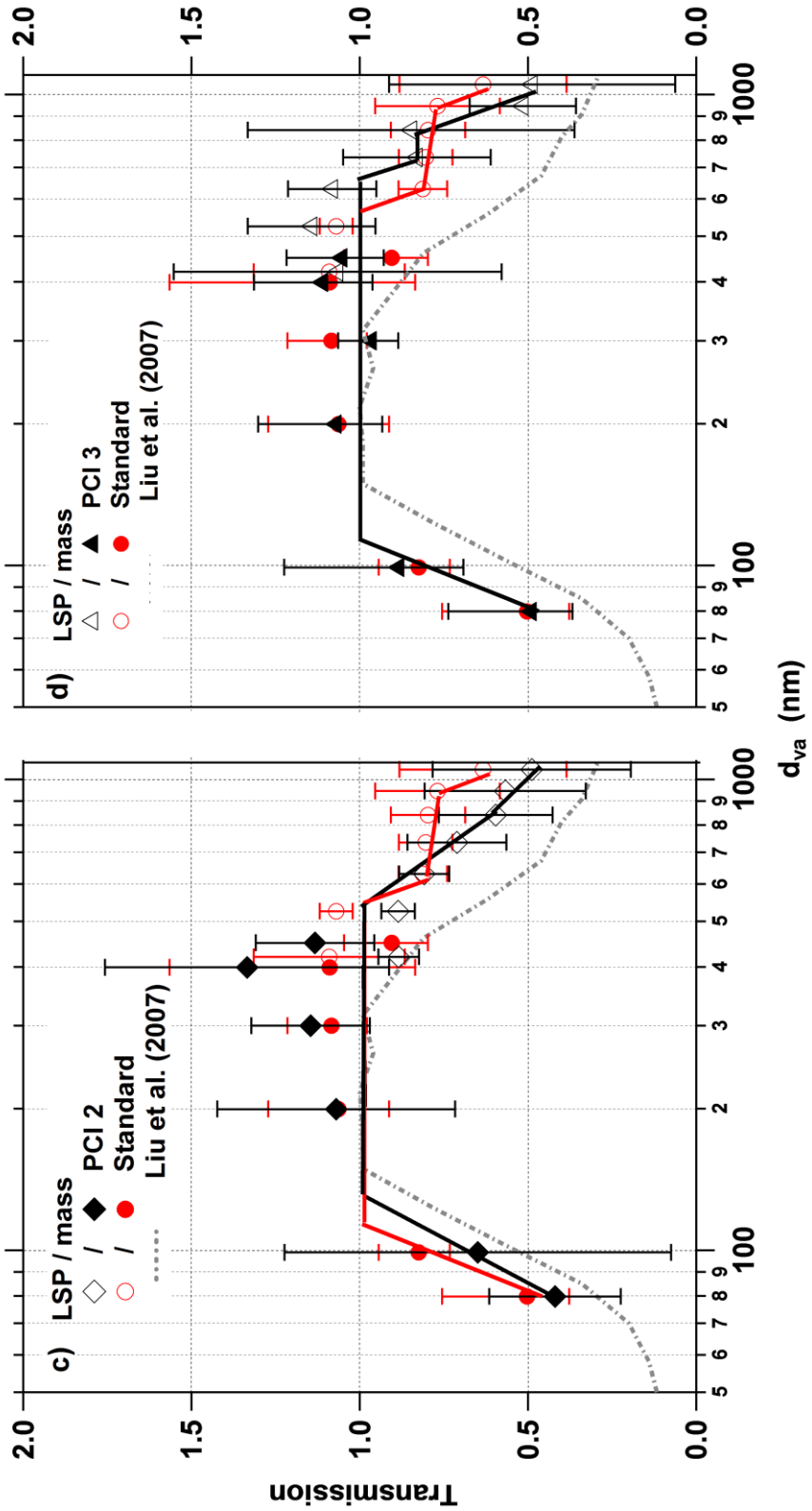


**Figure 17: Transmission efficiency of the AMS standard inlet, the PCIs, and as found by Liu et al. (2007). The lines are only drawn to guide the eye. [This figure is adapted from Schmale et al. (2010)].**

For the three PCIs with the second critical orifice greater than 160 µm the transmission efficiency is the same as for the standard inlet within the calculated error range. Generally, transmission from 200 to 400 nm $d_{va}$ particles for PCI POLARCAT and from 200 to 600 nm for all other inlets is close to 100 %. Thus, the respective data of the CONCERT campaign have not been corrected for differences in inlet transmission compared to the standard inlet. The POLARCAT inlet shows lower transmission for particle sizes smaller than 200 nm $d_{va}$ and greater than 400 nm resulting in an overall inlet transmission of approximately 54 % compared to the standard inlet. In theory, a size dependent correction would have to be conducted. Practically, this is impossible since the signal of ambient aerosol is almost always too noisy during aircraft measurements to derive a size distribution. Without the aerosol size distribution no size resolved transmission correction can be applied. Hence, all acquired mass concentrations have been corrected by the factor of 0.54. Generally, PCIs with a larger second orifice have higher transmission for small and large particles and are similar to the standard inlet. Table 4 shows the respective intermediate pressures, lens pressures and size cut-offs for all PCIs.

Generally, the PCI allowed detection for particles between 84 and 735 nm $d_{va}$, however very low ambient pressure forced the cut-off partially down to approximately 400 nm $d_{va}$ caused by lower lens pressures and thus less acceleration within the particle time-of-flight region in the vacuum chamber. Less acceleration translates into longer flight times which exceed the maximum time threshold for data recording as chosen with the electronic acquisition settings. For POLARCAT the maximum data acquisition was set to 5 ms, for CONCERT to 4.4 ms. The pressure regime where $P_{PCI}$ was kept constant by the control valve is termed "*core* $P_{amb}$". For ambient pressures outside of the core $P_{amb}$ regime, $P_{PCI}$ is a function of $P_{amb}$. These pressure regions are termed "*high* $P_{amb}$" and "*low* $P_{amb}$".

Size calibrations for each PCI were performed at different $P_{Lens}$. Thus, in theory size distributions could have been determined for all flight altitudes and lens pressures if the ambient signal had been large enough. As this calibration is an AMS standard procedure independent of the PCI it shall only be described very briefly. Monodisperse particles of known size, density and shape *S* are generated, dried and measured by the AMS. Typically PSL particles are used. The particle velocity in the vacuum time-of-flight region is then related to the particle size by means of a function which depends on the gas velocity at the exit of the aerodynamic lens (nozzle) $v_g$, the gas velocity within the aerodynamic lens $v_l$ and two constant fit parameters commonly denoted as *D** and *b*. $v_g$ and $v_l$ depend on the lens pressure. The upper cut-off diameter depending on the electronic acquisition settings and the actual calibration curve can thus be determined. For example, in the case of PCI 2 under low $P_{amb}$ conditions the velocity of a 455 nm $d_{va}$ particle is 86 m $s^{-1}$ which translates into a flight time of 4.4 ms, the upper acquisition threshold. The actual largest diameter to be distinguished from noise was 420 nm. These experimental values are shown in Table 4.

With respect to future AMS deployments on HALO where altitudes of up to 15 km will be reached, the current PCI design has to be optimized. As mentioned above, $COr_2$ should be as large as possible to permit the maximum particle size range to be transmitted. At the same time, both orifices need to be maximized for measurements at low ambient pressures (high altitudes). This, however, will result in over pressure in the aerodynamic lens at low altitudes because the maximum opening of the PID valve will not allow sufficient withdrawal of excess air. Hence, installing two or more PID valves in parallel

can solve this problem. All valves can be controlled in the same way as is done currently based on the intermediate pressure.

**Table 4: Pressure controlled inlet (PCI) specifications for the CONCERT and POLARCAT campaign ($P_{amb}$ ambient pressure; $P_{PCI}$ pressure in the intermediate region; $P_{Lens}$ pressure in AMS lens); core $P_{amb}$: $P_{PCI}$ is constant, high $P_{amb}$ / low $P_{amb}$: $P_{amb}$ too high or low to keep $P_{PCI}$ constant, $P_{PCI}$ becomes a function of $P_{amb}$. The upper cut-off diameter has been converted from $d_{mob}$ to $d_{va}$.**

| | **CONCERT** | | | **POLARCAT** |
|---|---|---|---|---|
| Design | PCI 1 | PCI 2 | PCI 3 | PCI Polarcat |
| Orifice 1 and 2 (µm) | 380, 200 | 400, 200 | 380, 250 | 400, 160 |
| Aircraft operated on | 10/27/08 | 10/28/08<br>10/29/08 | 10/31/08<br>11/01/08 | 06/30 –<br>07/14/08 |
| high $P_{amb}$ (hPa) | > 800 | > 600 | > 600 | |
| $P_{PCI}$ function | $P_{PCI}$ =<br>0.22*$P_{amb}$+2.76 | $P_{PCI}$ =<br>0.36*$P_{amb}$-35.7 | $P_{PCI}$ =<br>0.29*$P_{amb}$-73.2 | |
| $P_{Lens}$ (hPa) | 2.4 – 2.2 | 2.9 – 2.3 | 2.9 – 2.3 | |
| upper cut-off $d_{va}$ (nm) | 735 | 735 | 735 | |
| core $P_{amb}$ (hPa) | 800 – 295 | 600 – 200 | 600 – 180 | 1000 – 350 |
| $P_{PCI}$ function | $P_{PCI}$ = 190 | $P_{PCI}$ = 188 | $P_{PCI}$ = 110 | $P_{PCI}$ = 387 |
| $P_{Lens}$ (hPa) | 2.2 | 2.2 | 2.2 | 2.2 |
| upper cut-off $d_{va}$ (nm) | 800 | 800 | 800 | 800 |
| low $P_{amb}$ (hPa) | < 295 | < 200 | < 180 | < 350 |
| $P_{PCI}$ function | $P_{PCI}$ =<br>0.33*$P_{amb}$ +96.5 | $P_{PCI}$ =<br>0.58*$P_{amb}$+69.5 | $P_{PCI}$ =<br>0.27*$P_{amb}$+61.8 | $P_{PCI}$ =<br>0.89*$P_{amb}$+53.5 |
| $P_{Lens}$ (hPa) | < 2.2 | < 2.2 | < 2.2 | < 2.2 |
| upper cut-off $d_{va}$ (nm) | 420 | 420 | 800 | 800 |

### *2.3.3 Coupling to aircraft inlets*

On each aircraft, the AMS was connected to a forward facing inlet for isokinetic sampling. For the DLR-Falcon, the inlet has been described in Fiebig (2001) and Schneider et al. (2006a). The sampling facility extends 30 cm beyond the fuselage probing the air outside the boundary layer of the aircraft. The upper end diameter is larger than 1.3 µm, thus not interfering with the upper cut-off diameter of the AMS inlet. Inside the aircraft, a 1/8" outer diameter stainless steel tube of less than one meter length connected the aircraft inlet with the AMS pressure controlled inlet (PCI) system. To guarantee isokinetic sampling the flow rate through this tube was kept constant at 2.5 l/min. Since the PCI had a flow rate of only 1.2 l/min a bypass with a throughput of 1.3 l/min was installed not affecting the sample flow.

During POLARCAT, the AMS sampled from the French community aerosol inlet (CAI) fabricated by COMAT as described by J.-L. Brenguier et al. (Community aerosol inlet, paper presented at ARM AVP workshop on Aircraft Instrumentation, Urbana-Champaign, IL, USA, 2008) and by McNaughton et al. (2007). The inlet was originally designed by the University of Hawaii. CAI is an isokinetic and isoaxial inlet with an estimated 50 % detection efficiency at 2.5 µm, thus not impairing AMS measurements. The mass spectrometer was connected via a ¼" OD stainless steel tube of approximately 2 m total length to the aircraft inlet.

## *2.4 AMS data acquisition, corrections, errors, and limit of detection*

During both campaigns, the AMS was operated in the so-called *general alternation mode*. For POLARCAT, one data point corresponds to 30 seconds sampling time spending three times five seconds in each mode. The final data was averaged to 2 minutes. These data represent a horizontal resolution of 12 km and approximately 600 m in the vertical during ascents and descents. For CONCERT, the time resolution was ten seconds with each mode recording half of the time. Additionally, the *FMS mode* with one second time resolution was applied during certain intervals. Data presented in this work are 30 second averages translating into a horizontal resolution of 6 km for a speed of 200 m $s^{-1}$ and a typical vertical resolution of 260 m.

The AMS data analysis was conducted with the standard software SQUIRREL (SeQUential Igor data REtRivaL) using versions 1.45 to 1.49. In addition, a number of campaign and instrument specific correction factors needed to be determined and considered for the final quantification and error estimation. Also, the limit of detection was calculated. This section explains how the individual factors were derived. They are presented in the order of application to the data.

### *2.4.1 Data Correction and Error estimation*

#### 2.4.1.1 Filter measurements

To be able to make experiment specific editions to the fragmentation table by means of which the signal of each recorded *m/z* is attributed to a certain chemical species, the AMS is operated with a particle filter in front of the inlet at certain intervals. For POLARCAT these intervals were kept at a minimum in order not to lose any precious ambient data during flights. Filter measurements were taken during three flights for a total of 40 min. The obtained spectra were averaged and served as the basis for the fragmentation table edition. During CONCERT it was tested if "surface filter" and "in-flight filter" data differed significantly. Since this was not the case, particle free air was measured after each scientific flight for approximately 30 min.

#### 2.4.1.2 Ionization efficiencies

To quantify aerosol mass concentrations, the ionization efficiency of chemical species in the AMS (see also section 2.1.1) is determined. *IE* is the ratio of ions detected by the MCP and the total amount of molecules of the chemical compound (e.g. nitrate). This standard procedure is described in Jayne et al. (2000) and Allan et al. (2003). Default relative *IEs* (*RIE*, relative to nitrate) for ammonium, sulfate, organics, and chloride are provided by the standard analysis software. However, these values are not necessarily valid for all individual instruments, so additional experiments were conducted for each electronic acquisition setting. Particles were generated from a solution of known ratio of ammonium nitrate, ammonium sulfate and succinic acid ($C_6H_{12}O_6$*$H_2O$), dried by two diffusion dryers and measured by the AMS in *MS mode*. Succinic acid was chosen as a representative for organic matter as it has a high O:C ratio (1.2), i.e. highly oxygenated, which is also expected for organic matter encountered in the Greenland troposphere and in the tropopause. By dividing the original composition ratio of the species by the ratio obtained with the AMS the instrument specific *RIE* values were determined as shown in Table 5.

**Table 5: Relative ionization efficiencies during the CONCERT and POLARCAT campaigns**

| Flight | $RIE_{SO4}$ | $RIE_{NH4}$ | $RIE_{Org}$ |
|---|---|---|---|
| October 27 | 1.00 ± 0.04 | 3.12 ± 0.02 | 1.76 ± 0.07 |
| October 28 | 0.96 ± 0.08 | 3.09 ± 0.03 | 1.77 ± 0.26 |
| October 29 | 1.03 ± 0.81 | 3.11 ± 0.08 | 1.76 ± 0.29 |
| October 31 | 0.98 ± 0.17 | 3.19 ± 0.04 | 1.78 ± 0.36 |
| November 02 | 0.94 ± 0.02 | 3.05 ± 0.2 | 1.73 ± 0.10 |
| all POLARCAT | 1.12 | 4.00 | 1.40 |
| default from SQUIRREL | 1.20 | 4.00 | 1.40 |

For this calibration it was assumed that each chemical compound forms particles in such a way that the mass of the particles reflects the compound's concentration in the solution and the relative abundance in comparison to the other compounds. Figure 18 shows that all particles were formed in the same size mode with a mode diameter of 270 nm $d_{va}$. Therefore, the potential error in the species' quantification due to different mass size distributions can be excluded.

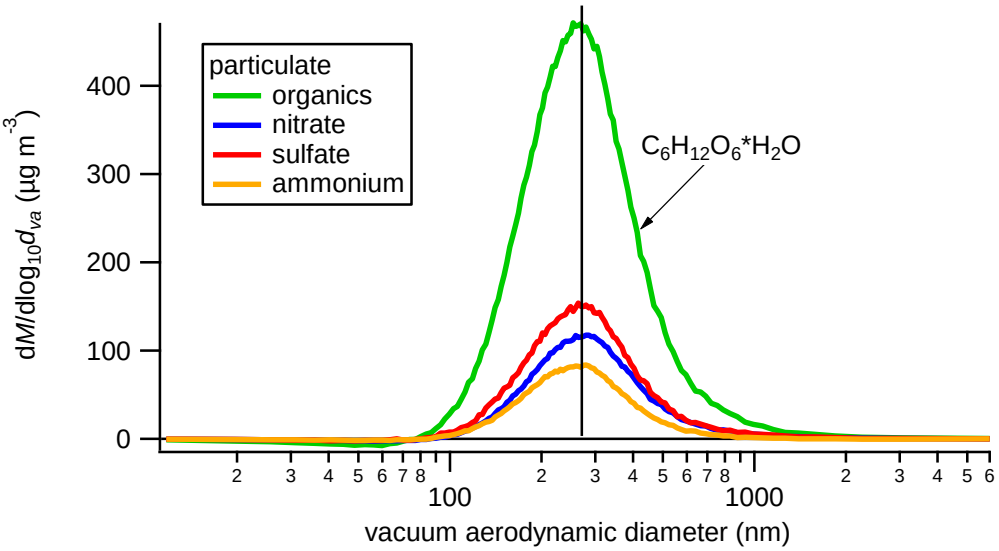


**Figure 18: Size distribution of "chemical cocktail" for the determination of relative ionization efficiencies.**

The reason for deviation from the default values might be related to the actual settings of the ion extraction lenses and of the mass spectrometer voltages, so that the ion transmission as a function of the *m/z* value is different from that during the experiments when the default *RIE* values were established. Regarding $RIE_{Org}$, additionally the type of ionized organic fragments might play a role meaning that ions of highly oxygenated organic matter fragments can be extracted to a different degree than ionized fragments from hydrocarbons (Jimenez et al., 2003).

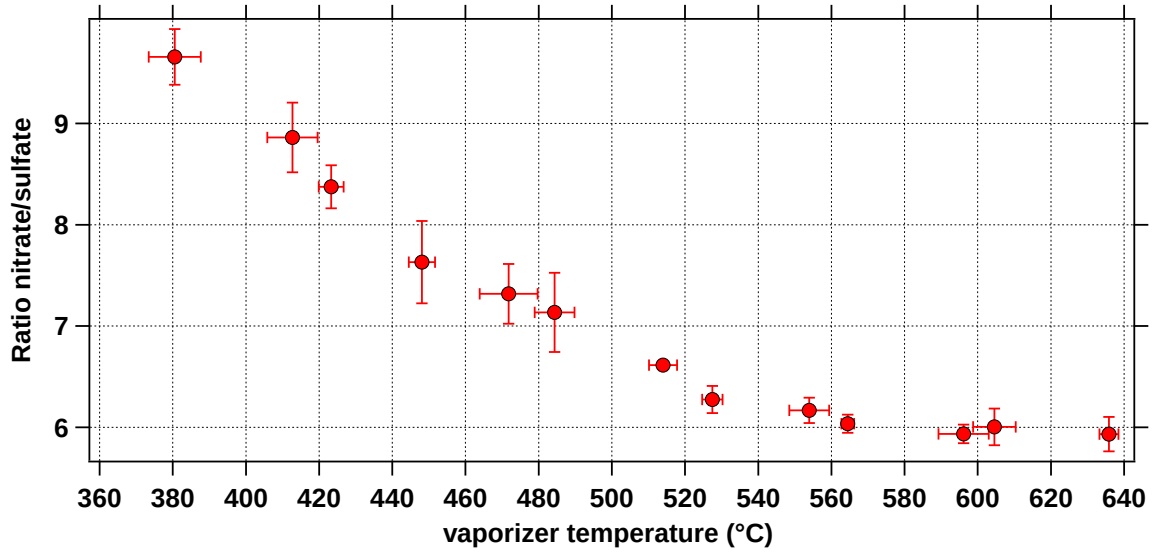


**Figure 19: Ratio of nitrate and sulfate dependent on the vaporizer temperature. The heater should be operated at a temperature of more than 560°C to ensure correct measurement of sulfate.**

Also, the actual temperature of the vaporizer plays a role for $RIE_{SO4}$. To quantify this, the temperature of the vaporizer was scanned from 370 to 640 °C and a known mixture of ammonium nitrate and ammonium sulfate was measured. The data was binned into 20 °C intervals as shown in Figure 19. The bars denote the standard deviation from the mean per bin. The graph shows that lower heater temperatures cause an underestimation of sulfate mass as the aerosol component is only partially evaporated. For the field experiment, data between 520 and 640 °C are relevant. In this range a deviation of 5 % from the mean is observed. This needs to be considered when calculating the error for sulfate mass concentrations. In the respective range, each bin represents between 6 and 18 data points (the bin between 560 and 580°C only contains 2 data points).

#### 2.4.1.3 Campaign related corrections

**POLARCAT - Jump Mass Mode**

Due to very low mass concentrations (total average of 0.54 µg $m^{-3}$) observed during the POLARCAT-summer experiment many of the mass to charge ratios contributing to the organic spectrum were close to or even below zero. This adds noise to the total organic signal and increases the limit of detection (LOD). The LOD depends on the instrument's background signal ($I_b$) and is calculated from three times the standard deviation of $I_b$ times $\sqrt{2}$ to account for the noise in the background and measurement signal which are subtracted from each other for the determination of the aerosol mass concentration. Therefore, only a selection of m/z, i.e. their contributions to the organic mass spectrum, was chosen to represent the total organic mass similar to the jump mass mode (*JMS*) used for quadrupole AMS data analysis as described by Crosier et al. (2007) and as suggested by Drewnick et al. (2009). The considered mass to charge ratios were derived from an organic mass spectrum obtained during sampling a pollution plume, thus accounting for mass to charge ratios present in the background and pollution events. The final selection criterion was a combination of three factors:

(1) an increased number of points above LOD compared to the total organic mass signal,

(2) a maximum ratio of the correlation coefficient (Pearson's R), from the linear regression of the organic selection versus the total organic spectrum, and the LOD, and

(3) the highest representation of mass of the total organic mass after fulfillment of points 1 and 2.

Figure 20 illustrates the combinations of *m/z* which were tested to represent the total particulate organic mass. The horizontal axis denotes the ratio of Pearson's *R* correlation coefficient and the limit of detection: the higher the value of the ratio, the better the selection because this implies a higher correlation and a lower limit of detection. *R* is derived from the same number of points (182) for each combination of *m/z*. The vertical axis shows the fraction of data points within the selected group of *m/z* that are greater than the LOD compared to the standard organic mass concentration data points. The more points are greater than the detection limit the better the selection. Therefore, the best selection is theoretically located in the upper right corner.

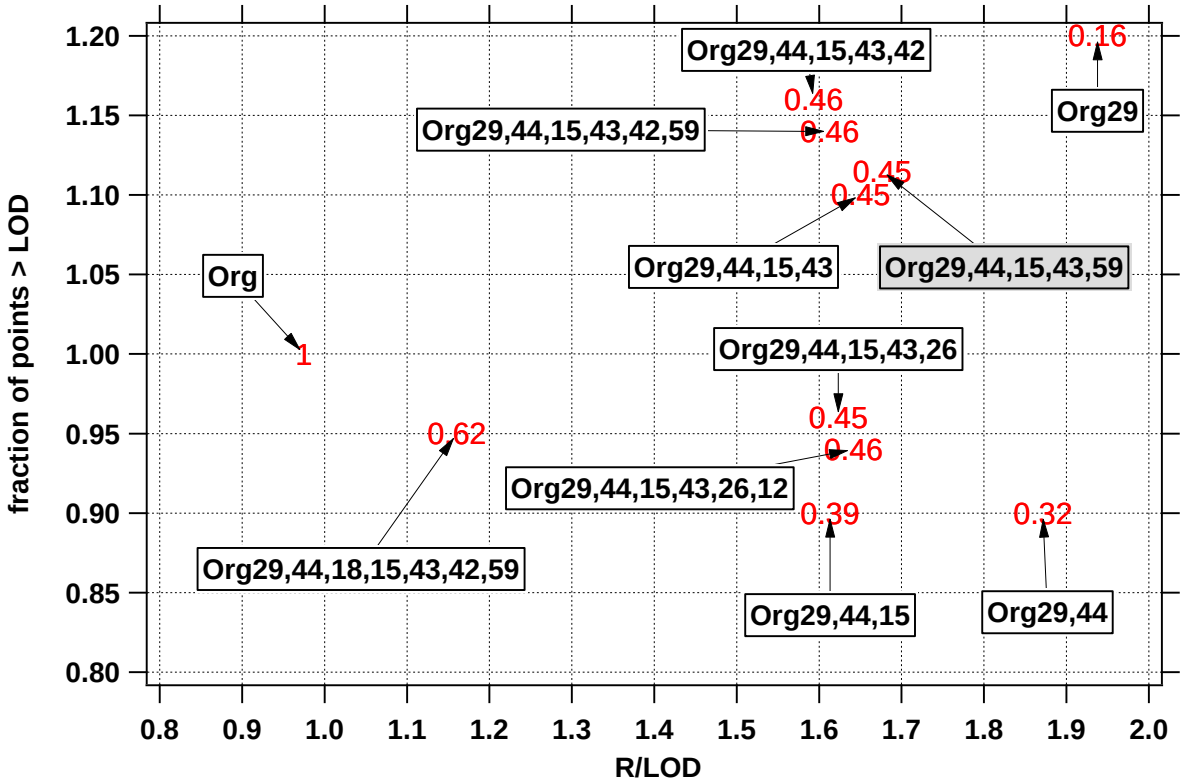


**Figure 20: Determination of the *m/z* used to represent organic mass during POLARCAT. R, Pearsons correlation coefficient of selected mass versus total mass; LOD, limit of detection; the red numbers denote the fraction of mass represented by the selection which is given in the boxes. The grey box shows the final choice.**

However, another factor, the fraction of the total organic mass that is represented by the selection, shall be as large as possible without sacrificing the quality of the selection. Choosing only *m/z* 29 (upper right corner) leads to a high *R/LOD* ratio and the highest number of data points above LOD but only 16 % of the total organic mass are represented. Selecting a group of *m/z* including 29, 44, 18, 15, 43, 42, and 59, yields a fraction of 62 % of mass, however with less data points above LOD than the standard organics. Therefore, the group indicated by the grey box was chosen resulting in the selection of five *m/z* (15, 29, 43, 44, and 59) corresponding to the most abundant ions observed that exhibited a

clear signature in all flights. Table 6 shows the Pearson correlation coefficient, number of data points included, and fraction of mass represented for each flight including the standard deviation of the linear regression. Organic aerosol mass data discussed in this work are based on these representative mass to charge ratios. This means that the mass selection has been divided by the numbers shown in column 2 of Table 6.

**Table 6: Representation of organic mass by the *m/z* selection for POLARCAT (sdev = standard deviation), Pearson correlation coefficient (*R*) of the linear regression**

| Flight Date | % mass ± sdev | *R* | Number of data points |
|---|---|---|---|
| June 30 | 38 ± 3 | 0.82 | 32 |
| July 08 | 49 ± 2 | 0.72 | 165 |
| July 10 | 47 ± 2 | 0.80 | 107 |
| July 12a | 52 ± 2 | 0.62 | 163 |
| July 12b | 60 ± 2 | 0.75 | 145 |
| July 13 | 52 ± 1 | 0.73 | 121 |
| July 14a | 49 ± 1 | 0.68 | 145 |
| July 14b | 43 ± 1 | 0.74 | 124 |

**CONCERT – Fast Mass Spectrum Mode**

Different acquisition settings for general alternation and *FMS* mode had to be corrected for. The general alternation settings (baseline, threshold and offset voltages) were calibrated according to the standard procedure with the Data Acquisition Software. Since the *FMS mode* was applied for the first time it was not known that the determined acquisition settings were not automatically adopted for all other modes. Instead the software's default values were applied. The difference in the electronic threshold values, which determine when a signal originates from ambient particles opposed to electronic noise, resulted in unequal final mass concentrations for the same aerosol load. Thus, laboratory generated particles from an ammonium nitrate, ammonium sulfate and succinic acid solution were measured by the AMS in both modes with each flight's electronic settings. Division of the *FMS* mode values by the general alternation mode values yielded the correction factor or each *m/z*. As Figure 21 shows, the *FMS* correction factor (open red circles) for *m/z* ratios smaller than 100 varies slightly. For *m/z* larger than 100 the factor becomes noisy which is mainly due to the low signal intensity in the recorded mass spectrum (black bars). However, *m/z* larger than 110 were not detected during CONCERT.

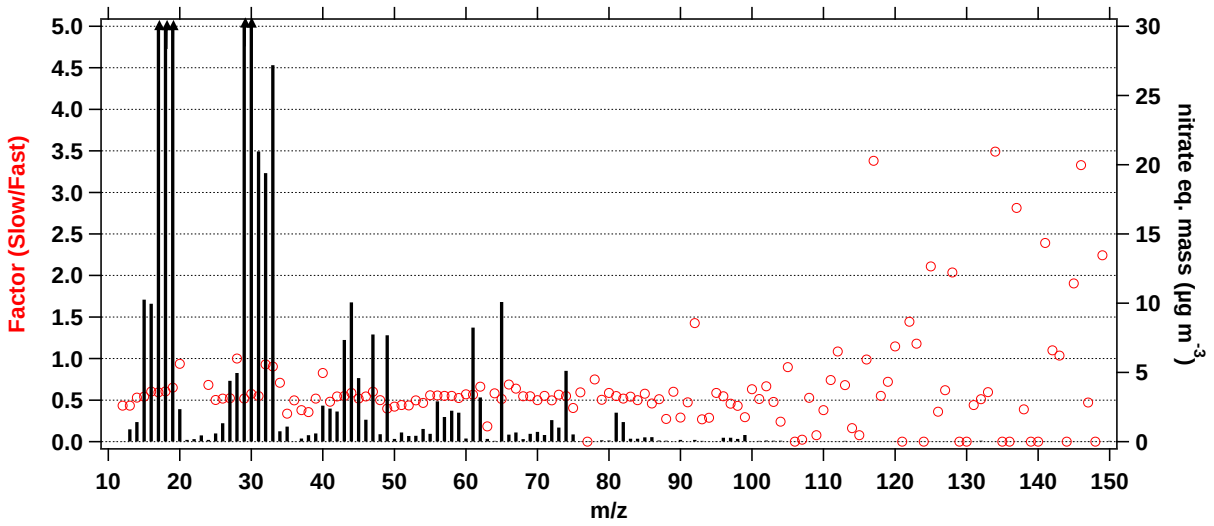


**Figure 21: m/z dependent correction factor for fast mass spectrum mode**

Due to the slight variations dependent on the mass to charge ratio the final *FMS* correction factor was determined per chemical species (see Table 7):

**Table 7: Fast mode correction factors for CONCERT particulate species including standard deviation**

| Flight | # of points | Organics | Sulfate | Nitrate | Ammonium | Chloride |
|---|---|---|---|---|---|---|
| October 27 | 372 | 0.62 ± 0.01 | 0.63 ± 0.01 | 0.64 ± 0.02 | 0.66 ± 0.01 | 0.65 ± 0.09 |
| October 28 | 372 | 0.59 ± 0.01 | 0.60 ± 0.01 | 0.62 ± 0.02 | 0.64 ± 0.02 | 0.61 ± 0.05 |
| October 29 | 379 | 0.56 ± 0.01 | 0.58 ± 0.01 | 0.60 ± 0.01 | 0.63 ± 0.01 | 0.56 ± 0.04 |
| October 31 | 312 | 0.54 ± 0.01 | 0.56 ± 0.01 | 0.57 ± 0.01 | 0.61 ± 0.01 | 0.54 ± 0.06 |
| November 02 | 438 | 0.60 ± 0.01 | 0.61 ± 0.02 | 0.63 ± 0.02 | 0.64 ± 0.02 | 0.62 ± 0.05 |

#### 2.4.1.4 Pressure controlled inlet related correction

With the employment of the PCI the recorded data refer to conditions in the intermediate chamber at $P_{PCI}$. Conversion to STP is done by the following equation:

$$C_{STP} = C_{AMS} * \frac{V_{meas}}{V_{COr}} * \frac{P_{STP}}{P_{PCI}}$$

Eq. 6

with $C_{STP}$ being the concentration at STP conditions, $C_{AMS}$ the mass concentration obtained after standard AMS data processing and applying the actual *RIE*, $V_{meas}$ the flow rate measured by the pressure sensor in the aerodynamic lens calibrated for standard pressure and a critical orifice of 100 µm, $V_{COr}$ the nominal flow rate through the last critical orifice ($COr_2$), and $P_{STP}$ being equal to 1013.25 hPa.

#### 2.4.1.5 Collection efficiency

Next to losses occurring in the inlet and lens system ($E_L$) and losses due to non-focusing of irregularly shaped particles after having passed through the aerodynamic lens ($E_S$), there are certain types of particles which hit the heater and bounce-off immediately ($E_B$). These particles cannot be vaporized and their mass is not accounted for. In order to compensate for these artifacts, the so called collection efficiency (*CE*) factor, the product of all three effects ($CE = E_L * E_S * E_B$), is introduced (Huffman et al., 2005). It has been shown that a *CE* factor of 0.5 represents quite well the sampling of ambient aerosol as determined and applied in various field campaigns (e.g. Allan et al., 2004a; Drewnick et al., 2004; Hings et al., 2007). Based on this experience and the lack of opportunity to compare AMS mass concentrations to data recorded by other instruments for the campaigns considered in this work, the *CE* factor was set to 0.5. An additional argument in favor is that particles were sampled at ambient temperatures between -30 and -64° C (CONCERT) and between -10 and -34 °C (POLARCAT) at low relative humidity most of the time. Since the sampling line in the aircraft was not cooled, temperature differences between the outside and inside were on average 79 K with a maximum difference of 107 K (CONCERT) and 48 K average and 75 K maximum for POLARCAT. Thus, it is assumed that most of the water contained in the particles evaporated within the sampling line. So particles entering the AMS were dry and would therefore bounce off the heater more likely. Studies by Matthew et al. (2008) have shown that solid phase particles have low collection efficiencies around 20 to 30 % opposed to liquid phase particles with *CEs* around 100 %. On the other hand, it was found that very acidic aerosol, mainly composed of sulfuric acid, tends to have a *CE* of 1 in a marine environment (Quinn et al., 2006). However, except for the volcanic aerosol, the particles measured during POLARCAT and CONCERT were composed of more than 50 % organic matter. Here a *CE* of 0.5 is applied for all CONCERT measurements, while for POLARCAT a $CE_{PCI}$ of 0.5*0.54 = 0.27 is used, including the PCI transmission efficiency (see section 2.3.2.).

#### 2.4.1.6 Total Error

The total error related to each data point is comprised of two types of uncertainties:

(1) A statistical error can be attributed to each measurement point based on ion counting statistics (Allan et al., 2003). For POLARCAT it is near 30 % for sulfate data points greater than the three standard deviation LOD (see section 2.4.2) and 41 % for organics for 30 seconds time resolution. For CONCERT the errors are around 16 % and 57 %, respectively, for 10 second data. These large statistical errors become plausible when considering that the actual detected ion signal from ambient aerosol is only about 1 % higher than the instrument background signal in most cases. Figure 22 shows an example for the flight on 8 July, 2008.

(2) The results are subject to a systematic error caused by the collection efficiency as described in section 2.4.1.5 including the pressure controlled inlet transmission efficiency which is near 30 %, see Figure 17 and Schmale et al. (2010). This error cannot be determined on a point by point basis. Equally, the campaign specific correction factors were not calculated on a single point basis. In the case of the *JMS* mode for POLARCAT the standard deviation of the factor as derived from the linear regression is given in Table 6. For CONCERT the standard deviation of the *FMS* correction factor is given in Table 7.

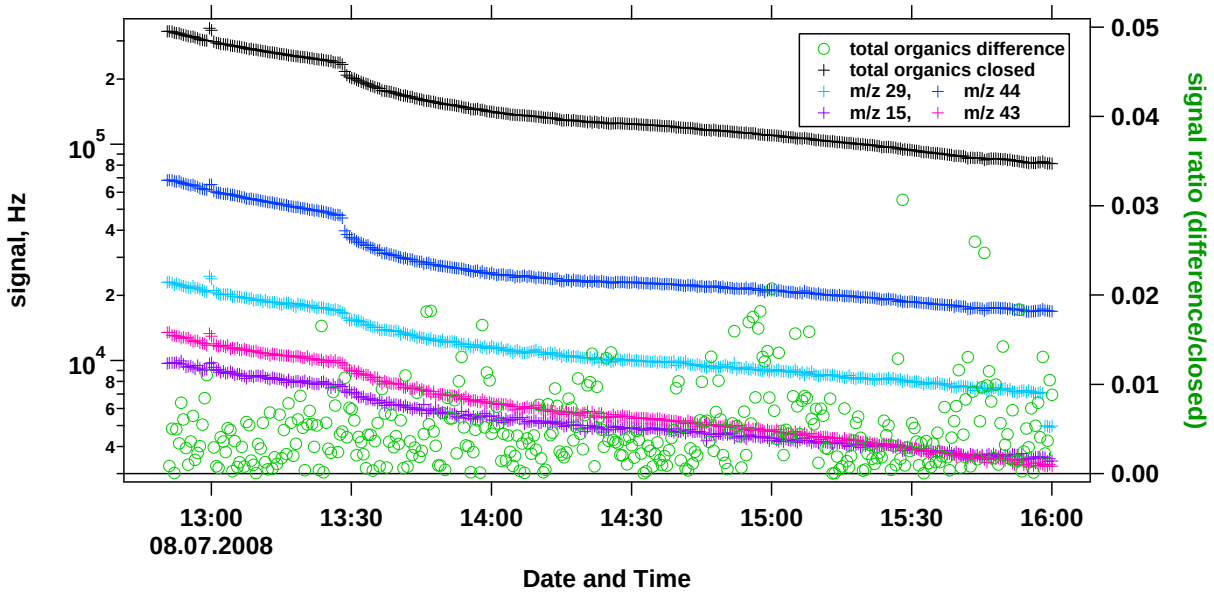


**Figure 22: Signal (Hz) for organic matter during the flight on 8 July, 2008. The right vertical axis denotes the ratio of difference and closed signals.**

In the end, for each AMS data point an error was calculated. It comprises uncertainties derived from counting statistics (Allan et al., 2003) and for sulfate containing particles during CONCERT additionally an uncertainty of 5 % due to variations in the relative ionization efficiency (see discussion in section 2.4.1.2).

### *2.4.2 Limit of Detection*

Classically, the limit of detection (LOD) for each species is calculated from the standard deviation of the aerosol mass concentration in air sampled through a particle filter, such that the mean aerosol mass concentration is expected to be 0 µg $m^{-3}$ and deviation from this value indicates the sensitivity of measurement. For aircraft deployments, however, special circumstances apply. Adequately long filter measurements during flights cannot be afforded (see section 2.4.1.1) and background values change significantly during flights. Alternatively, after Drewnick et al. (2009) the LOD can be calculated as three times the standard deviation from the closed signal of each chemical species multiplied by √2. The factor √2 is due to the fact that the open signal which is used to determine the difference is subject to the same deviation. However, the closed, i.e. instrumental background signal, during flights is subject to variations. This is due to the circumstance that the vacuum can only be established within a relatively short period of time before take-off. For CONCERT and POLARCAT roughly four hours were available for pumping. As a consequence, the background concentration is relatively high at the beginning and decreases during the flight due to the continued pumping and low ambient aerosol loadings. Different *m/z* decrease at distinct rates which results in difficulties finding an appropriate fit function to the closed signal of chemical species such as organics that are composed of many *m/z*. Figure 22 shows the decay of the organic closed signal (black crosses) and selected *m/z* for an example flight. A long-scale decreasing trend is visible on which short- and small-scale noise is superimposed.

To determine the standard deviation from the mean closed signal composed of the different-scale signatures an algorithm developed by Reitz (2011) was applied. This algorithm separates the short-

scale noise of a curve from its long-term trend by local cubic interpolation, such that the standard deviation of the curve with respect to the short-scale noise can be calculated. The algorithm provides the LOD including its estimated error at the one and three sigma level, i.e. at the 68.30 and 99.73 % confidence interval. Table 8 shows the 2 min values for POLARCAT with the 30 second LOD in parenthesis for comparability with the 30 second CONCERT data.

**Table 8: Three sigma limit of detection (µg $m^{-3}$ STP) per flight during POLARCAT for 2 minutes and 30 second data in parenthesis, and CONCERT for 30 second average data**

| Flight | Particulate Sulfate | Particulate Nitrate | Particulate Ammonium | Particulate Organics | Particulate Chloride |
|---|---|---|---|---|---|
| June 30 | 0.08 (0.16) | 0.03 (0.06) | 0.35 (0.70) | 0.80 (1.60) | x |
| July 08 | 0.06 (0.12) | 0.02 (0.04) | 0.27 (0.54) | 0.22 (0.44) | x |
| July 10 | 0.03 (0.06) | 0.01 (0.02) | 0.18 (0.36) | 0.18 (0.36) | x |
| July 12a | 0.03 (0.06) | 0.01 (0.02) | 0.20 (0.40) | 0.21 (0.42) | x |
| July 12b | 0.04 (0.08) | 0.02 (0.04) | 0.25 (0.50) | 0.23 (0.46) | x |
| July 13 | 0.10 (0.20) | 0.04 (0.08) | 0.41 (0.81) | 0.53 (1.06) | x |
| July 14a | 0.08(0.16) | 0.02 (0.04) | 0.18 (0.36) | 0.25 (0.50) | x |
| July 14b | 0.05 (0.10) | 0.03 (0.06) | 0.35 (0.70) | 0.42 (0.84) | x |
| October 27 | 0.02 | 0.03 | 0.12 | 0.14 | 0.04 |
| October 28 | 0.03 | 0.02 | 0.17 | 0.11 | 0.04 |
| October 29 | 0.02 | 0.03 | 0.10 | 0.10 | 0.03 |
| October 31a | 0.03 | 0.02 | 0.13 | 0.10 | 0.03 |
| October 31b | 0.02 | 0.02 | 0.13 | 0.07 | 0.03 |
| November 02 | 0.02 | 0.02 | 0.15 | 0.11 | 0.03 |

### *2.4.3 Example calculation for aerosol mass concentration corrections and error estimations*

Table 9 illustrates how the final mass concentrations of particulate sulfate and organics were calculated including all corrections and error estimations for the POLARCAT and CONCERT campaigns. The individual steps of the calculation are labeled as “corrections” and shown in the order of application. Statistical errors were added by taking the square root of the sum of the squares of each single error.

The following equation (Eq. 7) elaborates how the mass concentration of a species *s* is calculated based on the ion counting rate which corresponds to “correction step” 2 in Table 9. Here, the laboratory calibration of the ionization efficiency of nitrate is used (see section 2.4.1.2).

$$C_{sAB} = \frac{1}{RIE_s} * \frac{\sum_f I_{sf}}{N_A * Q_{in}} * \frac{MW_{NO_3}}{IE_{NO_3}} * 10^{12} * AB_{corrf} \quad \textbf{Eq. 7}$$

With $C_{sAB}$: mass concentration of a chemical species *s* in µg m$^{-3}$ of air, $RIE_s$: relative ionization efficiency of species *s*, $\sum_f I_{sf}$: total signal intensity in ions s$^{-1}$ of species *s* summed over all contributing fragments, $N_A$: Avogadro's number (6.02*10$^{23}$ mol$^{-1}$), $Q_{in}$: flowrate into the instrument (1.28 cm$^3$ s$^{-1}$), $MW_{NO3}$: molecular weight of nitrate (62.007 g mol$^{-1}$), $IE_{NO3}$: ionization efficiency of nitrate, $AB_{corrf}$: air beam correction factor, and 10$^{12}$ is the conversion factor from g cm$^{-3}$ to µg m$^{-3}$.

Example for particulate sulfate during CONCERT:

Default $RIE_{SO_4}$:

$$0.33\ \mu g\ m^{-3} = \frac{1}{1.2} * \frac{1804.7\ s^{-1}}{6.02*10^{23}\ mol^{-1}*1.28\ cm^3\ s^{-1}} * \frac{62.007\ g\ mol^{-1}}{3.04*10^{-7}} * 10^{12} * 0.825$$

Measured $RIE_{SO_4}$:

$$0.29\ \mu g\ m^{-3} = \frac{1}{1.4} * \frac{1872.5\ s^{-1}}{6.02*10^{23}\ mol^{-1}*1.28\ cm^3\ s^{-1}} * \frac{62.007\ g\ mol^{-1}}{3.04*10^{-7}} * 10^{12} * 0.825$$

**Table 9: Example calculation of aerosol mass concentrations for particulate sulfate and organics for one data point during the POLARCAT and CONCERT campaigns**

| | Correction | POLARCAT | | | | CONCERT | | | |
|---|---|---|---|---|---|---|---|---|---|
| | | 14 July, 2008, 16:05:01 | | | | 31 October 2008, 15:12:30 | | | |
| # | Description / section | Particulate sulfate | Error | Particulate organics | Error | Particulate sulfate | Error | Particulate organics | Error |
| 1 | Frag table edition based on particle filter measurement / 2.4.1.1 | n.d. | n.d. | Correction factors for: Air *m/z* 29: 1.07 $CO_2$ *m/z* 44: 1.25 | n.d | n.d. | n.d. | Correction factors for: Air *m/z* 15: 0.014 Air *m/z* 29: 0.64 $CO_2$ *m/z* 44: 0.64 | n.d |
| | Value (Hz) / ion counting error (Hz) | **2185.9** | **210.28, 9.6 %** | **4273.81** | **1497.65, 35.0 %** | **1804.7** | **26.3, 1.4 %** | **1872.5** | **134.2, 7.2 %** |
| 2 | Application of air beam correction factor and conversion to µg $m^{-3}$ (see Eq. 7) | $AB_{corrf}$: 0.658 $Q_{in}$: 1.26 $cm^3$ $s^{-1}$ $IE_{NO3}$: $3.54*10^{-7}$ | | | | $AB_{corrf}$: 0.825 $Q_{in}$: 1.28 $cm^3$ $s^{-1}$ $IE_{NO3}$: $3.04*10^{-7}$ | | | |
| | Initial value (µg $m^{-3}$) / ion counting error (µg $m^{-3}$) | **0.28** | **0.03, 9.6 %** | **0.46** | **0.16, 35.0 %** | **0.33** | **0.005, 1.4 %** | **0.29** | **0.02, 7.2 %** |
| 3 | Application of RIE as determined from laboratory experiments (section 2.4.1.2) | $RIE_{SO4}$: 1.12 | ± 5 % uncertainty in final mass concentration | n.d. | n.d. | $RIE_{SO4}$: 0.98 (see Table 5) | ± 5 % uncertainty in final mass concentration | $RIE_{Org}$: 1.78 (see Table 5) | |
| | Value (µg $m^{-3}$) / error (µg $m^{-3}$) | **0.29** | **0.03, 10.8 %** | **0.46** | **0.16, 35.0 %** | **0.42** | **0.02, 5.2 %** | **0.23** | **0.02, 7.2 %** |

| | | | | | | | | | |
|---|---|---|---|---|---|---|---|---|---|
| 4 | Campaign specific corrections (section 2.4.1.3) | n.d. | n.d. | *JMS* correction factor: 2.33 (see Table 6: 1/0.43=2.33) | ± 2.3 % uncertainty of correction factor | *FMS* correction factor: 0.56 (see Table 7) | ± 1 % uncertainty in final mass concentration | *FMS* correction factor: 0.54 (see Table 7) | ± 1 % uncertainty in final mass concentration |
| | Value (µg $m^{-3}$) / error (µg $m^{-3}$) | **0.29** | **0.03, 10.8 %** | **1.08** | **0.38, 35.0 %** | **0.24** | **0.01, 5.3 %** | **0.12** | **0.01, 7.3 %** |
| 5 | PCI correction (section 2.4.1.4) | See Eq. 6 With $V_{meas}$ = 1.26 $cm^3$ $s^{-1}$; $V_{COr}$ = 3.54 $cm^3$ $s^{-1}$; $P_{PCI}$ = 387.0 hPa | | | | See Eq. 6 With $V_{meas}$ = 1.28 $cm^3$ $s^{-1}$; $V_{COr}$ = 7.8 $cm^3$ $s^{-1}$; $P_{PCI}$ = 110. hPa | | | |
| | Value (µg $m^{-3}$) / error (µg $m^{-3}$) | **0.28** | **0.03, 10.8 %** | **1.03** | **0.36, 35.0 %** | **0.36** | **0.02, 5.3 %** | **0.18** | **0.02, 7.3 %** |
| 6 | Collection efficiency (section 2.4.1.5) | $CE_{PCI}$ = 0.27 | | | | CE = 0.5 | | | |
| | Final value (µg $m^{-3}$) / error (µg $m^{-3}$) | **1.04** | **0.11, 10.8 %** | **3.82** | **1.34, 35 %** | **0.72** | **0.04, 5.3 %** | **0.32** | **0.04, 7.3 %** |
| | Difference from initial value | **373 %** | | **830 %** | | **218 %** | | **110 %** | |
| | Total statistical error | | Ion counting statistics + RIE uncertainty: 0.11, 10.8 % | | Ion counting statistics + *JMS* uncertainty: 1.34, 35 % | | Ion counting statistics + RIE uncertainty + FMS uncertainty: 0.04, 5.3 % | | Ion counting statistics + *FMS* uncertainty: 0.04, 5.3 % |
| | Total systematic error (section 2.4.1.6) | | ± 30 % 0.31 µg $m^{-3}$ | | ± 30 % 1.14 µg $m^{-3}$ | | ± 30 % 0.22 µg $m^{-3}$ | | ± 30 % 0.10 µg $m^{-3}$ |
| | Limit of detection (µg $m^{-3}$) | **0.10** | | **0.84** | | **0.02** | | **0.11** | |

## 2.5 Complementary Data

For an extensive chemical analysis and source identification of particle pollution plumes it is necessary to combine AMS data from POLARCAT and CONCERT with complementary aerosol, trace gas, meteorological, trajectory, and model data. Furthermore, aerosol chemical composition, water vapor, ozone, CO, $SO_2$, and acetonitrile ($CH_3CN$) data from the ARCTAS spring and summer missions were used to create a more complete overview on high latitudinal free tropospheric and tropopause perturbations. This section introduces the respective instruments, data and models and gives an overview of how these data were integrated into the final interpretation. [The following descriptions are adapted from Schmale et al. (2010) and (2011).] Basic positioning data (latitude, longitude, altitude) and meteorological data (pressure and temperature) were taken from aircraft standard instruments and are not further commented. All data related to the ARCTAS campaigns were obtained online from the DC-8 60 seconds validated merged files at http://www-air.larc.nasa.gov/cgi-bin/arcstat-c-pre-www (January 2011, if not stated otherwise).

### 2.5.1 Aerosol Data

**Aerosol size distribution**

For plumes detected during POLARCAT, in-situ aerosol size distribution data for particles smaller than 500 nm $d_{mob}$ were provided from a scanning mobility particle sizer (SMPS) system (Villani et al., 2007; Quennehen et al., 2011) operated by the group from Laboratoire de Météorologie Physique, Université Blaise Pascal, Aubière, France. Data was acquired continuously aboard ATR-42 at 130 seconds time resolution. These data were used to identify pollution plumes and wash-out events during POLARCAT (see section 2.7.3), and to determine the average size distribution of certain pollution source types, e.g. North American biomass burning. The SMPS volume size distribution data can be compared qualitatively to AMS mass concentration within certain constrains. The particle size ranges of the SMPS, 20 – 500 nm $d_{mob}$, and the AMS, 80 – 1000 nm $d_{va}$, are comparable (see Eq. 2). Assuming a Jayne shape factor of 1, i.e. spherical particles, as most particles are aged after long-range transport, and a density of roughly 1.7 g $cm^{-3}$ based on a density of 1.84 g $cm^{-3}$ for sulfuric acid and 1.5 – 1.7 g $cm^{-3}$ for aged organic matter (Dinar et al., 2006), an SMPS vacuum aerodynamic diameter range from 34 to 850 nm is obtained. It can thus be expected that whenever the SMPS detects a clear signal in accumulation mode particles the AMS will detect a mass signal. Even though the SMPS detects refractory particles such as black carbon and dust (and sea salt which is of minor relevance in this context) which the AMS cannot vaporize, these particles will most likely be coated with non-refractory material that is detected by the AMS. BC is emitted from BB and FF simultaneously with VOCs and $SO_2$ in the latter case. These gas phase components will undergo chemical change over time and transport and partition to the particle phase (e.g. Hallquist et al., 2009; Jimenez et al., 2009).

**Aerosol chemical composition**

ARCTAS aerosol chemical data were taken from HR-ToF-AMS measurements conducted by Mike Cubison, University of Boulder, Boulder, Colorado, USA. The results are comparable to the C-ToF-AMS data (see section 2.1.2) and were used to establish a history of particulate sulfate loadings in the tropopause before the eruption of Mts. Okmok and Kasatochi in July and August, 2008. These data

were downloaded in October 2009. Additionally, the data were used for two case studies and integrated in the final resume of particulate sulfate and organics concentrations in the perturbed and unperturbed free troposphere and tropopause in mid and high latitudes.

For putting CONCERT particulate sulfate data into a larger context they were compared to publications from Martinsson et al. (2005) and (2009) that are based on CARIBIC (Civil Aircraft for the Regular Investigation of the atmosphere Based on an Instrument Container) measurements. CARIBIC is a scientific project which deploys a freight container equipped with trace gas and particle instruments on commercial long-distance flights to study atmospheric chemical and physical processes. Particulate sulfur is obtained by means of filter samples which are analyzed in the laboratory by particle-induced X-ray emission (PIXE) for particles in the range between 0.07 and 1.5 µm (Martinsson et al., 2001). Even though particles larger than 1 µm are taken into account the data is still comparable to AMS measurements as experience shows that more than 90 % of the mass is carried by particles smaller than 0.6 µm (Martinsson et al., 2005).

### *2.5.2 Trace Gas Data*

**Table 10: Utilization of trace gas measurements for aerosol data interpretation**

| Trace Gas | Property | POLARCAT | ARCTAS | CONCERT |
|---|---|---|---|---|
| **$O_3$** | stratospheric tracer | determination of the chemical tropopause<br>determination of stratospheric air mass influence<br>identification of pollution plumes | not used | not used |
| **CO** | tropospheric tracer, emitted by FF and BB | determination of the chemical tropopause<br>identification of BB and FF pollution plumes | | not used |
| **$H_2O_{vap}$** | tropospheric tracer | presence of clouds | tropospheric air mass influence in lower stratospheric air masses | |
| **$SO_2$** | emitted by FF and volcanoes | not used | identification of FF pollution | identification of volcanic pollution plumes |
| **$NO_y$** | tracer for FF off-gas*) | not used | not used | identification of contrail interception |
| **$CH_3CN$** | BB tracer | not used | identification of BB pollution plumes | not used |

*) off-gas means exhaust

Table 10 provides an overview on the kind of trace gases and why they were used for data interpretation. The column "property" only states the most relevant aspect for the context of this work. $O_3$, CO and water vapor ($H_2O_{vap}$) are available for all three missions, while $SO_2$ was not recorded during POLARCAT and acetonitrile ($CH_3CN$) only during ARCTAS. Total $NO_y$ is available for CONCERT and ARCTAS but was only relevant for contrail measurements within the scope of this work. Detailed information on how exactly trace gas data were applied is given in section 2.7.

**Ozone**

The ATR-42 ozone instrument (Ancellet et al., 2009) is based on UV absorption with two cells and has a precision of 2 nmol $mol^{-1}$ at a time resolution of four seconds. On the Falcon, ozone measurements were performed with a two cell (zero, sample) UV absorption photometer switching chambers every four seconds. Pressure and temperature data is also recorded by the instrument at a 1 Hz rate. Ozone values are generated every four seconds. This data is then corrected for pressure and temperature. The range of the instrument is 0 to 1000 nmol $mol^{-1}$ with a detection limit of 1 nmol $mol^{-1}$ (Brough et al., 2003). The CARIBIC project measures ozone also by UV absorption.

**Carbon Monoxide**

Carbon monoxide was detected on board the ATR-42 by means of a CO analyzer (Nedelec et al., 2003) based on an IR absorption technique. It has a precision of 5 nmol $mol^{-1}$ with a lower detection limit of 10 nmol $mol^{-1}$. On the Falcon, CO measurements are based on fluorescence detection. The instrument can be operated to less than 100 mbar and has been calibrated regularly during flights by injection of a known CO standard. The time resolution is one second and response is linear between 0 and 1000 mmol $mol^{-1}$ while the detection limit is smaller than 6 nmol $mol^{-1}$ and precision is 1.5 nmol $mol^{-1}$ (Brough et al., 2003).

**Water vapor**

On both aircraft, a Lyman-Alpha hygrometer (Buck, 1976) was used to provide fast response water vapor measurements. On the ATR-42, a slower response General Eastern 1011B hygrometer designed for airborne applications was mounted in close proximity and used to normalize the Lyman-Alpha signal. The water vapor mixing ratio can be converted into relative humidity which indicates the atmosphere's saturation with water vapor and the possible presence of clouds. This information was used primarily for the interpretation of POLARCAT data.

**Sulfur Dioxide**

Sulfur dioxide measurements were performed with an IT-CIMS (ion trap chemical ionization mass spectrometer), (Fiedler et al., 2005; Speidel et al., 2007; Fiedler et al., 2009). The IT-CIMS instrument was equipped with an $SF_5^-$ ion source using a selective reaction for the detection of $SO_2$. The time resolution of the instrument is 1.6 s for trapping and read-out of a spectrum from 15 to 170 atomic mass units (amu) with a mass resolution of 0.3 amu. Calibration was performed after the flight. The detection limit for a running mean over 10 spectra is 18 pptv for $SO_2$ (Jurkat et al., 2010). The IT-CIMS results were integrated in the characterization of volcanic aerosol plumes. $SO_2$ data from the DC-8 were used for the identification of anthropogenic influenced air masses during ARCTAS.

**$NO_y$**

Total $NO_y$ was measured with a forward facing inlet on Falcon. Here, particulate nitrate is evaporated and then reduced to NO by means of CO in a heated gold converter together with all gaseous $NO_y$ species. The subsequent chemiluminescence reaction of NO and $O_3$ is detected in the near infrared. Temporal resolution is 1 second, the detection limit 5 pmol $mol^{-1}$ and the accuracy ± 8 % (Voigt et al., 2010).

## 2.6 Modeling Tools

Table 11 provides an overview of models and model data included in the AMS data interpretation. The OFFLINE model was run at the Institute for Climate and Atmospheric Science, School of Earth and Environment, University of Leeds, UK; Lagranto was run at Deutsches Zentrum für Luft und Raumfahrt, Institut für Physik der Atmosphäre, Oberpfaffenhofen, Germany; FLEXPART was run at the Norwegian Institute for Air Research, Kjeller, Norway; ECMWF potential vorticity data was calculated at Deutsches Zentrum für Luft- und Raumfahrt, Oberpfaffenhofen. All other data and models were processed and operated by the author of this thesis.

### 2.6.1 ECMWF analysis data

To obtain information on the height of the dynamical tropopause, the potential vorticity was calculated from ECMWF analysis data. Based on ECMWF analysis data the altitude of the 2 PVU border along the Falcon flight curtain and the actual PV value on the flight track were determined. ECMWF analyses were available four times daily (00, 06, 12 and 18 UTC) at a resolution of 0.25 degrees in the horizontal and 91 hybrid sigma-pressure levels in the vertical direction. The model PV was interpolated linearly in time and space to the Falcon flight track.

### 2.6.2 HYSPLIT

The National Oceanic and Atmospheric Administration's (NOAA) Air Resource Laboratory's Hybrid Single-Particle Lagrangian Integrated Trajectory (HYSPLIT) is a system for computing simple air parcel trajectories and complex dispersion and deposition simulations. For this work, the online application available at http://ready.arl.noaa.gov/hysplit-bin/trajtype.pl?runtype=archive was used exclusively for trajectory (backward and forward) calculations. The trajectories were driven with 3-hourly National Centers for Environmental Prediction Global Data Assimilation System (NCEP GDAS) analysis data on a 1° by 1° grid and on 23 pressure levels and run backward or forward in time for 10 days. Meteorological data such as pressure, temperature, potential temperature, precipitation and relative humidity are calculated along the air parcels' tracks. Trajectories can only be started at the full hour.

**Table 11: Overview of models and model data used for AMS data interpretation**

| Name | Short description | Data input | Used for… | Main reference |
|---|---|---|---|---|
| ECMWF analysis data | European Centre for Medium-Range Weather Forecast | Observational data | Determination of the dynamical tropopause during CONCERT | http://www.ecmwf.int/ |
| HYSPLIT trajectory model | Online available trajectory model, provides meteorological parameters along the track | Global Data Assimilation System (GDAS) | Determination of altitude of selected back trajectories during CONCERT<br>Source identification of selected ARCTAS plumes<br>Quantification and localization of precipitation events along back and forward trajectories during POLARCAT and ARCTAS | Draxler and Rolph (2011); Rolph (2011) |
| OFFLINE model | Trajectory model of the University of Leeds, provides meteorological data along the track | ECMWF analysis data | Determination of the meteorological history of selected back trajectories from POLARCAT | Methven (1997) |
| LAGRANTO | Lagrangian Analysis Tool for backward trajectories, provides meteorological data along the track | ECMWF analysis data | Identification of a specific aerosol wash-out event during POLARCAT | Wernli and Davis (1997) |
| FLEXPART | Lagrangian Particle Dispersion Model, indicates source-receptor relationships, models the spatial distribution of chemical tracers from anthropogenic and biomass burning sources (trace gases and aerosol) | ECMWF analysis data<br>GFS analysis data (Global Forecast System) | Source identification for identified plumes during POLARCAT, distinction of biomass burning and anthropogenic emission contributions, determination of aerosol wash-out and stratospheric air mass contribution<br>2 PVU meteorological values along ARCTAS flight tracks | Stohl et al. (2005) |
| CiTTyCAT | Cambridge Tropospheric Trajectory Model, chemical box model | measurement data (ARCTAS, POLARCAT) | Determination of the possibility of enhanced particulate sulfate formation during mixing of tropospheric and stratospheric air masses during POLARCAT | Wild (1996) |

### *2.6.3 FLEXPART*

FLEXPART, a Lagrangian particle dispersion model, calculates the dispersion of hypothetical air parcels based on mean winds interpolated from meteorological analysis fields together with random motions representing turbulence and convection (Stohl et al., 2005). The model was driven with analysis data with a horizontal resolution of 0.5°x 0.5° and 91 vertical model levels at three hour time steps. In addition, FLEXPART was run with GFS data with a horizontal resolution of 0.5°x0.5° and 26 pressure levels in the vertical. These GFS calculations were used to identify possibly problematic cases where ECMWF and GFS results did not agree. All plumes discussed in this work are represented in the results by both types of input data. The data are available at http://zardoz.nilu.no/~andreas/POLARCAT_FRANCE/.

Backward simulations as described in Stohl et al. (2003b) were run to determine potential pathways and source contributions of the observed pollution plumes. 60,000 virtual particles were released at each time step when the aircraft position changed more than 0.30° horizontally or 150 m vertically. The virtual particles carrying tracers with passive and aerosol-like characteristics were followed for 20 days backward in time with the aerosol-like tracer species additionally being subject to dry and wet deposition. 20 days are a commonly used time frame for FLEXPART products (e.g. Paris et al., 2009, Hirdman et al., 2010), age spectra reaching 30 days or more backward in time have been published as well (e.g. Stohl et al., 2006, Stohl et al., 2007). This allows for determination of emission sensitivities and source contributions, both calculated at 0.5° horizontal resolution, based on available emission fluxes (Stohl et al., 2003b). The emission sensitivity does not consider any specific emission source or a specific tracer. Only later, as part of the post-processing, the emission sensitivity is folded with specific emission fields such as for sulfur, BC or CO. Thus, the difference between the various aerosol-like tracers is based solely in the emission source distribution. The term emission sensitivity denotes in how far the measured air parcel is susceptible to contributions from certain regions in the considered domain. This means that a high sensitivity to a certain sector is given when the virtual particle residence time there was large. Figure 23 provides an example for a column-integrated emission sensitivity plot. The color-scale denotes the sensitivity to the respective coordinates. The unit ns m $kg^{-1}$ is proportional to the residence time (ns) of the virtual particles (kg) in that respective grid cell integrated over the whole vertical domain (m). It is a measure for the simulated mixing ratio at the receptor that a source of unit strength (1 kg $s^{-1}$) in the respective grid cell would produce. The pink and purple regions indicated the highest sensitivities and remind of classical back trajectories. The black numbers denote the days backward in time. The red and black dots indicate MODIS fire counts for forests and other land use, respectively. This aspect is explained two paragraphs further below. The black cross over Greenland stands for the position of the aircraft at the time for which this graph was created. For aircraft measurements it is particularly important to consider the integrated column sensitivity which takes all model levels into account as well as the footprint sensitivity (see Figure 41 a, b) which accounts only for the lowest 100 m where surface sources inject their tracers. (This is why the unit of the footprint tracer sensitivity is ns $kg^{-1}$.) If the footprint sensitivity is small (white or purple color) but the column sensitivity large it is rather unlikely that this region, where the target air parcel is sensitive to, contributed to the measured pollution.

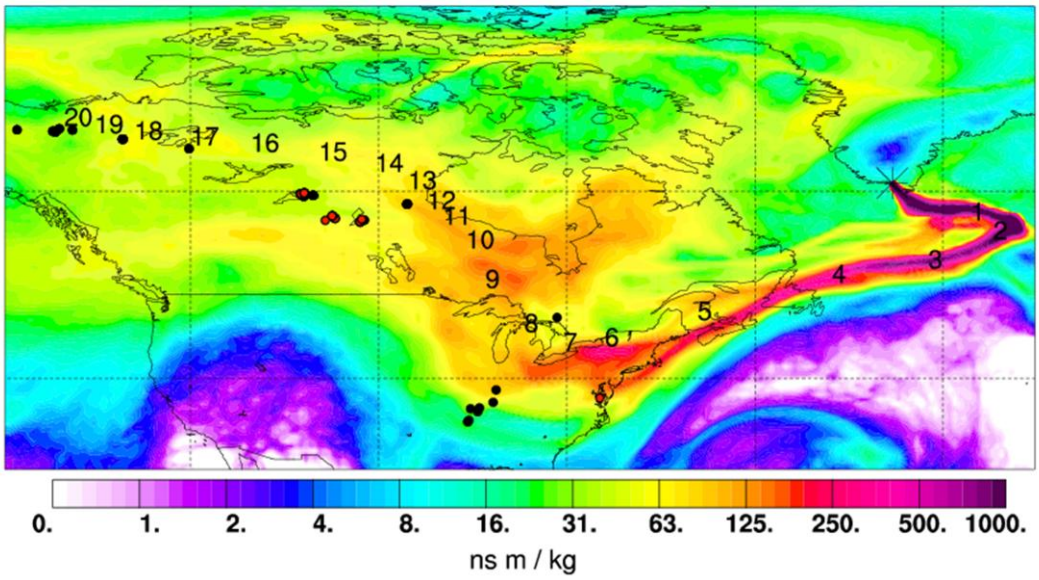


**Figure 23: Example plot for FLEXPART column-integrated emission sensitivity. (same as Figure 51 b)**

Meteorological data from 20 day long backward runs were not used for the interpretation of pollution plumes as they gain quickly uncertainty with "age". Only the column-integrated emission sensitivity and the footprint tracers were considered to determine the origin of a polluted air mass. Uncertainties of the source-receptor relationship and uncertainties related to FLEXPART tracer calculations can be evaluated by comparison with independent data. Ideally, a tracer experiment is conducted where the source strength of a substance is known exactly and accurate measurements downwind of the source are known. FLEXPART has been extensively evaluated using data from such tracer experiments (Stohl et al., 1998; Forster et al., 2007). In absence of a unique tracer, CO enhancements are often used as indication of how well a model can reproduce them along a flight track. For this specific campaign however, the sources of CO were highly uncertain (e.g. forest fires) and the enhancements encountered during the measurements were relatively small. This makes the comparison of modeled and measured CO enhancements very sensitive to the assumed background mixing ratios which might have varied throughout the campaign and even within individual plumes. Other compounds which could serve as tracers for a model evaluation were not measured on board the ATR-42. However, to confirm the source region for each single plume, both FLEXPART calculations with ECMWF and GFS input data were compared.

For anthropogenic emissions, the EDGAR emissions inventory version 3.2FT for the year 2000 (Olivier and Berdowski, 2001) was used outside of North America and Europe, while the inventory of Frost et al. (2006) for North America and the EMEP inventory for 2005 for Europe were applied. For black carbon emissions, the inventory of Bond et al. (2004) was used. Emissions from BB were modeled as described by Stohl et al. (2007) using fire locations detected by the moderate-resolution imaging spectrometer (MODIS) on the Aqua and Terra satellites and a land-cover vegetation classification. Smoke was injected within the lowest 100 m above the surface; it quickly mixed vertically to fill the planetary boundary layer.

Domain-filling forward simulations were used for the determination of the vertical extent of the polluted air masses for direct comparison with POLARCAT flight tracks. Passive CO tracers and

aerosol-like BC tracers were released at the surface, using the same emission information as for the backward simulations. FLEXPART total CO values are given as excess CO meaning that 100 nmol $mol^{-1}$ assumed background concentration was subtracted a priori. For both, forward and backward calculations, the concentrations of these two tracers bracket the loading of actual aerosol particles. The passive tracer does not suffer any wash-out at all while the aerosol-like tracer's wet deposition is overestimated as scavenging properties similar to sulfate are assumed and the scavenging is applied immediately after emission when real BC still would have hydrophobic properties. Thus, the passive tracer concentration indicates a possible maximum aerosol loading while the aerosol-like tracer represents the lower limit. The ratio of aerosol-like and passive tracer results in the potential wash-out of aerosol particles. Even though CO and BC do not necessarily have exactly the same sources (e.g. a controlled industrial combustion is expected to release less soot particles than a wild fire), it seems suitable to compare these tracers within the uncertainties of this source-receptor analysis. Additionally, a CO passive fire tracer was calculated for the purpose of distinguishing between CO contributions from biomass burning and anthropogenic activities. Total CO minus fire tracer CO represents CO from anthropogenic contribution. Also, passive $SO_2$ tracer mixing ratios were determined based on the emission inventories to identify fossil fuel combustion contributions. Along each flight track the contribution of stratospheric air masses in percent is provided by the number of particles residing in the stratosphere, i.e. with a PV greater than 2. Potential vorticity values for each point of the flight curtains during POLARCAT were calculated, as well as the altitude, pressure and potential temperature of the 2 PVU isoline along all ARCTAS flights.

### *2.6.4 OFFLINE model*

10-day kinematic back trajectories were calculated by integration of 6-hourly operational ECMWF analysis fields using the OFFLINE trajectory model (Methven, 1997; Methven et al., 2003). Trajectories were initialised from the aircraft position every one minute for each flight, and advected backwards with a 30-minute time step. The 1.0125-degree resolution analyses fields are interpolated to the Lagrangian particle positions using cubic Lagrange interpolation in the vertical followed by bilinear interpolation in the horizontal and linear interpolation in time. The model output provided 6-hourly data of temperature, pressure, specific humidity, and potential vorticity along the tracks.

### *2.6.5 LAGRANTO*

Backward transport analysis was conducted based on the Lagrangian Analysis Tool (LAGRANTO) (Wernli and Davies (1997) for a wash-out event during POLARCAT. The input data for the trajectory calculations are retrieved from the ECMWF operational analyses using the same space and time resolution as the OFFLINE model. Trajectory start points are set every minute along the flight track. An ensemble of 100 trajectories is released from a box centred at each start point. The box has a horizontal diameter of 1 km and a height of 200 m. The single starting positions of one trajectory ensemble are randomly distributed inside the respective box. The trajectories are calculated backwards for 240 h using a calculation time step of 30 minutes. Meteorological data like temperature, humidity, and cloud cover are retrieved from the ECMWF archive and interpolated along every single trajectory.

### *2.6.6 CiTTyCAT*

The Cambridge Tropospheric Trajectory Model (Wild, 1996) was used to specifically investigate the concurrence of high ozone mixing ratios and high particulate sulfate concentrations when particulate sulfate simultaneously contributed a high fraction of mass to the total aerosol loading during POLARCAT. The presumption was that particulate sulfate production might be enhanced when dry ozone rich stratospheric air masses mix with humid and polluted tropospheric air masses.

CiTTyCAT is a zero dimensional model, i.e. box model, in which the chemical evolution of an air parcel can be studied in great detail at user definable time steps. It consists of a chemical, photolysis and physical scheme and was used in a simplified version paying special attention to the sulfur chemistry. The physical scheme, i.e. non-chemical sources and sinks of compounds such as emission sources or deposition mechanisms, was omitted for this purpose. The photolysis scheme was adopted as a whole. This scheme is particularly important for modeling the chemical evolution of an air parcel in high latitudes during summer as the OH radical production depends strongly on the incoming solar radiation. The main reactions are R1 – R3, they are also the limiting steps in the sulfuric acid production.

$H_2O + h\nu \rightarrow OH + H$ **R 1**

$O_3 + h\nu \rightarrow O^1D + O_2$ **R 2**

The chemical scheme comprises a list of reactions determined by reaction rates and production and loss terms for each considered species. No aqueous and heterogeneous chemistry was considered. Therefore, a simple assumption was made to study the production of particulate sulfate: All model produced sulfuric acid ($H_2SO_4$) was considered to be in the condensed phase forming particulate sulfate. The key reactions and their respective reaction rate coefficient ($k$) in the respective units underlying the sulfur chemistry are as follows (from CiTTyCAT manual):

$O^1D + H_2O \rightarrow OH + OH$ ($k = 2.2x10^{-10}$) **R 3**

$SO_2 + OH + M \rightarrow HOSO_2 + M$ ($k = 3.12x10^{-31}*(T/300)^{-3.3}$) **R 4**

$SO_2 + HO_2 \rightarrow SO_3 + OH$ ($k = 1.00x10^{-18}$) **R 5**

$SO_2 + O_3 \rightarrow SO_3 + O_2$ ($k = 3.00x10^{-12}*\exp(-7000/T)$) **R 6**

$HOSO_2 + O_2 \rightarrow HO_2 + SO_3$ ($k = 1.30x10^{-12}*(\exp(-330/T))$ **R 7**

$SO_3 + H_2O \rightarrow H_2SO_4$ ($k = 6.00x10^{-15}$) **R 8**

M denotes a collision partner, T is in Kelvin.

Furthermore, reactions involving volatile organic compounds are included as they mainly consume but also produce OH and $HO_2$. The following species were considered (see also Appendix E): PAN (polyacrylnitril, $C_3H_3N$), $C_2H_6$; $C_2H_4$, $C_2H_2$, $C_3H_8$, $C_3H_6$, $C_4H_{10}$, $C_5H_{12}$, $C_6H_{14}$, isoprene, $C_6H_6$, $C_7H_8$, methylaldehyde, methylketone, ethanol, formaldehyde, $C_4H_8$. Respective mixing ratios for tropospheric and stratospheric background conditions in the Arctic were obtained from ARCTAS measurements on 9 July 2008 over Greenland. Also, the $NO_x$ chemistry is important in particular in interaction with VOCs. In a regime of low $NO_x$ and high VOC mixing ratios ($NO_x$ sensitive regime)

$O_3$ is formed while in a regime of high $NO_x$ and rather low VOC abundance (VOC sensitive regime) $O_3$ is destroyed (Sillman and He, 2002). The key $NO_x$ reactions are (from CiTTyCAT manual):

$NO_2 + h\nu \rightarrow NO + O$ **R 9**

$O+O_2 +M \rightarrow O_3 + M$ $(k = 5.63x10^{-34}*(T/300)^{-2.8})$ **R 10**

$NO + O_3 \rightarrow NO_2 + O_2$ $(k = 1.8x10^{-12}*exp(-1370/T)$, $NO_x$ titration) **R 11**

$NO_2 + O \rightarrow NO + O_2$ $(k = 6.50x10^{-12}*exp(120/T))$ **R 12**

To initialize a model run values for $SO_2$, $H_2SO_4$, CO, $O_3$, OH and $HO_2$, temperature, pressure and relative humidity had to be given for the air parcel. These values were taken from in-situ data if available or from co-located ARCTAS data on 9 July, 2008, (especially OH, $HO_2$).

CiTTyCAT was run in two different modes: Initially, the chemistry was run for up to 10 days without any interaction with other air masses or any movement of the box. The starting values for $SO_2$ and $O_3$ were varied simulating tropospheric and stratospheric conditions. Also temperature and relative humidity effects were evaluated. In a second step, the box was run along a forward trajectory. The OFFLINE backward trajectory parameters for the specific scenarios were inverted in time to provide forward trajectory data and were linearly interpolated to the 5 min model time step. Position and basic meteorological data (temperature, pressure, relative humidity) are thus dictated by the trajectory. The sensitivity to the concentration of VOCs was also tested (see Appendix E). Appendix E also provides a description of the basic model output and an example calculation how particulate sulfate concentrations were obtained.

## 2.7 Air mass classification and plume identification

As one focus of this work is to determine whether the particulate matter was encountered in the free troposphere or upper troposphere and lower stratosphere, this section specifies how air masses were classified. Likewise, the second focus, which is the identification of pollution plumes and their origins and emission source types, is explained. For both purposes in-situ measurements and model data as introduced in section 2.6 were applied.

### 2.7.1 Free troposphere or tropopause?

The various definitions of the tropopause (thermal, dynamic, and chemical) are discussed in section 1.4. Here, the concepts of tropopause that were applied in each specific case are presented.

During POLARCAT, as ATR-42 had a maximum altitude ceiling of 7.6 km, the tropopause region was never really reached. However, on several occasions, the ozone concentration was elevated by such a high degree that chemical production could most likely be ruled out and stratospheric air mass influence was assumed. For these cases, the chemical definition was applied by looking at the tracer-tracer space created by ozone and carbon monoxide (see Figure 3 b). As CO might be elevated in pollution plumes and therefore point to a rather tropospheric regime, FLEXPART stratospheric tracer contributions were consulted, additionally. Contributions larger than 10 – 15 % indicate stratospheric influence.

For ARCTAS data analysis the chemical definition of the tropopause was used and compared to with the dynamic definition. Pollution episodes were attributed to the tropopause when both criteria were fulfilled. With respect to the history of particulate sulfate in the UTLS in the year 2008 for comparison of sulfate aerosol loadings before and after the volcanic eruptions, the empirical chemical definition only based on the ozone mixing ratio by Zahn and Brenninkmeijer (2003) was applied. As ARCTAS and CONCERT data were compared, the Zahn and Brenninkmeijer definition was found to be more appropriate than the CO-$O_3$ tracer definition because the latter does not provide a definite threshold value in terms of a trace gas mixing ratio which however is given by the purely ozone-based definition. For consistency, the same criterion was used in the final compilation of aerosol chemical composition and concentration in mid and high latitudes in the free troposphere and tropopause.

CONCERT data were classified according to all tropopause definitions except the thermal one. The purpose was to demonstrate that the high altitude aerosol layer was encountered in the UTLS and not in the free troposphere in order to rule out surface-bound anthropogenic emission sources.

### 2.7.2 Probability density functions

Probability density functions (PDF) provide a simple tool to track the evolution of concentrations of trace species from the free troposphere to the lower stratosphere. Stratosphere-troposphere exchange and tropospheric influence in the tropopause or vice versa can be studied amongst other aspects. PDFs generated from CONCERT and ARCTAS data in this work are based on the unpublished compilation "The UTLS cookbook: Some recipes" by Hoor (2007) which is a result of publications by Hoor et al. (2004; 2005) and Engel et al. (2006).

First, a key criterion to define the tropopause is chosen, which for this work was 2 PVU. Based on a second parameter, e.g. pressure, potential temperature, or altitude, at least one regime below the threshold and two above are defined. Here, three layers were established based on potential temperature units for CONCERT (-30 to 0, 0 to 30 and 30 to 60 K from the 2 PVU potential temperature (see Figure 24 and Figure 34) and based on pressure units for ARCTAS (550 – 150, 150 – 0, and 0 - -150 hPa from the tropopause pressure (see Figure 46). All trace species data of interest within each layer are binned into adequate concentration intervals and the probability of occurrence of each concentration bin is calculated and displayed. The layer below 2 PVU should reflect tropospheric characteristics while the uppermost layer shows stratospheric properties as can be seen in Figure 24 where the tropospheric region (blue line) and the stratospheric region (green line) do not overlap. The regime in between (red line) is considered a transition region and shows characteristics of the other two layers. The thickness of the transition layer depends on the mixing state of the tropopause. Therefore the chosen intervals are campaign or even flight specific.

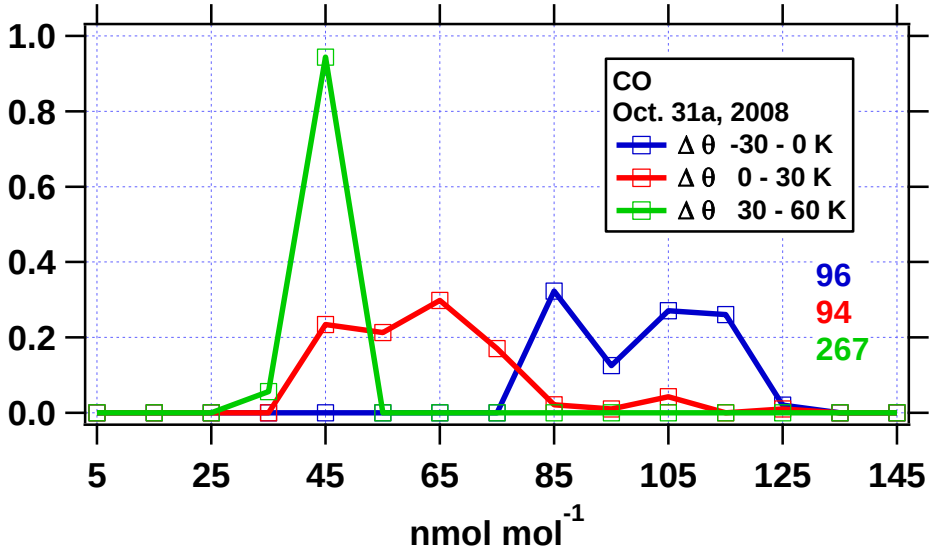


**Figure 24: Example probability density function (PDF) for carbon monoxide from the CONCERT flight on 31 October, 2008, bin size is 10 nmol mol-1. The colored numbers indicate the number of data points available for each regime.**

In this work, PDFs were applied to trace gas and aerosol data. The application of PDFs represents a new approach since to my knowledge, aerosol PDFs have not been published previously. Comparing PDFs of gaseous and particulate tracers from the same source, for instance $SO_2$ and particulate sulfate, can reveal information on the discrepancy in dispersion between gases and aerosol during long-range transport and across the tropopause border. Here, the PDF tool is used to thoroughly investigate the behavior of chemical species in the time intervals when the aircraft flew in the UTLS. The results can therefore not be used as climatological mean data for modeling studies which is a potential application of trace gas data PDFs.

### *2.7.3 Pollution plume criteria and categories*

To identify the various types of pollution plumes, i.e. of volcanic origin, from biomass burning and fossil fuel combustion, and from aircraft exhaust, criteria had to be established. Table 12 provides an

overview of the requirements to be fulfilled. The term "background" refers to conditions when the plume criterion is not fulfilled.

**Table 12: Pollution plume identification criteria**

| Plume type | Criteria |
|---|---|
| **Volcanic** | CONCERT: Elevated particulate sulfate concentration with respect to immediate surroundings above the tropopause |
| **"pure" BB** | POLARCAT : plume criterion (defined below) + FLEXPART indication for BB + organic matter is the dominant component |
| | ARCTAS: $CH_3CN$ > 0.2 nmol $mol^{-1}$ + CO > 80 nmol $mol^{-1}$ + back trajectories point towards BB source + organic matter is the dominant component |
| **BB and FF mixed** | POLARCAT: plume criterion + FLEXPART indication for BB and FF + elevated particulate sulfate compared to "pure" BB |
| | ARCTAS: $CH_3CN$ > 0.2 nmol $mol^{-1}$ + CO > 80 nmol $mol^{-1}$ + $SO_2$ enhanced relative to immediate surroundings + back trajectories point towards BB and FF sources + elevated particulate sulfate compared to "pure" BB |
| **FF dominated** | POLARCAT: plume criterion + FLEXPART indication for FF + elevated particulate sulfate compared to BB and FF mixed plumes |
| | ARCTAS: CO > 80 nmol $mol^{-1}$ + $SO_2$ enhanced relative to immediate surroundings + back trajectories point towards FF source + elevated particulate sulfate compared to BB and FF mixed plumes |
| **Contrails** | CONCERT: $NO_y$ > 2 nmol $mol^{-1}$ while "chasing" airline aircraft |
| **Background** | POLARCAT: plume criterion not fulfilled |
| | ARCTAS: $CH_3CN$ < 0.2 nmol $mol^{-1}$ + CO < 80 nmol $mol^{-1}$ |
| | CONCERT: no contrail and no volcanic plume |

Two types of pollution plumes are relevant for CONCERT data, i.e. the volcanic aerosol layer and contrails. The criterion for enhanced aerosol loadings to be of volcanic origin in this context was simply the residence in the tropopause region opposed to the free troposphere (see also section 2.7.1). For aerosol to be potentially from aircraft exhaust $NO_y$ mixing ratios of greater 2 nmol $mol^{-1}$ were used as threshold when the Falcon was chasing other aircraft.

The identification of pollution plumes during POLARCAT was conducted by the author by taking into consideration the following parameters:

1. Increased concentrations of at least 0.1 µg $m^{-3}$ (STP) of particulate sulfate and/or organic aerosol relative to the immediate surroundings,

2. a particle signature of at least 0.01 $\mu m^3 cm^{-3}$ (STP) in the volume size distribution (*dV/dlog(dp)*) of accumulation mode particles measured by the SMPS,

3. an increase of at least 10 nmol $mol^{-1}$ CO and/or $O_3$ mixing ratio relative to the immediate surroundings, and

4. an identifiable source-receptor relationship modeled by FLEXPART.

For an episode to be recognized as plume either 1) and 2) and 4); or 3) and 4) had to be fulfilled. The shortest identified pollution episodes involve three AMS data points of 2 minute time resolution. Since the AMS limit of detection was elevated during most of the flights 9 plumes were below the 3 sigma LOD but above the 1 sigma LOD and 8 plumes were below the 1 sigma LOD. In some of these pollution plumes only gaseous tracers were enhanced, while during others either particulate sulfate or organics were elevated and the other below LOD due to the nature of the emission source. These events were still accounted for as aerosol wash-out might have occurred in case only gaseous tracers were enhanced. In total, 48 plumes were identified as listed in Appendix B. They were categorized into five different classes based on the FLEXPART column-integrated emission sensitivity, the general footprint tracer, and the CO, CO fire, BC and $SO_2$ tracer contributions. First, 13 subclasses were established and then comprehended in 5 categories to obtain more robust statistics for each class. The classes are "pure" BB (I), in quotation marks as influence from other sources cannot be ruled out completely, BB dominated and FF influenced air masses without Asian contribution (II), FF dominated and BB influenced air masses without Asian contribution (III), Siberian BB and Asian FF mixed plumes (IV), and Asian FF dominated air masses influenced also by Siberian BB (V). [See also Schmale et al. (2011).]

Since the ARCTAS campaigns' objectives were detection of Arctic haze in spring and influence of biomass burning in summer, large amounts of data represent perturbations of the Arctic atmosphere. Based on Warneke et al (2006), BB influence was assumed when the thresholds of 0.2 nmol $mol^{-1}$ acetonitrile and 80 nmol $mol^{-1}$ CO were exceeded. Furthermore, local enhancement of $SO_2$ mixing ratios was used to identify FF pollution. No fixed threshold value was applied as FF plumes originated from rather close sources as well as from distant regions such as East Asia. During the long-range transport $SO_2$ mixing ratios decrease due to dilution and conversion into particulate sulfate. These criteria were used to identify measurement periods unperturbed from FF and BB plumes in order to compare the $SO_4$ data from before the volcanic eruption of Mt. Okmok and Mt. Kasotochi to the measurements during CONCERT (Schmale et al., 2010)

# 3. Results

## *3.1 Natural perturbation of the free troposphere and tropopause – volcanic eruptions*

Volcanic eruptions are a sporadic source of atmospheric aerosol at high altitudes. During the CONCERT campaign, on 28 and 31 October, 2008, the opportunity of measuring three months old volcanic aerosol in-situ in the tropopause region occurred. These measurements represent the first AMS measurements of volcanic aerosol under such conditions. The fact that a volcanic eruption was responsible for the observed aerosol enhancement was not known before or during the flights and only discovered several months later. This section focuses on how these measurements can be related to the volcanic eruptions of Mts. Okmok and Kasatochi on 12 July and 7 August 2008, respectively, and subsequently discusses the chemical properties as well as the size distribution of the volcanic particles and potential implications. Most results from this section were published in Schmale et al. (2010). Additionally, in subsection 3.1.3 measurements from crossing a tropopause fold are used to study the behavior of submicron aerosol in the transition layer between troposphere and stratosphere.

### *3.1.1 Detection of a volcanic aerosol plume*

Enhanced particulate sulfate loadings were found during three CONCERT flights over Central Europe and the North Sea (28 October) and over Western Europe and the Atlantic Ocean (31 October, flights a) and b) as shown in Figure 25 by the color-coded tracks. The observed aerosol layer thicknesses were between 240 and 3340 m which depend of course on the chosen flight altitudes and thus provide only a rough approximation of the extent of the plume.

The actual entrance into and exit out of the volcanic plume are marked by rapid changes in the sulfate aerosol concentration as indicated in Figure 26 (hatched areas). More than 50 % of the duration of each flight was spent in the layer. The uppermost panel in Figure 26 presents the sulfate aerosol measurements including every $10^{th}$ statistical counting error and uncertainties related to the fluctuation of the AMS vaporizer. Oscillation beyond this scale (approximately 8 % of the measured signal) is due to inhomogeneity within the layer. Above 8 km altitude, in chronological order, the mean sulfate particle concentration including standard deviation was $0.54 \pm 0.22$, $0.82 \pm 0.36$, and $0.79 \pm 0.50$ µg $m^{-3}$ with a maximum observed value of 1.98 µg $m^{-3}$. These average values are all larger than the mean planetary boundary layer concentration of 0.50 µg $m^{-3}$ with large variability and the background sulfate aerosol concentration at equivalent UTLS altitudes with $0.17 \pm 0.06$µg $m^{-3}$ as observed during CONCERT. These are strong indications for an exceptional source of aerosol in the UTLS. Compared to earlier AMS airborne measurements above Europe by Schneider et al. (2006a) and Morgan et al. (2009) the layer concentrations are significantly higher. Morgan et al. found about 0.39 µg $m^{-3}$ particulate sulfate loading above 8 km. Values for the free troposphere between 3 and 8 km however are in very good agreement with 0.23 µg $m^{-3}$ (Morgan et al.) and $0.22 \pm 0.27$ µg $m^{-3}$ (CONCERT). Background loadings are discussed in chapter 4 in more detail.

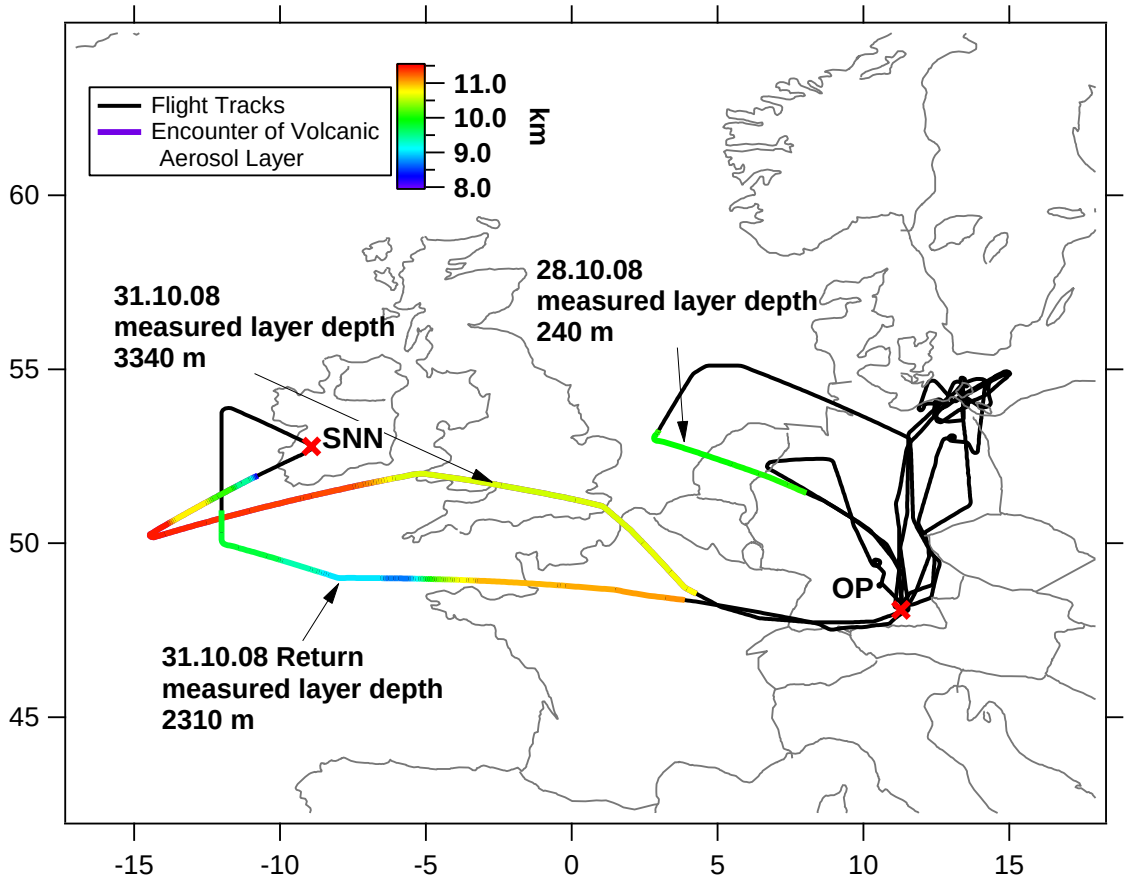


**Figure 25: All CONCERT flight tracks, colored sections indicate observations of volcanic aerosol (OP: Oberpfaffenhofen, SNN: Shannon)**

Figure 26 also shows sulfur dioxide concentrations which co-vary well with particulate sulfate. This indicates that $SO_2$ has been converted into particulate sulfate to a certain degree but not entirely. Dividing the amount of sulfur contained in the particles by the total amount of sulfur from both species Jurkat et al. (2010) derived that about 80 % of the sulfur dioxide was converted into particulate sulfate.

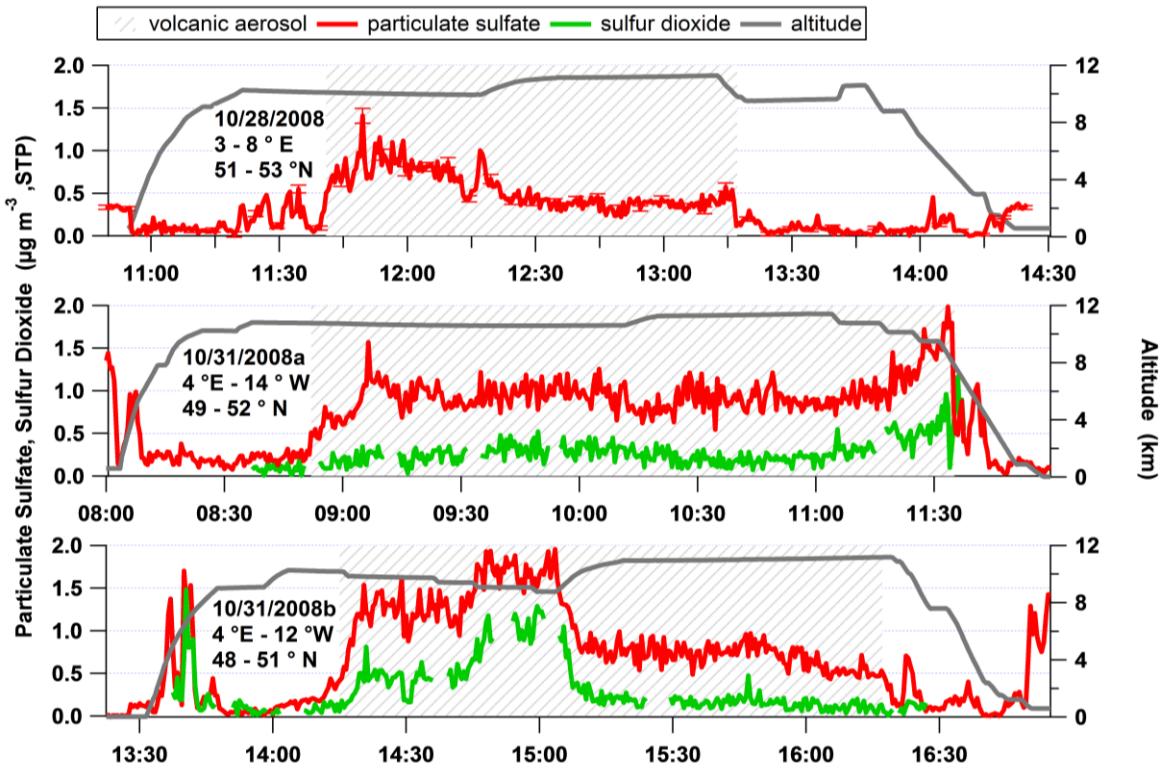


**Figure 26: Time series of elevated particulate sulfate loadings during three flights and increased sulfur dioxide concentrations during two flights when the volcanic aerosol layer was encountered (hatched areas). The error bars in the uppermost panel denote the statistical counting error and uncertainties in the sulfate quantification due to heater temperature fluctuations. [Figure adapted from Schmale et al. (2010).]**

### *3.1.2 Identification and vertical classification of a volcanic aerosol plume*

This unusually high sulfate concentration might originate from a variety of sources. In-situ, the production of the aerosol could have been caused by air traffic through the combustion of sulfur containing kerosene. This option however was ruled out based on data obtained directly in contrails when chasing commercial aircraft liners during the CONCERT campaign on 27 and 29 October and 2 November (for details see section 3.3). Concentrations did not exceed 0.51 µg $m^{-3}$ and were 0.17 ± 0.08µg $m^{-3}$ on average. Alternatively, convective transport from surface sites that burn fossil fuels could have uplifted the particles to the UTLS. To test for such recent high reaching emissions, trajectories were computed with HYSPLIT (see section 2.6). They were initialized at the horizontal coordinates of the flight tracks during the layer encounter episodes in 15 minutes intervals. Vertical positions were set to 8, 10 and 12 km as the actual flight altitude varied (compare Figure 25 and Figure 26). Computations were initialized at the time of observation and additionally 3 hours earlier and later and run backward in time for 10 days. In total, 234 trajectories were generated out of which 79 % stayed at altitudes between 10 and 14 km. Only 21 % and 12 % of the air parcels saw altitudes below 6 and 4 km, respectively, while it has to be noted that starts points of these trajectories were almost exclusively at 8 km, i.e. below the actual altitude of plume detection. Hence, this result strongly suggests that surface emissions are not responsible for the observed particulate sulfate concentrations. Also, based on observations of fossil fuel plumes during POLARCAT it is not very likely, that "conventional" surface emission sites would cause a pollution plume with such large extension.

The last conceivable cause for the existence of the aerosol layer is thus the injection of $SO_2$ into the lower stratosphere by a volcanic eruption and subsequent conversion into particulate sulfate. In such a case, aerosol can remain suspended several months above the tropopause (Borrmann et al., 1993) as no wet deposition occurs in this region of the atmosphere. Injection only into the upper troposphere does not suffice as particles would have been removed by cloud processes (von Glasow et al., 2009). The only potential candidates for such an injection are the eruptions of Mts. Okmok and Kasatochi on 12 July and 7 August 2008, respectively, reaching into the stratosphere. For a more complete discussion on the injection heights and amounts of $SO_2$ see section 1.5.1.

As no direct evidence through conventional trajectories can be established for a time span of three months between emission and detection sites nor available satellite data could establish the link at the time of the manuscript preparation of Schmale et al. (2010) the detection of the Okmok and Kasatochi aerosol layer was proven indirectly. Excluding air traffic and anthropogenic influence already implies a volcanic source. However, by additionally demonstrating that the plume resided above the local tropopause as opposed to in the upper troposphere due to a powerful volcanic injection an even stronger argument is established. In the following, the various definitions of the tropopause as introduced in section 1.4 are used to show that the layer was encountered primarily in the lower stratosphere in all cases.

When applying the dynamical tropopause definition after Holton et al. (1995) at 2 PVU the high particulate sulfate and $SO_2$ concentrations are observed above this specific isosurface (see Figure 27). It becomes obvious that the layer resided above the dynamical tropopause. The potential vorticity was calculated based on ECMWF data. The altitude of the tropopause varied strongly between 500 and 250 hPa during the campaign. There is a clear difference in aerosol loading above the tropopause between the three flights on 28 and 31 October and the other three flights (Figure 27 a). The mean sulfate loading at PV values greater or equal to two is $0.79 \pm 0.39$ µg $m^{-3}$ during the flights with layer encounters, i.e. 3.5 times higher than during the other flights. Below 2 PVU in the free troposphere, there is no significant difference between $0.15 \pm 0.09$ µg $m^{-3}$ and $0.18 \pm 0.21$ µg $m^{-3}$, respectively. Some of the higher particulate sulfate concentrations in the free troposphere are related to other sources (see 3.2.3.4) and did not occur in the vicinity of the volcanic plume as can be seen in the time series from Figure 26.

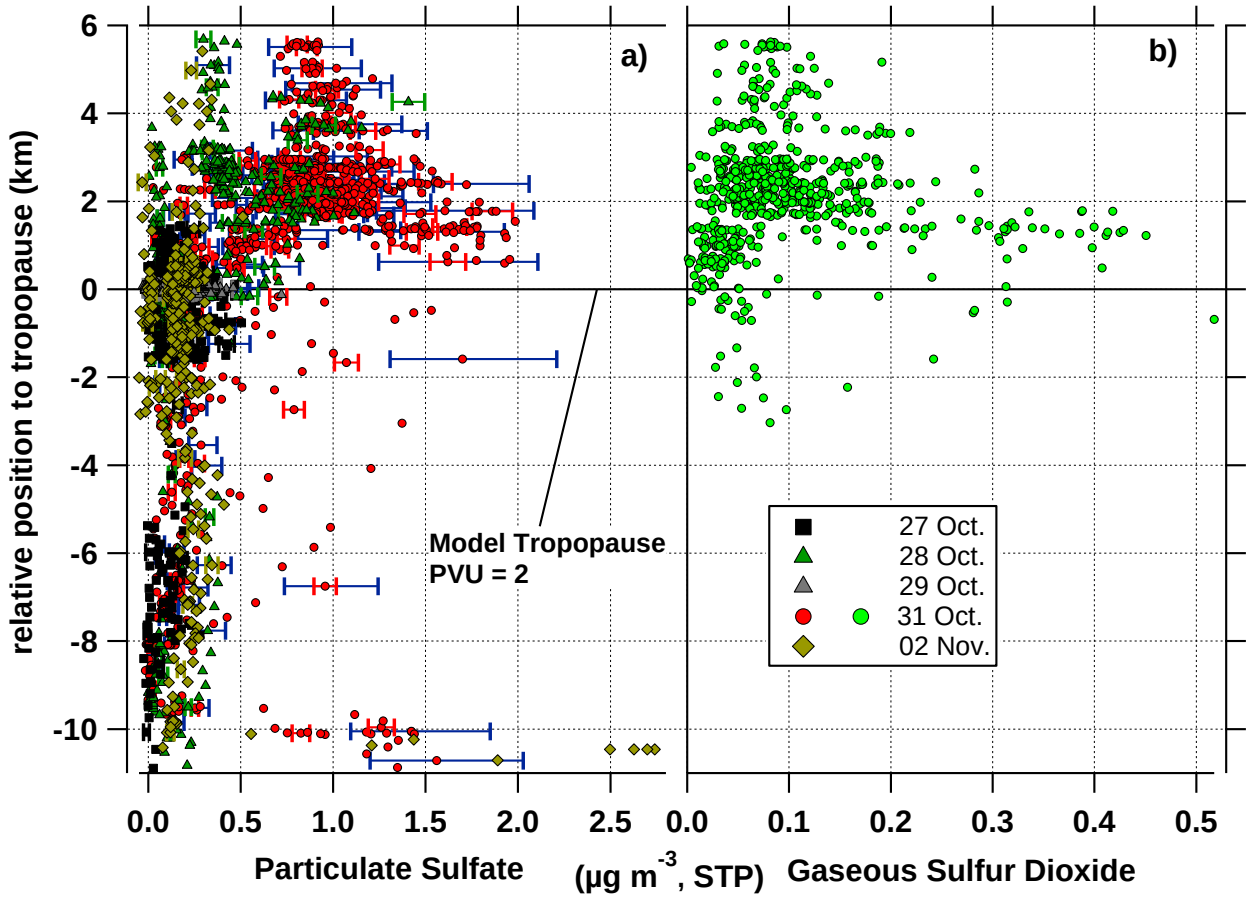


**Figure 27: Particulate sulfate (a) and $SO_2$ (b) concentrations relative to the dynamical tropopause at 2 PVU. The blue error bars indicate the overall uncertainty of the measurement value including the transmission efficiency while the red bars denote the statistical ion counting error. [This figure is adapted from Schmale et al. (2010).]**

To assure that the layer resided in the lower stratosphere, the data were applied to chemical tropopause definitions as well. A relatively simple approach is to compare the vertical profiles of the aerosol load with the ozone mixing ratio. After Zahn and Brenninkmeijer (2003) the ozone threshold for the tropopause is 71 nmol $mol^{-1}$ for the respective days. As the black horizontal lines in Figure 28 indicate, the pronounced sulfate aerosol signature is encountered above this chemical (ozone) tropopause. On 28 October, the simultaneous increase in both tracers is very sharp. On 31 October, the vertical profile of ozone indicates that the structure of the tropopause is more complex as mixing ratios larger than 71 nmol $mol^{-1}$ occur at several altitudes. Figure 28 d) confirms this. A tropopause fold can be observed at the beginning of the return flight which is crossed during the ascent and most likely also during the descent in the first flight on 31 October (31a). The sulfate aerosol concentration is also enhanced during these periods (signature between the two black horizontal lines in Figure 28 b) and c).

**Figure 28 (next page): (a-c) Vertical profiles of measured particulate sulfate and ozone mixing ratio on 28 and 31 October, 2008. The black horizontal lines denote the ozone tropopause boundaries after Zahn and Brenninkmeijer (2003) with a threshold of 71 nmol $mol^{-1}$. (d) Dynamical tropopause along flight b on 31 October at 12 UTC. The dashed red line denotes the 2 PVU isosurface, the color codes the potential vorticity units.**

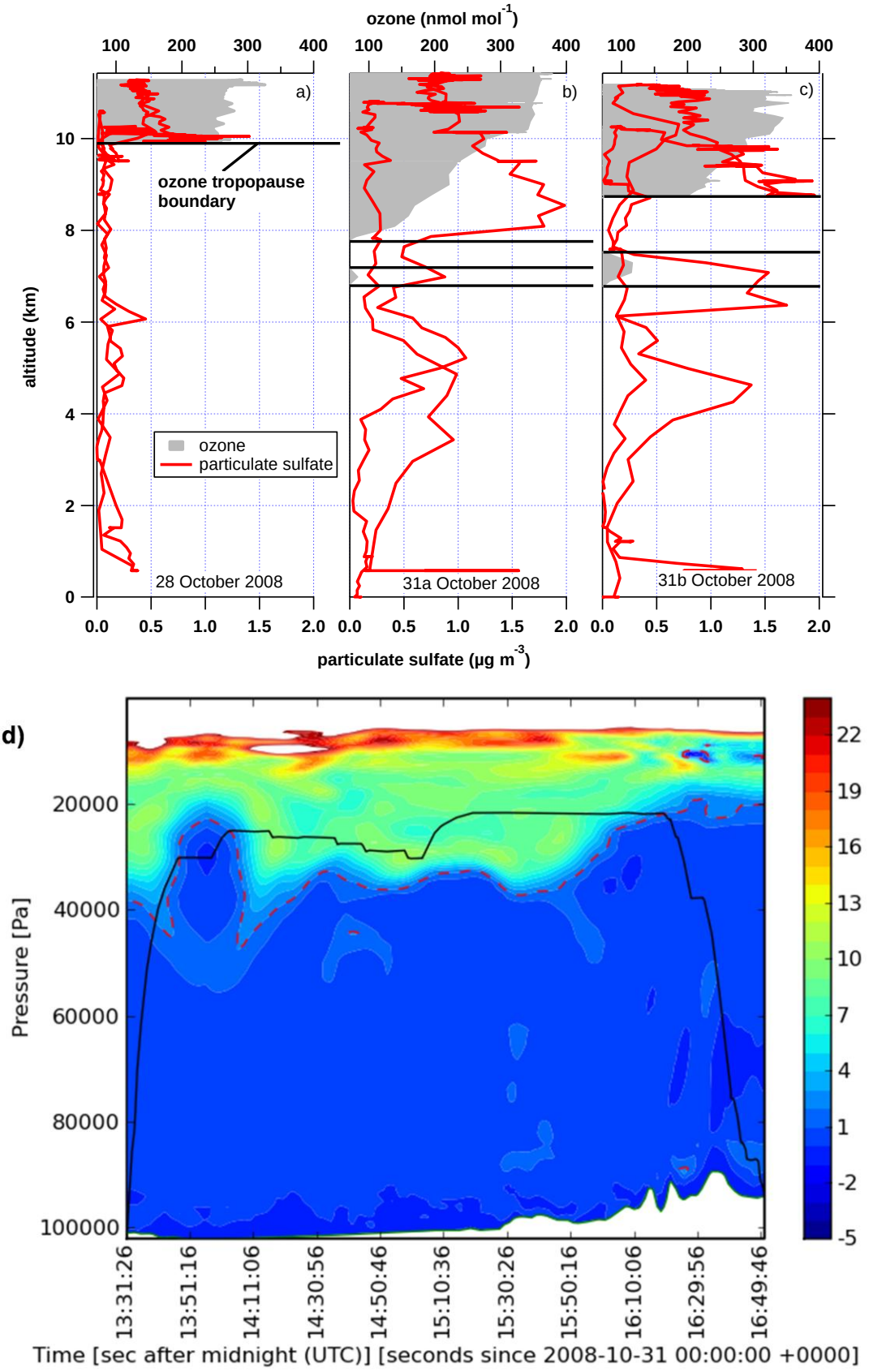
ozone (nmol mol-1)
100
200
300
400
a)
b)
c)
ozone tropopause boundary
altitude (km)
0
2
4
6
8
10
ozone
particulate sulfate
28 October 2008
31a October 2008
31b October 2008
0.0
0.5
1.0
1.5
2.0
particulate sulfate (µg m-3)
d)
Pressure [Pa]
20000
40000
60000
80000
100000
22
19
16
13
10
7
4
1
-2
-5
13:31:26
13:51:16
14:11:06
14:30:56
14:50:46
15:10:36
15:30:26
15:50:16
16:10:06
16:29:56
16:49:46
Time [sec after midnight (UTC)] [seconds since 2008-10-31 00:00:00 +0000]

As the chemical tropopause definition after Zahn and Brenninkmeijer (2003) was derived from measurements only between 35 and 45°N it is not applicable to this data in a strict sense. In addition, the parameterization was derived from a climatological set of data and can therefore not be applied to unusual dynamical situations such as tropopause folds. However, it can be used to show the deviation from the considered case from the climatological mean. Even if the threshold value of 71 nmol $mol^{-1}$ is not considered, the vertical profiles show that the enhancement of particulate sulfate is clearly linked to increasing ozone values in the tropopause and beyond.

Another way of chemically defining the tropospheric, stratospheric and transition regime and the linkage of particulate sulfate concentrations to them, is to look at the shape of the ozone (stratospheric tracer) versus carbon monoxide (tropospheric tracer) correlation as shown in Figure 29 and introduced in section 1.4. Again, it becomes obvious that high aerosol concentrations are seen in the stratospheric branch. However, this plot also shows, that slight enhancement is observed in the transition region implying that mixing of the volcanic particulate matter into the troposphere has taken place. This in consequence means that the respective aerosol becomes prone to wet deposition and is lost from the layer which thus diminishes with time. In the purely tropospheric regime only low concentrations are encountered, the single red points reflect peak loadings during take-off and landing. The characteristics of the transition layer are discussed in more detail in section 3.1.3.

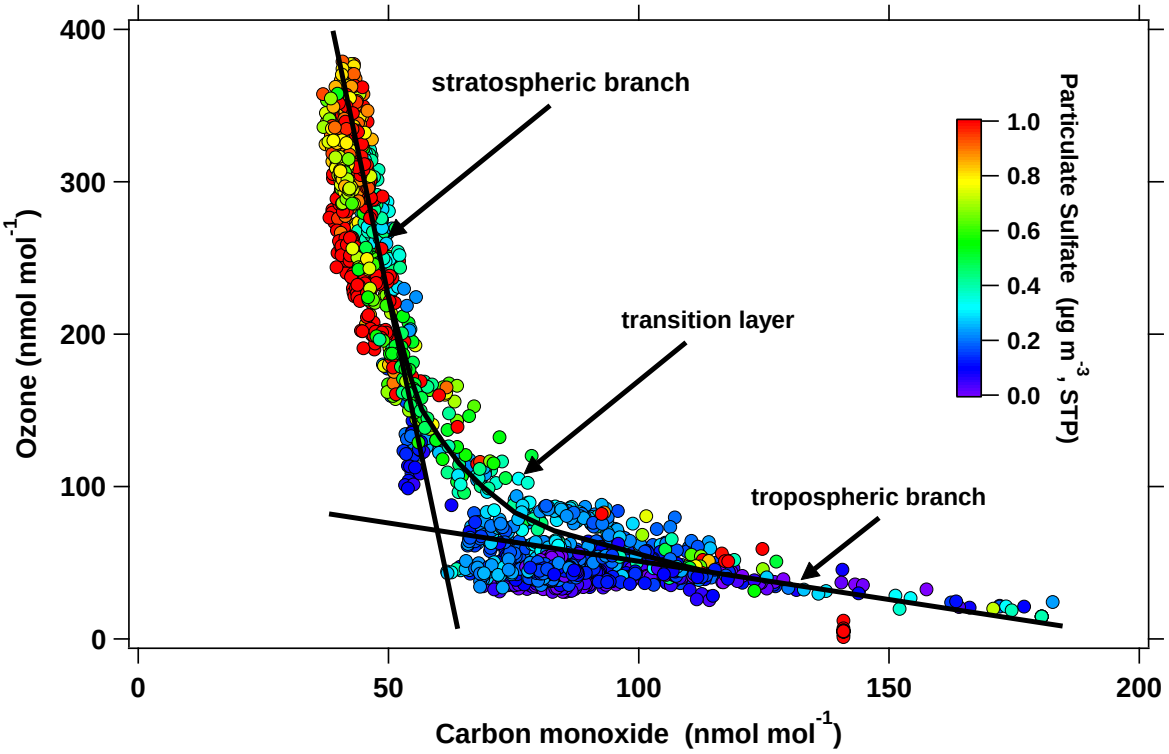


**Figure 29: Ozone and carbon monoxide correlation for all CONCERT flights. The color-code indicates the concentration of particulate sulfate. The different atmospheric regimes are marked. [This figure was published in Schmale et al. (2010).]**

To put the measured particulate sulfate concentrations into a larger context, they were compared to findings by Martinsson et al. (2005). The authors describe the concentration of particulate sulfur above 8.2 km as a function of potential vorticity during volcanically quiescent periods. They binned sulfur

loadings in intervals of [0,1], [1,1.5], [1.5,2.5], [2.5,5], and [5,7] PVU and found an average concentration of 15.9 ng $m^{-3}$ for the first two intervals and a linear increase up to 62 ng $m^{-3}$ at 7 PVU, see black line in Figure 30. During CONCERT concentrations at 2 and 7 PVU were 71 and 238 ng $m^{-3}$, respectively (red line in Figure 30). A linear fit through the average concentration in each bin results in a slope which is about a factor 4 higher than during "clean" periods between 1999 and 2002. Even accounting for the uncertainties in the AMS collection efficiency of 0.5 the slopes would remain significantly different from the literature value. The sulfur concentration derived from AMS particulate sulfate data and measurements described in Martinsson et al. (2005) are comparable as explained in section 2.5.1.

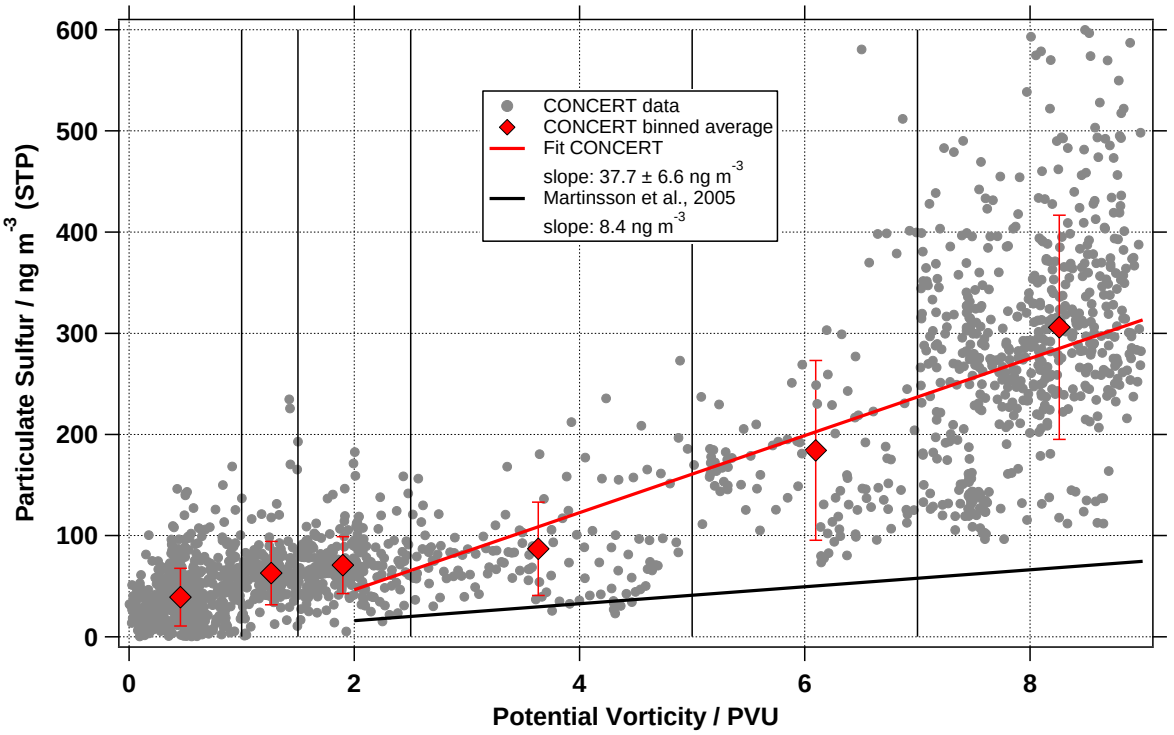


**Figure 30: Comparison of particulate sulfur trends as a function of potential vorticity units during volcanically quiescent periods (Martinsson et al., 2005) and Okmok/Kasatochi impacted air masses (Schmale et al., 2010). The grey points represent all individual CONCERT data, while the red symbols show the bin average including the standard deviation.**

As mentioned above, satellite data could not establish the link between the Kasatochi eruption and the aerosol layer detected 82 to 85 days later. However, the ESA Support to Aviation Control Service (http://sacs.aeronomie.be/archive/index.php) made measurements from several satellites detecting $SO_2$ available. According to these observations an $SO_2$ enhancement was detected from 8 August on until early September. During this time the volcanic plume had surrounded and spread over the entire Northern Hemisphere. An indirect continuation of these satellite measurements until the date of detection by the AMS is given by lidar (light detection and ranging) observations. Several EARLINET (European Aerosol Research Lidar Network, http://www.earlinet.org/) lidar stations observed the volcanic haze layer. Figure 31 presents backscatter coefficient data from two German lidar stations at Kühlungsborn (54°N, 12°E, Rayleigh-Mie-Raman, 532 nm) and Leizpig (51°N, 12°E, Raman, 1064 nm) starting 23 days after the eruption of Mt. Kasatochi (Mattis et al., 2010; Schmale et al., 2010). In

the leftmost panel the aerosol layer is detected between 16 and 18 km altitude while later on enhancements in the UTLS between 11 and 13 km are visible as highlighted by the grey bar. The Kühlungsborn data on day 78 after the eruption is only an average over 30 min between 11 and 13 km altitude while the remaining data is averaged over all night. Additionally, a second pronounced layer is present in higher altitudes which can be explained by the varied injection altitudes of the eruptions (Kristiansen et al., 2010; Bitar et al., 2010). AMS data on days 82 and 85 suggest that the layer descended down to 8 km. This drop in altitude is most likely due to tropopause folds (see also section 3.1.3). Sedimentation alone cannot be responsible as such large vertical distances cannot be covered in such short time by particle sizes between 0.1 and 1 µm, a diameter which is expected to prevail based on experiences from Mt. Pinatubo.

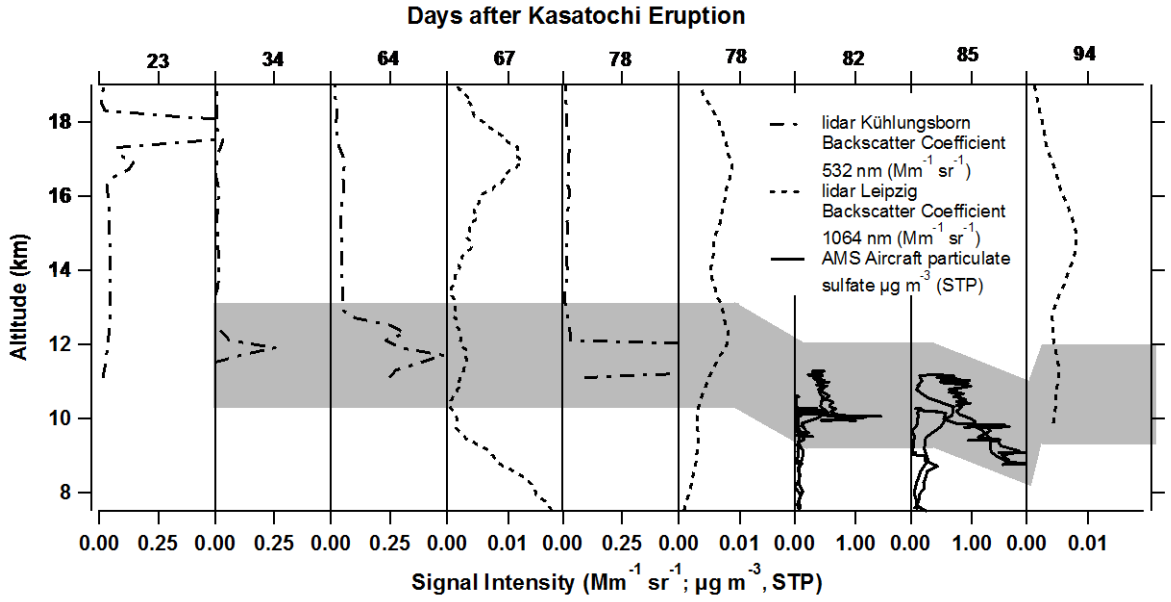


**Figure 31: Time series of lidar and AMS aerosol vertical profiles after the Mt. Kasatochi eruption. The signal intensity represents the backscatter coefficient for lidar and mass concentration for AMS data. The shaded area highlights the observed volcanic aerosol layer in the UTLS. [This figure was published in Schmale et al. (2010).]**

Combining all above findings it becomes very likely that the observed aerosol layer originated from the eruptions of Mts. Okmok and Kasatochi.

### *3.1.3 Case study – trace species in the transition regime*

The flight from 28 October offers the rare opportunity to study the characteristics of sulfate aerosol along the 2 PVU isosurface. Figure 32 a) illustrates the time series of particulate sulfate while b) shows the flight track through the vertical structure of the atmosphere. While the sulfate aerosol loading is especially enhanced when flying above the 2 PVU boundary, slight enhancements can be observed when the aircraft flew almost exactly on the 2 PVU isosurface as indicated by the blue box.

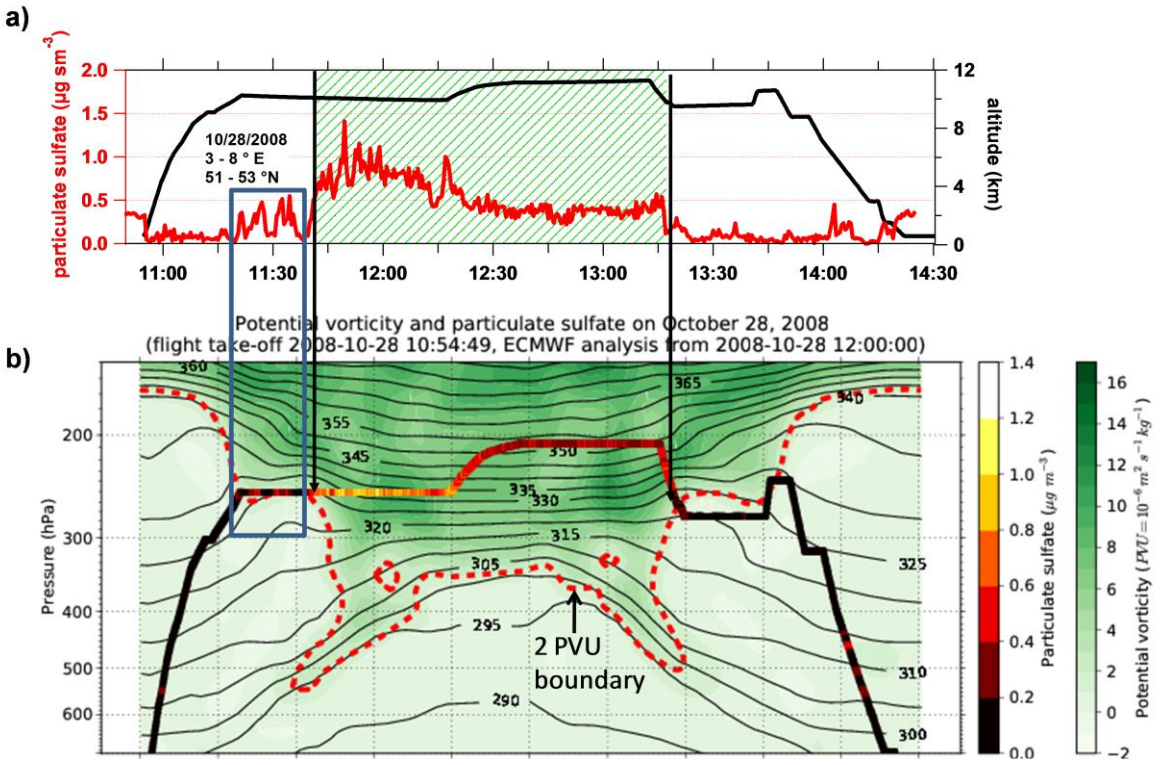


**Figure 32: a) Time series of particulate sulfate and flight altitude on 28 October. The green hatched area indicates the passage above 2 PVU. b) Vertical structure of the atmosphere [published in Schmale et al. (2010)]: The black contour lines represent potential temperature isolines, the color-code indicates the potential vorticity units, while the red dashed line denotes the 2 PVU isosurface. The flight track is shown in black with color-coding for the particulate sulfate concentration. The blue box circles the time of interest, when the Falcon flew almost exactly on the 2 PVU isosurface.**

In Figure 33 a) the chemical structure of the tropopause is investigated by the tracer plot of ozone and carbon monoxide. The transition regime between the tropospheric and stratospheric branch can be identified clearly (see also black circling). An important number of data points within this regime are from the time when flying very near the 2 PVU boundary (blue box). The potential temperature difference of the actual data point from the value at the 2 PVU isosurface ranges between 0 and 30 K in this area. Figure 33 b) explores how the particulate sulfate behaves in this transition regime by displaying the particulate sulfate concentration versus carbon monoxide. The squares indicate the data points of interest. There are more squares in b) than in a) due to a lack of ozone data for this period. The figures show clearly that these data points bridge the gap between the low tropospheric and the enhanced stratospheric particulate sulfate concentration. This is an indication that mixing of air masses is happening in this regime and that volcanic aerosol is lost to the troposphere. Additionally, the water vapor mixing ratio is represented by the color-code. Again the squares clearly denote an area of transition. In the stratospheric branch the water vapor is near 5 mmol $mol^{-1}$ while in the troposphere mixing ratios far greater than 100 mmol $mol^{-1}$ are reached.

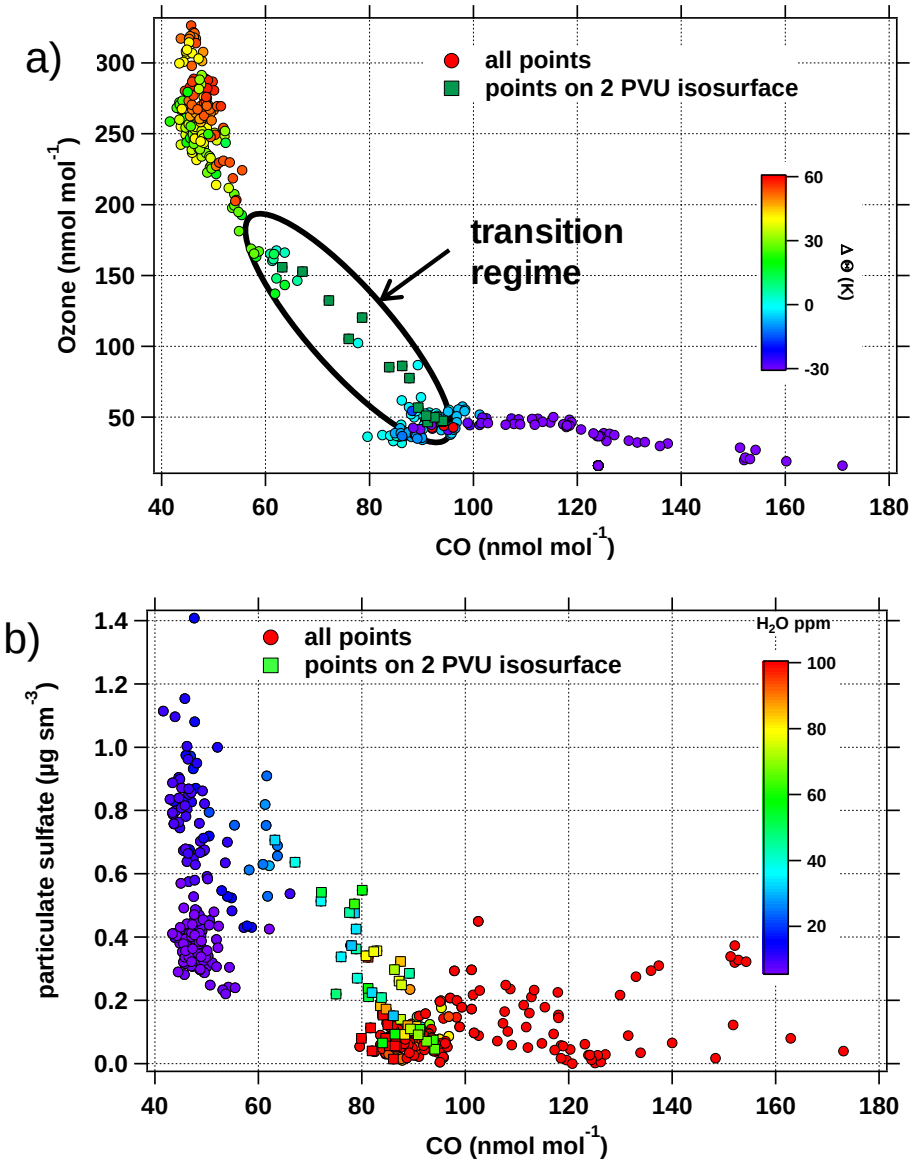


**Figure 33: a) Tracer plot for 28 October, 2008. The color-code indicates the deviation of potential temperature of the actual measurement point from the 2 PVU value. b) Particulate sulfate versus carbon monoxide color-coded with the water vapor mixing ratio. The circles represent all data points from this flight while the squares refer to the values obtained while flying on the 2 PVU isosurface.**

Statistically, the mixing of air masses can be explored by means of probability density functions as described in section 2.7.2. Figure 34 shows PDFs for ozone (a), carbon monoxide (b) and particulate sulfate (c) for three regimes. The regimes are defined as the difference in potential temperature of the actual data point from the value at the 2 PVU boundary (compare also Figure 33 a). The blue interval denotes tropospheric characteristics, while the green one stands for the stratosphere and the red one represents the transition layer. The tropospheric and stratospheric mixing ratios for ozone and CO are clearly separated as Figure 34 a) and b) show. The probability of values in between is 0 as expected. The red curve shows that the transition region has characteristics of both atmospheric regimes as the curves overlap. For particulate sulfate (c) the case is similar, however a bit more complex: In the troposphere the concentration is likely to be very low, while in the stratosphere two probability peaks, clearly higher than in the troposphere, can be observed. As illustrated by the green shaded area in

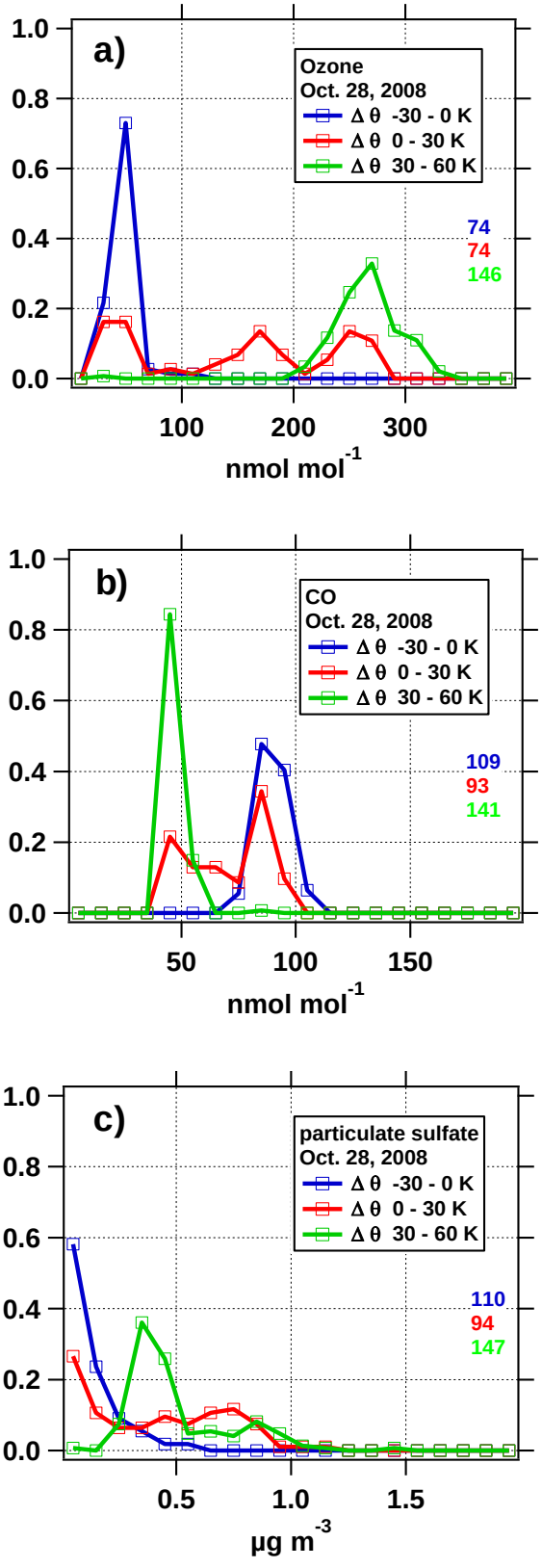


**Figure 34: Probability density functions for ozone (a), carbon monoxide (b) and particulate sulfate (c) for the flight on 28 October, 2008. The colored numbers indicated the number of data points for each regime.**

Figure 32 a there is a period when particulate sulfate concentration is near 1 µg $m^{-3}$ and another one with values near 0.4 µg $m^{-3}$. Both are reflected by the green curve in Figure 34 c). The red curve again represents concentration properties from the other two regimes.

With this case study the varying concentrations of particulate sulfate with altitude can be explained to great detail. It also shows how air masses from the stratosphere adopt tropospheric properties including enhanced humidity in their downward motion which can ultimately lead to wet deposition of the volcanic aerosol. Thus mixing of air masses in the transition region can become an important factor of stratospheric aerosol removal since particle settling velocities at sizes smaller than or equal to 1 µm are too small for significant removal rates through sedimentation (Jaenicke, 1980). After Hinds (1999) a 1 µm particles has an approximated settling velocity of 11 m per $day^{-1}$ at 200 hPa and -60°C (see Appendix C). According to Bourassa et al (2010) the stratospheric aerosol background concentration was reached 7 months after the eruptions. In this time particles would have lost around 2 km in height.

### *3.1.4 Chemical characteristics and size distribution of volcanic aerosol*

So far, only the particulate sulfate component of the volcanic aerosol was used for the identification of the haze layer because commonly sulfuric acid particles are associated with volcanic aerosol (Fahey et al., 1993; Keim et al., 1996; Borrmann et al., 1997). Through the chemical composition measurements however, more detailed data is available. To put the composition of the volcanic aerosol into context also particles from other observed atmospheric layers such as the boundary layer, the free troposphere and background UTLS are considered in the following. Figure 35 presents the average organic mass spectra for each atmospheric layer and by means of pie charts the relative contribution of each measured chemical species to the total submicron particle composition. In the boundary layer, aerosol concentration was highest with 3.6 µg $m^{-3}$ with strong contributions from nitrate, organics and ammonium. The particulate matter is rather alkaline with an acidity coefficient larger than one (defined as the molar equivalence ratio of measured ammonium and the sum of measured sulfate and nitrate, all in µmol $m^{-3}$, see Quinn et al. (2006)). Alkaline aerosol is rather unusual, but has already been observed on other occasions near a pig farm (Martin et al., 2008). In the free troposphere, the aerosol becomes very acidic due to a particulate sulfate contribution of almost 50 %. No nitrate is found. This and the observation that only 0.3 µg $m^{-3}$ particulate matter are present, a factor 12 less compared to the boundary layer, leads to the conclusion that most of the aerosol was washed out. The background aerosol concentration and composition in the UTLS is comparable to the values in the free troposphere. However, during volcanic aerosol layer encounters in the UTLS the composition changes significantly. 71 % of the aerosol is composed of sulfate, 21 % of organics and 8 % of ammonium. The acidity coefficient is 0.29 and the average total aerosol mass within the layer is 1.2 µg $m^{-3}$. The fact that more than 20 % of the mass is contributed by organic matter is surprising as this was not expected for volcanic aerosol.

The organic mass spectra in Figure 35 provide additional information on the nature of the organic matter. The error bars denote uncertainties from ion counting statistics while pink bars represent data below detection limit. Near the surface, lowermost panel, the average mass spectrum shows the typical sequence of uneven *m/z* that are associated with hydrocarbon-like organic aerosol (HOA) (Zhang et

al., 2005a) which originates from fossil fuel combustion (Schneider et al., 2006b). Also, oxygenated organic aerosol (OOA) is present as represented by the dominant *m/z* 44 ($CO_2^+$) peak (Zhang et al., 2005a). To compare the oxygenation of one aerosol type to another the ratio of the organic contribution to *m/z* 44 over the total organic mass is formed. In the boundary layer the value is 0.11 ± 0.002. The error denotes the 95 % confidence interval of the linear regression fit to *m/z* 44 versus OA data. After Aiken et al. (2008) the elemental O:C ratio from a C-ToF-AMS can be derived through an equation based on a linear regression fit to high resolution versus unit resolution data (O:C ratio vs *m/z* 44:OA). In this case the O:C ratio results in 0.50 ± 0.025. Such organic aerosol mass spectra have been identified as urban oxygenated organic aerosol (Alfarra et al., 2004; Zhang et al., 2005a). In the free troposphere the O:C ratio is higher with 0.69 ± 0.022 (*m/z* 44:OA 0.16 ± 0.003) and thus aerosol more oxygenated or aged. This is even more pronounced in the UTLS where the O:C ratio is 0.88 ± 0.019 (*m/z* 44:OA 0.21 ± 0.004). This type of organic mass spectrum with prevailing contributions from *m/z* 29 and *m/z* 44, 45 % and 21 % respectively of the organic mass spectrum, were observed on other occasions and identified as oxygenated organic aerosol "OOA-1" (Lanz et al., 2007; Ulbrich et al., 2009) or more recently as low volatile oxygenated organic aerosol "LV-OOA" (Jimenez et al., 2009). In the volcanic aerosol layer the O:C ratio is 0.69 ± 0.021 (0.16 ± 0.003). For an extended discussion of the O:C ratio of volcanic aerosol see section 4.3.2.

Figure 36 illustrates the average vertical structure of particulate sulfate and organic concentrations including one standard deviation. In the volcanic aerosol layer the concentration of organics with 0.25 ± 0.12 µg $m^{-3}$ was found to be a factor 1.4 larger than in the background UTLS with 0.18 ± 0.11 µg $m^{-3}$. Compared to the free troposphere the enhancement is 190 %. Even though this increase is statistically not significant the trend can clearly be observed from the figure. It is possible that the AMS collection efficiency increased during plume encounters due to the dominant presence of sulfuric acid (Quinn et al., 2006). In this case, the increase in organic mass would not be real. However, there is no reason to assume that the collection efficiency in the free troposphere, background UTLS or within the haze layer changed significantly as the overall compositions are comparable. But as the uncertainties from AMS measurements are too large (in the order of 30 %) the increase in organic matter in the volcanic aerosol cannot be verified. However, the data clearly show that the volcanic aerosol contains organic matter. This is backed up by measurements reported by Martinsson et al. (2009) who also found carbonaceous matter in the Mts. Okmok and Kasatochi plumes.

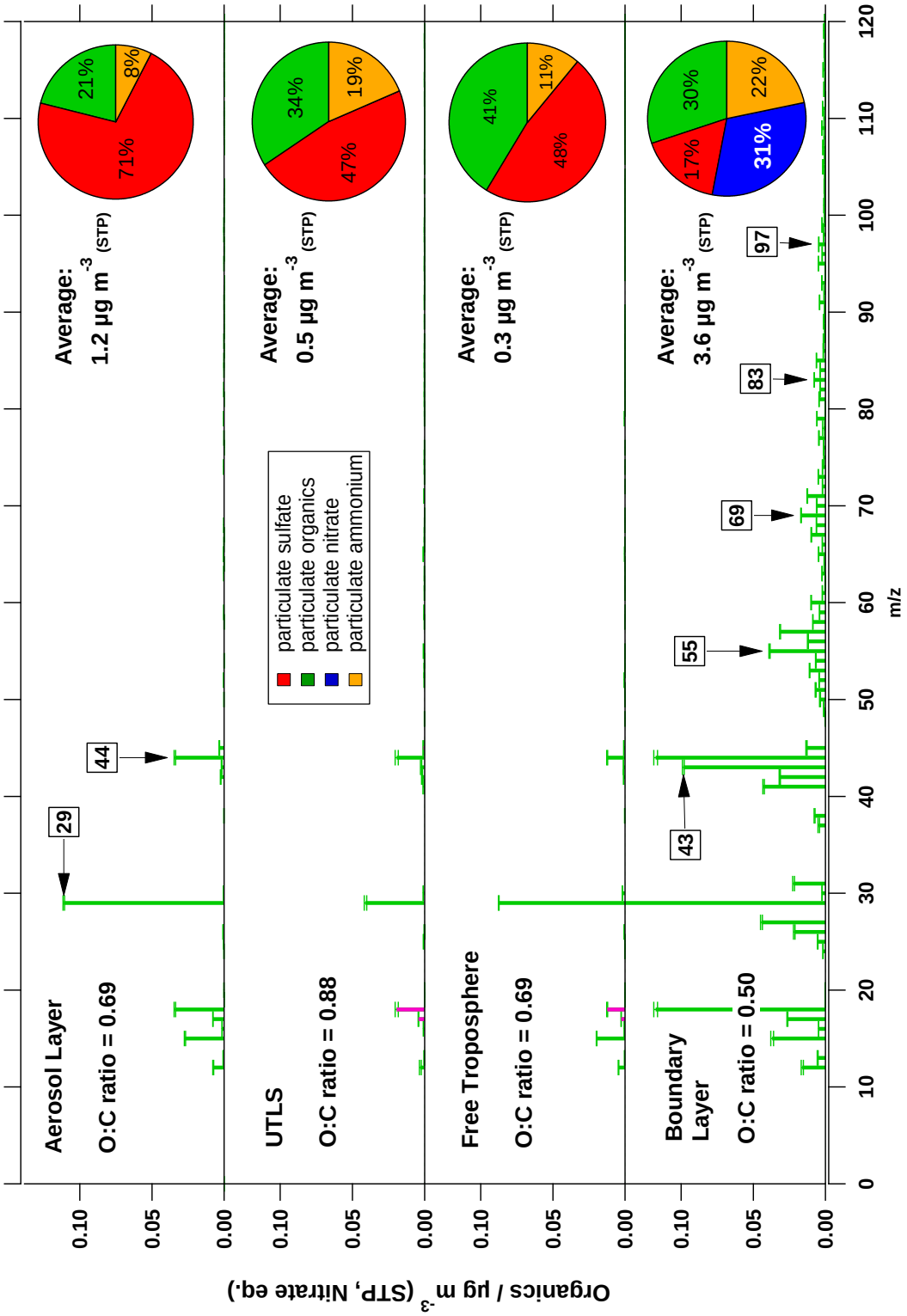


**Figure 35: Average organic mass spectra from different atmospheric layers. At the left side the O:C ratio indicates the degree of oxygenation of the aerosol. On the right side the pie charts indicate the relative contribution of each chemical species to the aerosol composition. The average concentration is also indicated. Bars in pink are below detection limit. The error indicates the uncertainty from ion counting statistics. [This figure is adapted from Schmale et al. (2010).]**

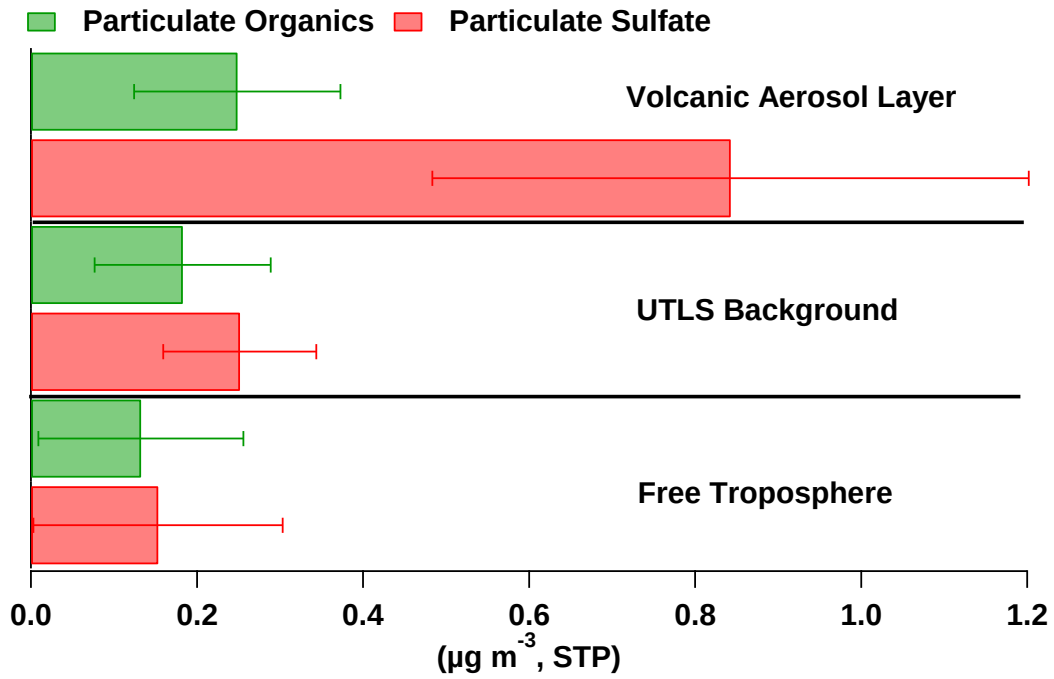


**Figure 36: Average concentrations of particulate organics and sulfate including one standard deviation. [This figure was published in Schmale et al. (2010).]**

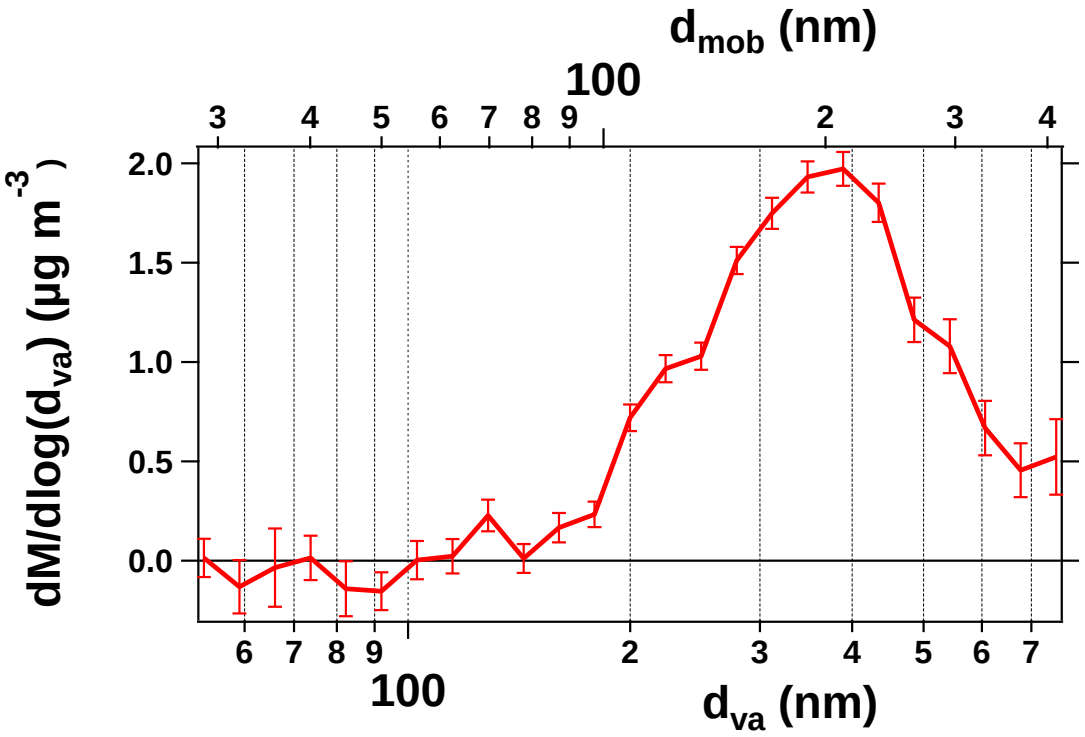


**Figure 37: Size distribution of particulate sulfate in the volcanic aerosol layer with a resolution of 25 bins between 50 and 800 nm *dva*. The error bars denote the statistical counting error. [Adapted from Schmale et al. (2010).]**

After finding this, the intriguing question arises why and how organic matter forms part of stratospheric volcanic aerosol. Organic matter is not assumed to be present in the extremely hot inner earth material which the eruption column injects because organic material would not survive the high temperatures. It is however conceivable that organic vapors and particulate matter from the boundary layer and troposphere are entrained in the eruption column and thus uplifted even across the tropopause (see Figure 4). Especially considering that the eruptions took place in a period of extensive biomass burning in Canada resulting in a highly perturbed troposphere (Jacob et al., 2010; Singh et al., 2010) it is possible that larger amounts of particulate and gas phase organics than during other seasons were injected into high altitudes through the volcanic eruptions. Also, high reaching pyro-convection (Fromm et al., 2005) during biomass burning events can be a source of organic matter in the stratosphere. Fromm et al. (personal communication) observed pyro-cumulonimbus clouds penetrating the tropopause during ARCTAS II in July 2008 when Mt. Okmok erupted. Another source of organics in the lower stratosphere can be troposphere to stratosphere exchange. This however seems to be less likely as the trend from Figure 36 suggests that less organic material was present in the UT than in higher altitudes. In any case, the observation that organic matter is present in the UTLS has been made before e.g. by Murphy et al. (2007) and Froyd et al. (2009b). This implies that carbonaceous matter is frequently supplied to this region of the atmosphere independently from volcanic eruption events. Once organic vapors entered the stratosphere, semi- and low-volatile components possibly can contribute to the formation and growth of particles. Ekman et al. (2008), for example, found for the tropical upper troposphere that organics seem to play a role next to sulfate in the formation and growth of small particles. This has implications for the efficiency of heterogeneous reactions which can occur in/on volcanic aerosol. Usually, for the corresponding calculations reactive uptake coefficients are adopted assuming the volcanic particles to consist of pure binary sulfuric acid solution droplets (Fahey et al., 1993; Keim et al., 1996; Borrmann et al., 1997). The observed presence of a significant organic component of 20 % may substantially influence the reactive uptake.

Figure 37 shows the average mass size distribution of the sulfate component in the volcanic aerosol. The error bars represent the statistical counting error, as explained and discussed in Appendix D. The mode diameter is 360 nm $d_{va}$ with a geometric standard deviation of 1.4. According to Wilson et al. (1993) the submicron volumetric size distribution of stratospheric aerosol after the Pinatubo eruption at a comparable age of 78 days showed a mode diameter between 300 and 400 nm $d_{mob}$ measured by a focused cavity aerosol spectrometer (Jonsson et al., 1995). Converting the vacuum aerodynamic particle diameter into the mobility diameter after deCarlo et al. (2004) assuming a density of 1.84 g $m^{-3}$ for sulfuric acid a mode diameter of 200 nm $d_{mob}$ is obtained (see upper horizontal axis in Figure 37). The fact that Mts. Okmok/Kasatochi aerosol seems to be smaller may reflect the larger amount of $SO_2$ injected by Mt. Pinatubo (1.6 Mt compared to 20 Mt) leading to higher particle formation and growth rates after the eruption in 1991.

In summary the key findings from this detailed study of naturally emitted aerosol type are:

1. The volcanic aerosol layer is characterized by a sharp increase in particle load in the tropopause region. On average the volcanic aerosol had a concentration of $1.09 \pm 0.39$ µg $m^{-3}$ while background UTLS and free tropospheric aerosol had a concentration of $0.43 \pm 0.16$ and $0.28 \pm 0.23$ µg $m^{-3}$, respectively.
2. Volcanic aerosol was found to consist of only 71 % particulate sulfate and contained a significant amount of organic matter of about 21 %. This might have important implications for modeling heterogeneous reactions in the stratosphere. Nevertheless, it is far more acidic than background UTLS and free tropospheric aerosol where particulate sulfate contributed 47 % and 48 % and organics 34 % and 41 %, respectively.
3. Applying several tropopause definitions, the volcanic aerosol was located in the lower stratosphere. Based on detailed tracer studies, enhancement of particulate sulfate in the transition region between troposphere and stratosphere was observed. This might be an indication for an important removal process of the lower stratospheric aerosol, because settling velocities cannot explain the rapid depletion of the Mts. Okmok/Kasatochi aerosol layer within 7 months.

## *3.2 Mixed natural and human-induced aerosol release to the atmosphere*

In the following the focus is laid on atmospheric perturbations resulting from biomass burning (BB) and surface-bound fossil fuel combustion (FF) and their various transport patterns. Within the scope of the POLARCAT and CONCERT campaigns no opportunity occurred to measure emissions from either only BB or FF because measurements were conducted in remote geographical (Greenland) and atmospheric (free troposphere, UTLS) regions so that pollution plumes had to be transported over long distances and periods of time before sampling. Consequently, mixing of air parcels influenced by different emission source types occurred frequently. This effect was particularly enhanced for the source regions in North America and Siberia/Asia where BB occurred in relatively close vicinity to anthropogenic activity compared to the distance of transport towards Greenland. Another aspect to consider when referring to BB is the fact that it is not always obvious whether the fires were naturally induced by lightning or triggered intentionally by humans. So a differentiation of BB as either purely natural or anthropogenic emission source is difficult.

Bearing above considerations in mind, the probed pollution episodes were classified into five categories:

I. "pure" BB (mainly BB influenced plumes)

II. BB / FF no Asia (BB dominated air masses with FF contribution but no Asian influence)

III. NA / EU, FF / little BB (air masses with origin in North America and Europe with pronounced FF characteristics and some BB influence)

IV. Sib BB / Asia FF (plumes primarily influenced by Siberian BB and to lesser extent by East Asian FF)

V. Asia FF / Sib BB (pollution episodes with enhanced contribution from Asian FF and some influence of Siberian BB)

VI. NA FF (mainly North American FF influenced plume)

Section 2.7.3 describes how individual pollution plumes were identified and how they were categorized. With a total of 48 plumes found during POLARCAT and additional pollution episodes from CONCERT and ARCTAS, only specific examples are discussed in the following subsections. The case selection takes the various emission regions, source types and air mass transport pathways into account. All but the last pollution episode in this section originate from POLARCAT measurements. As the ATR-42 research aircraft was unable to reach the tropopause region, ARCTAS data is used to complement individual plume studies by focusing on pollution transport to and in the UTLS. Emphasis is laid on this aspect because aerosol lifetime increases significantly in the tropopause (Farina et al., 2010) and consequently potential effects (direct and indirect radiative forcing, heterogeneous chemistry) might be enhanced. Additionally, these are the first real-time particle chemical composition measurements available for high northern latitudes at high altitudes. The integrated analysis of all pollution episodes and background conditions is conducted in chapter 4. The following table provides an overview of all plumes discussed below in detail. Section 3.2.4 on

page 136 resumes the key parameters such as location, extension and chemical composition of the gas- and particle phase of each plume for better comparability.

**Table 13: Overview of individually discussed plumes**

| Name | Date / Time | Category | Transport |
|---|---|---|---|
| Plume I | 8 July, 2008 / 13:14 – 13:32 | "pure" BB | Tropospheric transport (POLARCAT) |
| Siberian BB | 5 July, 2008 / 01:01 – 01:30 | "pure" BB | Air mass uplift to the UTLS (ARCTAS) |
| Plume II | 8 July, 2008 / 14:52 – 15:02 | NA / EU, FF / little BB | Frontal transport, warm conveyor belt (POLARCAT) |
| Plume III | 13 July, 2008 / 19:56 – 20:02 | Sib BB / Asia FF | Warm conveyor belt, strong wet deposition (POLARCAT) |
| Plume IV | 8 July, 2008 / 15:40 – 15:50 | NA / EU, FF / little BB | Low level transport over the Atlantic (POLARCAT) |
| Plume V | 13 July, 2008 / 18:42 – 19:06 | Asia FF / Sib BB | Stratospheric intrusion (POLARCAT) |
| East Asian, FF | 5 July, 2008 / 02:49 – 03:03 | Asia FF | Air mass uplift to the LS (ARCTAS) |
| Plume VI | 31 October, 2008 / 11:39 – 11:44, 13:37 – 13:41 | NA FF*) | Tropospheric cross-Atlantic transport (CONCERT) |

*) This category of North American almost pure fossil fuel combustion did not occur during POLARCAT, it is introduced here to identify this observed pollution episode during CONCERT.

The following two figures (Figure 38 and Figure 39) provide basic information on the POLARCAT pollution episodes to be discussed. Panel a shows the flight altitude in blue for 8 and 13 July together with the trace gas mixing ratios for ozone and CO. The AMS measurements of particulate organics and sulfate are given in panel b. The stacked results allow for reading the total AMS derived submicron aerosol mass concentration. Panel c displays the FLEXPART calculations of excess CO (CO minus 100 nmol $mol^{-1}$) from BB (brown filled area) and from all sources (total CO in grey). The difference can be attributed to anthropogenic activity. The black trace indicates the measured excess CO for comparison with the model. The FLEXPART derived ratio of BC aerosol-like over passive tracer in panel d approximates the amount of aerosol that has not been wash-out along the trajectory. For reasons stated in section 2.6.3 the wet deposition of the aerosol-like tracer is overestimated. Nevertheless, the ratio shows that strong wash-out events had occurred before both flights. In the lowermost panel the SMPS derived volume size distribution is displayed for particles between 20 and 500 nm $d_{mob}$. In both figures the trends of the volume size distribution and the aerosol mass concentrations correlate well. The blue hatched areas denote episodes with relative humidity greater or

equal to 100 %, i.e. crossing of clouds. The black vertical lines and roman numbers indicate the specific episodes of interest.

The flight on 8 July started in Kangerlussuaq, passed over the Greenland ice sheet heading south, flew over the Atlantic Ocean, and then returned to Narsarsuaq, Southern Greenland. Due to an intense low pressure system tracking from North America towards southern Greenland, mainly air masses influenced by BB from Canada and FF from the United States were probed (see Figure 40). A strong warm conveyor belt (WCB) associated with this low pressure system lifted warm and humid air masses from North America up to 400 hPa and advected them towards southern Greenland over approximately 3 days. According to FLEXPART, transport times from North America for all events during this flight were between three and nine days.

On 13 July 2008, the ATR-42 flew from Kangerlussuaq straight over Baffin Bay in NW direction to a turning point at 70.1°N, 60.4°W from where it returned on the same path. The first leg was flown at 7.3 km altitude while during the return the altitude varied between 4.6 and 5.8 km a.s.l. (above sea level) to cross forecasted pollution plumes at various altitudes. During this period, Asian pollution was transported across the pole associated with the development of a low pressure system over the East Siberian Sea (Sodemann et al., 2010). At the same time another low pressure system travelled north along the eastern coast of Greenland. Pollution plumes sampled between these two low pressure systems were in a region of stretching and filamentation indicated by CO mixing ratios leading to the formation of fine-scale features in the measurements (shown in detail by Sodemann et al. (2010)). According to FLEXPART, this flight was influenced by a variety of air masses from different origins leading to high variability in air mass transport times which ranged between 10 and 17 days for Asia and around one week for NA and Europe. However, the focus of this analysis is placed on Asian plumes.

**Figure 38 (next page): Time series of the flight from 8 July, 2008. a) Aircraft altitude (blue) and trace gas mixing ratios (grey $O_3$, black CO) in one second time resolution, the blue hatched areas denote relative humidity equal to or greater than 100 %. b) AMS sulfate and organic aerosol concentration in two minutes time resolution. c) FLEXPART excess total and biomass burning (BB) CO and measured excess CO (actual concentration minus 100 nmol mol$^{-1}$), d) ratio of FLEXPART BC aerosol-like and passive tracer, e) SMPS volume size distribution at STP. The areas between the black bars with roman numbers indicate the discussed plumes. [This figure is adapted from Schmale et al. (2011).]**

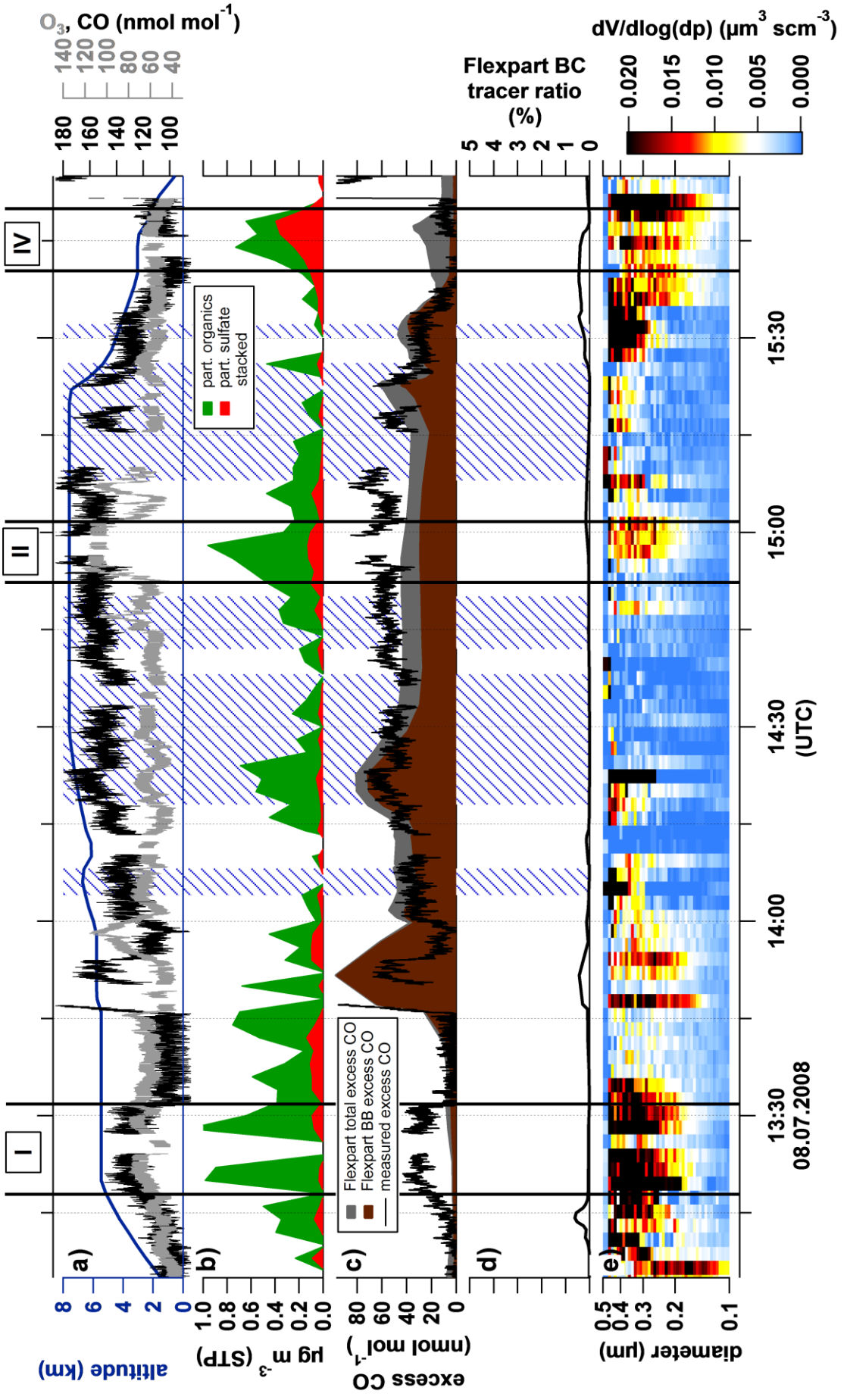
O3, CO (nmol mol-1)
Flexpart BC tracer ratio (%)
dV/dlog(dp) (µm3 scm-3)
part. organics
part. sulfate
stacked
Flexpart total excess CO
Flexpart BB excess CO
measured excess CO
altitude (km)
µg m-3 (STP)
excess CO (nmol mol-1)
diameter (µm)
I
II
IV
13:30
08.07.2008
14:00
14:30
(UTC)
15:00
15:30

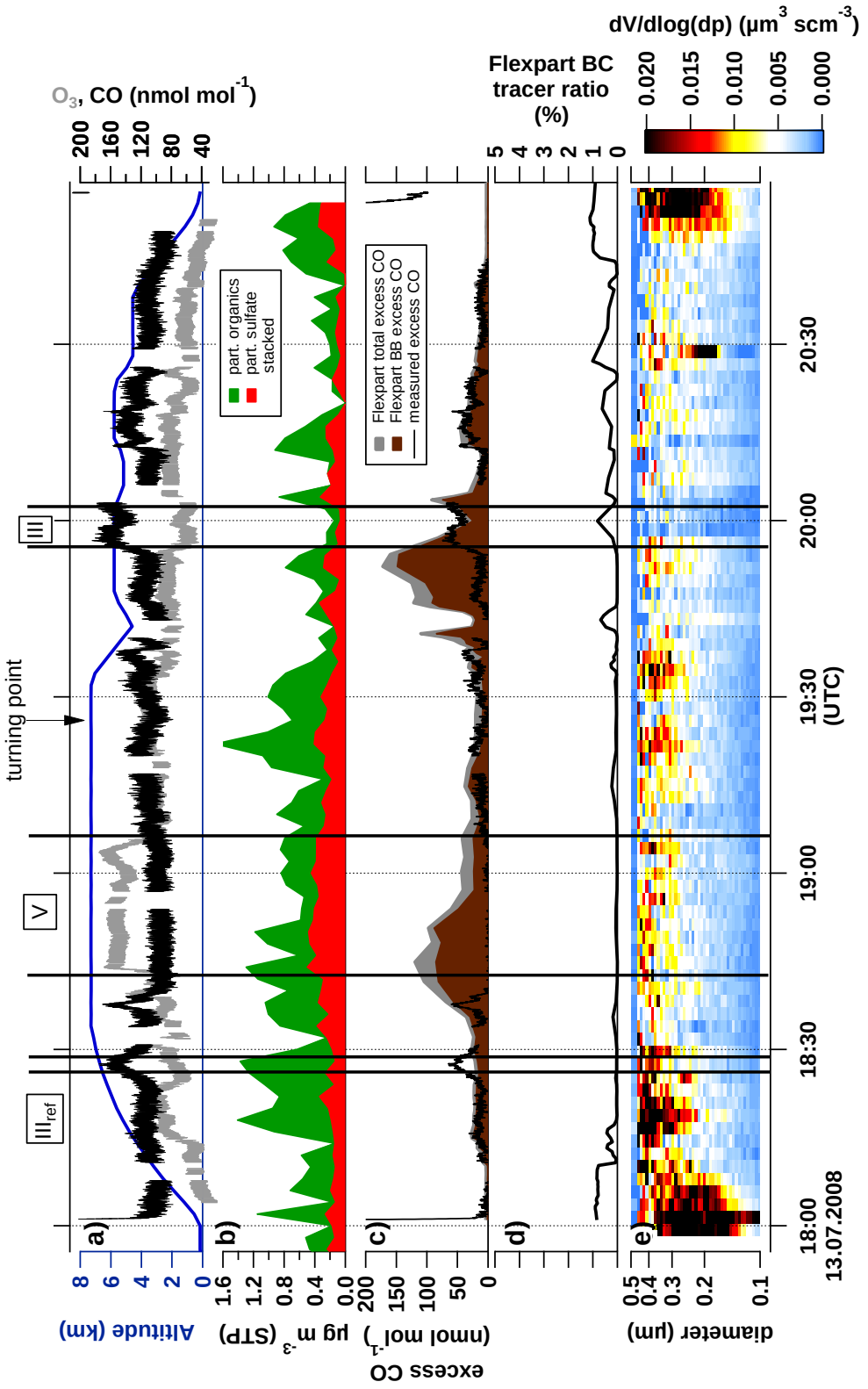


**Figure 39: Time series of the flight on 13 July, 2008. Same as in Figure 38. [This figure is adapted from Schmale et al. (2011).]**

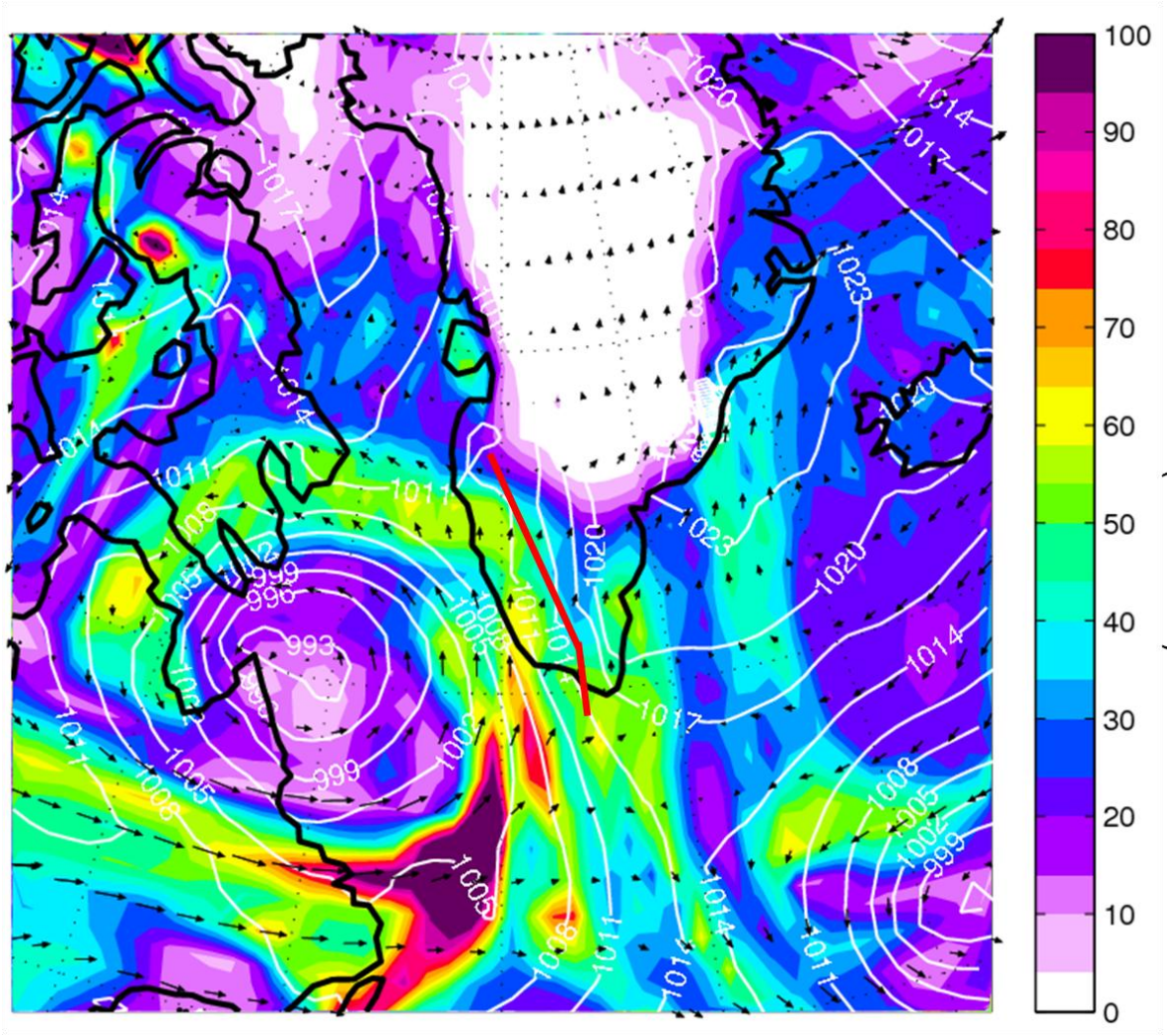


**Figure 40: Low pressure system west of Greenland on 8 July at 15 UTC at 5000 m altitude. The color-code denotes FLEXPART derived excess CO mixing ratio in nmol mol$^{-1}$, the white contours represent surface pressure levels from 980 to 1030 hPa in 3 hPa intervals. The red line indicates the ATR-43 flight track. [This figure was published in Schmale et al. (2011).]**

### *3.2.1 Biomass burning dominated plumes*

Two plumes are discussed in the following. They give examples for the advection of polluted air masses in the free troposphere and uplift to the tropopause with potential subsequent cross-tropopause-transport.

#### 3.2.1.1 Tropospheric transport of BB from Canada

The here presented plume was observed over inland ice in the free troposphere on 8 July, 2008, (see Figure 38, I). All gaseous and aerosol tracers are elevated during this event and drop simultaneously between 13:24 and 13:26 UTC. The CO detector shows no signal during these two minutes due to internal calibrations. The horizontal extension of the measured plume segment was 108 km. The chemical composition of the aerosol is characterized by a mass fraction of 90 ± 12 % organics, an average total mass of 0.82 ± 0.35 µg m$^{-3}$, while ΔCO is 30 nmol mol$^{-1}$, and $\Delta O_3$ is 10 nmol mol$^{-1}$ for the period during which the aircraft moved at a constant altitude. The trace gas delta values are

calculated by subtracting the average mixing ratio before and after the plume from the peak value during the pollution episode. Even though, according to Figure 38 c) and d) the ATR-42 flew only through a faint CO and mostly "washed-out BC" signature, it is obvious from the FLEXPART column-integrated emission sensitivity in Figure 41 a) that this air mass was influenced by BB in Canada.

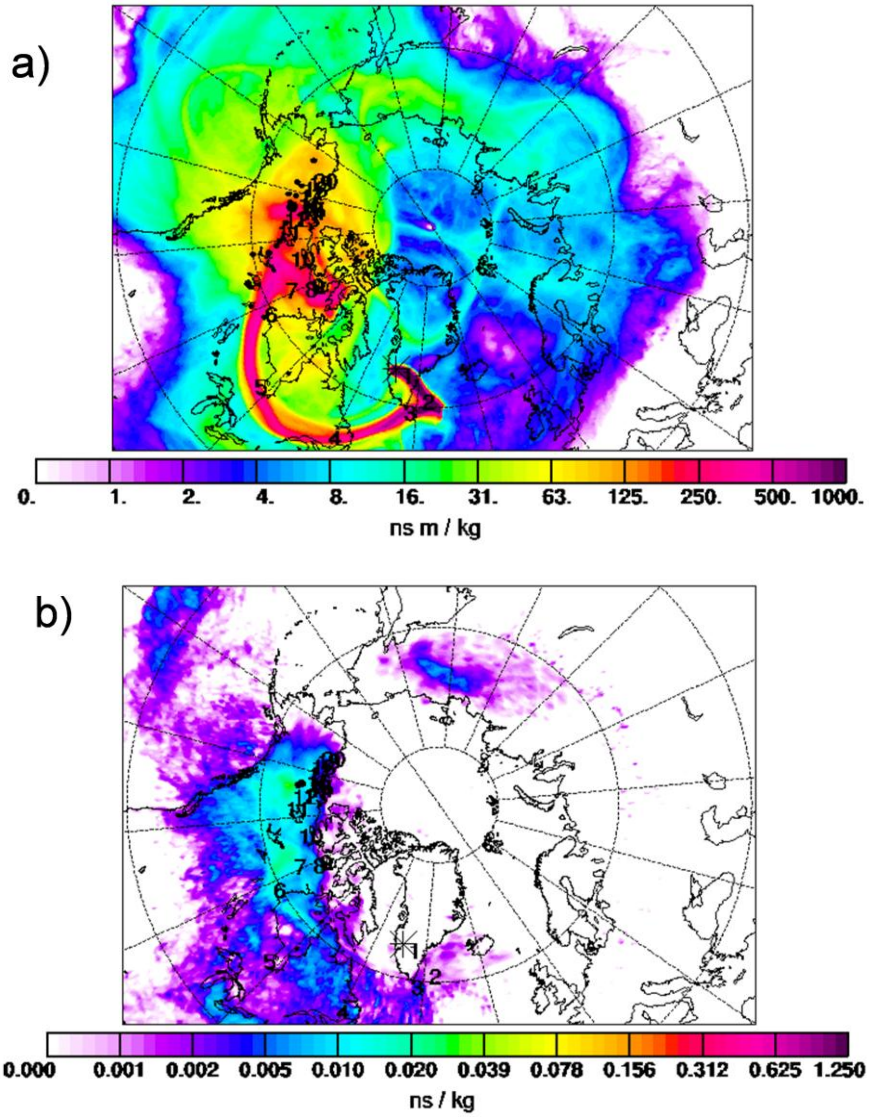


**Figure 41: "Pure" biomass burning pollution plume from Canadian forest fires transported towards Greenland on 8 July, 2008, 13:14 – 13:32 UTC. a) FLEXPART column integrated sensitivity, b) footprint sensitivity; numbers indicated age of plume.**

To determine whether the region which the probed air mass is sensitive to, is influenced by surface emissions it is important to consider the footprint tracers as shown in Figure 41 b). Especially for aircraft as opposed to ground based measurements it is likely that the column-integrated signal points towards a source region where at the time of interest no surface emissions were released. In this case however, both panels indicate fires in Saskatchewan as source of the observed aerosol. A possible explanation for the discrepancy between the clearly identified emission origin and the low CO contribution in the FLEXPART calculations can be the standardized injection height of about 100 m.

If this parameter is too low long-range transport might be underestimated (see also Figure 42). Sessions et al. (2010) discuss this difficulty of modelled BB injections of boreal forest fires based on measurements during ARCTAS.

The FLEXPART CO fire tracer constitutes roughly 58 % of the total CO passive tracer contribution in this case which is probably too low due to the mentioned reasons. The plume travelled for approximately 7 days through the free troposphere before detection in a rather dry air mass with 20 – 30 % relative humidity based on in-situ measurements. According to back trajectory calculations by the OFFLINE model (Figure 42), most of the air masses picked up BB signatures between 850 and 550 hPa, were lifted to about 400 hPa and then travelled between 600 and 400 hPa before interception. About 130 hours prior to arrival it can be seen nicely that air masses gained in relative humidity when they were uplifted. Even though the indicated relative humidity barely reaches 50 % it cannot be excluded that precipitation events occurred along the track. The average of the meteorological input data for each time interval might smooth out high values of relative humidity that occurred for short periods. [This paragraph is adapted from Schmale et al. (2011).]

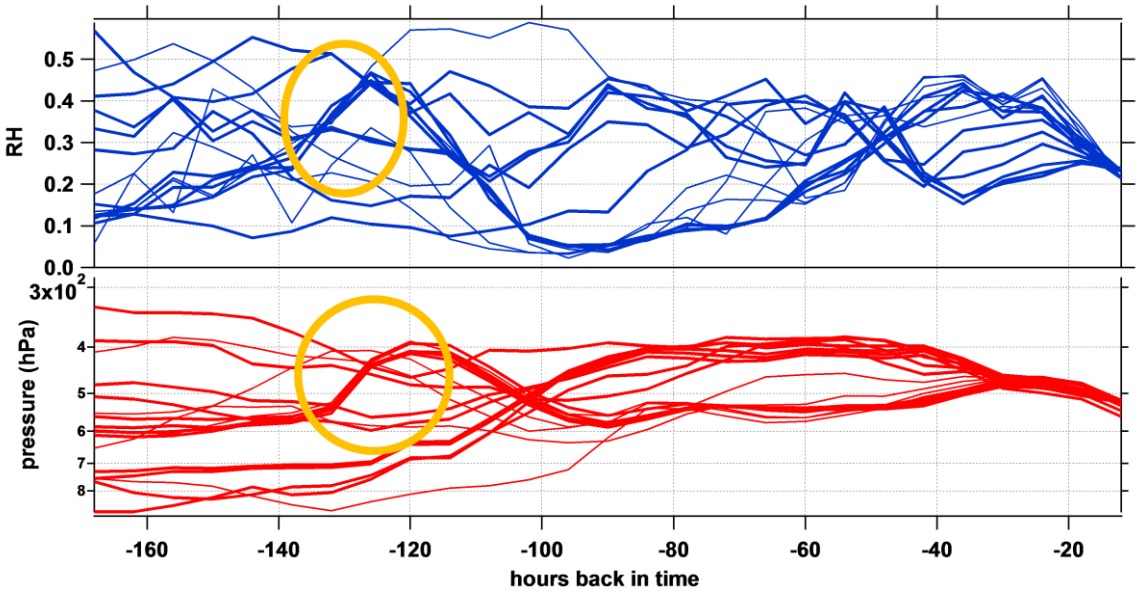


**Figure 42: Plume I (8 July, 2008, 13:14 – 13:32) back trajectories calculated with the OFFLINE model: lower panel ambient pressure, upper panel relative humidity (0.5 corresponds to 50 % RH). The thin lines indicate the trajectories for the time period when little aerosol concentration was measured. The orange lines encircle when uplifting occurred and the air mass gained in relative humidity.**

### 3.2.1.2 Uplift of Siberian BB to the tropopause

The upper case is an example for BB emission export through the free troposphere where after a week on average an aerosol concentration of below 1 µg $m^{-3}$ was left. Complementary, a second case of relatively pure wild fire emissions from Siberia shall be discussed which reached tropopause altitudes. Figure 43 shows the last three hours of the ARCTAS flight that started on 4 July, 2008, between 52 and 58 N and 84 and 112°W over Canada. Panel a) shows the mixing ratio of $CH_3CN$ as color-code along the flight altitude in hPa. The roman number I between the first two vertical black bars indicates the period of interest when the aircraft flew very close and slightly above the dynamical tropopause as

indicated by the green 2 PVU isoline. Episode II is discussed in section 3.2.3.3. According to Warneke et al. (2006) BB influence can be assumed starting from a $CH_3CN$ mixing ratio of 0.2 nmol mol$^{-1}$. Between 01:01 and 01:30 UTC in altitudes between 11.7 and 11.9 km the concentration is clearly enhanced. According to FLEXPART calculations (see Figure 44 a) the source region of the roughly 14 days old air mass is Siberia and East Asia. Potentially, there is thus anthropogenic influence, however, panel b) in Figure 43 shows a low $SO_2$ mixing ratio with < 20 pmol mol$^{-1}$. Therefore, it can be assumed that primarily BB is responsible for this plume. 69 % of the aerosol is composed of organic matter based on organic and sulfate mass alone. On average the mass concentration of particulate organics is 0.68 µg m$^{-3}$ while for sulfate it is 0.31 µg m$^{-3}$. The relatively large fraction of sulfate suggests contribution from fossil fuel burning. Significant amounts of $SO_2$ might have been converted into sulfuric acid and condensed into the particle phase during transport. For further discussion on the evolution of BB aerosol and $SO_2$ chemistry see sections 1.5.2 and 3.2.3, respectively.

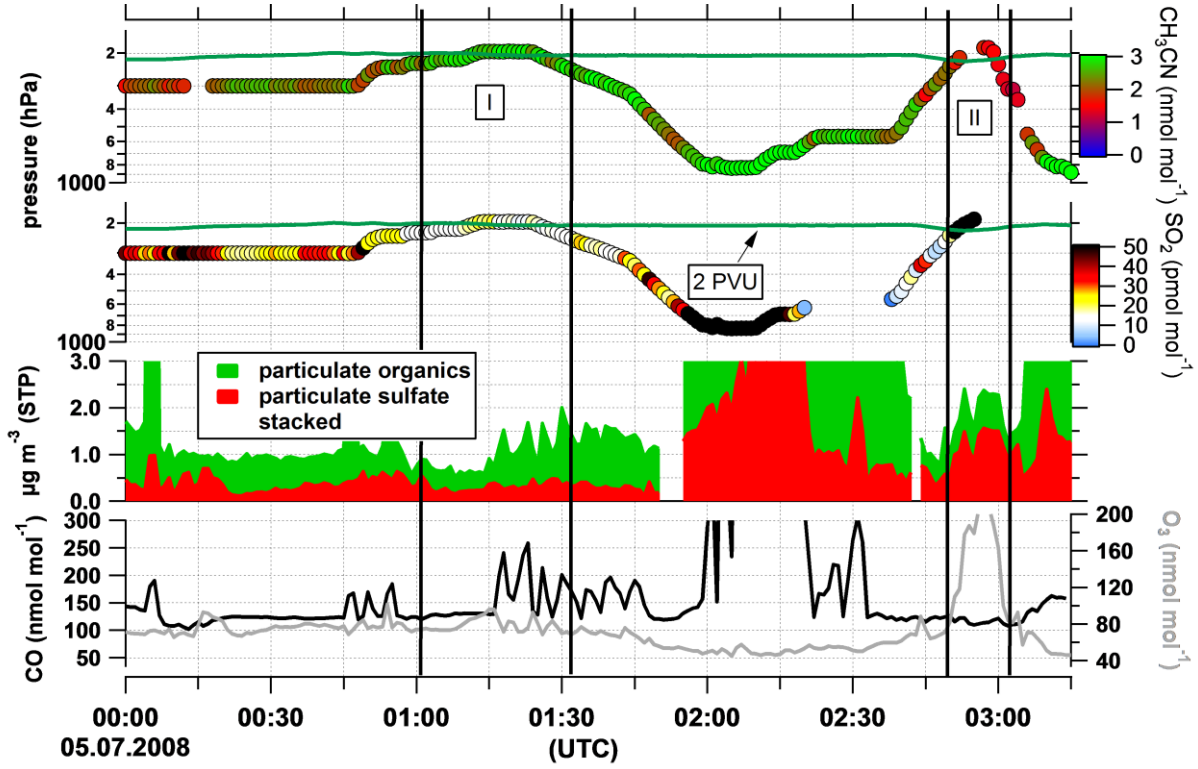


**Figure 43: This ARCTAS-summer flight started on 4 July, 2008. The plot shows the last 3 hours of the flight on 5 July, 2008. Panels a) and b) show the mixing ratios of $CH_3CN$ and $SO_2$ along the flight paths. The green line indicates the dynamic tropopause. Panel c) presents the stacked AMS derived concentrations for particulate sulfate, and organics (the scale is optimized for the periods of interest) and panel d) displays the CO and ozone mixing ratios. The roman numbers indicated the episodes of interest as discussed in the text.**

The carbonaceous matter shows strong fluctuations within the interval that are reflected by the CO mixing ratio as shown in panel d. ΔCO values reach up to 129 nmol mol$^{-1}$ based on the last value before the steep increase within the period. The ozone mixing ratio is anti-correlated and has a mean value of 79.1 ± 7.7 nmol mol$^{-1}$ near the dynamical tropopause which corresponds to the range of values observed during all ARCTAS flights (vertical profile in Figure 72). The stratospheric

contribution as derived from FLEXPART is between 10 and 16 %, i.e. rather low, and according to HYSPLIT trajectory analysis the air mass had ascended into higher altitudes, potentially the tropopause region, about 3 days prior to the encounter (see Figure 45 b). It is likely that the air mass was exported along the Pacific storm track, was uplifted in a WCB and subsequently followed the jet stream path from Siberia/Asia towards North America as the trajectories follow the typical meander (a). Panel b) shows that significant wet removal happened between 150 and 100 hours before interception.

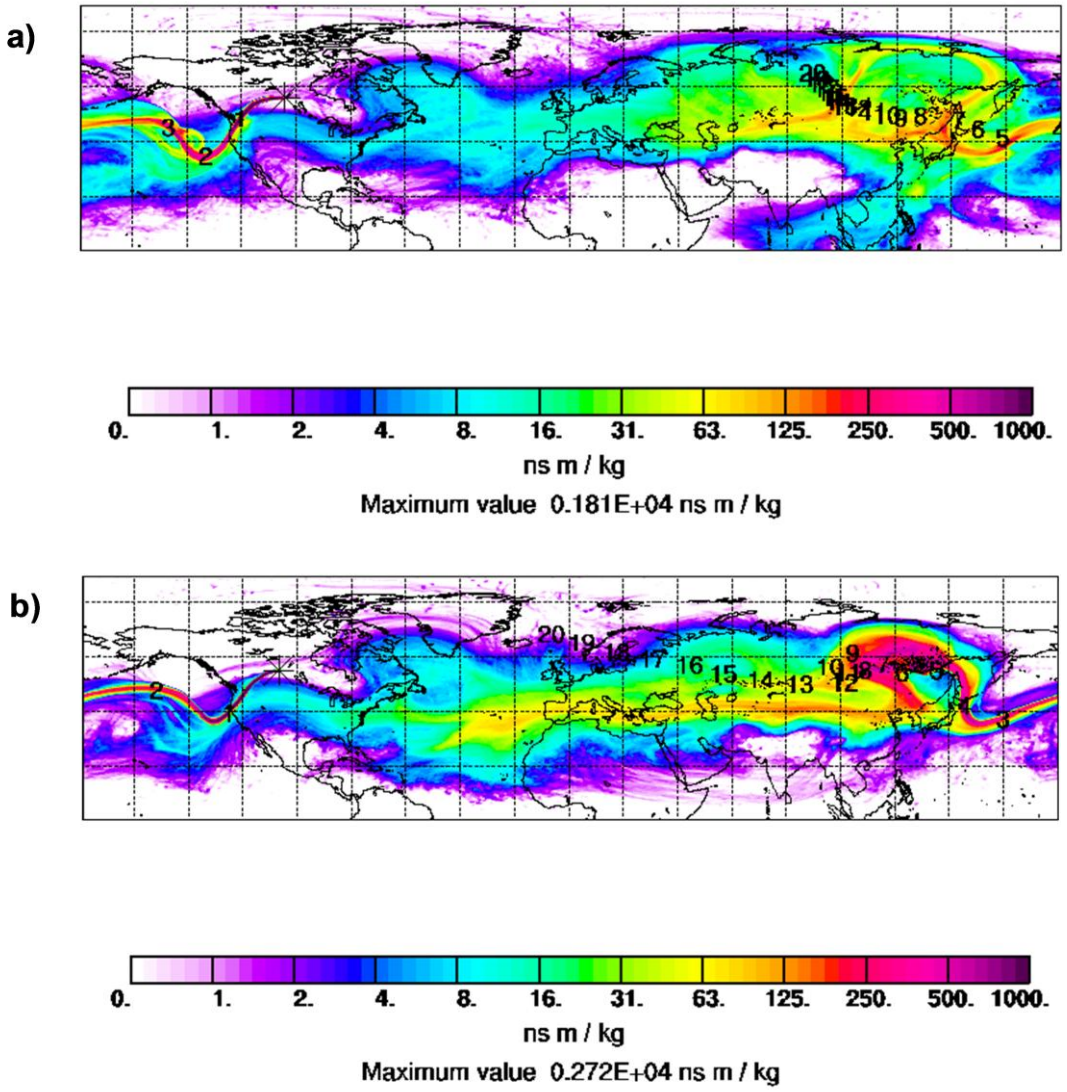


**Figure 44: FLEXPART column-integrated emission sensitivity for the 4 July, 2008, flight. a) For episode I as indicated in Figure 43 (00:59:50 – 01:01:33 UTC). The data suggest influence from fires in Siberia and possibly anthropogenic activity in East Asia. b) For episode II as indicated in Figure 43 (02:52:52 – 02:53:49 UTC). The data indicate contributions from anthropogenic emissions in East Asia and possibly BB from Siberia.**

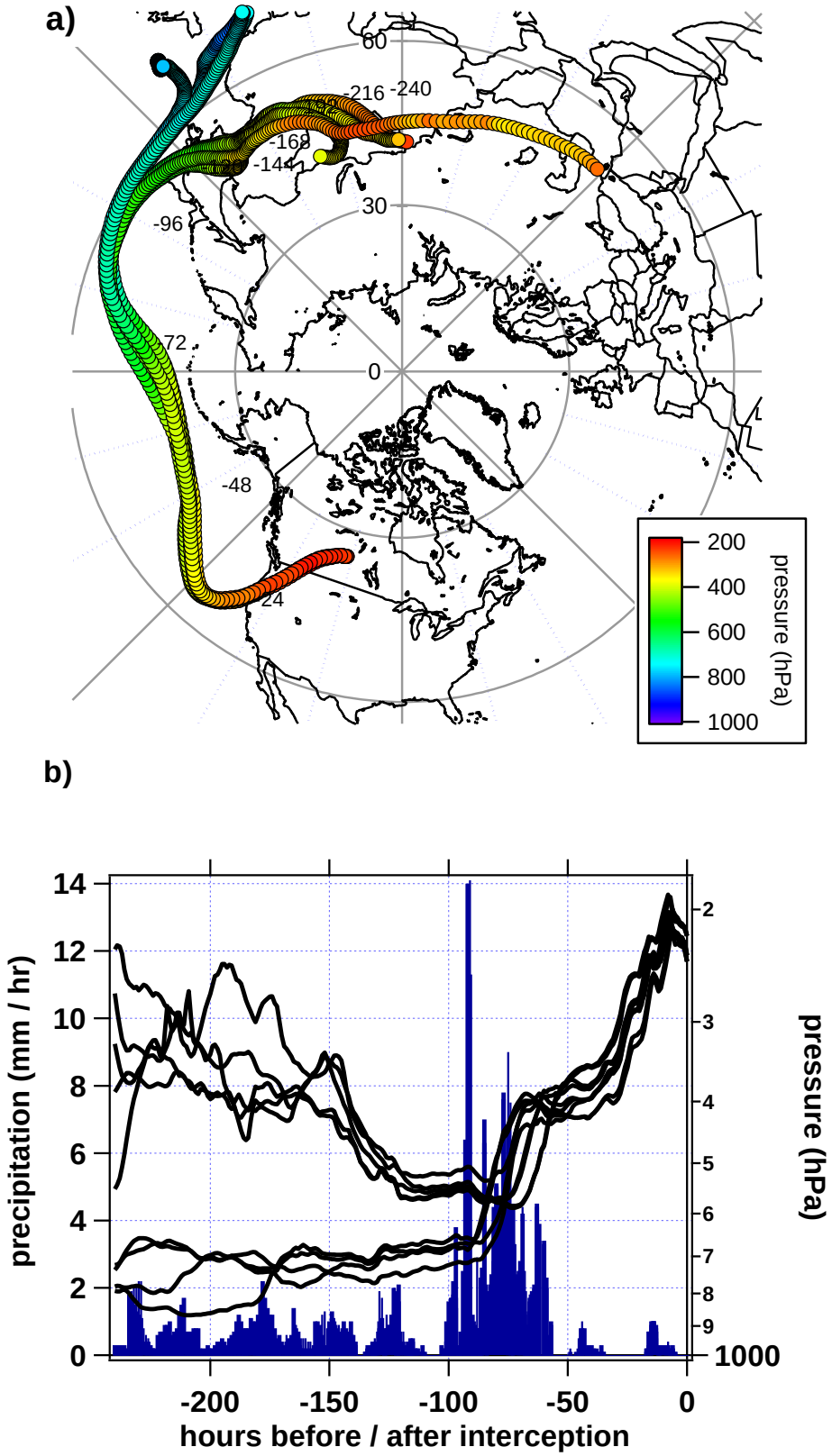


**Figure 45: HYSPLIT 10-day back trajectories for episode I at 01:01 – 01:30, 5 July, 2008. The trajectories were started at 01:00 on 5 July, 2008. a) The air masses travelled most likely along the jet stream path. The negative numbers indicate hours before sampling. b) Precipitation (blue) and altitude (black) along the trajectories. Trajectory release heights were 11.5, 11.7, and 12.0 km, plume interception was between 11.7 and 11.9 km.**

From above shown data it is not completely clear whether tropospheric and stratospheric air masses had mixed during pollution episode I. According to the vertical profile of the back trajectories, rather air mass uplift into a regime with higher PV occurred than air mass mixing. This hypothesis is supported by the tracer correlation as shown in Figure 46 a). The data points from period I are marked in green and are located along a line with a relatively constant ozone value. Varied ozone mixing ratios would indicate air mass mixing. Also, the probability density functions for the whole flight (Figure 46 (b-d)) indicate that air masses in all three layers have similar properties. For all trace gases, the concentrations from each regime overlap. Especially the ozone trace in the lower stratosphere (green line) should be distinct from the lowermost (blue) trace if stratospheric air had contributed to the measured air mass. Unfortunately, only few data points are available for the layer above the tropopause which results in poor statistics and spikes in the PDF. For acetonitrile, however, the strong enhancement from episode I can clearly be observed from the peak with a probability of around 0.35.

From the above observations it can be concluded that this pollution episode is a case of air mass and aerosol uplift into the tropopause region where irreversible air mass mixing has not (yet) taken place. It is possible that this transport pathway is associated with a jet stream based on the meander as described by the trajectories and as elaborated in Fuelberg et al. (2010). Also, the approximate velocity calculated from the HYSPLIT back trajectories was roughly 40 $m\,s^{-1}$ for the last 24 hours. As troposphere to stratosphere transport at the poleward side along jet streams has been observed earlier (Zahn et al., 2000) it is conceivable that a case of (starting) cross-tropopause-transport was sampled. For a detailed consideration, Figure 47 shows an enlargement from Figure 43 of the respective period when the aircraft flew above the 2 PVU boundary. Additionally, the potential and ambient temperatures are plotted. It can clearly be seen that enhancements of carbon monoxide and organic aerosol are anti-correlated with temperature and the ozone mixing ratio. The potential temperature indicates tropopause properties. After Zahn et al. (2000) this indicates that tropospheric air intruded into lower stratospheric air masses.

Even though no hard evidence for irreversible cross-tropopause-transport can be given for this case it demonstrates nevertheless that uplift of polluted air masses originating from Siberia/East Asia within the Pacific storm track influences the chemical composition in the tropopause and potentially even in the lower stratosphere. It is known that troposphere to stratosphere exchange takes place in this region (Sprenger and Wernli, 2003).

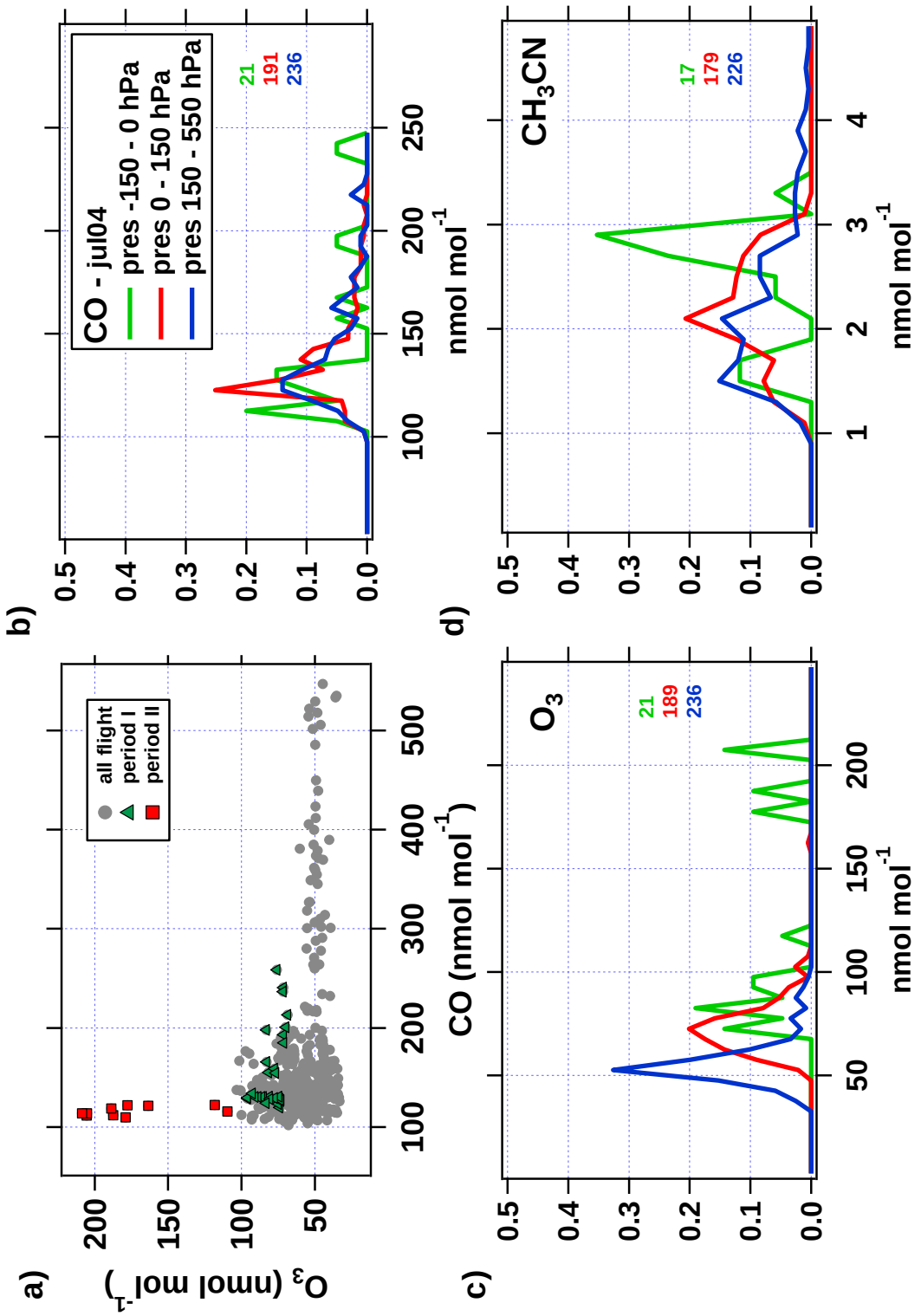


**Figure 46: a) Tracer plot for the whole flight from 4 July, 2008. The data points from episode I are marked by green triangle and from episode II by red squares. The black line guides the eye along a mixing line. b-d) Probability density functions of trace gases CO, $O_3$ and $CH_3CN$ from 550-150 (blue), 150-0 hPa (red) below the 2 PVU boundary, and 0-150 hPa above the 2 PVU isosurface (green line). The colored numbers indicate the number of data points. CO and $O_3$ bin width is 5 nmol $mol^{-1}$ and for acetonitrile 0.2 nmol $mol^{-1}$.**

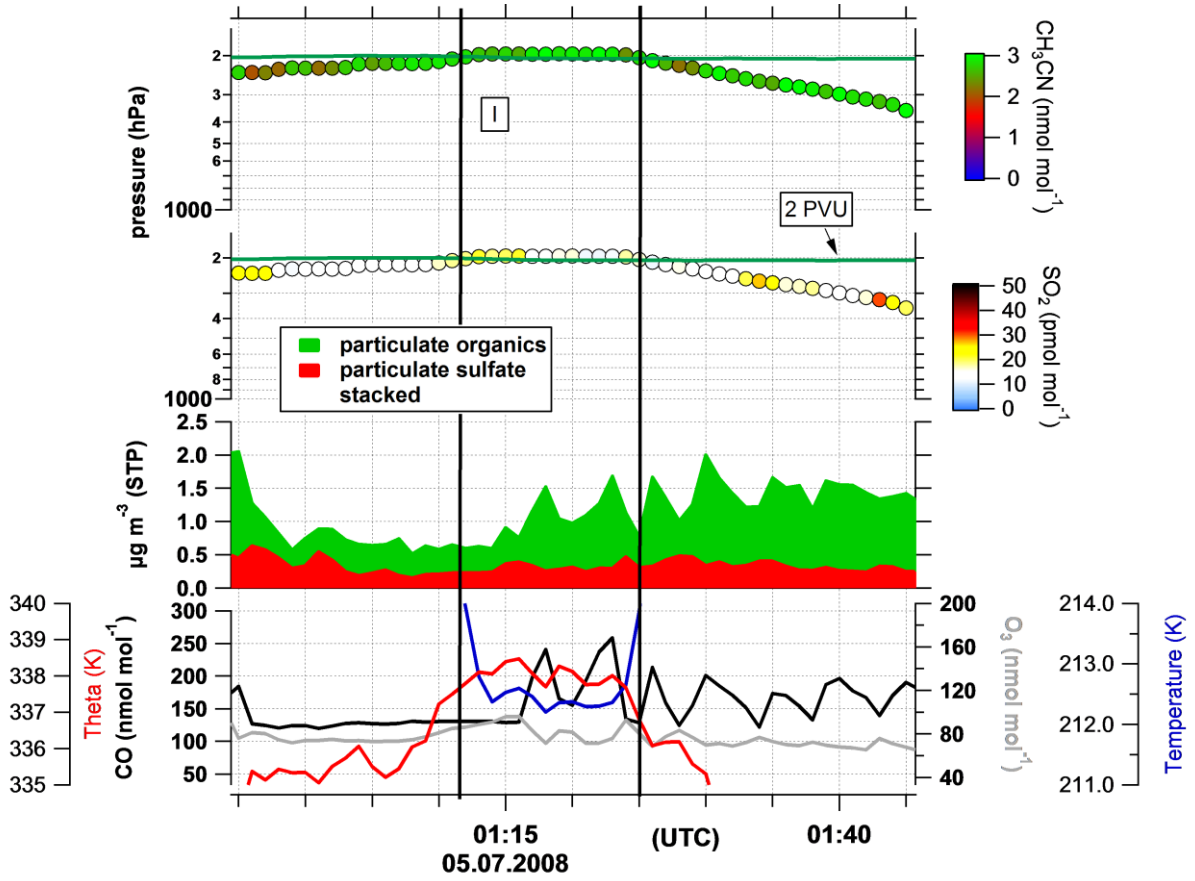


**Figure 47: Enlargement of ARCTAS pollution episode I (01:01 – 01:30, 5 July, 2008). This figure shows the same time series as Figure 43 and additionally the data of static and potential temperatures in blue and red, respectively. The black vertical bars enclose the period when the aircraft flew above the 2 PVU level.**

### *3.2.2 Mixed biomass burning and fossil fuel combustion pollution*

This subsection elaborates three cases of pollution transport: Transport associated with warm conveyor belts out of North America and Siberia/Asia and related precipitation events, and low-level tropospheric advection across the North Atlantic from North America towards southern Greenland.

#### 3.2.2.1 Frontal and warm conveyor belt associated transport out of North America

This pollution episode over the southern coast of Greenland, measured on 8 July, 2008, at 14:52 – 15:02 UTC, is characterised by elevated trace gas mixing ratios with $\Delta O_3$ approximately 45 nmol mol$^{-1}$, and $\Delta$CO at least 27 nmol mol$^{-1}$ (see Plume II in Figure 38). The $\Delta$CO is a lower estimate since internal instrument calibration took place during this period, and so the highest recorded CO value throughout the plume was used as peak value for the calculation. Outside this defined plume period $\Delta$CO is some 60 nmol mol$^{-1}$ assuming 100 nmol mol$^{-1}$ as background value (Figure 38 c). This implies that the event discussed here was embedded in an extensive polluted area. Both aerosol instruments show clear enhancements during the plume encounter compared to the surroundings. The

AMS submicron aerosol mass has a mean of $0.62 \pm 0.35$ µg $m^{-3}$, peaks at 0.96 µg $m^{-3}$, and is composed of 82 ± 14 % organic carbon.

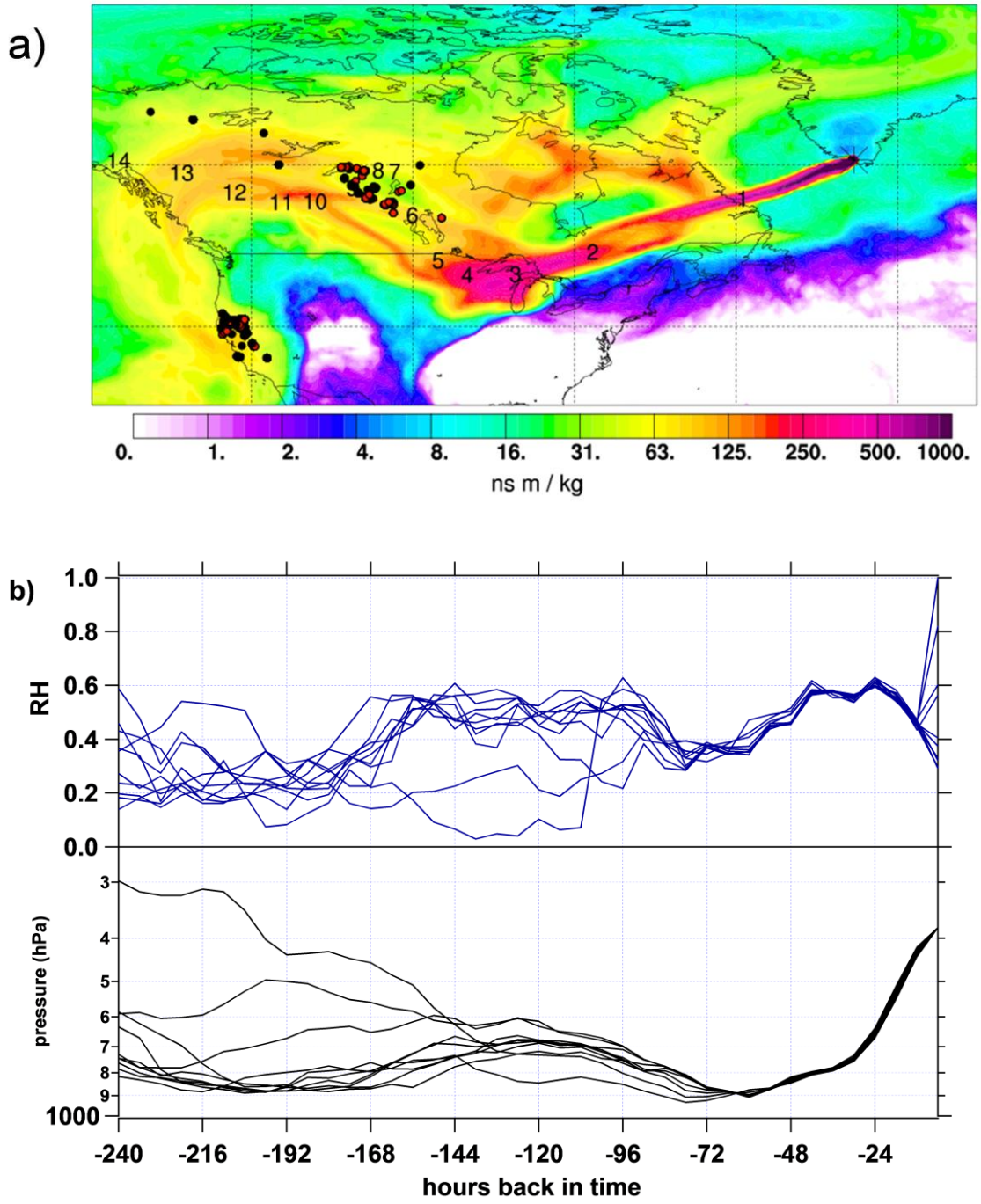


**Figure 48: a) FLEXPART column-integrated emission sensitivity for plume II during the 8 July flight from 14:56:03 – 15:01:40 UTC. b) Pressure and relative humidity along the trajectories as calculated by the OFFLINE model.**

Figure 48 a) shows that this plume is composed of a mixture of anthropogenic emissions from the Great Lakes area and forest fire emissions in Canada and possibly also at the US west coast. Transport times vary significantly depending on the source region: 3-4 days from the Great Lakes, 6-11 days from Canada, and more than 12 days from the west coast. According to the OFFLINE model all

trajectories raised from 900 hPa between 72 and 60 hrs prior to plume detection at 380 hPa (see Figure 48 b). Thus air masses were subject to a strong and rapid uplift within 2 - 3 days and a humidity change in the last 24 hours. In-situ measured relative humidity was between 29 and 32 % in the maximum of the pollution episode and up to 100 % when entering and leaving the plume. A low pressure system travelled from the North American east coast to the west coast of Greenland between 6 and 8 July (Figure 40). The enhanced pollution in the warm sector of the cyclone and the above described trajectory analyses suggest that the pollution plume was carried upwards by a warm conveyor belt (WCB, for details see 1.4). Since condensation and precipitation are widespread and intense within the ascending air masses of a WCB the question arises, how much of the original particulate pollution remains after the transport to the atmosphere above Greenland. The FLEXPART BC tracer ratio indicates (Figure 38 d) that less than 1 % of the aerosol-like tracer arrived at the point of interception which holds for the entire flight. The detection of Plume II, however, shows that aerosol wash-out in a WCB is not complete which was also observed by Park et al. (2005) for Asian outflow and Roiger et al. (2011) during POLARCAT-Grace which took place at the same time as POLARCAT-France. Also note that the ozone mixing ratio is strongly elevated for the duration of the plume. FLEXPART stratospheric air mass contribution is however < 5 % which is in good agreement with the history of the air mass (Figure 48 b). In theory, the enhancement of 45 nmol mol$^{-1}$ can thus be related to photochemical ozone production within this mixed BB and FF plume. Model calculations of photochemical $O_3$ production within 5 days in an Alaskan BB plume travelling towards Europe performed with CiTTyCAT resulted in an enhancement of 17 nmol mol$^{-1}$ (Real et al., 2007). [This paragraph is adapted from Schmale et al. (2011).]

#### 3.2.2.2 Strong wash-out during tropospheric transport from Siberia

The previous case gave an example of incomplete wash-out during rapid air mass uplifting in a warm conveyor belt. This episode shows a case of strong wash-out. Plume III (see Figure 39) was intercepted on 13 July, 2008, at 5.7 km over Baffin Bay. The CO mixing ratio is enhanced with 154 nmol mol$^{-1}$ on average with a ΔCO of 30 nmol mol$^{-1}$, while the $O_3$ mixing ratio drops to 61 nmol mol$^{-1}$, still slightly elevated, corresponding to a $\Delta O_3$ of -24 nmol mol$^{-1}$. Both aerosol instruments detect little signal. AMS aerosol total mass is 0.26 ± 0.26 µg m$^{-3}$.

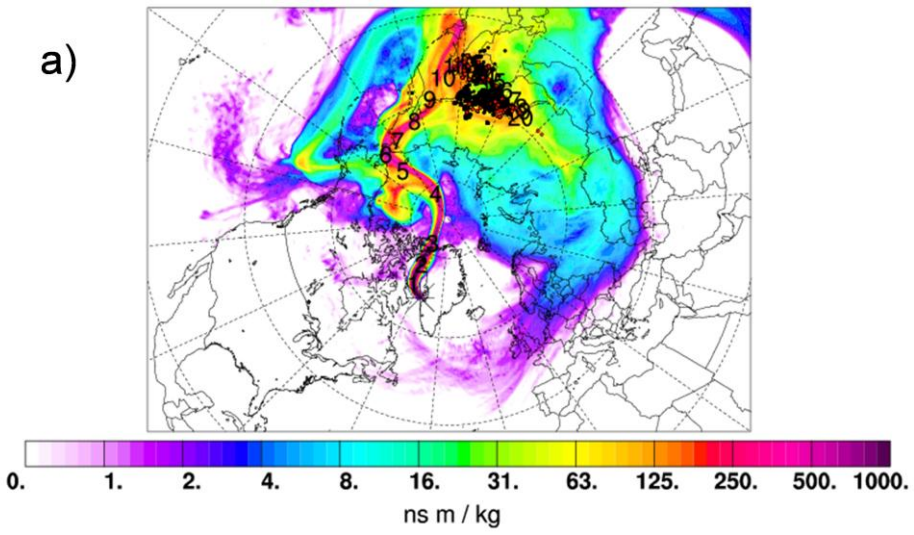

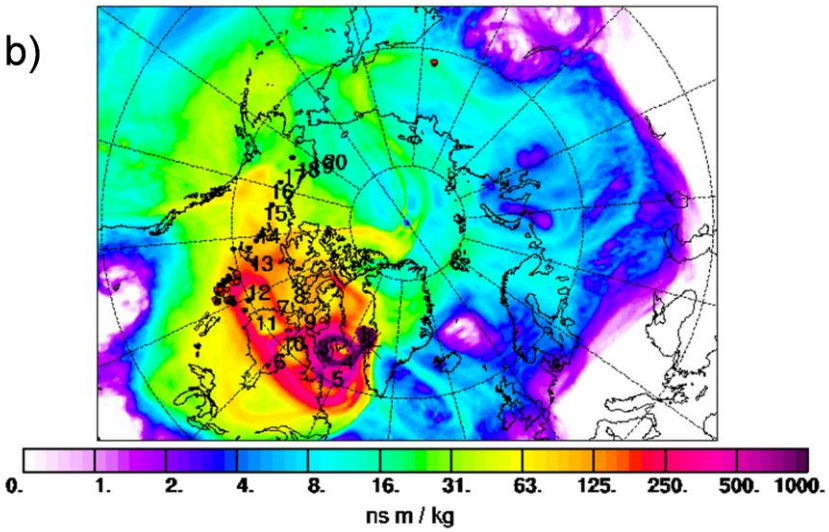


**Figure 49: a) FLEXPART column-integrated emission sensitivity for Plume III from 20:02:51 – 20:03:31 UTC on 13 July, 2008. Contributions from Siberian BB and Asian FF can be observed. b) Origin of air masses for Plume $III_{ref}$ from 18:22:52 – 18:24:00 UTC on 13 July, 2008, is primarily Canadian BB.**

However, the air mass is clearly influenced by Siberian BB and Asian FF according to the FLEXPART column-integrated emission sensitivity (Figure 49 a). The CO fire passive tracer indicates between 80 and 90 % BB influence. The combination of the elevated CO mixing ratio and the very low signal intensity for aerosol detection suggests that this is a case of aerosol wash-out. It is conceivable that the gas phase pollution tracer CO remained elevated after transport from East Asia and Siberia while particles were deposited en-route. To verify this hypothesis a reference period (marked $III_{ref}$ in Figure 39) with a similar CO mixing ratio of 151 nmol $mol^{-1}$ was chosen with an aerosol mass of 1.24 ± 0.40 µg $m^{-3}$. This plume corresponds primarily to Canadian BB and some US anthropogenic emissions (Figure 49 b). Meteorological field data along the trajectories for both periods were calculated with LAGRANTO. In Figure 50 a) it is clearly visible from the cloud cover and precipitation that aerosol wash-out happened around 110 to 70 hours prior to interception during air mass uplift which is most likely associated to a WCB. FLEXPART calculations (not shown) of relative humidity along the most probable mean pathway for this period indicate the same. The back trajectories of the reference period (Figure 50 b) only pass through a period of elevated cloud cover 100 to 80 hours before the encounter with much less probability for scavenging (see precipitation columns in Figure 50 b). The corresponding aerosol concentration is rather high within the context of measurements above Greenland. [This paragraph is adapted from Schmale et al. (2011).]

From the above discussed cases Plume II and III including the reference period two conclusions can be drawn. First, WCB transport is associated with precipitation during which aerosol might be washed-out to large extents which, however, is not necessarily always the case. Second, relating CO mixing ratio elevations to aerosol concentrations after long-range transport becomes difficult. Particulate matter is subject to aqueous removal processes while CO, with a lifetime of several weeks, is more likely to be preserved.

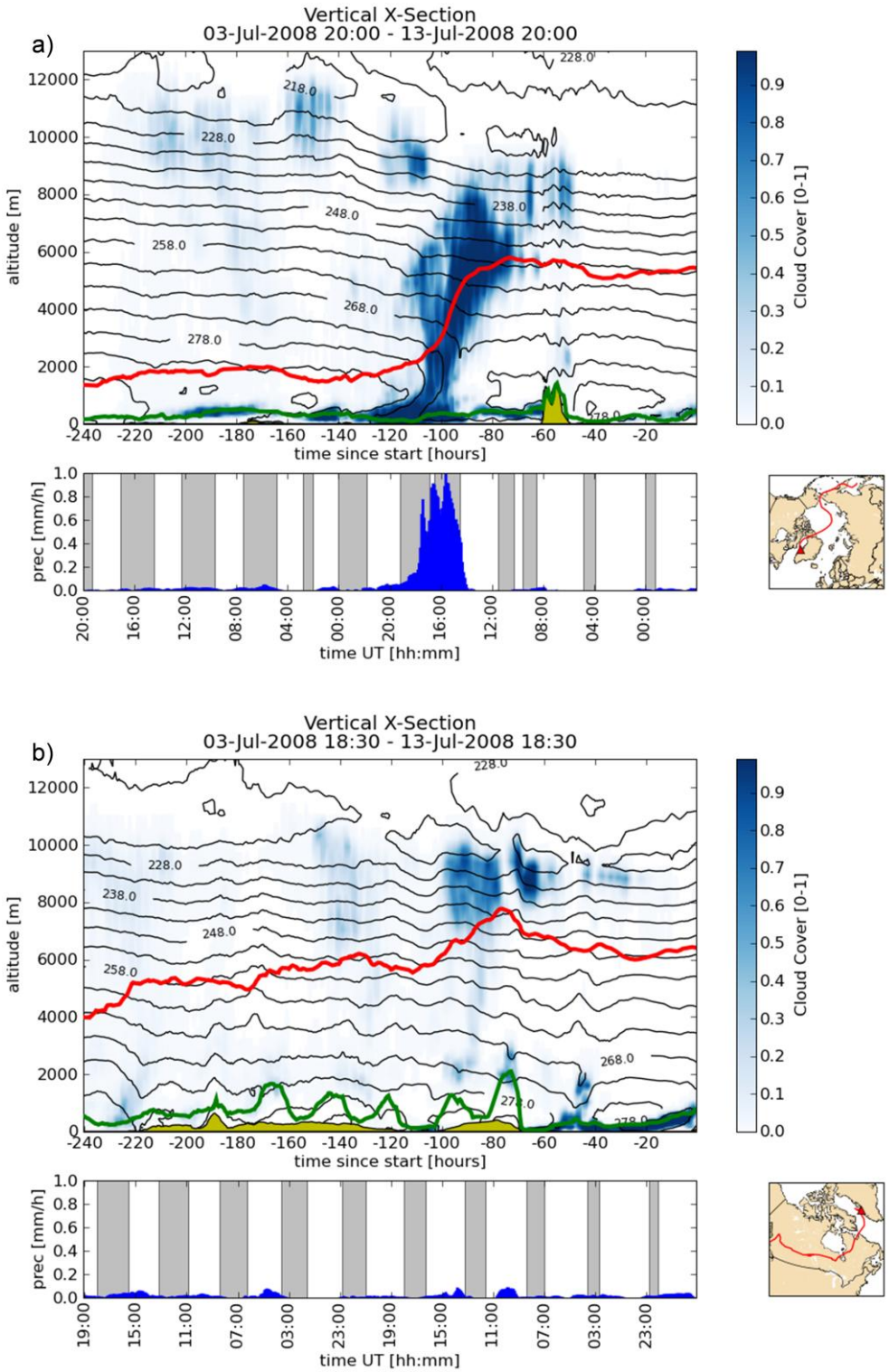


**Figure 50: Median values of the meteorological field data along the LAGRANTO-trajectories, released on 13 July, 2008, between 19:58:20 – 20:02:00 (a) and 18:26:40 – 18:28:24 (b). Blue shades indicate cloud cover, black contour lines temperature, the green line the boundary layer height, the yellow pattern the orography as given by the ECMWF data, and the red line the median position of the trajectory ensemble. The lower panel shows median precipitation values at the surface (blue columns) and night times along the trajectory pathway (grey shade). [This figure was published in Schmale et al. (2011).]**

### 3.2.2.3 Low-level transport out of North America

Plume IV was encountered on 8 July, 2008, at the same latitudinal and longitudinal coordinates as Plume II (Figure 38), however during the descent to Narsarsuaq, southern Greenland, between 3.0 and 2.1 km altitude. In-situ measurements and observations indicate high relative humidity and the presence of clouds. Gas phase parameters do not show a signature which can be identified as pollution. However, both aerosol instruments indicate a clearly defined particle plume. Organic matter increases steeply from below detection limit to 0.49 µg $m^{-3}$ until 15:44 UTC, while particulate sulfate peaks around 15:48 UTC with 0.39 µg $m^{-3}$. The subsequent occurrence of peaks suggests that there are two distinct emission sources intermingled in the 10 minute measurement interval within 60 km. The FLEXPART column-integrated emission sensitivity (Figure 51 a and b) suggests that the first part is influenced by Canadian BB, whereas during the second part the source region shifts south to more anthropogenic sources such as the Great Lakes area and the Ohio Valley. The figure nicely shows the presence of two "streams" from the different source regions that unite near Narsarsuaq. The latter region is known for its steel plants and thus coal combustion activities which may explain the high contribution of sulfate aerosol to this plume. The ratio of FLEXPART $SO_2$ and CO passive tracers is significantly higher during this episode than during the rest of the flight (not shown). The FLEXPART CO fire tracer contributes less than 5 % during this episode to the total CO. Also note that the SMPS measured less particle volume in the accumulation mode during the high sulfate period compared to, for example, Plume I. This possibly indicates that less BC particles were involved in the anthropogenic plume than in the BB event resulting in a lower SMPS signal intensity as it measures both refractory and non-refractory aerosol while the AMS only detects non-refractory particles. Transport times were longer than one week for the BB contributions, and between 5 – 8 days for FF (Figure 51 a), b). Based on the OFFLINE model (Figure 52), the BB air mass trajectories were uplifted from approximately 800 hPa to 550 hPa after passing over the fires and then descended slowly within 42 hours to 700 hPa before detection over Greenland. The FF trajectories picked up pollution between 1000 and 850 hPa before transport at low level towards Greenland where they were measured between 840 and 710 hPa. Even though Plume IV was encountered at the same horizontal coordinates as Plume II it is unlikely that the same air mass was sampled. Plume II was located in the WCB outflow while Plume IV was detected below.

**Figure 51 (next page): a) Plume IV, 15:39:35 – 15:44:16 UTC on 8 July, 2008, presents BB influence from Canada and FF contribution from the Great Lakes area. b) Plume IV, 15:46:08 – 15:46:43 UTC, 8 July, 2008, shows contributions of FF from the Ohio Valley and Great Lakes area and some BB influence from Canada. [This figure was published in Schmale et al. (2011).]**

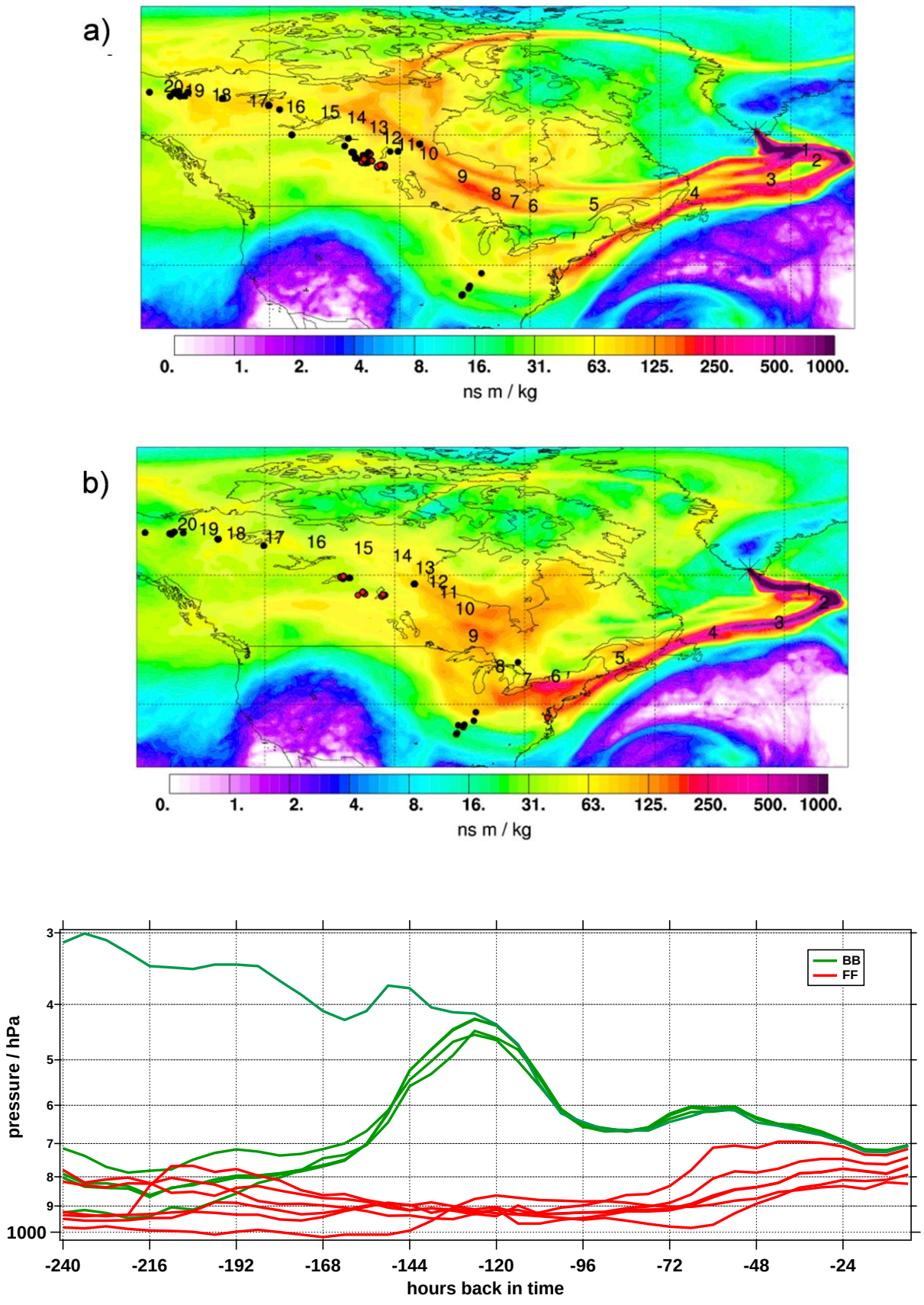


**Figure 52: OFFLINE model back trajectories for Plume IV from 15:40 to 15:50 UTC on 8 July, 2008.**

Such low tropospheric aerosol transport in high latitudes can have a great impact low-level Arctic cloud properties. Mauritsen et al. (2011) conducted a modeling study based on measurement results on how pollution aerosol acts in a CCN-limited cloud-aerosol regime. Over the Arctic Ocean, often not enough CCN are available to form clouds due to previous effective scavenging. With particle advection from emission source regions CCN might become more abundant. The authors found that during high summer season if more CCN are available the shortwave cooling effect might be more enhanced than longwave emissivity. The resulting effect depends strongly on the surface reflectivity. In late summer and early fall the dominant effect is assumed to be warming. Based on this study, the above described pollution aerosol transport might have important implications. Also, it is almost certain that the particles will get into contact with the surface near the sampling location and contribute to the acidification of the region. In chapter 4 the issue of particle deposition on Greenland is discussed in more detail.

### *3.2.3 Fossil fuel combustion dominated pollution plumes*

After having focused on pollution episodes which were characterized by both, biomass burning and fossil fuel combustion, this section introduces three plumes featuring mainly anthropogenic signatures. The first example is a complex case of a stratospheric air intrusion that was worthwhile to investigate further by model calculations using the Cambridge tropospheric photochemical box model CiTTyCAT. The second case discusses the uplift of Asian FF plumes to the tropopause as observed during ARCTAS and the third case shows that pollution from North America is not only transported towards Greenland but also continues to travel towards Europe.

#### 3.2.3.1 Stratospheric intrusion into East Asian pollution

Plume V (see Figure 39) was encountered on 13 July, 2008, over Baffin Bay at 7.3 km altitude between 18:42 and 19:06 UTC. The ozone mixing ratio is clearly enhanced with 145 nmol $mol^{-1}$ with $\Delta O_3$ being 50 nmol $mol^{-1}$. CO stays relatively low at 95 nmol $mol^{-1}$ on average with a $\Delta CO$ of -16 nmol $mol^{-1}$. It is conceivable that elevated plume CO concentrations might have been diluted by the mixing of the CO rich tropospheric and CO poor stratospheric air masses in this case. The SMPS shows an enhanced signal of up to 0.25 $\mu m^3$ $cm^{-3}$ for accumulation mode particles, and AMS total mass has a mean of $0.98 \pm 0.40$ $\mu g\ m^{-3}$, 1.45 times higher than the average of plumes encountered during the POLARCAT campaign. The fraction of organic mass is $52 \pm 22$ %. According to the FLEXPART column-integrated emission sensitivity (Figure 53 a), the sampled air masses arrived from Siberia (BB) and East Asia (FF from the Beijing area, Korea and Japan). The FLEXPART CO passive fire tracer contribution ranges between 54 and 90 % of the total CO contribution during this episode (Figure 39 c). This is only partly consistent with the AMS findings since the large fraction of particulate sulfate ($48 \pm 22$ %) reflects rather FF contribution than BB. This is an important observation which should be kept in mind at all times when working with trajectories or particle dispersion techniques to determine air mass origins and emission sources. These tools provide great facilities without which these plume analyses would not have been possible. Nevertheless, the model results remain subject to uncertainties. Especially with respect to particulate matter as opposed to gaseous tracers they still have major drawbacks as no chemical scheme is applied which reflects the formation and growing of particles. Dry and wet deposition schemes are available, however they

overestimate removal effects as discussed in section 2.6.3. The plume age varied over the sampling period from about 11 to 16 days (Figure 53 a). Air masses extending over the middle and upper troposphere (300 and 800 hPa, see Figure 53 a) moved from southern Siberia and East Asia over the North Pole towards Greenland. Sodemann et al. (2010) analyzed the performance of different models including FLEXPART with regard to cross-polar transport. They found that the Lagrangian particle dispersion model is trustworthy for such special cases of long-range transport. 72 hours prior to encounter all trajectories were above 430 hPa at 79°N from where they travelled south to the point of interception. According to the CO forward simulated passive tracer cross section (Figure 53 b) the aircraft flew through the maximum of the plume. Even though the modelled 2 PVU isosurface (red line in Figure 53 b) is located at roughly 9 km the high ozone mixing ratio suggests that this plume was probed in the upper troposphere with stratospheric air mass influence. FLEXPART calculations show a contribution of 20 to 25 % of stratospheric air masses for this period (not shown).

This pollution episode might be related to the case study described by Roiger et al. (2011) as back trajectory analysis with the OFFLINE model suggests. While the latitudinal coordinates coincide very well, there is a difference in roughly 5° longitude (ca. 200 km) and up to 200 hPa in the vertical. Roiger et al. (2011) discuss in detail how East Asian anthropogenic pollution was strongly and rapidly uplifted near the east coast of Russia and entered the Arctic lowermost stratosphere before it travelled across the North Pole towards Greenland where it was sampled on 10 July at 11.3 km altitude. The chemical in-situ data with up to 138 nmol $mol^{-1}$ CO and 100 nmol $mol^{-1}$ $O_3$ indicate a strong tropospheric influence in the lowermost stratosphere. Even though according to the trajectories the ATR-42 might have sampled the same plume 3 days later the trace gas data behave in rather opposite ways. As mentioned above, in Plume V the CO mixing ratio was slightly below tropospheric background with 95 nmol $mol^{-1}$ and $O_3$ was clearly elevated with 145 nmol $mol^{-1}$. It is possible that the ATR-42 probed a segment of the plume which had undergone further mixing within the past 72 hours. However, based on the available data an unambiguous linkage between these two cases cannot be established. [This paragraph is adapted from Schmale et al. (2011).]

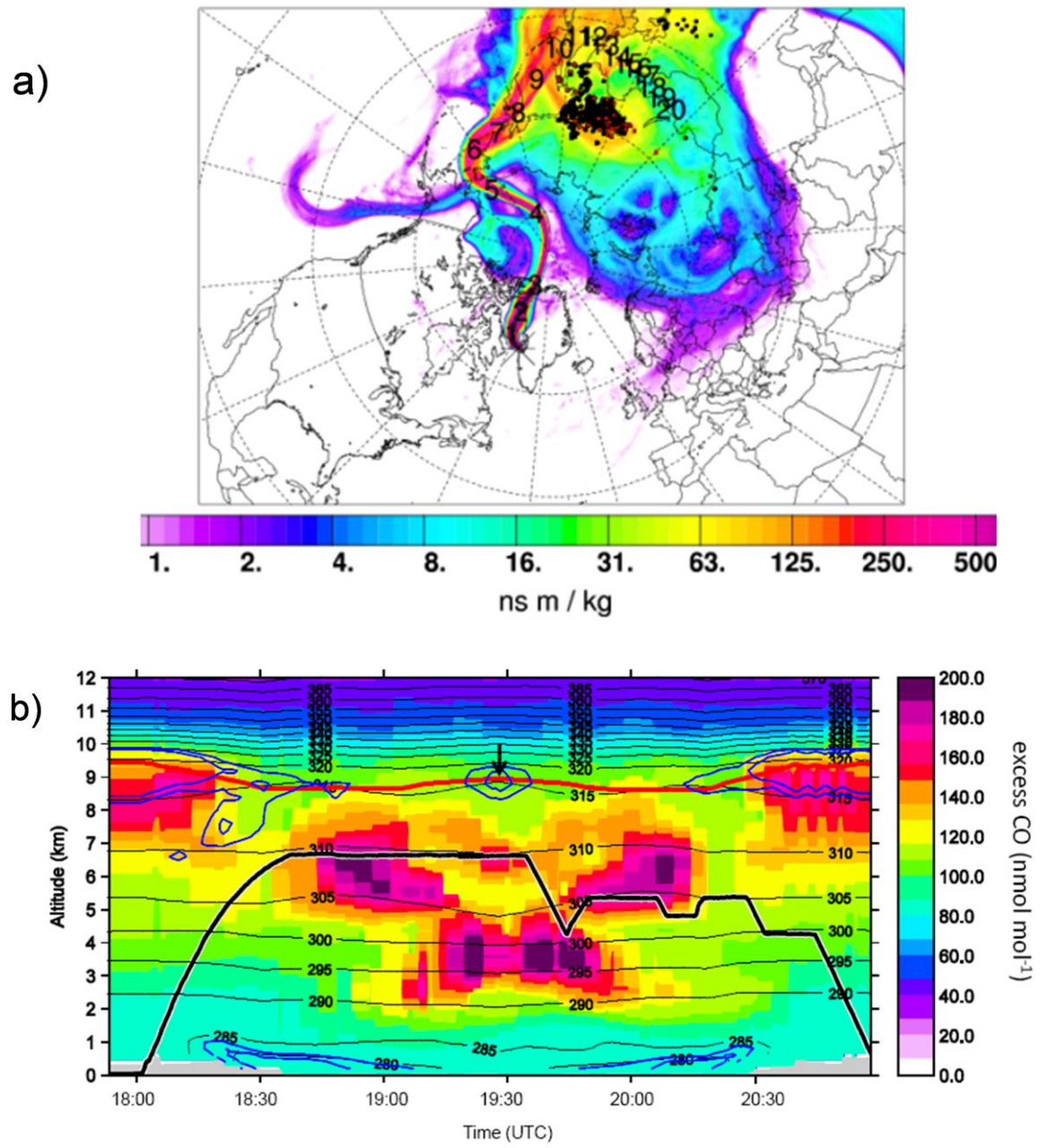


**Figure 53: a) FLEXPART column-integrated emission sensitivity for Plume V on 13 July, 2008, from 18:41:32 – 18:44:54 UTC. The air mass is influenced by FF from East Asia and BB in Siberia. b) FLEXPART calculations of excess CO passive tracer concentration in nmol mol$^{-1}$ along the flight track (thick black line). The thin black lines indicate potential temperature in K, the thick red line denotes the 2 PVU isosurface, the thin blue contours show 80 and 90 % relative humidity. The arrow indicates the turning point. [This figure was published in Schmale et al. (2011).]**

Nevertheless, both cases are examples showing that East Asian/Siberian pollution can be transported across the tropopause and significantly influence the chemical composition of the lowermost Arctic stratosphere. While the work by Roiger et al. (2011) focuses on gaseous tracers, the following chapter will study the implications for the formation of particulate matter, i.e. sulfate, when polluted tropospheric and stratospheric air masses mix.

#### 3.2.3.2 Modeling study – Does mixing of stratospheric and tropospheric polluted air masses enhance particulate sulfate production?

The case described in the previous section 3.2.3.1 raises the question whether the pronounced and long lasting enhancement of particulate sulfate in association with elevated ozone mixing ratios was the result of the mixing of polluted tropospheric and stratospheric air masses. In the following the episode is characterized in detail to gain more information on the processes preceding the measurement. Figure 54 a) shows a zoom into the time series of the flight for the respective period which is encompassed by the two vertical black bars. The uppermost panel illustrates that while flying at the same pressure (altitude) the potential temperature slightly decreases during the interval in question. This might be an indication for colder stratospheric air mass contribution. Also, the specific humidity $q$ in the middle panel (blue line) decreases and the ozone mixing ratio increases (grey trace in lowermost panel) which represent stratospheric properties. The CO mixing ratio clearly decreases. The figure also shows that the particulate sulfate concentration is markedly enhanced between the two black bars. Zahn et al. (2000) found in a case of troposphere to stratosphere exchange during a CARIBIC flight that nucleation mode particles were present in the mixed air masses. For this case however, no nucleation mode particles could be observed in the available SMPS data (see Figure 54 b). There is a first mode peak near 60 nm in the particle number size distribution and potentially a second mode near 90 nm and a third mode close to 110 nm. So at least there has not been any particle formation event close to the encounter. It is however possible that particle nucleation happened earlier and particles grew so that only accumulation mode particles could be observed which lead to the detection of enhanced particle mass by the AMS.

To verify the hypothesis of a stratospheric intrusion the ozone mixing ratio was plotted against carbon monoxide (Figure 55, grey points). The particulate sulfate data is represented by the color-coded triangles and the plume interval is marked by squares. The graph clearly shows that the data points are located in the stratospheric branch of the tracer space and also that the highest particulate sulfate concentrations can be found there. Unfortunately, all points of interest assemble in a cloud without a clear trend. The encountered ozone values are not high enough to draw a mixing line that would allow estimating the fractional contribution of each regime estimated.

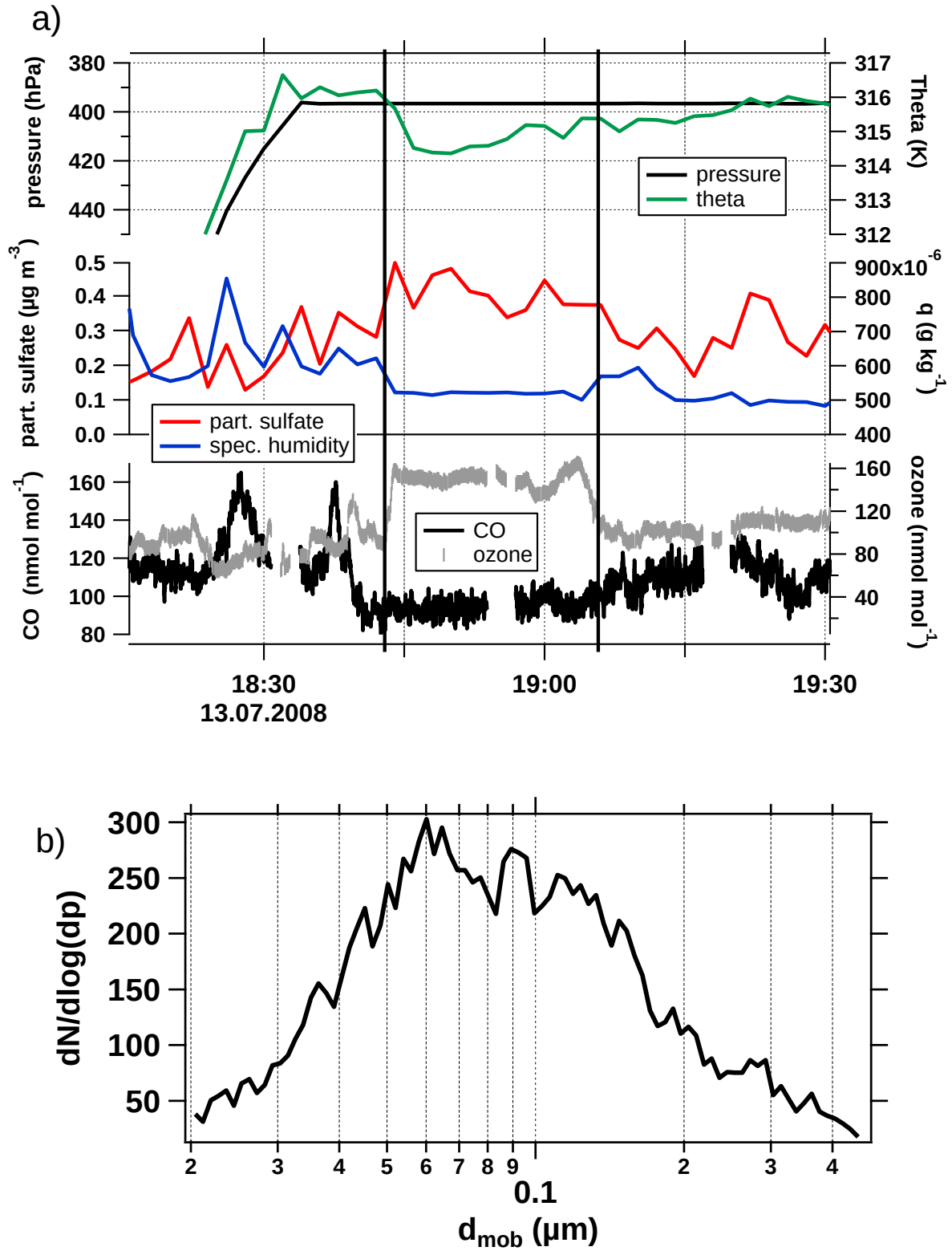


**Figure 54: a) Time series of several parameters during the encounter of Plume V on 13 July, 2008. b) Particle number size distribution for Plume V.**

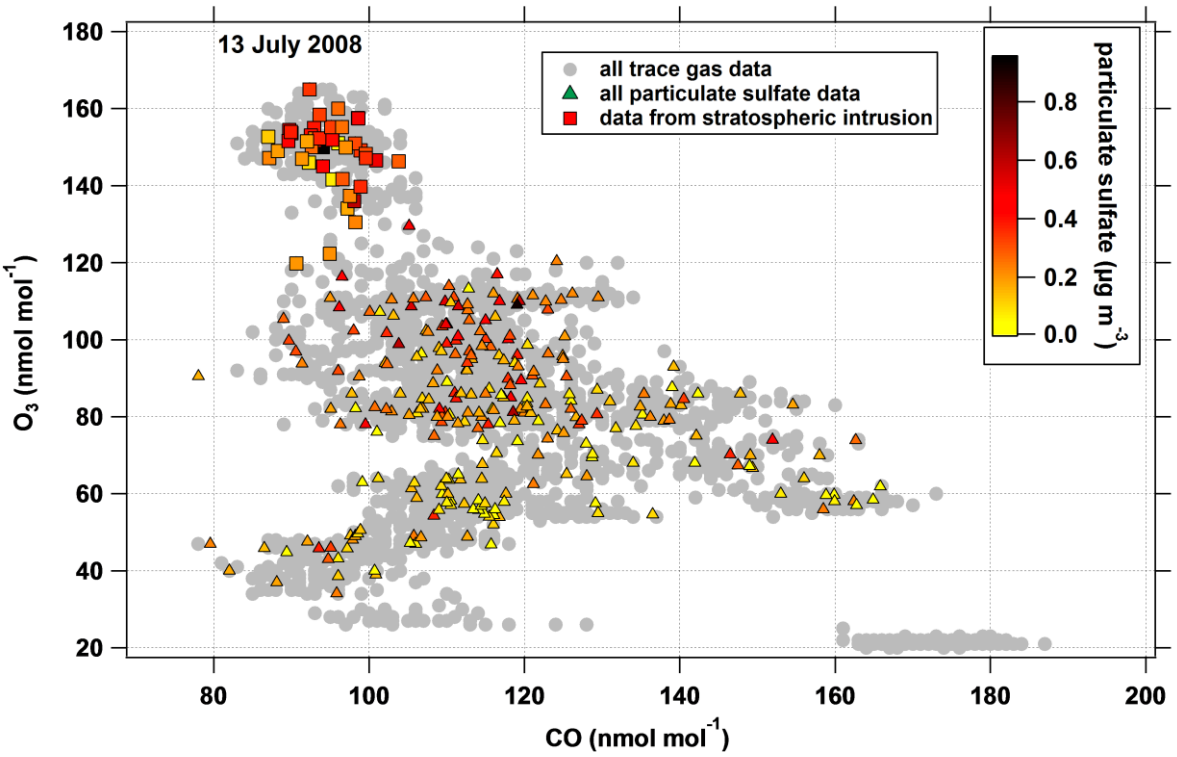


**Figure 55: Tracer plot ($O_3$ versus CO) for the flight on 13 July, 2008. The grey points show all one second trace gas data while the triangles show the averaged 2 minutes time resolution data color-coded by the mass concentration of particulate sulfate for the whole flight. The rectangles highlight the data points during the Plume V episode.**

Another question, especially with regard to the following modeling study, is the time frame during which mixing of the air masses took place. Generally, there is no established literature value but a period of 96 hours has been suggested by Sprenger and Wernli (2003) for troposphere to stratosphere mixing and vice versa. In this case, the only means at hand are the OFFLINE back trajectories as presented in Figure 56. Ambient pressure along the trajectories (panel a) shows that air masses from a wide range within the troposphere ascended and a few from the LS descended to constant level prior to the encounter. Between four and three days earlier the wide range narrows down to values near 400 hPa. The potential temperature (panel b) also covers a wide span of values, however, there seems to be a decreasing trend. Based on the specific humidity (panel c), two streams of water vapor rich and poor air masses come together about three days before the encounter. According to the PV values (panel d) the majority of air masses originated in the troposphere while only three trajectories show values higher than 2 PVU.

From all the above considerations it can be concluded that the encountered air mass was a mixture of stratospheric air intruding into ascending tropospheric air masses. Therefore, properties from both regimes can be found which explains the high ozone mixing ratio and the relatively high level CO concentration. For the modeling study with CiTTyCAT it is assumed that the air masses had mixed during three to four days prior to the encounter.

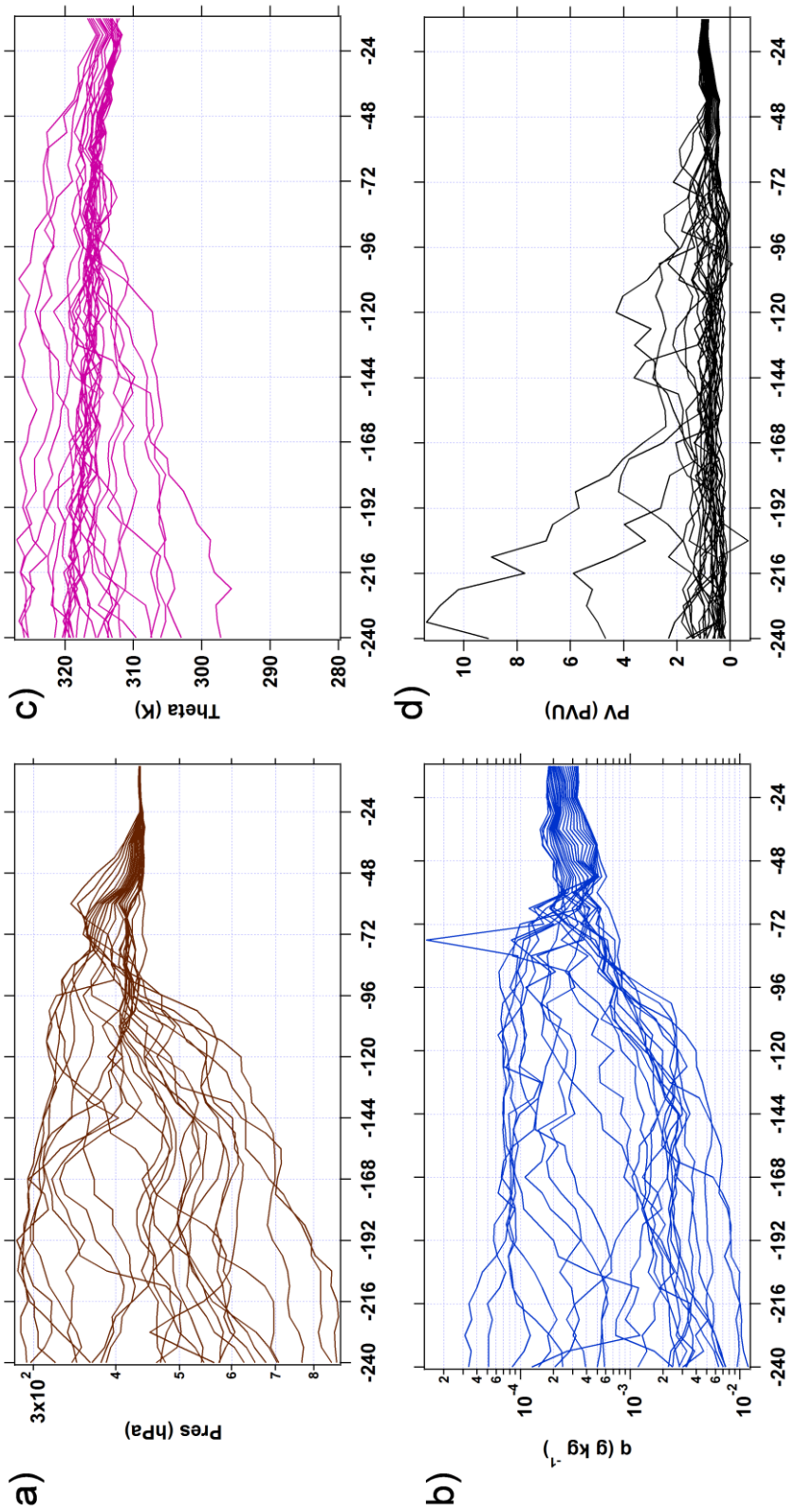


**Figure 56: OFFLINE model back trajectories for 13 July, 2008, from 18:42 – 19:06. The horizontal axis denotes hours prior to interception. On the vertical axes (a) pressure, (b) potential temperature, (c) specific humidity (q) and (d) potential vorticity (PVU in $10^{-6}$ $m^2$ $kg^{-1}$ $s^{-1}$) derived from ECMWF analysis data are displayed.**

Based on the above, the box model CiTTyCAT was run trying to answer the question whether the particulate sulfate enhancement is due to the air mass mixing or if it is simply a result of tropospheric heterogeneous chemistry during long-range transport coinciding with a stratospheric air mass intrusion. A basic scenario was designed for exploring the production of sulfuric acid from $SO_2$ in a fixed box without any interaction with the surroundings. Chemical reactions are run in an air parcel without any particulate sulfate but with a certain amount of $SO_2$. Sulfuric acid is formed through photochemical reactions and is assumed to condense completely into the particle phase and thus represents the mass of particulate sulfate ($SO_4^{2-}$ with 96 g $mol^{-1}$). Both tropospheric and stratospheric properties are attributed to the air parcel to simulate the irreversible mixing. The hypothesis is that $SO_2$ is converted more efficiently when humid (tropospheric) and ozone rich (stratospheric) air masses mix due to the formation of OH radicals. Another reason, why it is hypothesized that particulate sulfate is produces during such mixing events is that the overall available particulate surface area is reduced. If little surface area is present the sulfuric acid vapor condenses only to a very small degree onto pre-existing particles which leads to enhanced nucleation, if temperatures are low enough (Khosrawi and Konopka, 2003) Here, only chemical reactions are considered because no aerosol scheme was coupled to CiTTyCAT. The main reactions have been introduced in section 2.6.6. As the outcome depends strongly on the input parameters, mixing ratios of $SO_2$, $O_3$ and water vapor as a function of relative humidity at a fixed temperature were varied. Pressure and temperature were taken from in-situ measurements and one run was repeated at 10 K higher temperature. Other important input parameters are the amount of volatile organic compounds, NO and $NO_2$ which were taken from the ARCTAS-summer tropospheric background measurements (see Appendix E). The background is defined as described in section 2.7.3. CO was set to 95 nmol $mol^{-1}$ as given by in-situ measurements. The model was run at the coordinates of interception for a total of 10 days starting 10 days prior to the plume encounter to simulate the respective photochemistry. Table 14 shows the values of the respective parameters.

**Table 14: Input parameters for the CiTTyCAT fixed box run**

| **Parameter** | **Range / value** | **unit** |
|---|---|---|
| Pressure | 397 | hPa |
| Temperature | 240.8, 250.8 | K |
| Relative humidity (Specific humidity) | 10 ($6.30*10^{-5}$), 30 ($1.89*10^{-4}$), 50 ($3.15*10^{-4}$), 70 ($4.41*10^{-4}$), 90 ($5.67*10^{-4}$) | % and (g $kg^{-1}$) |
| $SO_2$ | 10 – 800 | pmol $mol^{-1}$ |
| $O_3$ | 50 – 290 | nmol $mol^{-1}$ |
| CO | 95 | nmol $mol^{-1}$ |

In the following only main results concerning the production of sulfuric acid are discussed. Details regarding the behavior of input species, intermediate products and sensitivity runs are presented in Appendix E.

Figure 57 (a-f) shows the concentration of particulate sulfate that results from $SO_2$ oxidation to sulfuric acid after 4 days. This period of time was chosen based on the merging of trajectories prior to the encounter (see Figure 56). The grey image shows the concentration of sulfate as a function of the $SO_2$ and $O_3$ mixing ratios. An average of 0.41 µg $m^{-3}$ particulate sulfate was measured during the Plume V episode. Assuming a generous uncertainty of a factor of 2 for the AMS measurements a range of values between 0.2 and 0.8 µg $m^{-3}$ can be assumed to match the observations. This interval is highlighted by the blue to red colored area. The results for 5 different relative humidity values are presented (panels a-e). The red dashed box indicates a realistic range of ozone and sulfur dioxide concentrations as derived from ARTACS-summer data vertical profiles (see Figure 73). Above 2 PVU no more than 100 pmol $mol^{-1}$ $SO_2$ were found and ozone values near the tropopause did not exceed 200 nmol $mol^{-1}$. At the upper right corner of this box the particulate sulfate concentration as generated by CiTTyCAT is indicated reflecting the maximum extreme value. All six panels show that not enough mass is produced in this scenario even when increasing the temperature by 10 K and assuming a high relative humidity of 90 % (panel f). A maximum of 0.15 µg $m^{-3}$ is reached at these conditions. Since an average of about 80 % RH within a range from 76 to 86 % RH were observed in-situ panel d) with 70 % RH was used as a base case for the following considerations. In theory, 90 % RH could also have been chosen. It can be found when moving along the vertical red dashed line that higher ozone availability results in only minor particulate sulfate enhancement after 4 days. At 100 nmol $mol^{-1}$ about 0.05 µg $m^{-3}$ are produced while at the measured ozone mixing ratio of roughly 160 nmol $mol^{-1}$ only an additional 0.02 µg $m^{-3}$ are obtained (0.04 µg $m^{-3}$ for 90 % RH). Furthermore, a difference of 0.02 µg $m^{-3}$ particulate sulfate could not have been detected because the detection limit for this flight was 0.10 µg $m^{-3}$ for 2 minutes resolution data. However, the calculations show that the more humid and the richer in ozone the air mass, the higher is the amount of chemically produced particulate sulfate. At higher ozone abundances more $O^1D$ can photolytically be formed that reacts with water vapor to OH. OH is also produced from photolytic reactions of water. Temperature is important for the formation of $HOSO_2$ from $SO_2$ and subsequent oxidation to $SO_3$ (see reactions R1-R8 in section 2.6.6).

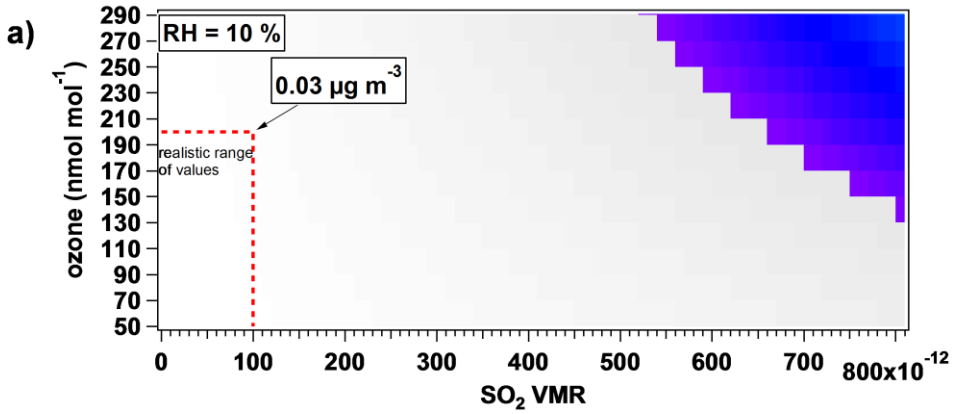

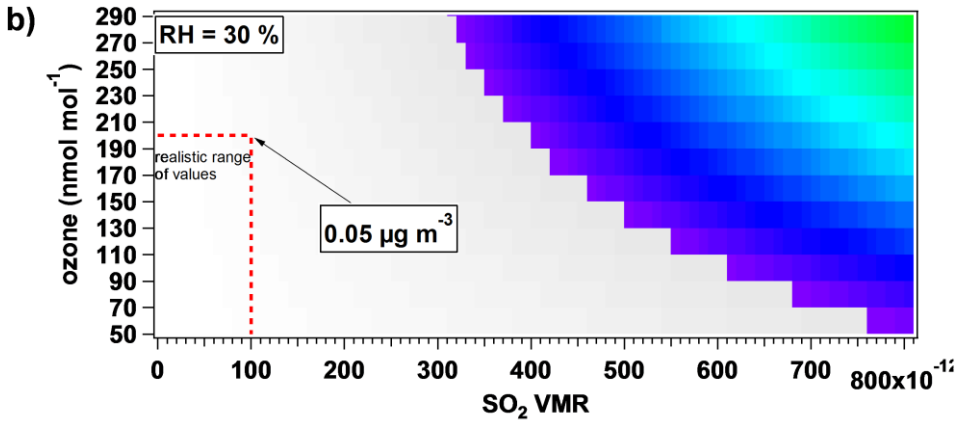
b)
RH = 30 %
realistic range of values
0.05 µg m-3
ozone (nmol mol-1)
290
270
250
230
210
190
170
150
130
110
90
70
50
0
100
200
300
400
500
600
700
800x10-12
SO2 VMR

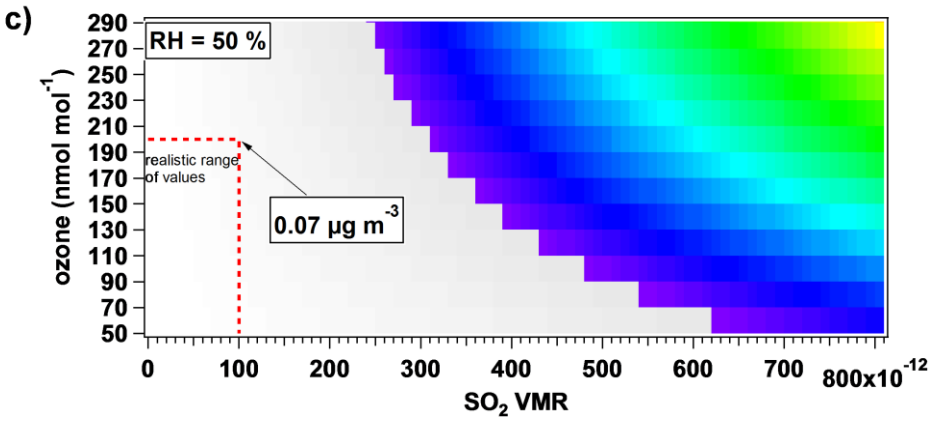
c)
RH = 50 %
realistic range of values
0.07 µg m-3
ozone (nmol mol-1)
290
270
250
230
210
190
170
150
130
110
90
70
50
0
100
200
300
400
500
600
700
800x10-12
SO2 VMR

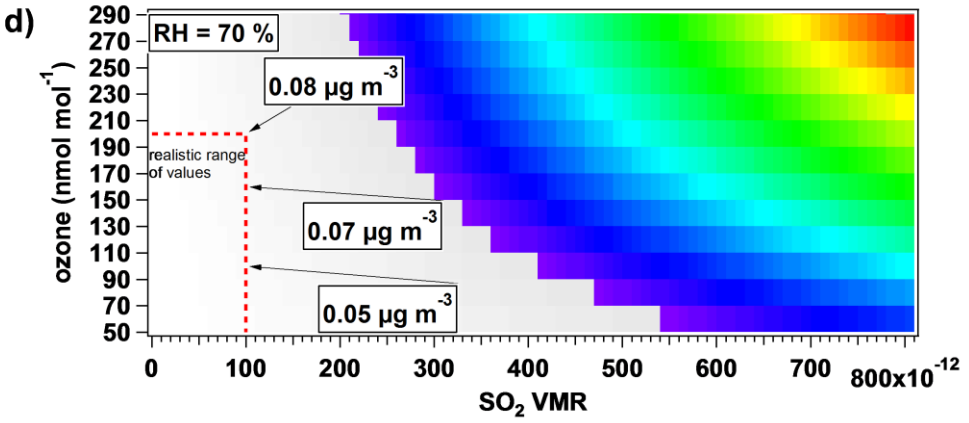
d)
RH = 70 %
0.08 µg m-3
realistic range of values
0.07 µg m-3
0.05 µg m-3
ozone (nmol mol-1)
290
270
250
230
210
190
170
150
130
110
90
70
50
0
100
200
300
400
500
600
700
800x10-12
SO2 VMR

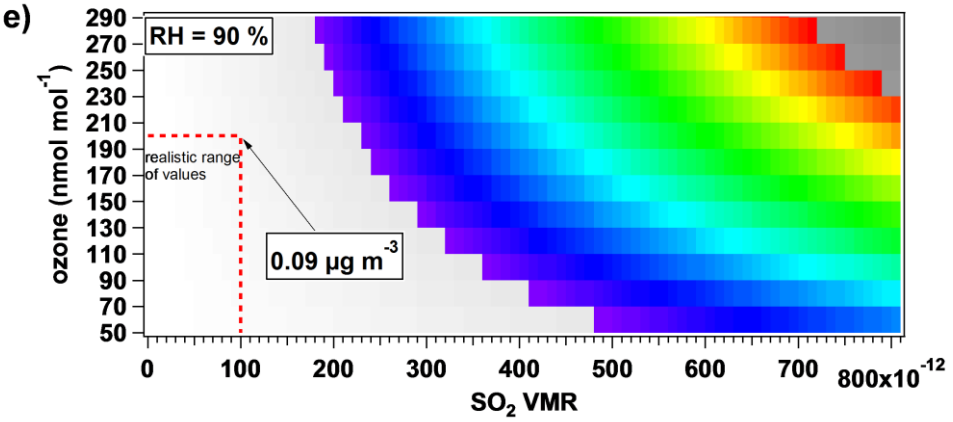
e)
RH = 90 %
realistic range of values
0.09 µg m-3
ozone (nmol mol-1)
290
270
250
230
210
190
170
150
130
110
90
70
50
0
100
200
300
400
500
600
700
800x10-12
SO2 VMR

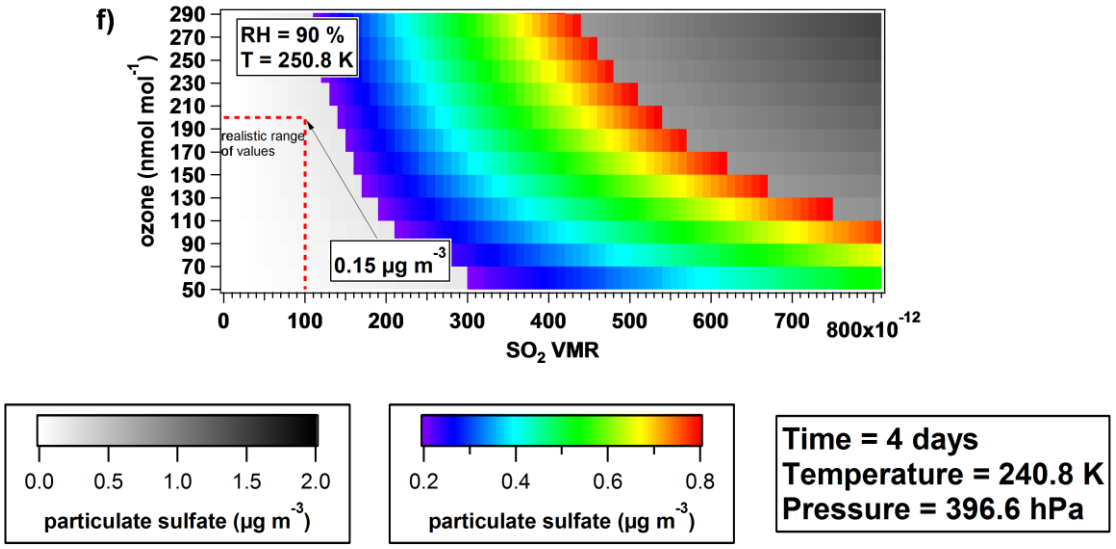


**Figure 57 (a-f): Particulate sulfate mass concentration produced after 4 days as a function of $O_3$ and $SO_2$ mixing ratios at varied relative humidity. The grey image denotes the concentration of particulate sulfate for all trace gas values while the rainbow-colored image shows the range between 0.2 and 0.8 µg $m^{-3}$. All calculations were conducted at the in-situ temperature of 240.8 K except for panel f) which was performed at 250.8 K. The red dashed box encompasses the range of realistic ambient values.**

The chosen time interval of 4 days was based on the trajectory analysis however it remains a subject of uncertainty. Therefore, a 30 day model run was conducted to estimate the amount of time needed to produce 0.2 µg $m^{-3}$ particulate sulfate at a relative humidity of 70 %, a temperature of 240.8 K and an ozone mixing ratio of 150 nmol $mol^{-1}$ (see Figure 58). The 0.2 µg $m^{-3}$ isoline intercepts the 100 pmol $mol^{-1}$ $SO_2$ mixing ratio after roughly 14 days. This is the time needed to reach the threshold. Hence, in theory, the respective amount of particulate sulfate could have been formed in this time interval which however is too long to match the observations.

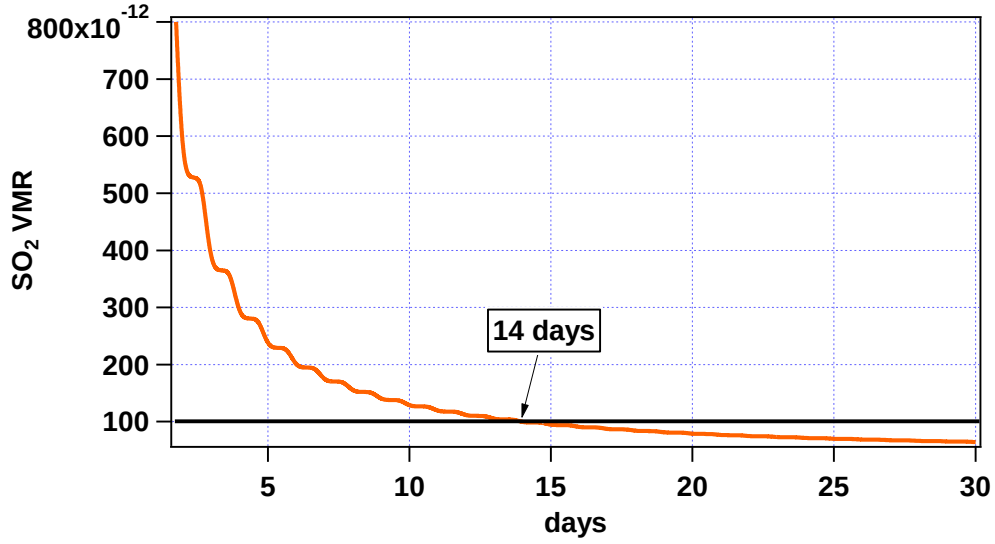


**Figure 58: Isoline of 0.2 µg $m^{-3}$ sulfate production (red line) as a function of $SO_2$ volume mixing ratio (VMR) at 70 % RH (green line) and 240.8 K. The lower black line indicates the 100 pmol $mol^{-1}$ $SO_2$ threshold for realistic concentrations in the UTLS.**

Another issue which has not been considered directly in the model calculations is the aspect of dilution. Given the scenario that the polluted tropospheric air mass mixes with the stratospheric streamer it can be expected that the stratospheric air contains less $SO_2$. Therefore, the total amount will decrease. This has only been accounted for indirectly by using the averaged observed $SO_2$ mixing ratios above the 2 PVU boundary during ARCTAS-summer as threshold for the CiTTyCAT results. Also, the assumption that all sulfuric acid is present as particulate sulfate is a slight overestimation of sulfate aerosol mass and the effect of heterogeneous chemistry due to the presence of particles is completely neglected as the aerosol scheme was not coupled to the model. Weigel et al. (2011) conducted calculations for aerosol nucleation from sulfuric acid in dependence of the pre-existing particulate surface area for the outflow region from deep convective cells in the tropical transition layer. The investigation shows that the less surface area is available the higher is the nucleation rate. However, for this case study neglecting the effect of aerosol surface area does not introduce a significant error to the calculation for mainly two reasons. First, only a comparison of measured and modeled (particulate) sulfate mass was conducted. In this respect, it does not matter whether the sulfuric acid formed from $SO_2$ condensed onto pre-existing particles or whether it nucleated. Second, nucleation events are characterized by high numbers of nucleation mode particles, e.g. up to 40,000 per $cm^3$ in the size range between 6 and 15 nm were observed by Weigel et al. (2011). However, such small particles hardly contribute to the overall aerosol mass concentration as the following mass balance shows:

$$MC_{H_2SO_4} = 40{,}000\frac{\#}{cm^3} * 10^6\frac{cm^3}{m^3} * (10^{-7})^3 cm^3 * \frac{1}{6} * \pi * 1.84 * 10^6\frac{\mu g}{cm^3} = 0.04\frac{\mu g}{m^3}$$

**Eq. 8**

with $MC_{H_2SO_4}$ mass concentration of $H_2SO_4$, $10^{-7}$ cm is the particle diameter (10 nm), and $1.84*10^6$ µg $cm^{-3}$ is the density of sulfuric acid. This high number of particles yields only a mass of 0.04 µg $m^{-3}$ which is an order of magnitude less than the measured value. The mass concentrations from the CiTTyCAT calculations are comparable to this simple estimation of particulate sulfate mass.

The conclusion from this limited modeling study is thus that a slight enhancement of sulfuric acid production occurs by the considered processes. However, under the given circumstances this is by far not enough to explain the observed enhanced particulate sulfur concentrations. Even assuming that a certain load of particles was present beforehand, the calculated enhancement at 240.8 K is in all cases below detection limit. Therefore, it is more likely that Plume V was a result of long-range pollution transport during which sulfate aerosol had already been produced in the fresh and less diluted plume at higher temperatures in the lower and free troposphere. To verify this conclusion CiTTyCAT was run forward along a representative trajectory as shown in Figure 59. Here, temperature, pressure, and humidity are given by the trajectory.

The result in Figure 60 shows that along the trajectory, assuming no scavenging, the amount of chemically produced particulate sulfate is enough to match the observations or even exceeds them. The red dashed line indicates again the range of realistic values. This time the maximum ozone mixing ratio is set to 90 nmol $mol^{-1}$ as the trajectory moved through the troposphere. The $SO_2$ mixing ratio,

however, can even be higher than accounted for in this model run given that the air mass carried a lot less diluted emissions from East Asia 10 days prior to the encounter. Dickerson et al. (2007) observed boundary layer $SO_2$ concentrations of up to 20 nmol $mol^{-1}$ and free tropospheric values around 2 nmol $mol^{-1}$.

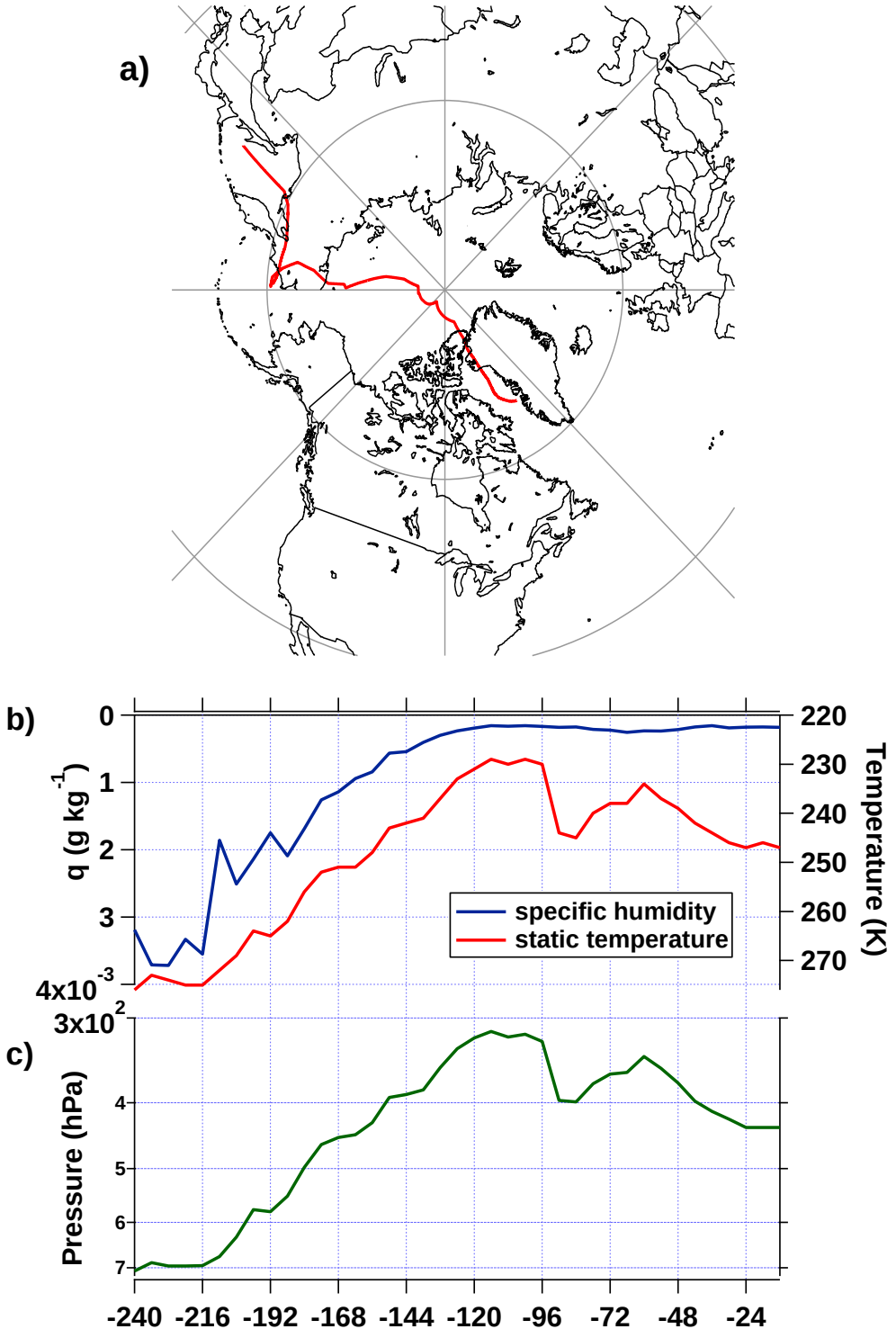


**Figure 59: Representative trajectory from Plume V on 13 July, 2008. a) cross-polar transport, b) temperature and humidity along the trajectory, c) pressure along the trajectory.**

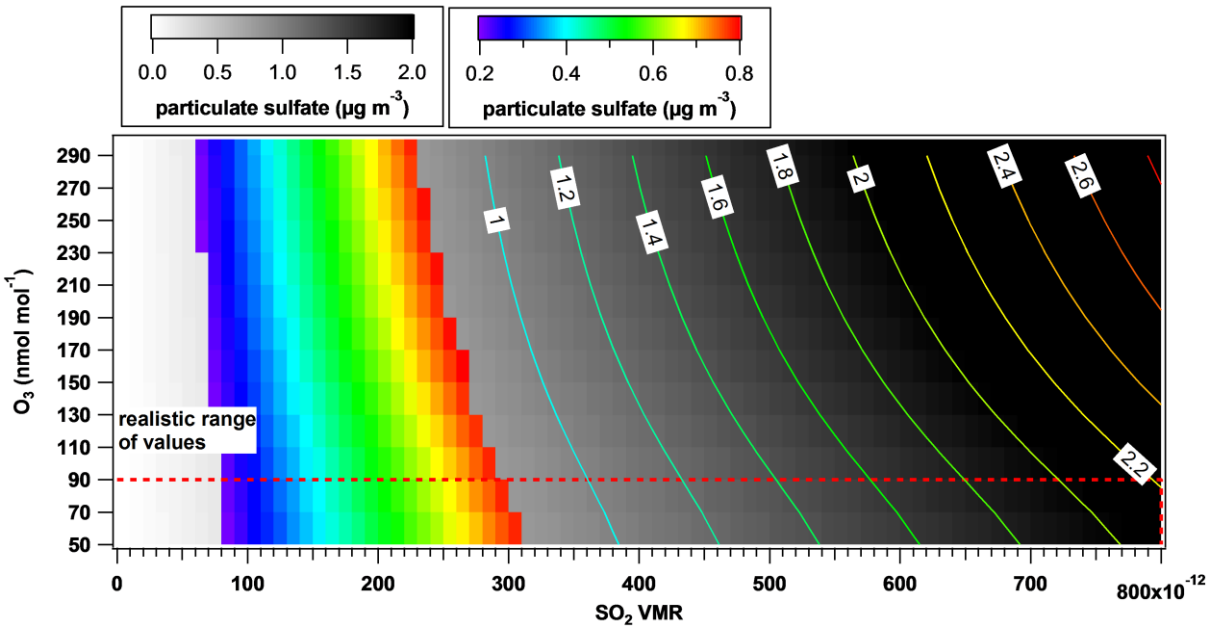


**Figure 60: Production of particulate sulfate along the trajectory after 10 days. The grey-scale indicates the concentration of particulate sulfate for $O_3$ and $SO_2$ values, the contour lines give the explicit values, and the rainbow-image highlights the range of values which match the observation.**

Considering only the last four days of the trajectory when the air mass moved between 400 and 300 hPa and tropospheric air has potentially mixed with the stratospheric streamer, the fixed box runs as described above can be compared to this calculation. Figure 61 shows the concentration of particulate sulfate that was produced between 17:26 UTC on 9 July and the same time on 13 July, 2008. Assuming for this consideration again the diluted tropospheric air mass mixed with stratospheric components the formed sulfate aerosol is far from the red dashed box with the realistic values. This result is comparable to the fixed box model runs at 10 and 30 % relative humidity. Note that for this case the production of sulfate aerosol is less within the considered period when ozone mixing ratios are higher. Figure 62 shows that the slope of $SO_2$ conversion decreases within the last days the higher the ozone mixing ratio. In other words, the lower the ozone mixing ratio the more potential for sulfate production is left.

Overall, considering all uncertainties and drawbacks of the CiTTyCAT model, it can be concluded that the mixing of polluted humid tropospheric and ozone rich stratospheric air masses results in only minor production particulate sulfate mass. Thus, such events seem not to be an important source for enhanced UTLS particulate sulfate mass concentrations. Based on the CiTTyCAT model run along the plume trajectory the major amount of particulate sulfate was produced during the first 6 days when the air mass was transported through the free troposphere (see difference in mass concentration in Figure 60 and Figure 61).

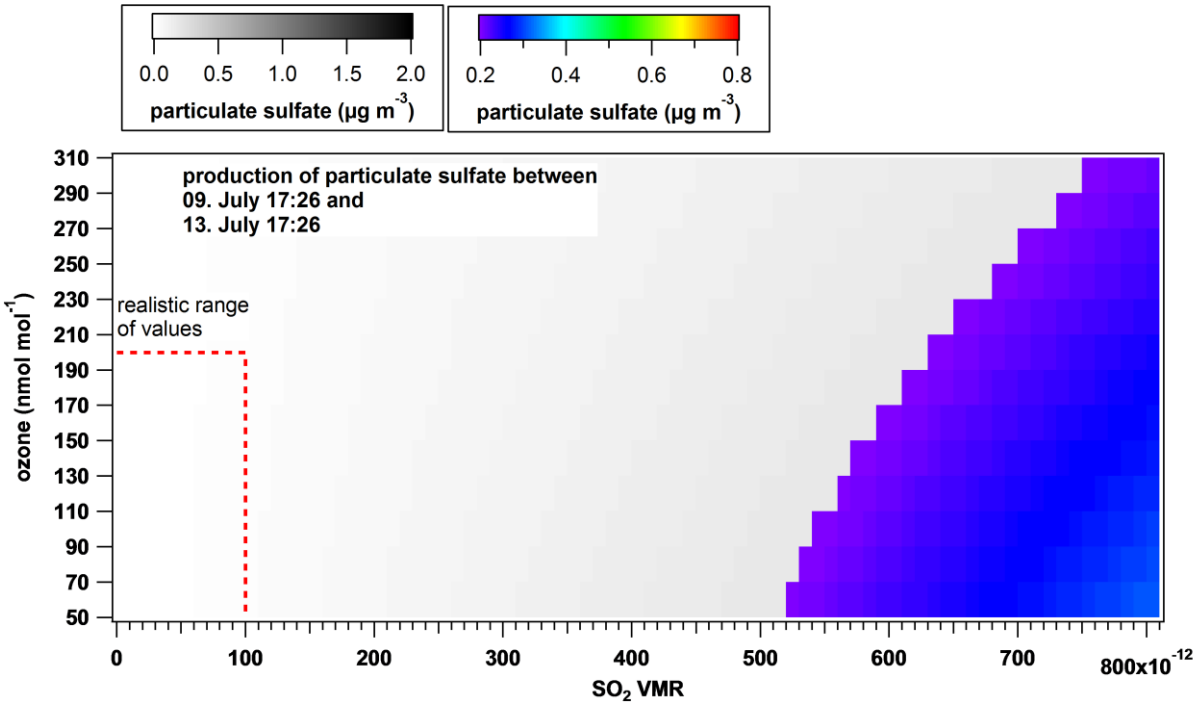


**Figure 61: Production of particulate sulfate between day 6 and 10 along the trajectory.**

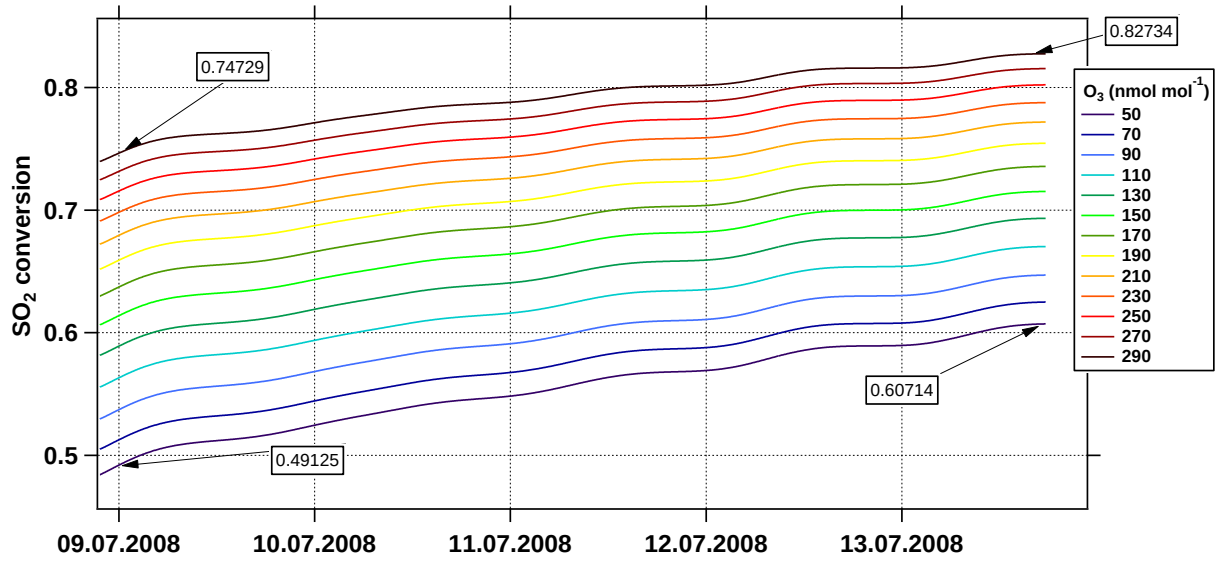


**Figure 62: $SO_2$ conversion with time along the trajectory for different ozone mixing ratios. The number tags show how much $SO_2$ has been converted at that particular point in time. The difference of the values for one ozone mixing ratio indicates which fraction of $SO_2$ was oxidized to particulate sulfate.**

Figure 63 resumes this section by comparing particulate sulfate measurements as a function of the ozone mixing ratio from two POLARCAT flights (13 and 14 (b) July, 2008) and fixed box model runs. The triangles represent results from 10-day runs with an availability of 100 pmol $mol^{-1}$ $SO_2$ at different relative humidity conditions at 240.8 K and at 90 % RH at 250.8 K (black solid line), while the squares denote the same for an initial $SO_2$ mixing ratio of 800 pmol $mol^{-1}$. The black dashed line refers to 90 % RH at 250.8 K. Measurements are indicated by the grey circles. The red solid line

denotes the median value for each 10 nmol mol$^{-1}$ ozone bin while the dashed lines represent the inter-quartiles. For 100 pmol mol$^{-1}$ $SO_2$ the box model does not produce sufficient sulfate aerosol to reflect concentrations near the median. However, this result can also be interpreted as follows: Around 100 pmol mol$^{-1}$ $SO_2$ are necessary to maintain a certain background concentration of particulate sulfate in the free troposphere when wet deposition occurs frequently and no nearby emission source is available. CiTTyCAT calculations performed with 800 pmol mol$^{-1}$ $SO_2$ yield produced sulfate values near and larger than the median of the measurements from the two considered flights. However, such high abundance of $SO_2$ was not observed in long-range transported air masses during ARCTAS-summer neither in the free troposphere nor in the UTLS. Even knowing that amounts twice as much have been observed in the free troposphere near emission source regions (Dickerson et al., 2007) it is difficult to relate these 10-day calculations to a realistic scenario because aerosol lifetime aspects such as wet deposition and dilution can hardly be estimated based on the available data for Asian pollution plumes.

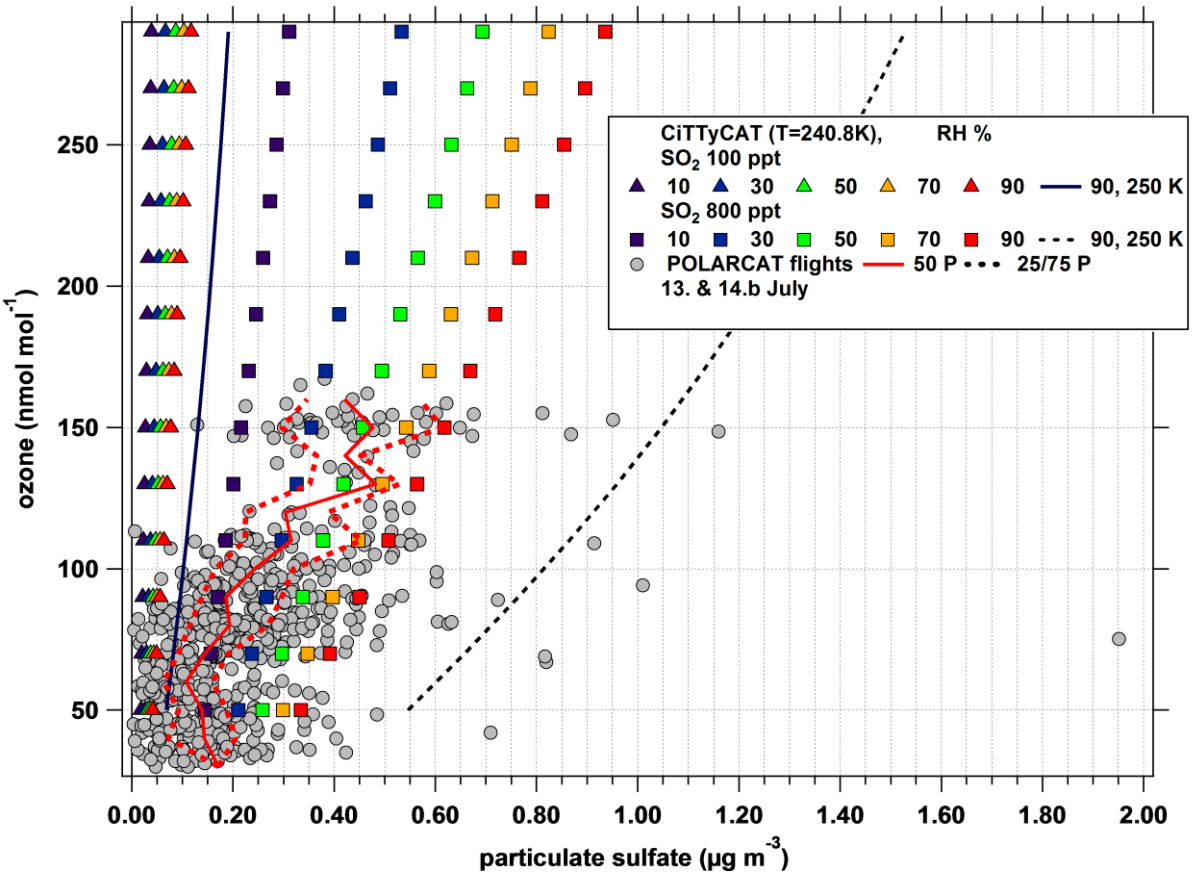


**Figure 63: Comparison of particulate sulfate measurements (grey circles) as a function of ozone mixing ratio during flights on 13 and 14 (b) July, 2008, with CiTTyCAT fixed box 10-day model runs at different relative humidity conditions at 240.8 K (and 90 % RH at 250.8 K) and $SO_2$ mixing ratios of 100 and 800 nmol mol$^{-1}$. The red line indicates the median of the measurement data, the red dashed lines the inter-quartiles in bins of 10 nmol mol$^{-1}$ ozone.**

### 3.2.3.3 Uplift of an Asian fossil fuel plume to the lower stratosphere

The here discussed plume episode, measured during the ARCTAS 4 July, 2008, flight covers the possibility of strong fossil fuel polluted air mass uplift into the lower stratosphere. The time series in

Figure 43 in section 3.2.1.2 indicates this episode with the roman number II. High $SO_2$ mixing ratios are encountered above the local 2 PVU boundary, while $CH_3CN$ concentrations drop and a major BB influence can be excluded. Ozone mixing ratios rise to a maximum of 208 nmol $mol^{-1}$ and clearly indicate lower stratospheric air mass properties while the CO concentration remains enhanced with values between 100 and 120 nmol $mol^{-1}$. Figure 64 shows that the air mass originated from East Asia and followed most likely the Pacific storm track while being uplifted rapidly through a WCB to the 200 hPa level within the last four days prior to the encounter. The uplift was accompanied by strong precipitation. However, the air mass which intruded into the lower stratosphere maintained a certain aerosol load of $1.30 \pm 0.26$ and $0.76 \pm 0.11$ µg $m^{-3}$ particulate sulfate and organics, respectively, corresponding to a relative composition of 63 and 37 %. This scenario also explains most likely why the CO mixing ratio remains relatively high in the LS.

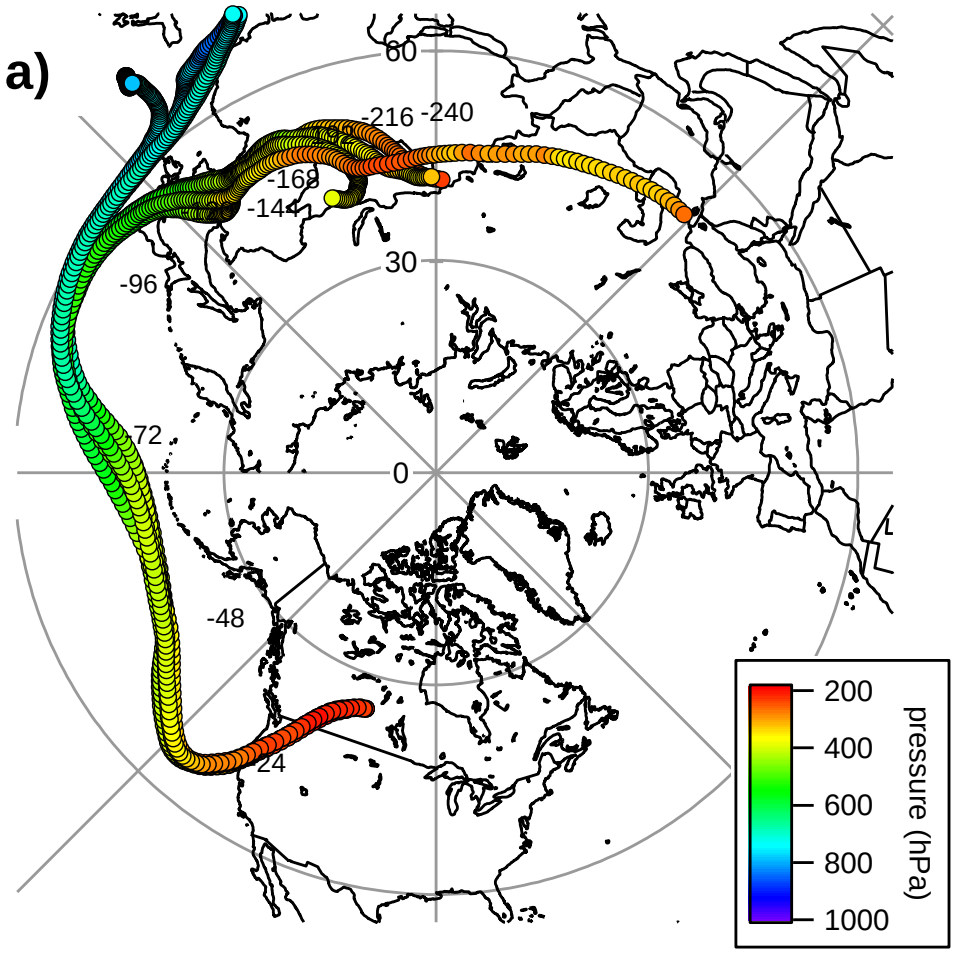

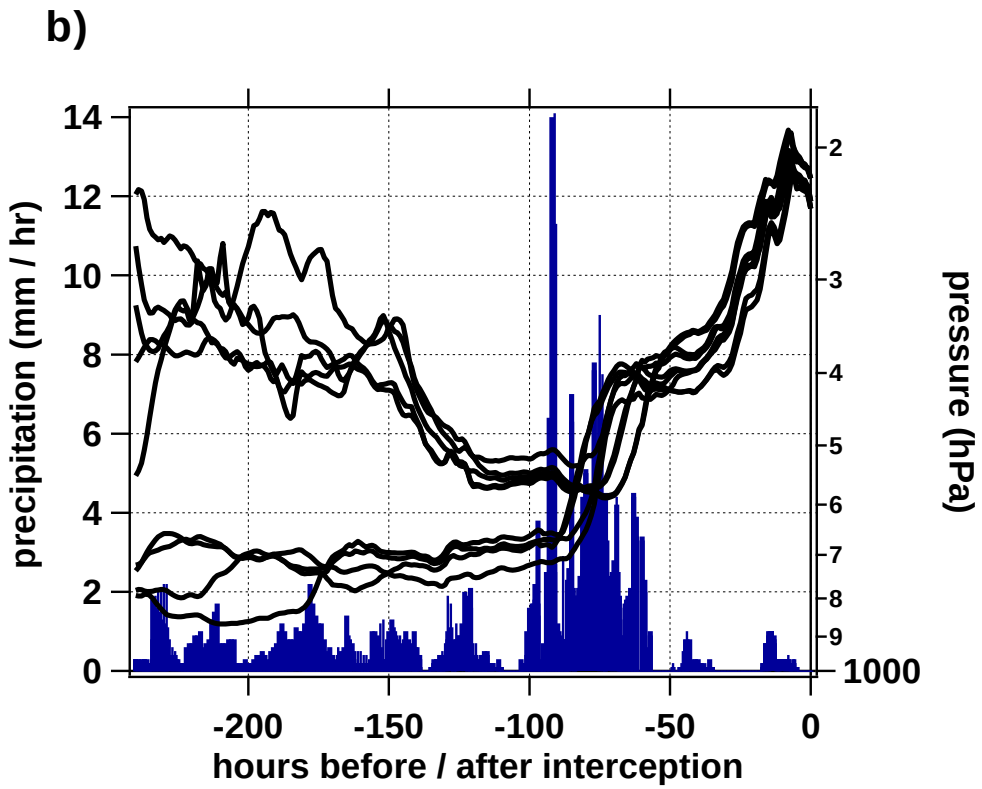


**Figure 64: HYSPLIT 10-day back trajectories for episode II (02:49 – 03:03 UTC on 5 July, 2008, as shown in Figure 43). a) The air masses travelled most likely along the jet stream path. The negative numbers indicate hours before sampling. b) Precipitation (blue) and altitude (black) along the trajectories. Trajectory release heights were 10.9, 11.0, and 11.5 km and the plume interception between 11.0 and 12.2 km.**

In the tracer plot shown in Figure 46 a) the respective data points are marked by red squares that are exclusively located in the stratospheric branch. This is another strong support for the hypothesis that this FF polluted air mass penetrated into the lower stratosphere at high northern latitudes. This case is thus very similar to episode I as discussed in section 3.2.1.2 where BB pollution was uplifted, and different from Plume V (see section 3.2.3.1) where probably cleaner stratospheric air descended to mix with polluted tropospheric air.

### 3.2.3.4 Tropospheric export of North American pollution to Europe

The plume discussed here is the observed case which comes closest to pure anthropogenic surface-bound emissions. Figure 65 illustrates the time series of particulate sulfate and $SO_2$ concentrations during the CONCERT return flight on 31 October, 2008, from Oberpfaffenhofen to Shannon, Ireland. The blue boxes indicate elevated aerosol loadings and $SO_2$ concentrations (data only available for flight leg b) in the troposphere which is not related to the volcanic aerosol in the lower stratosphere (see section 3.1.2). Both plumes were observed at comparable coordinates (leg a: 52.1 – 52.3°N, 10.1 - 9.9°W, 4.3 – 5.9 km altitude; leg b: 52.9 – 53.2°N, 9.8 - 9.2°W, 4.6 – 7 km altitude) within two hours (roughly 11:40 and 13:40 UTC) while descending into and flying out of Shannon.

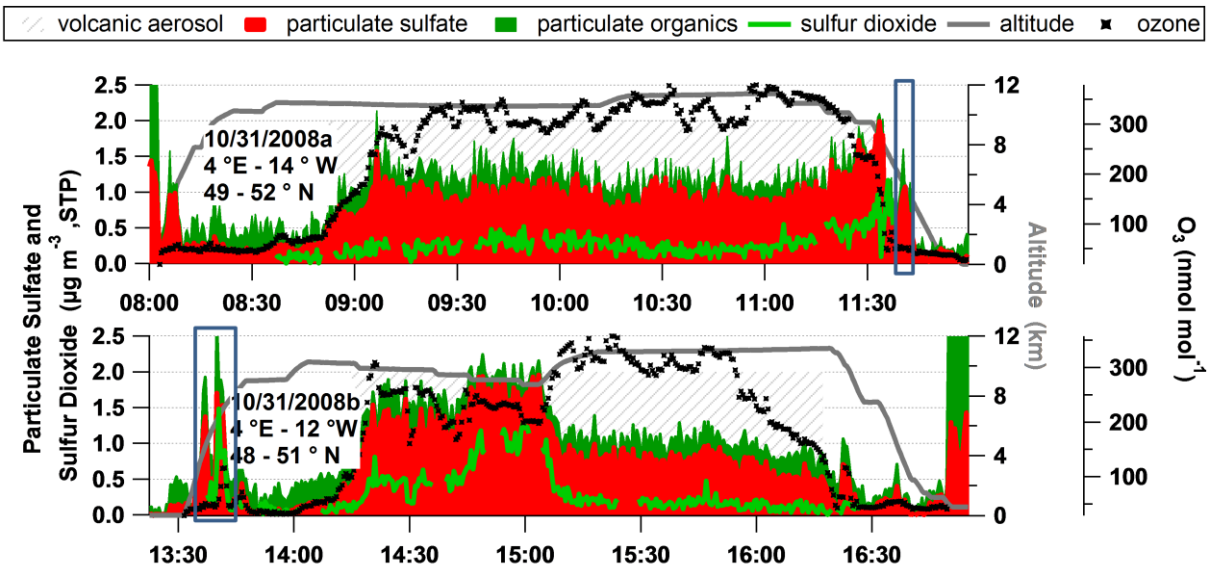


**Figure 65: Time series of flight altitude (grey), ozone mixing ratio (black symbols), particulate sulfate (red), organics (dark green), and sulfur dioxide (green) concentrations during two CONCERT flights on 31 October, 2008, from Oberpfaffenhofen, Germany, to Shannon, Ireland and back. The aerosol concentrations are stacked. The two blue boxes indicate the periods of interest.**

The origin of this plume was determined by means of HYSPLIT back trajectories. The model was run 10 days backward in time from the coordinates of the plume encounters at the hour of interception and an hour earlier and later. Figure 66 displays the respective map. It can be seen clearly that the majority of the trajectories must have picked up anthropogenic pollution from the boundary layer (blue color in plot) from the US east coast, the Ohio Valley and the Great Lakes area. It is noteworthy to state that the trajectory path until southern Greenland is very similar to observations from the low-level transport of the Ohio Valley plume as discussed in section 3.2.2.3. In this case also low tropospheric air mass movement occurred. Subsequently, the air is uplifted over the Greenland ice sheet (up to 3.2 km elevation) and travels in the free troposphere over Iceland towards Europe.

Chemically, this plume has a fossil fuel signature. In flight leg a), the average total AMS derived mass is 1.01 ± 0.33 µg $m^{-3}$ (accounting only for particulate sulfate and organics) with a contribution of 71 % by particulate sulfate. For the plume at the beginning of flight leg b), the average mass is 1.38 ± 0.73 µg $m^{-3}$ and the contribution of particulate sulfate is 65 %. Particulate nitrate and ammonium are in both cases below detection limit which is plausible as they might have been washed-out during the transport. The difference in total mass concentration provides an estimate of the inhomogeneity of the plume. $SO_2$ measurements are only available for the second crossing of this plume. From the average concentration of 0.66 ± 0.45 µg $m^{-3}$ (0.18 ± 0.14 pmol $mol^{-1}$) it can be derived that about 50 % of the sulfur has been converted from $SO_2$ into particulate sulfate. From the organic aerosol, O:C ratios of 0.54 and 0.42 for flight legs a) and b), respectively, have been calculated. Such low values indicate semi-volatile oxygenated organic aerosol, SV-OOA (see section 3.1.4). Even though only back trajectories are available for this case so that sensitivities to relevant emission fluxes from the potential source regions cannot be calculated, it is relatively safe to say that FF emission is dominant in this case. This statement can be based on the chemical signature and on the season of late fall when fire season is over. Some of the trajectories indicated in Figure 66 come from

high altitudes (> 10 km). One might argue that the pronounced sulfate signature might thus be related to the volcanic aerosol which was present in the lower stratosphere at that time (compare section 3.1.2). However, a significant stratospheric influence can be excluded as the ozone mixing ratio is only elevated during a very short period inside the observed plume during flight leg b. This episode might reflect the brief crossing of the tropopause fold as shown in Figure 28 d) but cannot be responsible for the high sulfate values in the plume that were observed for a much longer time period.

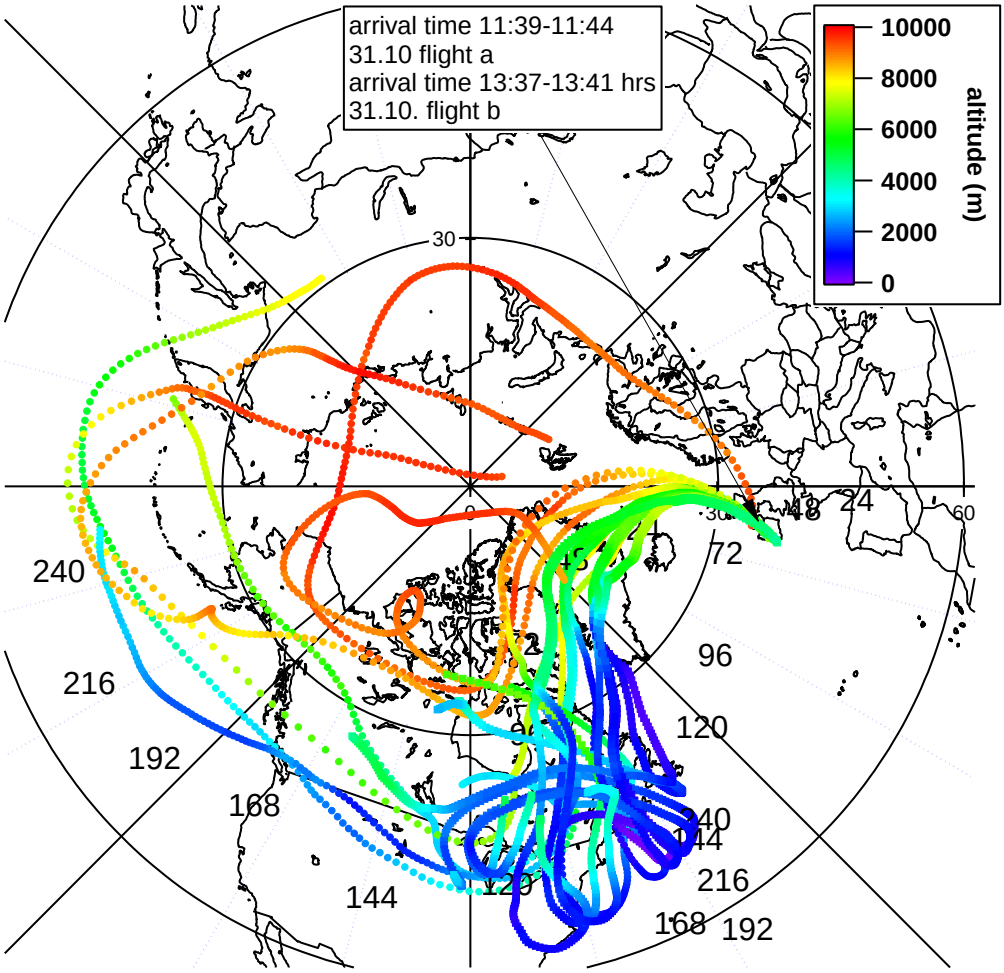


**Figure 66: HYSPLIT calculated 10-day back trajectories for the flight episodes marked with blue boxes in Figure 65. The color-code refers to the vertical position of the trajectory. Release heights were 4.3, 5.2, and 5.9 km at 12 UTC and 4.6, 6.0, and 7.0 km at 13 and 14 UTC.**

### *3.2.4 Resume of key parameters and variability of observed pollution plumes*

Altogether, the discussion of nine detected plumes shows the large variability in characteristics of long-range transported pollution reaching the sub-Arctic and Greenland during summer and Central and Western Europe during fall. At the beginning of July 2008, an intense low pressure system moving from North America towards southern Greenland was responsible for the advection of US American and Canadian polluted air masses with transport times between three and nine days. Later, two low pressure systems, one over the East Siberian Sea and another at the east coast of Greenland, facilitated cross-polar transport of East Asian and Siberian air masses towards Greenland where the

transport time was roughly between two and three weeks. Air masses detected above Canada were rather advected by the jet stream over the west Pacific where cases of UTLS air mass mixing were observed. For the general evaluation of long-range transport pollution, the observed cases show that both gaseous and particulate tracers need to be taken into account: Trace gases might not always be elevated when aerosol pollution is present (Plume IV). Also, air mass uplift in WCB over East Asia lead to nearly complete aerosol scavenging (Plume III) while trace gas mixing ratios remained elevated, whereas WCB transport out of North America was responsible for enhanced particulate and gaseous pollution over southern Greenland (Plume II). The high variability of chemical characteristics was even true within the same large scale pollution episode as cases III and V show (compare also right and left side of the turning point in Figure 53). [This paragraph is adapted from Schmale et al. (2011).]

In addition to the in-situ parameters the consideration of the air mass history is indispensible for a comprehensive data interpretation. After long-range transport of several days, dilution, wash-out, air mass mixing and chemical aging of certain gaseous and particulate tracers have occurred so that typical correlations of aerosol and gas phase tracers as encountered near a source are not obvious anymore, e.g. high CO mixing ratios emitted from BB are accompanied by enhanced particulate organic mass concentrations (see also introduction and section 4.4). Thus, in-situ data can only partially provide information about the origin of a pollution plume. Here, back trajectories or particle dispersion models can establish the link between source and receptor.

Table 15 compiles the main characteristics of each discussed plume.

**Table 15: Resume of key parameters of observed pollution plumes**

| | Plume I | Siberian BB | Plume II | Plume III | Plume IV | Plume V | East Asian | Plume VI |
|---|---|---|---|---|---|---|---|---|
| Campaign | POLARCAT | ARCTAS | POLARCAT | POLARCAT | POLARCAT | POLARCAT | ARCTAS | CONCERT |
| Category | "pure" BB | "pure" BB | NA / EU, FF / little BB | Sib BB / Asia FF | NA / EU, FF / little BB | Asia FF / Sib BB | Asia FF | NA FF |
| coordinates | 66.3 – 65.5°N, 49.9 – 49.1°W | 56 N, 103 - 104°W | 61.1 – 60.5°N, 45.4°W | 68.7 – 69.0°N, 55.6 – 56.4°W | 60.5 – 61.1°N, 45.4°W | 68.4 – 69.4°N, 54.8 – 57.8°W | 55°N, 106 - 108°W | 52°N, 10°W, 53°N, 9 - 10°W |
| altitude (km) | 4.2 – 5.0 | 11.5 | 7.6 | 5.7 | 2.1 – 3.0 | 7.3 | 11.0 | 4.3 – 5.9, 4.6 - 7 |
| date/time (UTC) | 8 July 2008, 13:14 – 13:32 | 5 July, 2008, 01:01 – 01:30 | 8 July 2008, 14:52 – 15:02 | 13 July 2008, 19:56 – 20:02 | 8 July 2008, 15:40 – 15:50 | 13 July 2008, 18:42 – 19:06 | 5 July, 2008, 02:49 – 03:03 | 31 Oct., 2008, 11:39 – 11:44, 13:37 – 13:41 |
| extension (km) | 108 | 522 | 60 | 72 | 60 | 150 | 252 | 60, 48 |
| age (days) | 7 | 14 | 6-11<br>3-4 | 6 – 11 | > 7<br>5 – 8 | 6 – 11 | 14 | 6-10 |
| Maximum mass ($\mu g\ m^{-3}$) | 1.11 | 2.00 | 0.96 | 0.22 | 0.73 | 1.30 | 2.40 | 1.60, 2.66 |
| fraction of organics (%) | 90 ± 12 | 66 ± 10 | 82 ± 4 | - | 55 ± 17 | 52 ± 22 | 37 ± 10 | 29 ± 14, 35 ± 19 |
| $\Delta CO$ ($nmol\ mol^{-1}$) | 30 | 129 | 27 | 30 | - | -16 | - | -, 36 |
| $\Delta O_3$ ($nmol\ mol^{-1}$) | 10 | - | 45 | -24 | - | 50 | 142 | -, 70 |

## *3.3 Contrails - Pure fossil fuel emissions*

This last category of emissions represents a pure anthropogenic source namely fossil fuel combustion emission from air traffic. During two flights of the CONCERT campaign (29 October and 2 November, 2008) commercial aircraft were chased with the Falcon and their contrails probed at varied ages. As aircraft kerosene contains a certain amount of sulfur, it is expected that $SO_2$ is emitted which subsequently forms sulfuric acid which can condense on soot particles from the off-gas or on other pre-existing ambient aerosol. Also, hydrocarbons will be emitted which potentially condense as well if they have a low vapor pressure. In theory, such particles can be detected by the AMS as they fall within the transmission range of the pressure controlled inlet system and the standard lens already at a contrail age of 10 seconds (Kärcher et al., 2007). Small particles which are below the transmission range however are expected to contribute most to the particle number density in contrails (Schneider et al., 2006a). In the following, three contrails probed on 2 November are discussed. Results from 29 October do not differ significantly.

Figure 67 presents the time series of particulate sulfate together with the mixing ratio of $NO_y$. High concentrations of $NO_y$ indicate the crossing of contrails. If known the respective aircraft is named in the plot. The particulate sulfate loading is generally very low throughout the flight with values below 0.2 µg $m^{-3}$, and no significant changes while measuring the contrails can be observed at first sight.

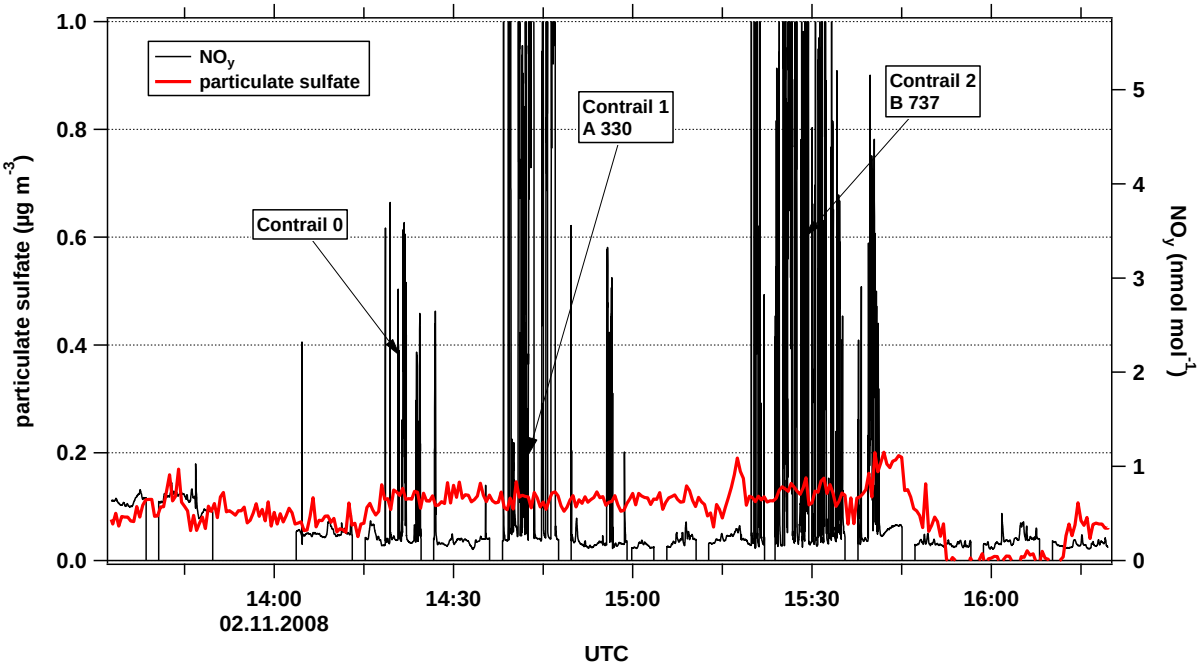


**Figure 67: Time series of particulate sulfate and $NO_y$ on 2 November, 2008. High $NO_y$ mixing ratios indicate the crossing of contrails.**

Therefore, a more detailed analysis was conducted by comparing the averaged mass spectrum while probing the B 737 contrail (red sticks, see Figure 68) with the mass spectrum obtained in the immediate surroundings of the contrail (black sticks), i.e. in the gaps of the high $NO_y$ mixing ratio. The error bars on the *m/z* sticks denote the ion counting statistics error. *m/z* of interest are 48 ($SO^+$), 64 ($SO_2^+$), 80 ($SO_3^+$), 81 ($HSO_3^+$) and 98 ($H_2SO_4^+$) as they are fragments of particulate sulfate. All these

fragments overlap within the error range for background and contrail spectra. So there is no significant enhancement of sulfate aerosol within the off-gas plume. Comparing the measured values to the limit of detection (green horizontal bars) only *m/z* 48 and 64 (within the error range) are above the threshold. Note that the green and blue horizontal bars exceed the boundary for the *m/z* they refer to only for illustrative reasons. This does not mean that these values are valid for the neighboring *m/z*. Additionally, considering the averaged UTLS background including one standard deviation of the sulfate mass to charge ratios from the entire flight, all masses are unambiguously lower. This result is true for all measured contrails. It can thus be concluded that for the young age of the probed aircraft off-gas plumes no particulate sulfate enhancement compared to the background UTLS conditions was found. Furthermore, no other *m/z* which could be associated to a fossil fuel combustion spectrum like e.g. *m/z* 43, 55, 57, 69, 71 etc. (Schneider et al., 2006b) is above background values.

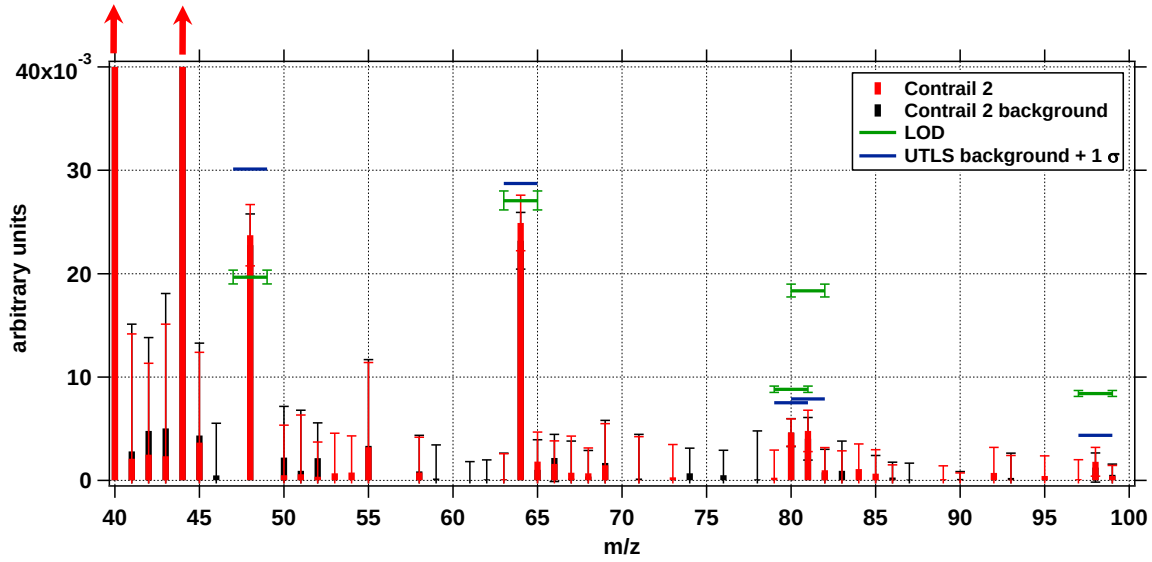


**Figure 68: Comparison of mass spectra obtained while flying in a contrail (red sticks) and from the immediate background (black sticks). The green horizontal bars indicate the limit of detection for the specific *m/z* including the variance. The blue horizontal bars represent the UTLS background plus one standard deviation averaged over the entire flight.**

From these measurement data it is thus obvious that no particulate sulfate enhancement was detected in the probed contrails. Figure 69 illustrates the theoretical considerations based on literature (Schumann et al., 1998) whether the particulate sulfate could have been observed or not. $SO_2$ mixing ratios as reported by Schumann et al. (1998) were converted into particulate sulfate concentrations (assuming 100 % conversion) as a function of contrail age (red points) and fitted exponentially. Based on literature (Kärcher et al., 2007) about 3 % of $SO_2$ is converted into sulfuric acid which constitutes the sulfate aerosol. This amount is indicated by the black line with the tag "3 %", added to the immediate background particulate sulfate value of contrail 2. Additionally, values for 10 % conversion are represented by the blue line and the respective tag. The grey shaded area indicates the background UTLS particulate sulfate concentration while the green area stands for contrail aerosol loadings that could clearly have been distinguished from the background. This is also highlighted by the two arrows at the right side saying "possible" and "not possible". The dark green line indicates the limit of detection for particulate sulfate. To correctly place the measured values of the three contrails in this

graph the contrail age had to be estimated. This was only possible for contrail 2 where a difference in temperature of 0.14 K between the contrail and the immediate surroundings was found. Data from 2 minutes before and after the contrail were used for the ambient temperature. Based on measurements by Schumann et al. (1998) this ΔT was converted into a distance of 14000 m which corresponds to a time of 70 seconds assuming that the B 737 moved at a speed of 200 m $s^{-1}$. Contrails 0 and 1 were placed around the calculated age for illustrative reasons (see triangles with standard deviation bars). The colored horizontal lines indicated the immediate surroundings of the individual contrails. Given that these assumptions are correct the observed data fit the theoretic consideration of 3 % $SO_2$ conversion to sulfate aerosol. It also becomes clear from this figure that only contrails with an age of less than 30 seconds would have contained enough particulate sulfate (given that the particles were large enough to be measured by the AMS) to exceed background conditions in November in northern Germany. For this theoretical consideration, it has to be kept in mind that oxidation of $SO_2$ to $H_2SO_4$ might not be fast enough to achieve a conversion of 3 % in the few seconds after emission. Also, the amount of direct $H_2SO_4$ emission was not considered here.

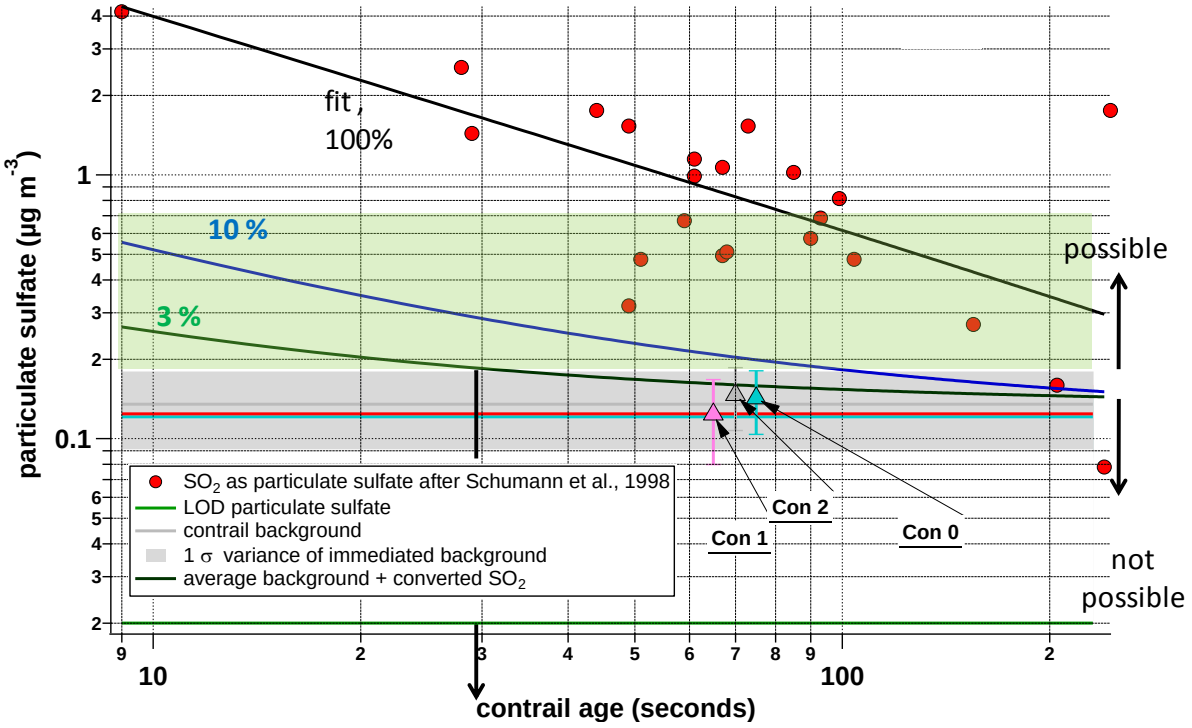


**Figure 69: Comparison of theoretical particulate sulfate concentration as function of contrail age with observations from three contrails on 2 November, 2008. Red points: $SO_2$ literature values, converted with 100 % into sulfate. Blue and black lines: Amount of particulate sulfate assuming $SO_2$ conversion rates of 10 and 3 %. Triangles: measurement values. Note that only the age of contrail 2 could be estimated. Cyan, magenta and grey horizontal lines: Particulate sulfate concentration from the immediate background of the respect contrail. Grey thick bar: UTLS background variation of sulfate aerosol. Green area: Concentrations of particulate sulfate that could have been clearly detected above background (also indicated by "possible" and "not possible" tags). Dark green line: Limit of detection for sulfate aerosol.**

This section illustrates that sulfur emissions from a single aircraft beyond a contrail age of 30 seconds are not enough to enhance ambient particulate sulfate mass concentrations because dilution of the

exhaust plume is too dominant. Whether a large number of contrails on a highly frequented route has the potential to significantly enhance the UTLS particulate sulfate load is difficult to estimate based on the above results, as aspects such as wind speed, fuel sulfur content and heterogeneous chemistry play an important role. This result is consistent with other experimental and model studies stating that the increase in particulate sulfate mass is rather small but particle number enhancements can be significant (short review in Kärcher et al. (2007)). But even though background levels might not be elevated significantly in terms of AMS detectable aerosol mass, air traffic near the tropopause adds particles to the background aerosol and leads to contrail and potentially cirrus cloud formation under certain circumstances in the upper troposphere where coating of soot particles with sulfuric acid and organic matter is important (Kärcher et al., 2007). They do have an impact on heterogeneous chemistry and consequently on the water vapor and ozone budget which is highly climate sensitive in this altitude (Forster and Shine, 2002), and also on the radiative balance of the atmosphere. Also, introducing particles into the lower stratosphere is a significant perturbation since particle lifetime is longer and thus small effects can grow important.

# 4. Resume - What have we learned about aerosol in the free troposphere and tropopause from POLARCAT, ARCTAS and CONCERT?

The high variety of pollution episodes observed in addition to measurements of background conditions during the three campaigns POLARCAT, ARCTAS and CONCERT in June/July and October/November 2008 in high and mid-latitudes helped to confirm and expand knowledge on aerosol properties in the free troposphere and UTLS. This chapter will combine and summarize the main findings by considering the following aspects:

- Vertical distribution of submicron aerosol and trace gases
- Evolution of sulfur containing aerosol in the UTLS during 2008
- Chemical properties
- Lifetimes and wet removal
- Size distributions

## *4.1 Vertical distributions*

Vertical distributions of submicron aerosol mass concentrations and simultaneously recorded trace gas data are shown relative to the local dynamic tropopause defined as the 2 PVU isosurface. This mode of coordinate system was chosen to clearly address the occurrence of aerosol pollution in the free troposphere and UTLS. As the local tropopause height varies from flight to flight, location and season a simple vertical axis (such as pressure or distance a.s.l.) cannot coherently represent the position of a pollution plume relative to the tropopause.

In Figure 70 the campaign median and inter quartile range of AMS derived aerosol vertical profiles are shown for POLARCAT, CONCERT and ARCTAS-summer campaigns, displayed relative to the 2 PVU tropopause height. The ARCTAS-summer data only comprises flights that were carried out at mid to high latitudes between 29 June and 10 July. For the POLARCAT flights, the median of the summed particulate sulfate and organics mass concentrations ranges between 0.25 and 0.50 µg $m^{-3}$. Only values in the free troposphere are available since the ATR-42 could not exceed 7.6 km altitude. Closer to the tropopause between -2 and -4 km there is a slight increase in particulate mass concentration which could possibly be attributed to higher altitude long-range pollution transport. This perception is backed up to a certain extent by the CO vertical profile (see Figure 68) where an enhancement with a median near 115 nmol $mol^{-1}$ in this altitude can be observed. Such enhancements have also been observed over high European latitudes during SPURT (Fischer et al., 2006). Given that the CO mixing ratio as a passive tracer is maintained, it can more reliably indicate an advection of pollution in a campaign average than submicron aerosol which is subject to wet deposition and whose concentrations are thus highly variable. The CO mixing ratio over Greenland seems to have a background concentration near 85 nmol $mol^{-1}$ between -9 and -6 km, 95 nmol $mol^{-1}$ between -6 and -4 km, and 102 nmol $mol^{-1}$ above -4 km based on the $10^{th}$ percentile (not shown).

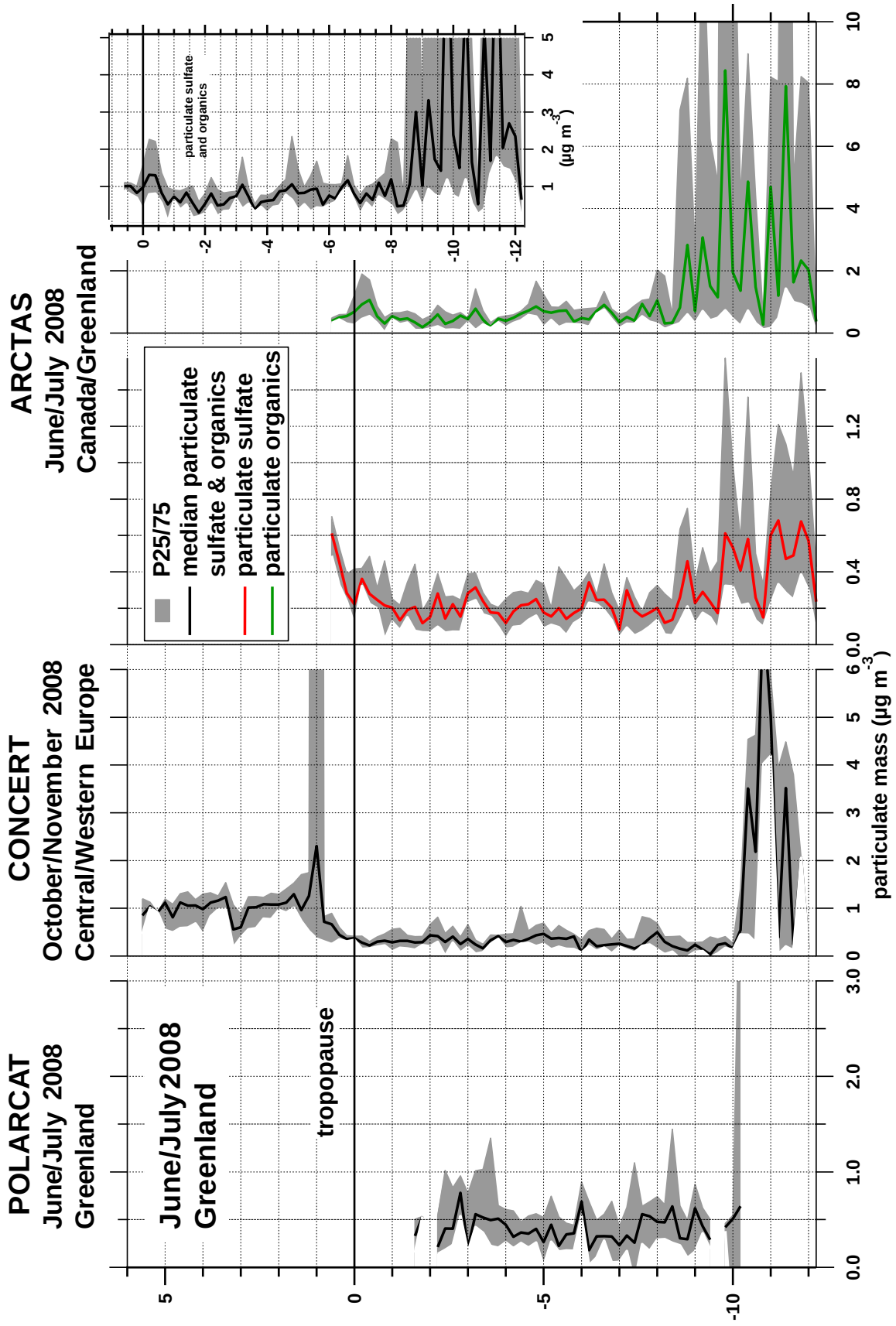
POLARCAT
June/July 2008
Greenland
June/July2008
Greenland
CONCERT
October/November 2008
Central/Western Europe
ARCTAS
June/July 2008
Canada/Greenland
tropopause
P25/75
median particulate
sulfate & organics
particulate sulfate
particulate organics
particulate sulfate
and organics
(µg m-3)
relative distance to dyn. tropopause (km)
particulate mass (µg m-3)

**Figure 70 (previous page): Vertical distribution of submicron aerosol mass in 200 m bins relative to the 2 PVU dynamical tropopause. The black lines show campaign median values for POLARCAT, CONCERT and ARCTAS (insertion upper right corner) of the summed particulate sulfate and organics. The two panels on the right represent ARCTAS data subdivided into particulate sulfate and organics. The grey shaded areas denote the 25$^{th}$ and 75$^{th}$ percentiles. This data refers to submicron particle measurements.**

The ozone mixing ratio steadily increases from 25 nmol mol$^{-1}$ to 100 nmol mol$^{-1}$ over the altitude range covered by the ATR-42. The stratospheric air mass intrusion as discussed in section 3.2.3.1 is also notable between -2 and -3 km. The aerosol concentration over Greenland is as high as over Central and Western Europe in October/November during the CONCERT campaign (Figure 70). There the boundary layer enhancement is clearly visible in contrast to the POLARCAT measurements where no boundary layer aerosol was observed. This might be due to the lack of local surface emission sources as almost no anthropogenic activity occurs and also vegetation is too scarce to cause the production of large amounts of particles. The high loadings at -10 km during both campaigns result from the aircraft's own exhaust. The volcanic aerosol from Mts. Okmok and Kasatochi dominates the lower stratospheric measurements during the CONCERT campaign. Above the local tropopause, aerosol loadings are higher on average (at least a factor of 2) than in the free troposphere where most likely scavenging occurred.

The CO vertical profile over Europe shows little variations in the free troposphere and decreases slowly towards the dynamical tropopause. The observed invariance in CO and aerosol data may indicate that very little long-range pollution transport was observed during this campaign. The only notable incident is discussed in detail in section 3.2.3.4 when anthropogenic pollution from North America was transported towards Ireland. The CO chemical tropopause seems to be shifted a little bit (roughly 200 ) to lower altitudes while the $O_3$ concentrations start increasing strongly about 100 m above the 2 PVU isosurface.

The ARCTAS-summer summed aerosol data (insertion in Figure 70) are a factor 2 higher than the measurements over Greenland. Considering the vertical distribution of particulate sulfate and organics it becomes clear that organic matter is the main contributor to this mass enhancement. This can be explained by the measurements' proximity to Canadian biomass burnings (Jacob et al., 2010; Singh et al., 2010). Strong injection signatures from organic aerosol, CO (Figure 68) and acetonitrile (Figure 73 a) are present in the boundary layer and lower free troposphere between -12 and -8 km. According to the threshold of 0.2 nmol mol$^{-1}$ $CH_3CN$ (Warneke et al., 2006) the entire free troposphere during the ARCTAS campaign was perturbed by biomass burning emissions. Next to the enhancement at lower altitudes there is a second increase in the trace gas mixing ratios (CO, $CH_3CN$) between -6 and -4 km which however is not reflected in the aerosol data. This again might be an indication for particle scavenging in the free troposphere.

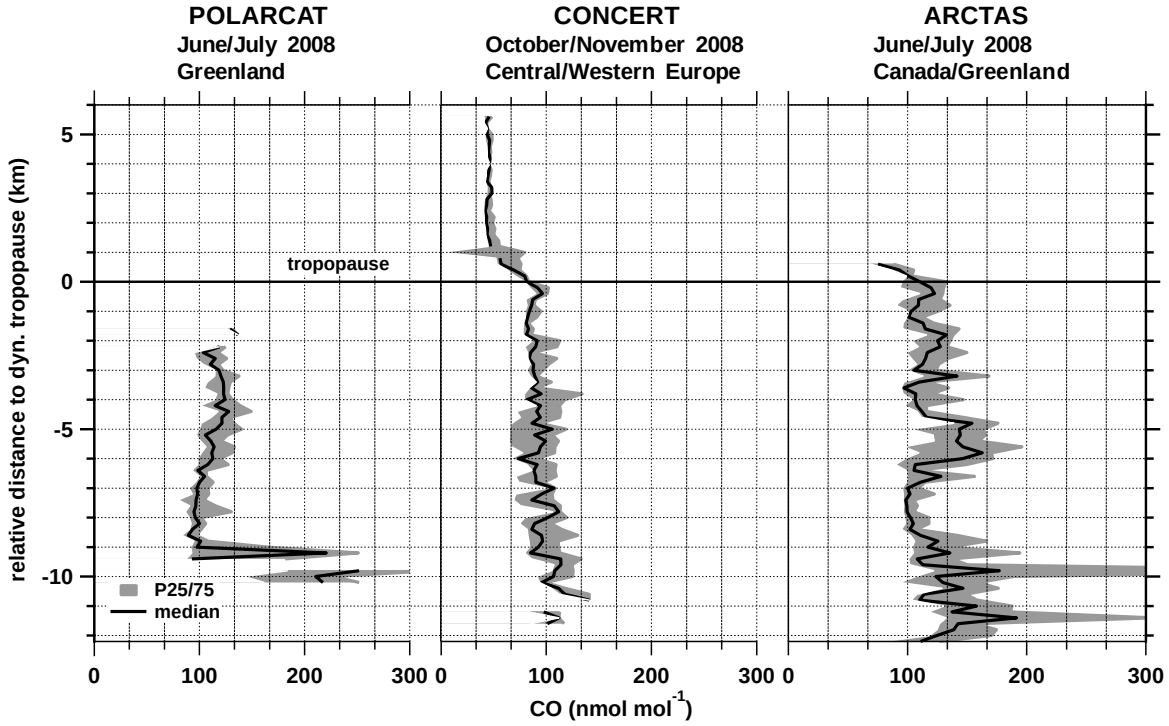


**Figure 71: Mean vertical profiles of carbon monoxide for the POLARCAT, CONCERT and ARCTAS (29 June – 10 July) data relative to the dynamical tropopause at 2 PVU in 200 m bins. The thick black lines indicate the median mixing ratio while the grey shaded area represents the inter quartiles.**

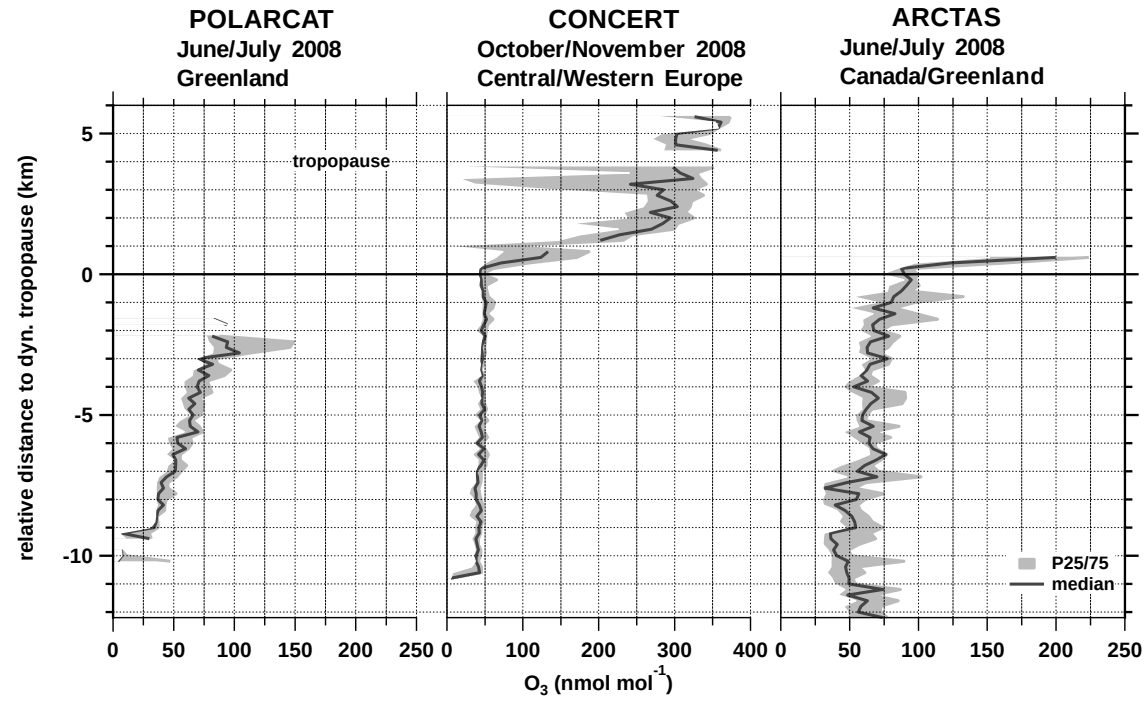


**Figure 72: Same as, but for ozone mixing ratios.**

Regarding sulfur species, particulate sulfate and $SO_2$ enhancements decrease above -8 km and concentrations remain relatively stable throughout the free troposphere. At the tropopause level, however, both species start to increase clearly with particulate sulfate even reaching boundary layer

loadings of 0.6 µg $m^{-3}$. This behavior of anthropogenic markers is opposite to the BB tracer $CH_3CN$, CO and organic aerosol that all decrease above the tropopause. ARCTAS CO and acetonitrile mixing ratios start diminishing just below the local 2 PVU boundary as also observed for CO data during the CONCERT campaign. ARCTAS $SO_2$ (Figure 73 b) increases like ozone slightly above the dynamical tropopause. It also has to be noted that ARCTAS organic aerosol shows a notable enhancement in the upper troposphere which might indicate long-range transport of pollution as discussed in section 3.2.1.2. The sources of the sulfur species above the tropopause cannot always be unambiguously identified. Two out of four cases that mainly represent these data point towards East Asian anthropogenic sources while the 10-day back trajectories for the other two cases remain primarily in the Arctic without intercepting any apparent emission source. The potential influence of the volcanic eruption on 12 July of Mt. Okmok can be excluded since only data until 10 July was used for this study.

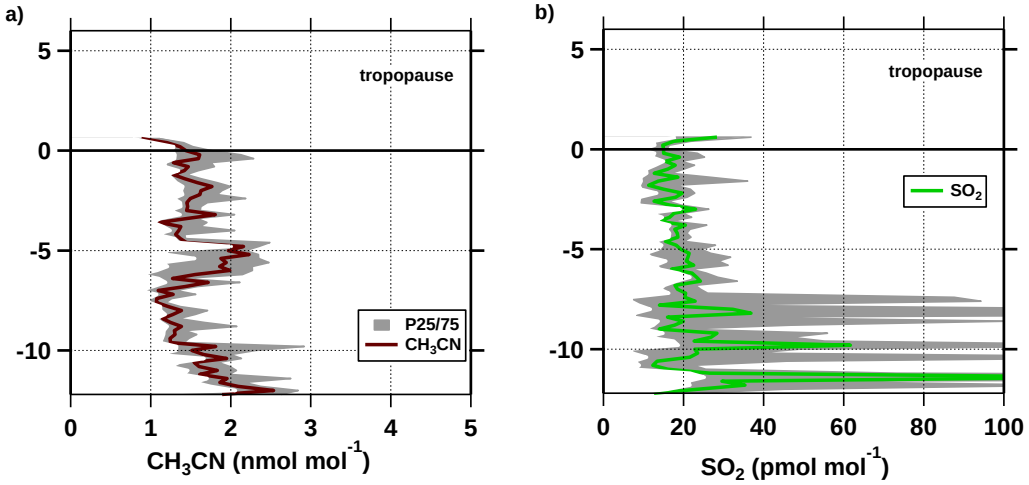


**Figure 73: ARCTAS (29 June – 10 July) mean vertical profiles in 200 m bins relative to the dynamical tropopause for (a) $CH_3CN$ and (b) $SO_2$ data. The thick lines denote the median value while the grey shaded areas show the inter quartile range.**

The vertical profile of $SO_2$ above the western Arctic and sub-Arcitc shows on average lower mixing ratios with 20 pmol $mol^{-1}$ than observations over other geographical regions. Fiedler et al. (2009) and (2011) see slightly higher mixing ratios over Western Europe and West Africa in the free troposphere. Compared to measurements by Möhler and Arnold (1992) over the European Arctic in winter where $SO_2$ mixing ratios ranged from 100 to 500 pmol $mol^{-1}$ between -6 and -1 km below the local tropopause level concentrations during summer 2008 were significantly lower. This might be explained by the extended polar dome during winter time which inhibits penetration of more sourtherly air masses into the Arctic troposphere and leads to accumulation of inner Arctic pollution. The authors, however, observe a strong decrease of $SO_2$ above the tropopause which is contrary to a series of previously conducted measurements (e.g. Georgii and Meixner (1980)). Georgii and Meixner (1980) observed either little variation of $SO_2$ mixing ratios above the tropopause or a slight increase. Values are between 30 and 70 pmol $mol^{-1}$. However, when comparing or contrasting such campaign based data sets it must not be forgotten that local influences or long-range transport of polluted air masses play a significant role so that the state of the atmosphere is not necessarily always comparable.

## *4.2 History of sulfur containing aerosol in the tropopause during 2008*

Due to the volcanic eruptions of Mts. Okmok and Kasatochi in July and August 2008 it is especially interesting to establish a history of sulfate containing aerosol in the UTLS (Schmale et al., 2010).

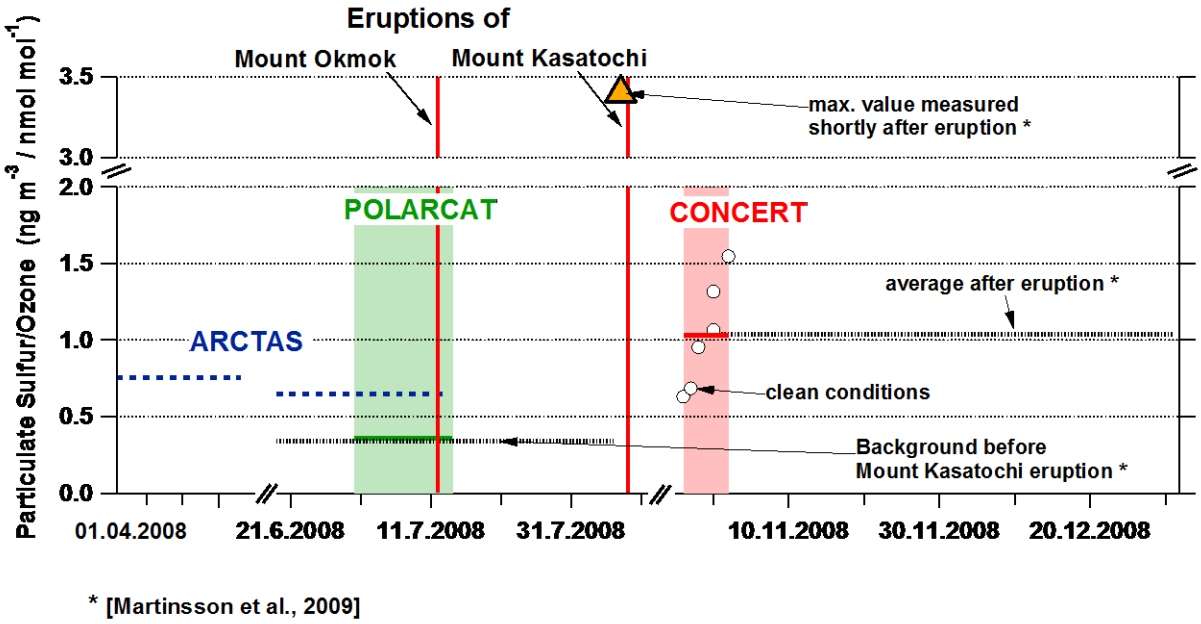


**Figure 74: Chronological overview of particulate sulfur to ozone ratio in 2008 in the UTLS including data sets from ARCTAS, POLARCAT and CONCERT aircraft campaigns, and CARIBIC data [This figure was published in Schmale et al. (2010).]**

Figure 74 shows the chronological overview as a function of the ratio of particulate sulfur concentration and ozone mixing ratio. Data from the two ARCTAS campaigns, POLARCAT, CONCERT and CARIBIC were available. The comparability of CARIBIC filter measurements and AMS observations has already been discussed in section 3.1.2. CARIBIC data as published by Martinsson et al. (2009) refer to values observed above the 1.5 PVU threshold as do CONCERT observations. For the two other campaigns the ozone tropopause criterion after Zahn and Brenninkmeijer (2003) was applied as at the time when establishing this overview potential vorticity data was not yet available. According to Martinsson et al., the average sulfur to ozone ratio before the eruptions was 0.34 ng $m^{-3}$ $nmol^{-1}$ mol, hereafter termed units, as illustrated by the dashed line between 21 June and 6 August. Shortly after the eruption a ratio of 3.4 units (orange triangle), a factor 10 higher, was observed which leveled out to 1.05 units at the beginning of October. According to Bourassa et al. (2010) it took about 7 months until background conditions were re-established. For comparison, after the Mt. El Chichón and Mt. Pinatubo eruptions it took more than 5 years to reach background values again (Thomas, 2003). CONCERT measurements from October show a mean value of 0.65 units for background conditions and 1.22 units within the volcanic layer (average of white circles that represent each one flight). The overall campaign average, flying in and out of the plume, results in 1.03 units (red line) which is very close to observations made by Martinsson et al. (2009). POLARCAT measurements (green line) in the upper troposphere represent quite well the average of the CARIBIC data with 0.36 units while ARCTAS background data, filtered as described

in section 2.7.3, show elevated ratios of 0.75 units in spring and 0.68 units in summer (blue dashed lines). These values are in line with CONCERT background findings (tag clean conditions) and well below the enhancement observed after the eruptions. From this compilation the short-term impact on the tropopause aerosol concentration of the two volcanic eruptions becomes visible. [This paragraph is adapted from Schmale et al. (2010).]

For the Northern Hemisphere, the data show that values for the ratio particulate sulfur / ozone range between 0.25 under background conditions to 3.5 units for a moderate volcanic eruption.

## *4.3 Aerosol chemical properties*

In sections 3 to 3.3 the chemical properties of individual pollution episodes were presented. Here the characteristics are resumed in pollution type categories as defined in section 2.7.3. The considered pollution types are volcanic aerosol from the CONCERT campaign and the listed categories from the introduction to section 3.2 which are a result of the POLARCAT campaign. Additionally, pollution episodes during ARCTAS are resumed in the class "Arctic free troposphere" (Arctic FT) and Arctic UTLS. Furthermore, out-of-plume episodes which are termed "background conditions" are presented for POLARCAT measurements, CONCERT free tropospheric and UTLS data and ARCTAS free tropospheric measurements.

### *4.3.1 Chemical composition*

Based on the nature of the emission source, in theory it is possible to distinguish source type categories as defined for the data set of this work by the chemical signature of the aerosol. Volcanic aerosol is clearly dominated by particulate sulfate, while FF exhibits an important contribution of inorganic matter and BB is dominated by organic matter (see sections 1.5.1 - 1.5.3 for the detailed discussion).

Figure 75 a) shows the derived sulfate and organic carbon ratios for the five different types of plumes for particulate sulfate and organics. The categories start from the left with the exclusively natural emission source volcano followed by "pure" BB, while the anthropogenic and Asian factors increase towards the right as highlighted by the dashed box and orange arrow. To the right, background values for the Arctic free troposphere above Greenland are shown in grey (Arctic FT). Next, ARCTAS FT values including undifferentiated pollution episodes are presented in red, while the open dashed box stands for the background values. After that, European background FT conditions are displayed (grey box). The line of categories ends with a comparison of UTLS air masses in the Arctic as measured during ARCTAS (red box) and over Europe (grey box) as measured during CONCERT excluding volcanic influence.

Volcanic aerosol is represented by a dominant particulate sulfate component of 75 %. "Pure" BB plumes are characterized by a median sulfate fraction of 0.22, which is also true for the second plume type, a mixture of prevailing BB and little FF from NA and Europe with no influence from Asia. This is consistent with findings by Heald et al. (2008) who also report around 20 % of sulfate for BB plumes, Singh et al. (2010) who found roughly 17 % for aged (1-5 days) BB/FF plumes from North America during ARCTAS spring and summer, and Brock et al. (2010) reporting on 26 % particulate sulfate during ARCPAC (Aerosol, Radiation, and Cloud Processes affecting Arctic Climate) 2008, accounting only for contributions from particulate sulfate and organics. It has been observed that in aging BB plumes the growth factor for particulate sulfate is higher than for organic carbon (Formenti et al., 2003; Yokelson et al., 2009) which can explain the relatively high percentage of sulfate in the detected BB plumes over Greenland. Within the third class, FF dominated plumes from the same source regions, the median sulfate fraction rises to 0.29, similar to plumes characterized mainly by Siberian BB and little Asian anthropogenic influence (0.30). Asian fossil fuel dominated plumes with little Siberian BB contribution reach a sulfate fraction of 0.37. This shows that the major contribution

of particulate sulfate and thus acidic aerosol in the troposphere above Greenland originates from East Asian anthropogenic activity which is also highlighted by the orange arrow in the figure. The highest concentration of particulate sulfate throughout the POLARCAT campaign was $1.95 \pm 0.12$ µg $m^{-3}$ observed in an Asian fossil fuel influenced plume on 14 July. This is consistent with observations of Asian industrial plume transport and evolution out of NE China (Li et al., 2010). The interpretation of ice core data from Summit, Greenland, by McConnell et al. (2007) also attribute the major sulfur contributions to East Asian industrial development within the last decades. Calculating the theoretical composition of "pure" Asian anthropogenic emission episodes based on the fraction of FLEXPART CO passive tracer fire contribution for these plumes (54 to 85 %) and the observation of 22 % sulfate contribution from "pure" fire plumes, the fraction of particulate sulfate in "pure" Asian anthropogenic emission plumes is estimated to be $88 \pm 34$. %. Siberian fires are estimated to contribute more than 56 % of Northern Hemispheric CO from extra tropical BB on a yearly average based on the period from 1997 to 2007 (van der Werf et al., 2006). However, based on the plumes detected during the POLARCAT summer campaign, it was not found that Siberian BB had a stronger influence on aerosol composition over Greenland than Canadian BB. This might be on the one hand due to the longer transport pathway from Asia, resulting in more complete removal en-route to Greenland, and on the other hand due to the meteorological conditions which favored transport of NA BB plumes. The median particulate sulfate fraction for non-plume periods over Greenland is 0.23 µg $m^{-3}$ with larger variability. [This paragraph is adapted from Schmale et al. (2011).]

ARCTAS free tropospheric measurements including pollution episodes show a median particulate sulfate fraction of 0.32 % which is comparable to the categories of FF/BB no Asia and Siberian BB with little FF from Asia. However, the variability is large. The respective background measurements result in smaller variations and a mean particulate sulfate contribution of 20 %. This might still reflect the important influence from local BB events that were persistent throughout the entire campaign. The European background free troposphere shows a higher contribution of sulfate aerosol with an average of 49 % which possibly represents the highly industrialized environment and absence of biomass burning in late October, 2008. Comparing the Arctic and European UTLS there is no significant difference in the data. Both regions are characterized by a mean sulfate contribution of about 60 %. This is coherent with the increase of sulfate aerosol above the local tropopause in both cases as discussed in section 4.1 and shown in Figure 70.

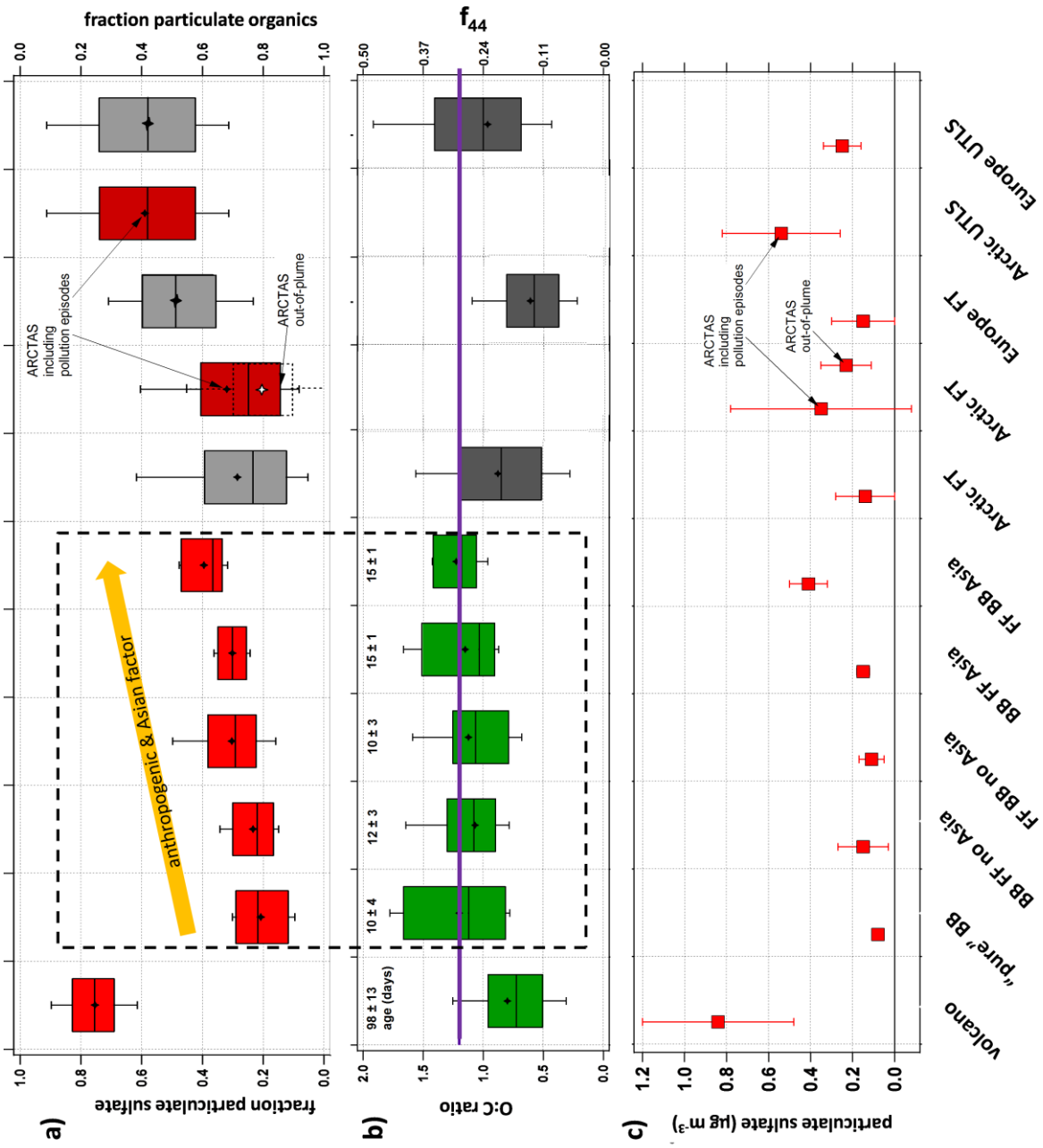


**Figure 75: Chemical aerosol properties of different air mass categories. Panel (a) presents the fraction of particulate sulfate and organics. The red boxes denote the variance of the inter quartile range, the whiskers the 10$^{th}$ and 90$^{th}$ percentile, the horizontal bar in the box the median and the star the average value. Grey boxes denote background conditions. Panel (b) uses the same notation for the O:C ratio and indicates the average age of the plumes. Panel (c) shows the particulate sulfate mass concentration of each plume category including one standard deviation.**

### *4.3.2 O:C ratio of organic matter*

Figure 75 b) indicates the average age of a plume class since emission. For the volcanic aerosol it was simply deduced by counting the days between eruptions and detections. POLARCAT plume age was calculated by averaging over the mean age of all individual pollution episodes within one category based on FLEXPART data. FLEXPART calculations derive a so-called age spectrum for each air mass probed by the aircraft for several types of tracers. For the average age calculation of a single plume the CO passive tracer age spectrum was used (Stohl et al., 2003). Each day's contribution (1 to 20 days back from the time of sampling) was weighted based on the excess CO mixing ratio per plume and multiplied by the specific day of contribution. The sum over the weighted daily contributions allows for an estimation of the average age of a pollution plume. The plot shows that long-range transport from North America and Europe took roughly 10 days while plumes from Siberia and Asia generally travelled 15 days or longer. These periods are comparably long for aerosol transport and make particles subject to a variety of processes along the way. Among others these processes include aging by photochemical processing.

The photochemical state of organic aerosol can be derived from the O:C ratio (e.g. Jimenez et al., 2009; Heald et al., 2010). The O:C ratio can be approximated with a unit resolution AMS by determining the ratio of the organic contribution of *m/z* 44 to the total organic mass, denoted as $f_{44}$ (Aiken et al., 2008; Ng et al., 2010). For all types of detected plumes in Greenland the median and average O:C ratio oscillated between 1.0 and 1.2 which corresponds to LV-OOA (Jimenez et al., 2009), i.e. aged organic matter. No significant difference between the youngest (~ 3 day) and oldest (~ 16 day) plumes within the categories could be found, which implies that the organic aerosol components are already highly processed after roughly one week of transport and that additional time spent in the free troposphere does not increase the O:C ratio significantly. The finding is consistent with results from Ng et al. (2010) who found an asymptotic trend towards an O:C ratio of 1.2 with age as indicated by the purple line in Figure 75 b). Furthermore, this implies that the characteristics of the organic aerosol advected to Greenland do not differ much in terms of chemical characteristics despite their distinct origins (shorter travelled particles correspond to NA, longer travelled ones to Siberia and East Asia) and they tend to form a uniform type of LV-OOA. This observation is coherent with observations by above mentioned authors who argue that organic aerosol "properties become remarkably similar" (Andreae, 2009) as they age in the atmosphere. The POLARCAT non plume O:C ratio (median: 0.85, mean: 0.88) implies that the aerosol background is less aged. A possible explanation is the contribution of local source emissions, presumably organic aerosol emissions from the North Atlantic Ocean. As the sea is also a source for sulfur containing aerosol this assumption is in good agreement with the relatively high sulfate aerosol concentrations for the non-plume periods (see panel a).

The volcanic aerosol O:C ratio is represented by a median of 0.72 and seems to be markedly lower than the other values, but the high variability indicated by the error bars shows that this finding is statistically not significant. One would expect stratospheric aerosol of roughly 100 days age to be even more oxygenated than tropospheric pollution plumes. Though it cannot be excluded that this deviation reflects the uncertainty of the O:C ratio determination from a unit resolution mass spectrometer there is a possible explanation for this observation. Zobrist et al. (2008) and Virtanen et al. (2010) argue that

secondary organic aerosol (SOA) forms amorphous solid-state, glass-like structures under ambient conditions not only in the upper troposphere at low temperatures but also even a few hours after particle nucleation onset. Given that temperatures in the stratosphere to where the volcanic aerosol was injected were at least as low as in the UT it is conceivable that the organic matter adopted such a glass like state which in consequence inhibits the diffusion of oxidants into the aerosol and blocks all further oxygenation (Zahardis and Petrucci, 2007). Based on such a scenario it becomes at least plausible that free tropospheric aerosol which might not have undergone such amorphous transformation to a comparable degree appears more oxygenated than far older stratospheric organic aerosol. The potential effect of enhanced bounce-off from the vaporizer in the AMS and a resulting reduced collection efficiency does not seem to play a significant role (Virtanen et al., 2010).

The O:C ratio in the European free troposphere is the lowest observed in this work with a median of 0.58. Considering the relative proximity to emission sources this seems plausible. Also, the increase in the O:C ratio with higher altitudes to a median value of 1.00 is comprehensible as emission might date back longer and photochemistry may be enhanced above clouds.

For ARCTAS measurements no O:C data was available.

### *4.3.3 Particulate sulfate mass concentrations*

To obtain an overview of the magnitude of aerosol mass concentrations for all plume classes and background conditions the average loading of particulate sulfate including one standard deviation was calculated (see Figure 75 c). Sulfate was chosen as this is the species with most data points above detection limit especially for out-of-plume categories. Volcanic aerosol shows the highest sulfate aerosol concentration most likely because of the strong emission source and the absence of wet removal processes in the lower stratosphere. Plume loadings encountered over Greenland are on average below 0.2 µg $m^{-3}$ except for the FF dominated Asian plumes. This is remarkable as these are the oldest observed plumes and were thus potentially subject to wash-out for longer time periods than the other aerosol plumes. Possibly this points towards the high emission source strength. Squares without vertical bars show such low standard deviation that they do not exceed the limit of the symbol. The Arctic free tropospheric background concentration measured during POLARCAT and ARCTAS is comparable to results from CONCERT and are located near the 0.2 µg $m^{-3}$ line. Non-background sulfate mass concentrations in the free troposphere and in the UTLS during the ARCTAS campaign show large variations indicating the frequent perturbations of the atmosphere through local and distant sources. The European UTLS shows a trend towards slightly higher mean particulate sulfate loading with 0.25 µg $m^{-3}$ compared to the European free troposphere.

## *4.4 Correlation between aerosol mass and carbon monoxide mixing ratio*

In the vicinity of a source, usually a positive correlation between CO or ΔCO and aerosol species, i.e. particulate sulfate and organic matter or black carbon, can be observed e.g. (Spackman et al., 2008; Singh et al., 2010; Yokelson et al., 2009). For all plumes discussed in this work, however, such a correlation cannot be expected for several reasons. Due to transport times between 3 and 16 or even near 100 days, the long distance from the source, aerosol scavenging during transport, especially in WCB events, and mixing of tropospheric and stratospheric air masses it is not possible to derive a correlation of total aerosol mass and CO mixing ratios. Also, a factor which needs to be taken into account when correlating CO enhancements with aerosol mass concentrations is that this technique works best when the trace gas enhancement is large compared to the background CO value. The plumes studied here do not show an intense increase of CO mixing ratio and the variability in background concentrations is difficult to quantify, hence the difficulties in deriving a correlation. Figure 76 shows the total aerosol mass concentration (particulate sulfate and organics) of all 48 identified plumes from POLARCAT measurements versus total CO mixing ratios in grey. There are several reasons for showing total instead of ΔCO values: On several occasions, individual plumes were embedded in long intervals of enhanced CO mixing ratios. In such cases ΔCO would be underestimated. Also, during mixing of tropospheric and stratospheric air masses ΔCO cannot be retrieved anymore. For background values no delta can be calculated even though there is variability to the vertical profile of CO. Episodes discussed individually in sections 3 to 3.3 are highlighted by symbols colored according to the measurement campaigns. Additionally, background conditions in the free troposphere (FT) and in the UTLS are indicated. As for ARCTAS only two individual plumes were discussed all perturbed FT episodes are resumed in one point (tag “FT plumes”) which is characterized by high variability in both aerosol mass concentration and CO mixing ratio. Average CO values for long-range transport plumes between 3 and 16 days range between 90 and 161 nmol $mol^{-1}$. The lower limit is highlighted by Plume V, the stratospheric intrusion observed during POLARCAT. The CO mixing ratio is possibly relatively low in this case because CO-poor air mixed into this plumes. Near the upper CO plume limit, Plume II, a relatively young (maximum 5 days old) air mass is found. Here, dilution might not be as advanced as in other cases. It is worth pointing out that this region of the plume space is also characterized by the tropospheric intrusion into the lower stratosphere by Siberian BB air masses.

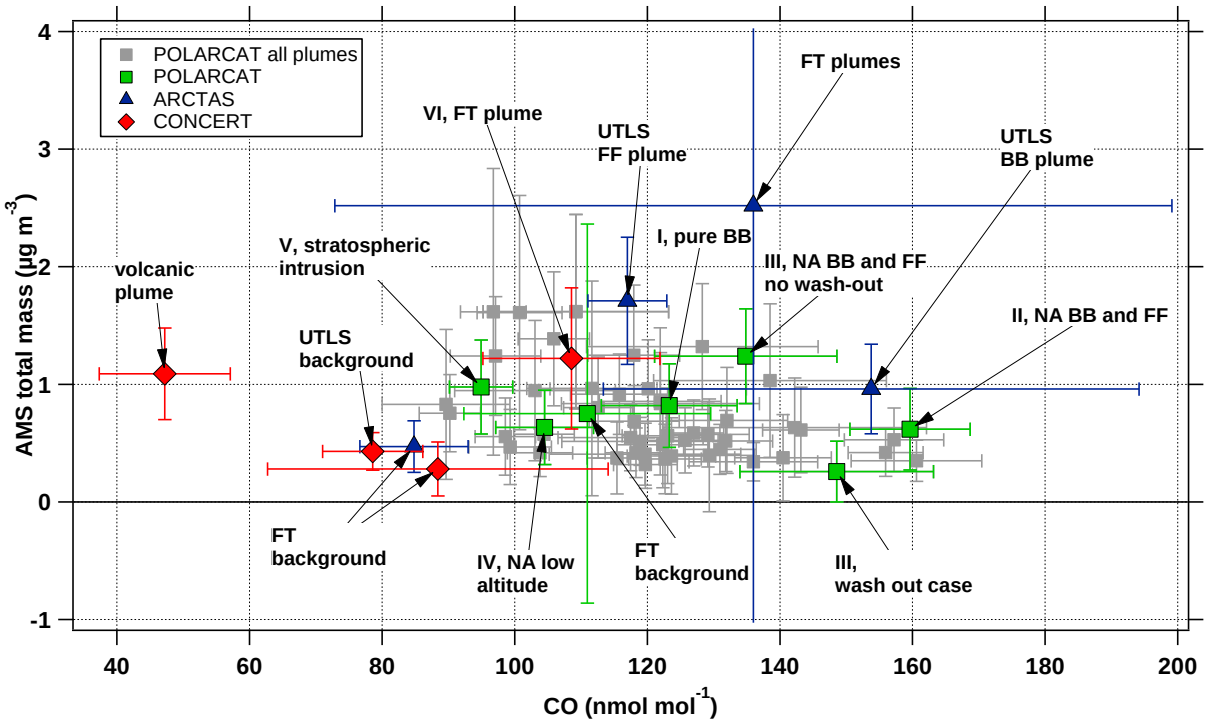


**Figure 76: Correlation of AMS total mass (sulfate and organics) and measured total CO. All individually discussed plumes are highlighted and colored according to the campaign name. The roman numbers refer the plume notation in Table 13 from section 3.2. Background values are also displayed. FT refers to free troposphere. The error bars denote one standard deviation from the average measurement value.**

The mean free tropospheric background values for ARCTAS and CONCERT are 85 and 88 nmol $mol^{-1}$, respectively. The POLARCAT unperturbed mean value is 111 nmol $mol^{-1}$ and displays a much larger variability than the other two points. This is most likely due to the difference in methods for background determination. While for ARCTAS a threshold criterion based on CO and $CH_3CN$ data could be applied, for POLARCAT all measurements which were not attributed to a pollution episode were declared unperturbed. For CONCERT only one tropospheric plume could be identified based on enhanced aerosol mass concentrations. On the left side, the volcanic aerosol data point stands out as this measurement denotes the only exclusively stratospheric plume.

## *4.5 Lifetimes and wet scavenging*

The difficulty of relating CO enhancements and aerosol mass concentration as discussed above is associated with the aspects of lifetimes and aerosol deposition. Generally, the CO lifetime exceeds the aerosol lifetime far enough to function as a passive tracer as it is not subject to wet deposition like particulate matter. Figure 5 (Jaenicke, 1988) in the introduction shows that accumulation mode particles have a lifetime between 1 and 10 days in the free troposphere which is prolonged in the tropopause region due to less scavenging by precipitation. Linked to this is the question of how much of the emitted and secondary aerosol particles reach the sampling area after long-range transport. To derive an aerosol lifetime, ideally particles from the same source region, i.e. same chemical quality, and comparable emission strengths, at a variety of ages are measured. However, despite the lack of detailed information on the source region and meteorology at the time of emission and thus source strength, it was possible to relate the total measured aerosol mass to the FLEXPART calculated age for 10 plumes during POLARCAT. This results in an exponential distribution from which an aerosol lifetime between 7 and 11 days can be derived (Figure 77 a), green line). For this calculation dilution and deposition over time were assumed to be similar for the chosen plumes as they have comparable chemical properties making them similarly hydrophilic/hydrophobic. The 10 selected plumes are characterized by mainly NA FF and little BB influence (see bold written plumes in Appendix B). The red cross in Figure 77 denotes an outlier. OFFLINE back trajectories suggest that this air mass was uplifted in a WCB event like Plume II as discussed in section 3.2.2.1. Furthermore, in-situ measured relative humidity was around 90 %. Thus, wet deposition along the pathway and/or in-situ is likely for this case. A $\tau$ ranging from 7 to 11 days is reasonable and consistent with lifetimes determined by other authors. Jaenicke (1988) finds a lifetime between 1 and 10 days, Paris et al. (2009) found an experimental equivalent black carbon lifetime of 5.1 days for Siberian forest fire emissions, Koch and Hansen (2005) a modelled BC lifetime of 7.3 days, and Farina et al. (2010) modelled 6.8 to 16 days for SOA depending on the scenario on a global scale. Exponential fits with lifetimes of 5, 7, 9, 11, and 16 days have been added to Figure 77 a) in grey. [This paragraph is adapted from Schmale et al. (2011).]

The aspect of aerosol growth with time by condensation of semi- and low-volatile gases is neglected in this consideration as no data is available. This effect might lead to a slight overestimation of the lifetime. Figure 77 b) shows the result of a CO lifetime calculation for the same 10 plumes. The total CO mixing ratio is related to the average FLEXPART age and shows an exponential correlation with an average $\tau$ of 26 days ranging between 19 and 42 days. This outcome is in good agreement with the common assumption of a global CO lifetime of 30 days in summer and the finding by Real et al. (2008) that CO lifetime decreases to roughly 23 in plumes with high oxidative capacity, i.e. with high ozone and water vapor abundance. Hence, CO might not always be the ideal tracer to identify pollution episodes. In this light the integral consideration of gaseous and particulate tracers for plume identification becomes even more important. Here, total CO was chosen instead of $\Delta$CO due to the high variability of background conditions and the embedment of single plumes in extended perturbed periods. Based on the assumptions mentioned above a comparable emission source strength makes such a correlation valid.

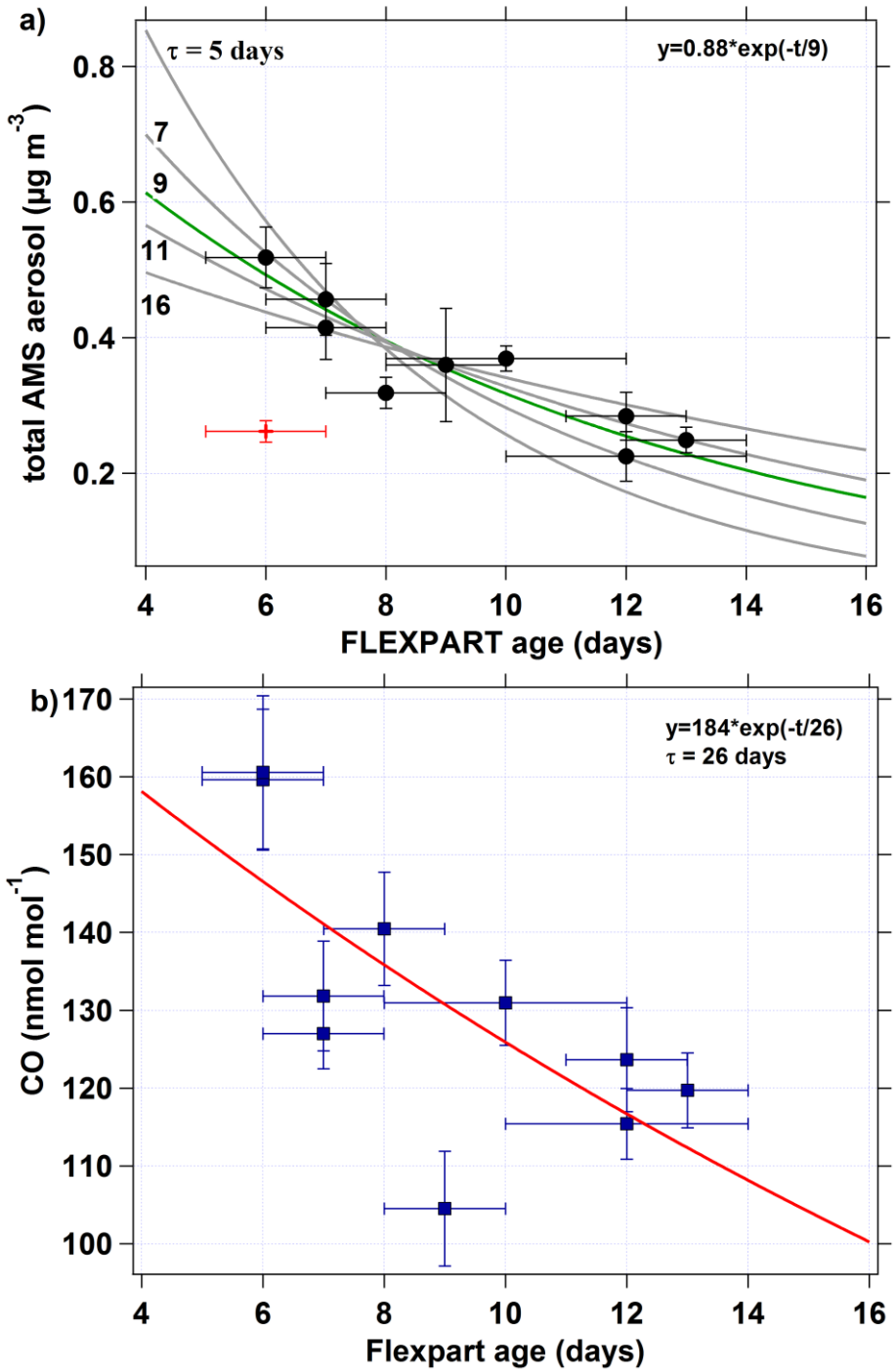


**Figure 77: a) Aerosol and b) CO lifetime in North American FF and BB influenced pollution plumes. The vertical and horizontal bars denote the one standard deviation from the mean value. In the upper right corner of each panel the exponential function is given with a τ of 9 and 26 days for aerosol and CO, respectively. [Panel (a) was published in Schmale et al. (2011).]**

A major factor in reducing aerosol mass over time is wet deposition. To investigate this aspect, HYSPLIT 10-days back trajectories were calculated from the sample position of each of the 48 plumes encountered during the POLARCAT campaign. Three trajectories per plume were released at the full hour closest to the encounter from the average plume coordinates (latitude, longitude, altitude) and at an altitude ± one standard deviation from the mean sample height. Results from the three trajectories

were averaged. Figure 78 shows the correlation of the ratio of total aerosol mass detected by the AMS and the CO mixing ratio to the amount of precipitation along the back trajectories based on HYSPLIT results (see section 2.6.2. on page 67).

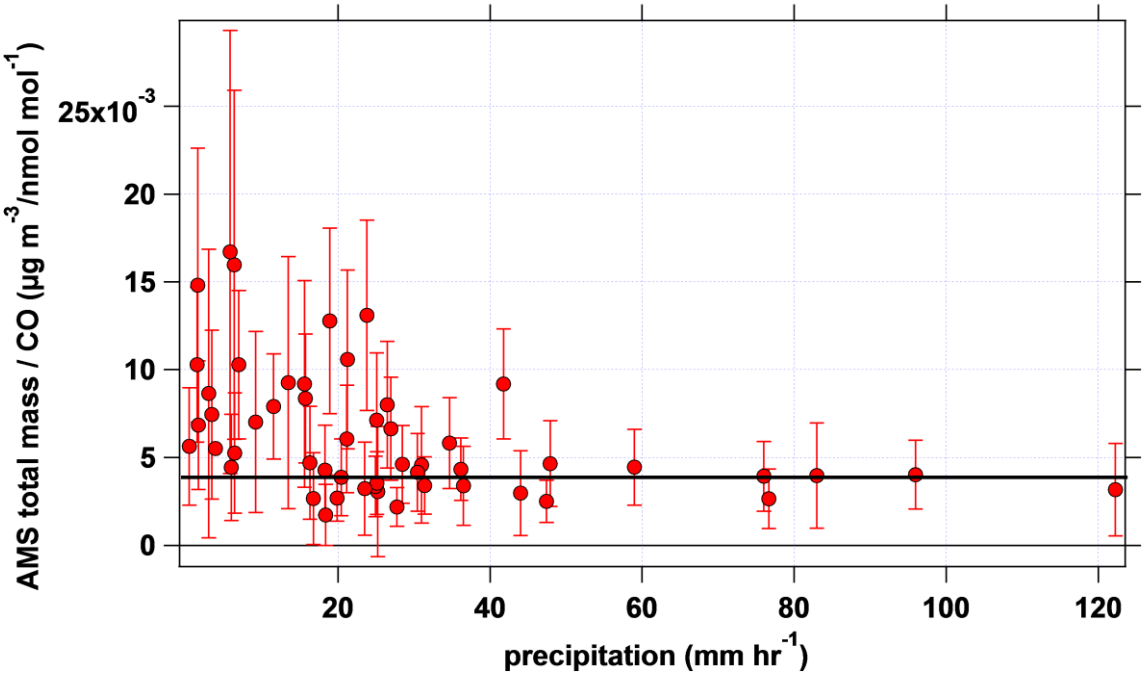


**Figure 78: Relation between the ratio of aerosol total mass and CO mixing ratio to the amount of precipitation along the 10-days back trajectories for each of the 48 plumes detected during the POLARCAT campaign. The vertical bars denote one standard deviation of the ratio. The horizontal bar at 0.004 µg $m^{-3}$ $nmol^{-1}$ mol indicates the average aerosol to CO ratio above 30 mm $hr^{-1}$ precipitation.**

All modelled precipitation events in the history of one plume were added. Even though the length of each rain event is not known the simple sum over all data points is an appropriate measure of the potential wash-out occasions (Matsui et al., 2011) since most of the aerosol is precipitated in the early phase of an event. Dividing the aerosol mass concentration by the CO mixing ratio provides a kind of normalization to effects like emission source strength and dilution. The vertical bars denote one standard deviation of the ratio. The figure shows that beyond 30 mm $hr^{-1}$ of precipitation the ratio of AMS aerosol mass and CO is nearly constant with an average value of 0.0004 implying that even if heavy rainfall events occur during transport not all aerosol is washed out. Accounting for an approximate 100 nmol $mol^{-1}$ CO background mixing ratio (see Figure 71) about 0.4 µg $m^{-3}$ submicron aerosol mass remains which reflects well the median mass loading ranging between 0.25 and 0.50 µg $m^{-3}$ in the vertical profile (see Figure 70). Below 30 mm $hr^{-1}$ there might be a trend indicating that the less precipitation along the pathway occurred the more aerosol arrives over Greenland. However, the variability in the data is very large and does not allow to draw a definite conclusion. More data needs to be analyzed for this purpose. Additional aerosol size distribution data is available from the POLARCAT-Grace campaign which was conducted out of Kangerlussuaq at the same time as POLARCAT-France.

## *4.6 Geographical locations of aerosol deposition*

When studying aerosol in the Arctic and high northern latitudes not only the direct and indirect radiative effects are of interest but also the deposition of particulate matter on the ground. FF emissions lead to acidic aerosol formation due to the high particulate sulfate content as illustrated in section 4.3.1. Scavenging of this type of aerosol fosters the acidification of the Arctic (AMAP, 2006) and bears consequences for ecosystems and biota. Deposition of FF aerosol in southern Greenland was found to be particularly dominant in summer (Doherty et al., 2010). BB related aerosol contains a significant amount of black carbon e.g. (Hegg et al., 2009) and thus reduces the surface albedo an effect which is particularly important on glaciers and snow covered surfaces as it results in enhanced surface warming and melting (Quinn et al., 2008). Hegg et al. (2010) and Doherty et al. (2010) found that 31 ± 10 and 20-52 %, respectively, of the light absorbing aerosol mass is composed of mainly organic carbon. So based on the amount of AMS detected organic matter the light absorbing effect of the observed pollution plumes can be estimated.

To investigate where aerosol got in contact with the surface for pollution episodes observed during the POLARCAT campaign precipitation events along the backward and forward HYSPLIT trajectories of each plume were plotted (see Figure 79). The same method for calculating these trajectories and the attributes as described for results shown in Figure 78 was applied. The first rainfall along the back trajectories (panel a, green circles) indicates events close to the source and shows that not much precipitation occurred over the Eurasian continent while emissions from North America seem to be precipitated rather near-source. Considering the last rainfall before plume sampling, the region of south-west Greenland appears to be impacted more severely than other snow and ice covered regions. This is underlined by the precipitation events following the measurements (panel b). Again south-west Greenland seems to be the main target region. However, according to Box et al. (2009) the western Greenland ice sheet experienced an overall negative precipitation anomaly of -250 mm in 2008. The measured pollution plumes are transported away from Greenland by the westerly winds towards Iceland and north-west and Central Europe where most of the rainfall occurred within the 10 days following the measurements. It can, however, be assumed that most of the particulate matter had been scavenged before reaching Europe even though single events of e.g. BB pollution have been reported (Petzold et al., 2007). Concerning this result in general, it has to be kept in mind that the here found primary target region in Greenland is biased by the available flight tracks. A mission out of e.g. north-east Greenland could yield a very different result. Nevertheless, the POLARCAT findings reflect observation by other authors. As mentioned above, Doherty et al. (2010) found that southern Greenland is impacted significantly by FF plume deposition. Events like Plume IV (Ohio Valley) are examples of how FF pollution is exported at low level from North America and deposited in southern Greenland even though it has to be kept in mind that a single measurement cannot make a statement about the frequency with which such events occur. McConnell et al. (2007) derived from their findings in ice-cores that Asian FF plumes play an increased role in the pollution of the Greenland ice sheet based on the enhanced concentrations of sulfur. This result can also be reflected by POLARCAT observations since cross-polar transport advects Asian pollution directly towards Greenland, and as Figure 75 a) and c) show, the sulfur content of Asian FF plumes is increased relatively and absolutely compared to the other categories that were measured.

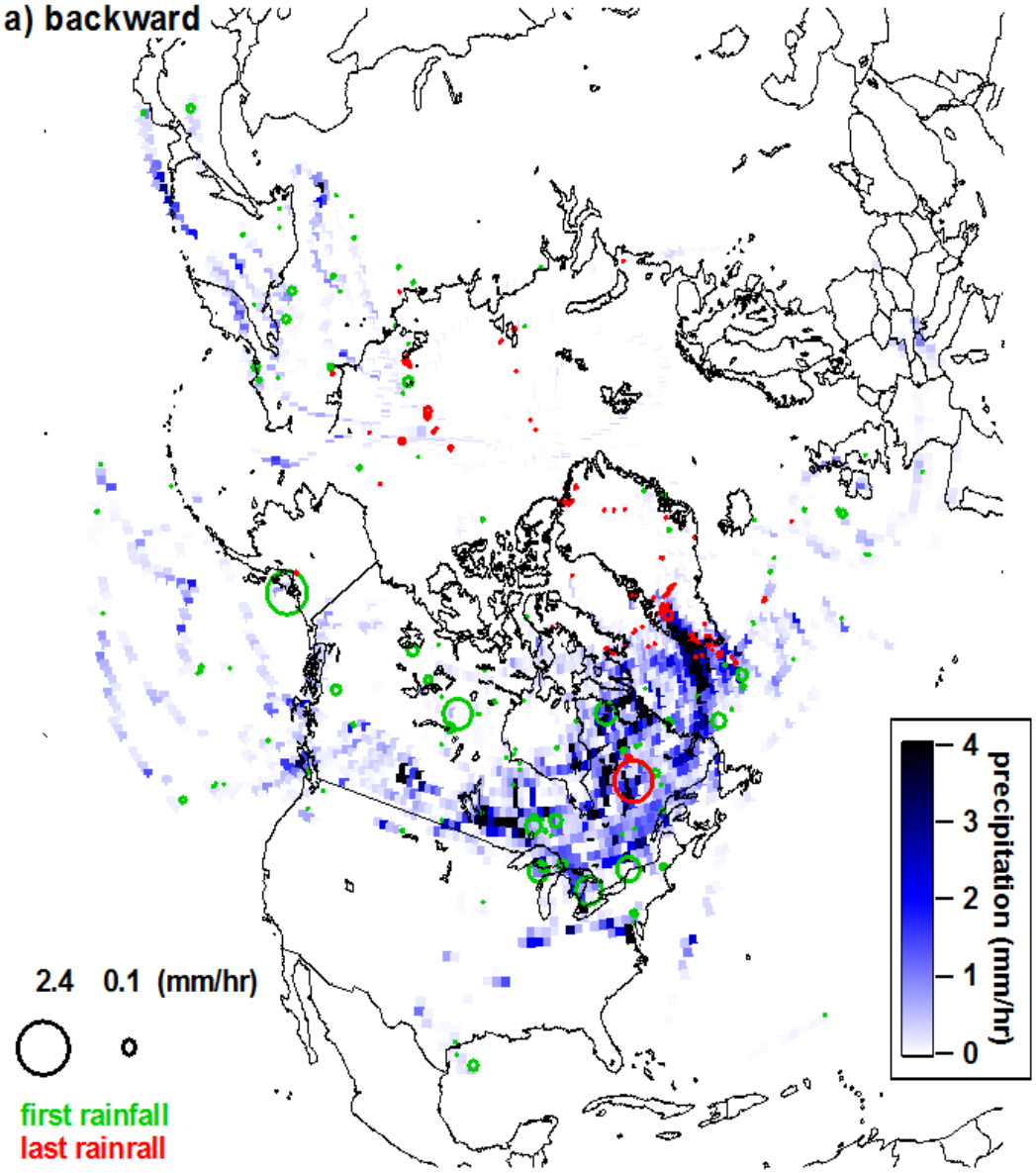
a) backward
2.4 0.1 (mm/hr)
first rainfall
last rainrall
precipitation (mm/hr)
4
3
2
1
0

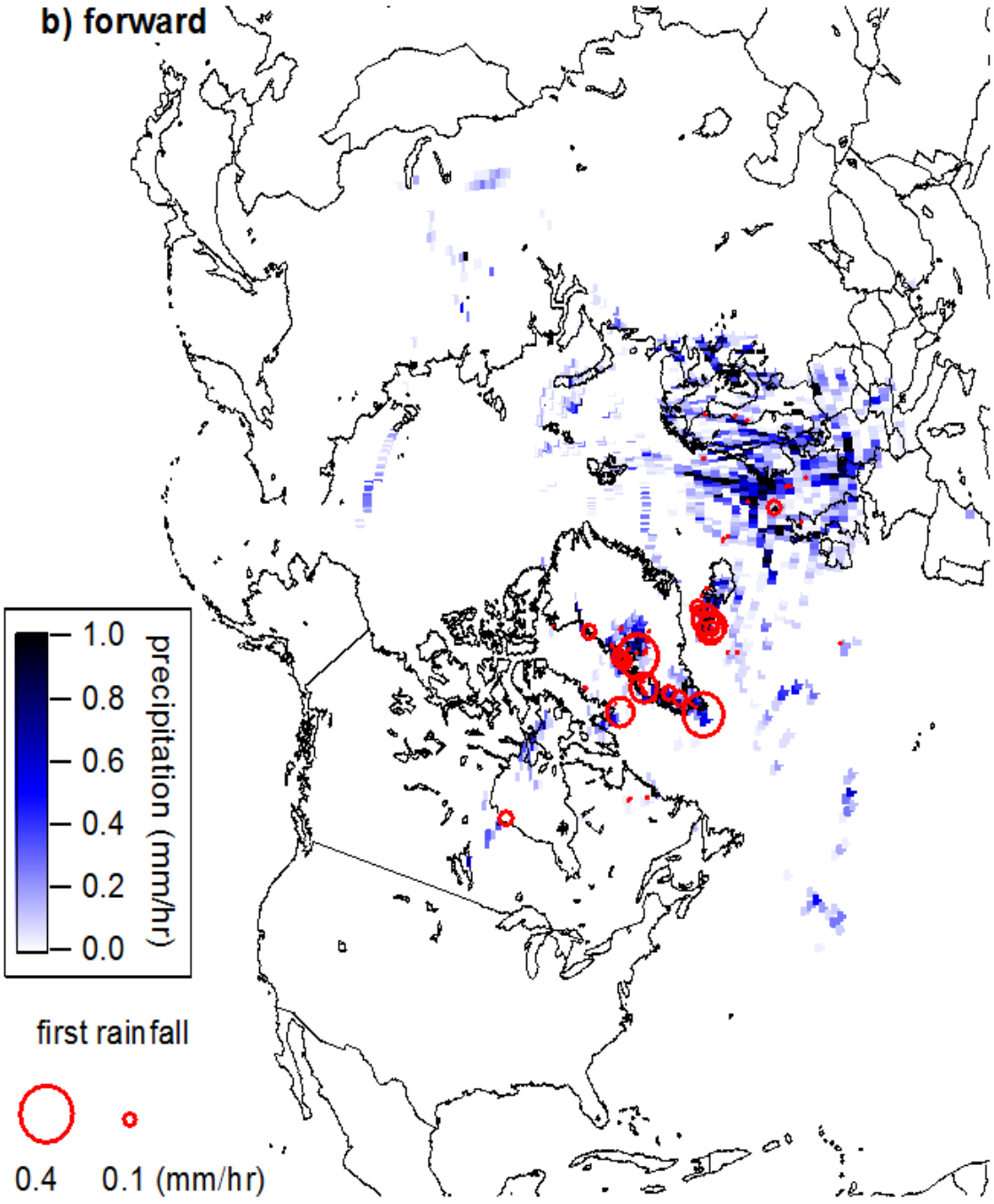


**Figure 79: Precipitation events along a) backward and b) forward 10-days trajectories of each pollution plume observed during the POLARCAT campaign. The green circles in a) indicate the location of the first rainfall after emission, the red circles the last rainfall before interception. In b) the red circles highlight the first precipitation after the measurement.**

## *4.7 Size Distributions*

Here an overview on derived size distributions for different pollution plume types is given. Due to the availability of data the focus is laid on the POLARCAT campaign. Since aerosol concentrations were very low for the determination of a mass size distribution with the AMS, only two plumes provided sufficient signal. For all other cases SMPS data are shown. Additionally, the volcanic aerosol size distribution is displayed.

Size distributions of aerosol number and volume concentrations measured by the SMPS during the POLARCAT campaign have been averaged for each of the five plume classes (see section 3.2) and for all out-of-plume periods (see Figure 80 (a and b) and fitted with lognormal functions (see Table 21 inAppendix F). All size distributions show clear enhancements in the accumulation mode as expected after transport times of one to two weeks (Jaenicke, 1980). The non-plume and "pure BB" size distributions ( Figure 80 a, b black and dark green trace, respectively) show a significant enhancement in Aitken mode particles between $24 \pm 1$ and $44 \pm 2$, and $66 \pm 11$ nm, respectively, based on the volume. An additional accumulation mode with $372 \pm 2$ nm in background conditions and with $387 \pm 48$ nm for BB perturbed conditions is present. Mainly BB influenced non Asian air masses also present two modes at $55 \pm 2$ nm and $150 \pm 12$ nm. For a detailed discussion on the North American BB plumes see Quennehen et al. (2011). Air masses with mainly Siberian BB contribution display a broad mono-modal size distribution (bright green trace) with $510 \pm 47$ nm. Asian FF dominated plumes again show two modes (red trace) with $180 \pm 44$ nm and $411 \pm 14$ nm. Comparing the FF dominated air masses from non-Asian to Asian regions, it was observed that the Asian second modal diameter is larger with $362 \pm 1$ nm versus $411 \pm 14$ nm, respectively. This is also true for primarily BB influenced pollution from Canada and Siberia. The accumulation modes of mixed BB dominated and FF episodes appear larger than FF dominated plumes with less BB contribution for both regions, North America and Siberia/Asia. In panel b the data of the observed volcanic aerosol in October 2008 is added as mass size distribution (*dM/dlog(dp)* in $ng*10^{-2}\ m^{-3}$) as a function of the mobility diameter. In section 3.1.4 the conversion from the vacuum aerodynamic to the mobility diameter has already been discussed. It is noticeable that the much older volcanic particles have a significantly smaller mean diameter of $195 \pm 2.4$ nm than the tropospheric aerosol. The result that the Mts. Okmok/Kasatochi aerosol was much smaller than Pinatubo particles of comparable age as discussed in section 3.1.4 was attributed to the lower abundance of $SO_2$ injected into the stratosphere. In comparison to tropospheric particles the low availability of water vapor in the stratosphere might be the significant factor that limits the growth of the volcanic particles despite the long residence time.

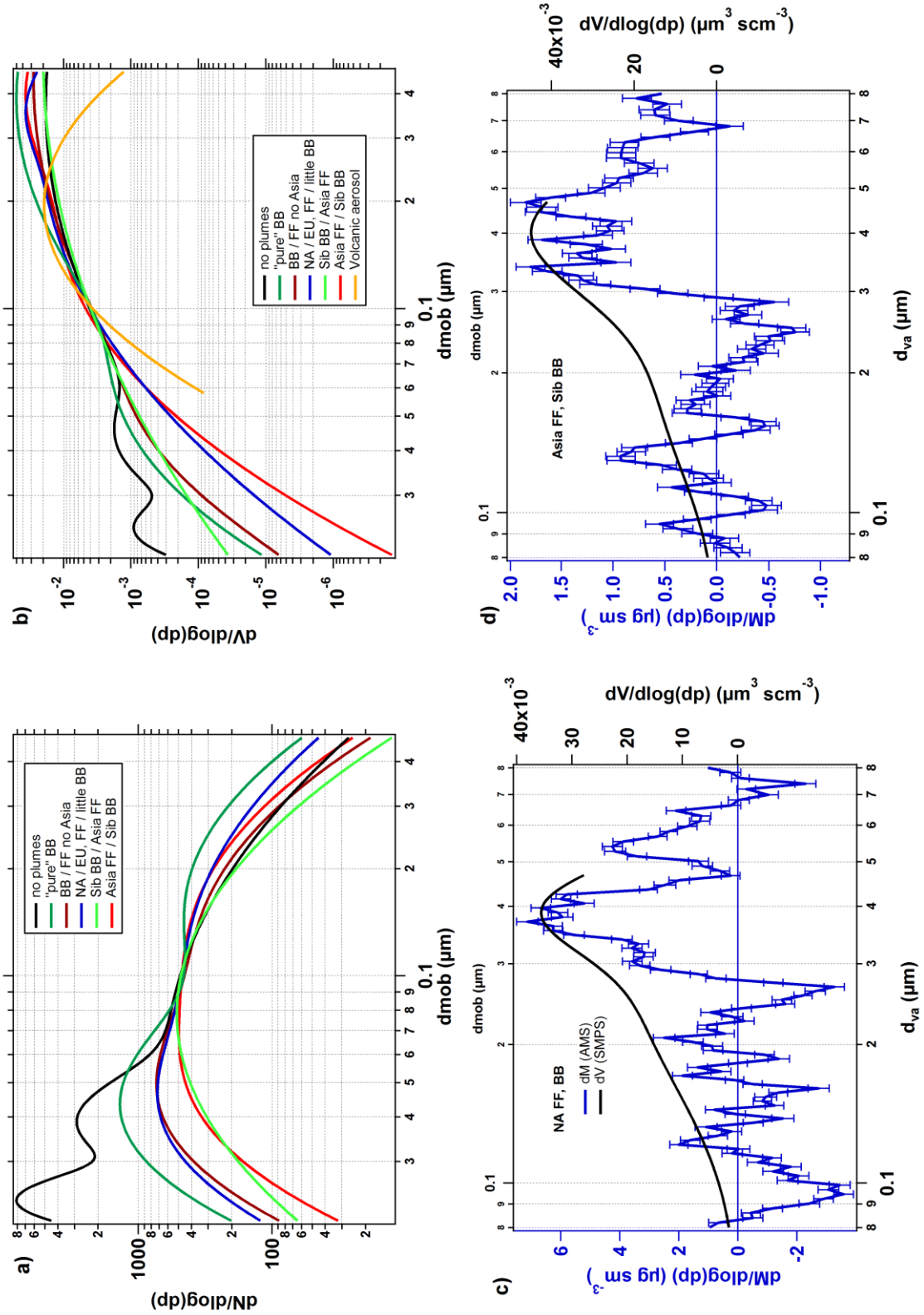


**Figure 80: Lognormal fits for SMPS number (a) and volume (b) size distributions for all five plume categories and all non-plume periods. Panel (b) shows additionally the volcanic aerosol size distribution as *dM/dlog(dp)* in ng*10$^{-2}$ m$^{-3}$ (compare Figure 37). (c) and (d): AMS mass and SMPS volume size distributions (lognormal fits) for an Asian FF and Siberian BB influenced plume (Plume IV), and a North American FF and BB influenced plume. The AMS data has been smoothed with a sliding average over 10 size bins and the statistical counting error is represented by the error bars.**

Panels (c) and (d) show the mass size distributions for 30 minutes of North American and 23 minutes of Siberian/Asian mixed plumes of 2 weeks age from AMS data along with the volume distributions from SMPS data. The lognormal fits to the AMS mass distributions (not shown) have a mean diameter ($d_{va}$) of 371 ± 3 nm with a full width at half maximum (FWHM) of 125 nm and $d_{va}$ = 435 ± 22 nm and FWHM = 253 nm, respectively. The North American plume possibly contains a second mode with a mean diameter of 548 ± 6 nm and a width of 88 nm at FWHM. The SMPS volume size distributions show two modes with 285 ± 80 nm and 400 ± 13 nm for the NA plume, and 186 ± 15 nm and 4215 ± 15 nm for the Asian plume. Based on these results Asian particles again appear slightly larger. This could be due to the longer transport times (see Figure 75 panel b) as particles have more time to grow. However, panels c) and d) clearly show that the AMS mass size distributions are very noisy up to roughly 300 nm. The statistical error (vertical error bars) is most likely underestimated because it should cross the zero line when the size distribution only reflects noise. Hence, the distribution up to 300 nm is not trustworthy. Furthermore, the distance from the zero line to the most negative and positive points below 300 nm can be used to estimate the inaccuracy for larger diameters. The larger the negative areas, the larger is the positive areas of the size distributions, because the integral over all diameters provides the total aerosol mass as measured in the mass spectrum mode. The purpose of showing these two AMS size distributions here is to illustrate that the obtained size distributions have to be interpreted very carefully. If data were more accurate one could speculate if the gaps in both size distributions between 200 and 300 nm are real and might reflect some refractive component of the aerosol. Considering that only 10.8 seconds (panel c) and 14.4 seconds (panel d) of particle time-of-flight measurements were averaged after accounting for the duty cycle and that the total mass of these two plumes was roughly 1.0 and 0.8 μg $m^{-3}$, it cannot be expected to obtain a highly accurate size distribution with the AMS. Instead the AMS could measure solely in mass spectrum mode while size information is provided by other instruments such as the SMPS. [This paragraph is adapted from Schmale et al. (2011).]

# 5. Conclusions and outlook

The interpretation and compilation of the data obtained during the POLARCAT and CONCERT campaigns complemented by ARCTAS results contribute to the limited knowledge we have about aerosol characteristics in the free and upper troposphere and lower stratosphere. So far, only very few aircraft-based in-situ measurements are available in altitudes above 8 km, as well as in such remote regions like the Greenland troposphere.

One of the main outcomes is the chemically resolved vertical profiles (see Figure 70) which reveal important information on a number of different aspects. The degree of perturbation of the remote Greenland troposphere during summer is such that aerosol mass loadings are in the same order of magnitude as over Europe. The chemical composition, however, is distinct (see Figure 75). European free tropospheric aerosol contains a higher fraction of particulate sulfate most likely due to the vicinity of anthropogenic emission sources. The sub-Arctic aerosol might have been influenced more strongly by biomass burning related to the time of year when measurements were conducted leading to a higher fraction of particulate organic matter. Also, the degree of oxygenation of organic matter over Greenland is higher than over Europe. This reflects the long transport times between 3 and 16 days for these plumes. Generally, the organic O:C ratio reached a value near one in all cases despite the different emission source types and regions. This implies that after a time of roughly 3 days organic aerosol reaches a uniform state of oxygenation in the free troposphere and that this homogenization may lead to similar radiative and hygroscopic properties. Additionally, a particle lifetime of 7 to 11 days was derived for North American BB and FF influenced aerosol. Such results, vertical profiles, chemical composition and lifetimes, are especially useful for modeling studies that depend on experimental values.

Next to these ensemble results many more details were revealed by the analysis of case studies. Among those, it is worthwhile to mention that despite frequent uplift of pollution outflow in WCB which are associated to wet deposition a significant amount of aerosol survives the lofting and thus perturbs the sub-Arctic and Arctic atmosphere. Furthermore, several cases of tropospheric polluted air mass intrusions into the lower stratosphere were observed. This is of particular interest because aerosol lifetime is enhanced in this regime since wet deposition as a removal factor does not play a significant role. The aerosol can be transported over even longer distances and effects, such as changing the abundance of climate sensitive species like water vapor and ozone, can grow important. This is also true for the direct injection of volcanic aerosol into the stratosphere. The new finding in this context is that the particulate matter in the volcanic aerosol layer was found to consist of 21 % organic material which has implications for heterogeneous chemistry that have not been considered yet. With respect to stratospheric air mass intrusions into the troposphere the results of a simple modeling study with CiTTyCAT suggest that the mixing of ozone rich and humid air masses does not contribute significantly to the formation of secondary aerosol mass in the UTLS.

Future trends of aerosol concentrations and composition in the atmosphere can change in many respects compared to the current situation. The industrial development of many countries is currently under way and it can be expected that emissions will increase, especially in regions like East Asia (Asian Development Bank, 2008). Thus more exhaust gases will be emitted and the primary and

secondary aerosol load will increase which bears consequences along the transport pathways and for receptor regions. Based on earlier observations and those made during POLARCAT and ARCTAS enhanced emissions in East Asia contribute already significantly to the pollution of the Arctic and will gain importance in the future. In addition, the soon likely opening of the Northwest and Northeast passages in the Arctic Ocean implies that inner Arctic emission sources will gain in significance. Not only ship traffic is likely to increase but also the exploitation of natural resources in the Arctic will attract emission related human activity. Knowing that the Arctic is a very climate-sensitive environment legislative and technological action must be taken to prevent uncontrolled aerosol and precursor gas emissions. However, while it seems more effective and technologically easier to prioritize the targeting of short-lived climate forcers such as black carbon, long-lived species like carbondioxide and methane must not be neglected. In addition to legislative or convention-based measures an extended network of Arctic monitoring stations could assure the compliance of potential polluters. Also, in a warming climate, it is hypothesized that boreal forest fires might gain in intensity, especially in Eurasia (see discussion in Girardin et al., 2009), which implies enhanced emissions bearing consequences for all receptor regions and especially the Arctic.

Another receptor region of increasing aerosol and precursor gas emissions from Asia seems to be the stratosphere (Hofmann et al., 2009), even though another study (Vernier et al., 2011) found that rather moderate volcanic eruptions are responsible for the enhanced particle backscatter signicals between 20 and 30 km altitude. In this light, the study of troposphere to stratosphere exchange involving aerosol transport becomes even more important as we are still far from understanding the source-receptor relationship, transport pathways, and how aerosol properties are changed in such processes. Both types of aerosol, of Asian anthropogenic and volcanic origin, which seem to contribute to the stratospheric aerosol layer are composed of particulate sulfate and organics. Therefore, further chemical measurements of lower stratospheric aerosol are important to provide a data basis for model calculations of heterogeneous chemistry in the stratosphere which influences the abundance of trace gases such as ozone. In this context, it is also advisable to investigate the influence on new particle formation events from pollution precursor gases during mixing events of stratospheric and tropospheric air masses more thoroughly. The modeling study conducted in this work shows that the chemical conversion of $SO_2$ to $H_2SO_4$ which is mainly present in the particle phase is enhanced during such mixing events. Even though the produced particulate mass is negligible in comparison to observed pollution events, the newly formed particles might be a source for stratospheric aerosol. While respective model calculations involved sulfuric acid and nitric acid (e.g. Khosrawi and Konopka, 2003) the influence of organic precursor gases on particle nucleation events has not been considered yet.

Given that the scientific community cannot yet quantify the aerosol radiative impact with high certainty based on the latest IPCC report in 2007, it seems even more important to enhance our knowledge on atmospheric aerosol. For this purpose, it has to be kept in mind that not only targeting highly polluted areas but also remote and almost unperturbed regions to obtain insights into aerosol background concentrations and properties (chemical, optical and microphysical) is necessary. Nevertheless, establishing knowledge of global aerosol transport pathways out of strong emission areas is important. To obtain a more multi dimensional view of aerosol than during the POLARCAT

and CONCERT campaigns could provide, combining mass spectrometry with black carbon detection (e.g. by an SP2 (single particle soot photometer)), CCN counters, and optical property measurements is necessary. Ideally, the results from in-situ measurements are subsequently combined with remote sensing techniques, such that e.g. satellite and lidar data can deliver more detailed information on aerosol properties. Using remotely operating instruments that exhibit a larger coverage in time and space than costly and labor-intensive snapshots provided by in-situ field experiments will yield enhanced and up-to-date information which can be fed to modeling tools for regional, global or forecasting studies.

# 6. Acknowledgements

The acknowledgements have been removed from the electronic version of this thesis due to data privacy protection.

# 7. Appendix

## 7.1 Appendix A - PCI

Calculation of the Reynolds number inside the PCI:

$$Re = \frac{\rho * v * d}{\eta}$$

**Eq. 9**

With $\rho$: density of air (kg $m^{-3}$); $v$: velocity of the sample flow (m $s^{-1}$); $d$: inner diameter of the tube (0.0106 m for the PCI main tube, 0.0017 m for the sampling line); and $\eta$: dynamic viscosity of air (kg $(ms)^{-1}$). The density of air was approximated by the product of air density at 1000 hPa and 20°C (1.204 kg $m^{-3}$) and the ratio of 1000 hPa and $P_{PCI}$. The dynamic viscosity was assumed to be $1.7*10^{-5}$ kg $(ms)^{-1}$ which corresponds to 20°C and 1000 hPa. Both values are only an approximation of the actual value, which however has minor influence on the final Reynolds number.

All Reynolds numbers are below the critical value of 2300, hence the flow is laminar.

**Table 16: Reynolds numbers in the sampling line inside the PCI ($Re_{sample\ line}$) and in the PCI main tube ($Re_{PCI\ main\ tube}$). $V_{sample}$ is the volumetric flow through the critical orifice in front of the AMS standard inlet ($COr_2$).**

| PCI number | $P_{PCI}$ (hPa) | $Re_{PCI\ main\ tube}$ | $COr_2$ diameter (µm) | $V_{sample}$ ($cm^3$ $s^{-1}$) | $Re_{sample\ line}$ |
|---|---|---|---|---|---|
| 1, 2 | 190 | 34 | 200 | 5.0 | 310 |
| 3 | 110 | 20 | 250 | 9.4 | 337 |
| POLARCAT | 387 | 69 | 160 | 3.5 | 442 |

Calculation of the Stokes number (St) and modified Stokes number (St') after Lee et al. (1993) (see section 2.3.1).

$$St = \frac{\rho_p D_p^2 C_c U_o}{18 \mu d_1}$$

**Eq. 3**

$$\sqrt{St'} = \sqrt{\frac{\rho_p D_p^2 C_c U_s}{18 \mu d_1}} \left(\frac{d_1}{D_t}\right)^{0.58}$$

**Eq. 4**

$$C_c = 1 + \frac{1}{PD_p} * \left[15.60 + 7.00 * exp\left(-0.059 PD_p\right)\right]$$

**Eq. 10**

$$U_s = \sqrt{\frac{\gamma RT}{MG}}$$

**Eq. 11**

$$U_o = \frac{Q_o}{A}$$

**Eq. 12**

**Table 17: Parameters for the calculation of the Stokes and modified Stokes number**

| | Parameter | Unit | Value | Reference if applicable |
|---|---|---|---|---|
| $\rho_p NH_4NO_3$ | Particle density | g $cm^{-3}$ | 1.72 | |
| $C_c$ | Cunningham slip correction | - | See Eq. 10 | Hinds (1999) |
| $U_o$ | Velocity upstream of $CO_{r1}$ | m $s^{-1}$ | See Eq. 12 | |
| $\mu$ | Dynamic viscosity of air | µPa s | 18.6 (300K) | Lide (1996) |
| $U_s$ | Sonic velocity at $CO_{r1}$ | m $s^{-1}$ | See Eq. 11 | |
| $\gamma$ | Adiabatic index for dry air | | 1.4 | |
| *MG air* | Molecular weight of air | kg $mol^{-1}$ | 0.02896 | |
| *R* | Gas constant | J $K^{-1}mol^{-1}$ | 8.314 | |
| $Q_o$ | Volumetric flow rate upstream of $CO_{r1}$ | $m^3$ $s^{-1}$ | 0.00002 | |
| *A* | Inner cross section of inlet tube upstream of $CO_{r1}$ | $m^2$ $s^{-1}$ | 1.46e-5 | |

**Table 18: Stokes and modified Stokes number for two critical orifices and the smallest and largest diameter of transmitted particles**

| **Orifice (µm)** | **380** | | | | **400** | | | |
|---|---|---|---|---|---|---|---|---|
| **Particle diameter (nm)** | **80** | | **750** | | **80** | | **750** | |
| Stokes number | $\sqrt{St}$ | $\sqrt{St'}$ | $\sqrt{St}$ | $\sqrt{St'}$ | $\sqrt{St}$ | $\sqrt{St'}$ | $\sqrt{St}$ | $\sqrt{St'}$ |
| 1000 hPa | 0.02 | 0.05 | 0.11 | 0.26 | 0.02 | 0.05 | 0.11 | 0.23 |
| 200 hPa | 0.04 | 0.10 | 0.15 | 0.36 | 0.04 | 0.10 | 0.15 | 0.36 |

**Photographs of the pressure controlled inlet**

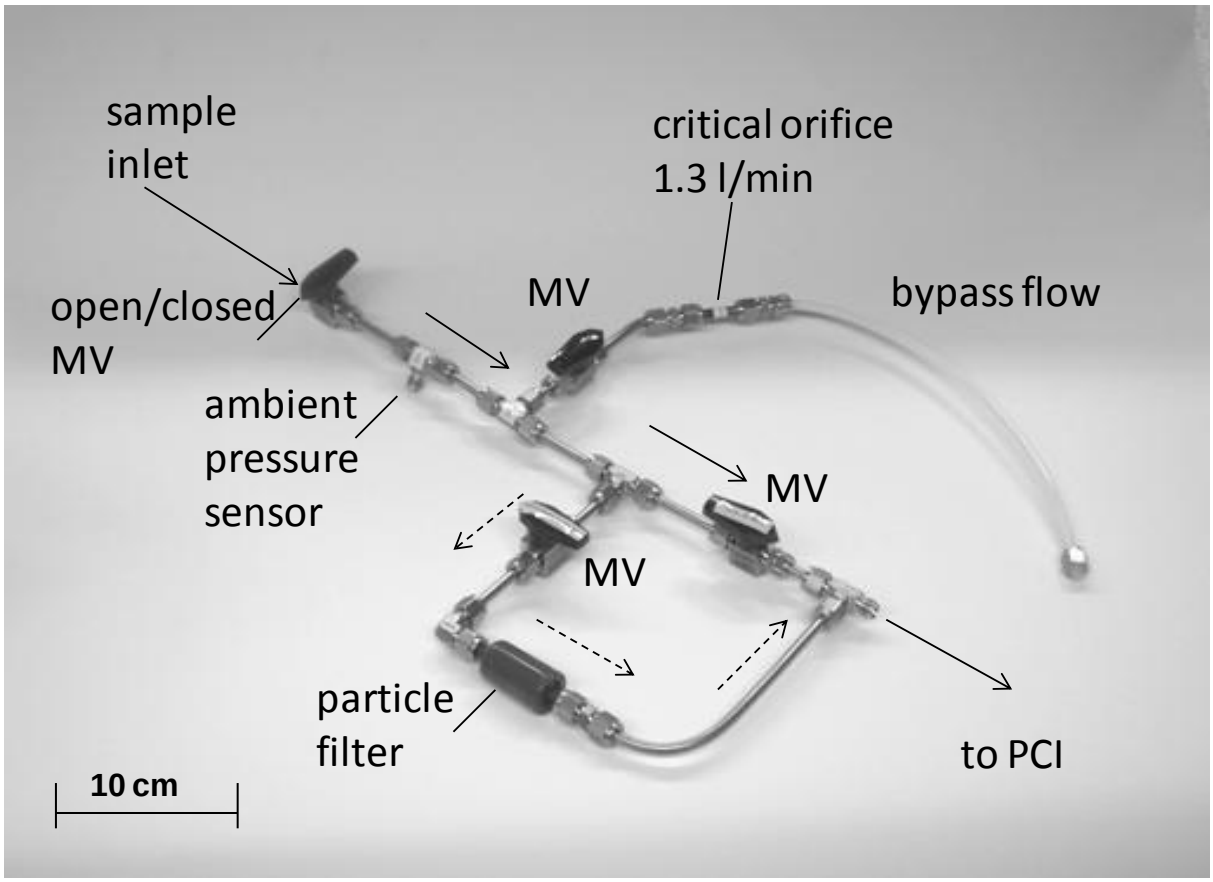


**Figure 81: This photograph of the pre PCI inlet system corresponds to what is shown in the technical drawing in Figure 14. The ambient sample can either go directly to the PCI (solid arrows) for regular measurements or can be directed through the particle filter (dashed arrows) for calibration. The sample flow is redirected by means of manual valves (MV).**

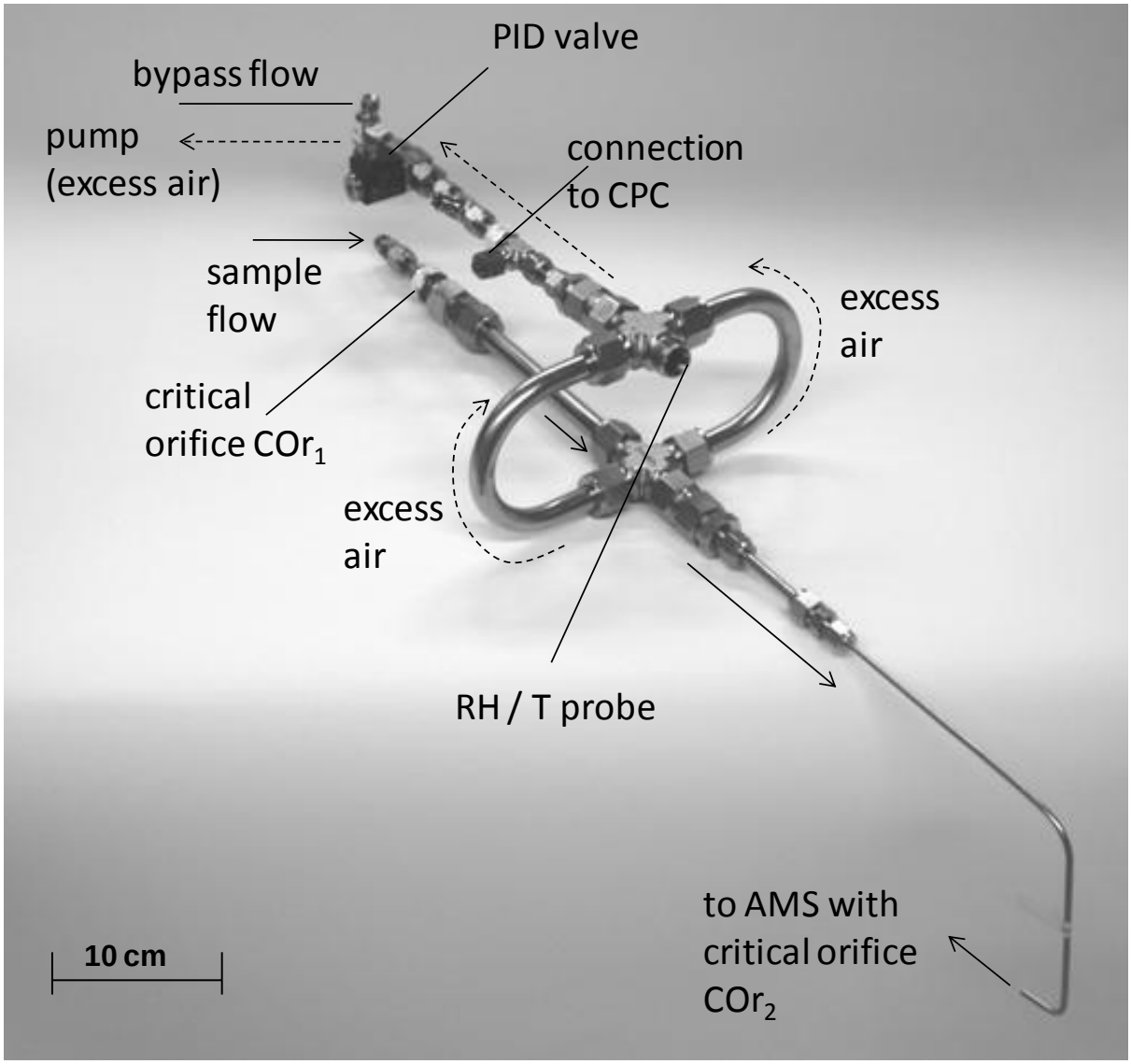


**Figure 82: This photograph of the PCI corresponds to the technical drawing in Figure 13. The solid arrows represent the sample flow into the AMS while the dashed arrows indicate the flow direction of the excess air.**

**Error calculations for the lens transmission functions**

**Mass Method:**

The mass of $NH_4NO_3$ derived by the CPC measurements is comprised of two uncertainties. There is a standard deviation from the mean CPC counts that leads to uncertainty in the mass of $NH_4NO_3$, termed $Mcpc_{sdev1}$ (in µg $m^{-3}$).

$$Mcpc_{sdev1} = Mcpc_{avg} * Pcpc_{sdev} \quad \textbf{Eq. 13}$$

with *Mcpcavg*: average mass of $NH_4NO_3$ derived by the CPC counts (in µg m-3) (see Eq. 5 on page 45), *Pcpcsdev*: standard deviation from the mean CPC counts. The standard deviation from the mean CPC counts was calculated by applying the LOD algorithm developed by Reitz (2011). The production of particles fluctuated over time so that the algorithm was used to distinguish between the long time scale trends in the order of several minutes from fluctuation in the order of seconds (see also section 2.4.2 for a brief introduction to the algorithm).

The second uncertainty in the derived CPC mass ($Mcpc_{sdev2,}$ in µg $m^{-3}$) is associated to the standard deviation found in the size distribution of the monodispers aerosol after selection by the DMA (see Figure 16 a).

$$Mcpc_{sdev2} = Mcpc_{avg} * \frac{SD_{sdev}}{PP} \quad \textbf{Eq. 14}$$

with $SD_{sdev}$: standard deviation from the mean of the particle number fraction of the size distribution of the monodispers aerosol at the selected diameter, *PP*: fraction of particles out of the entire size distribution at the selected diameter.

$E_{mass\_cpc}$ denotes the sum of both uncertainties (in µg $m^{-3}$).

$$E_{mass\_cpc} = \sqrt{Mcpc_{sdev1}^2 + Mcpc_{sdev2}^2} \quad \textbf{Eq. 15}$$

The final error for the transmission was divided into a positive ($E^+_{trans}$) and a negative ($E^-_{trans}$) deviation from the mean transmission. It was defined as the ratio of the AMS derived mass (*Mams*) and the CPC derived mass (*Mcpc*) of $NH_4NO_3$. The AMS mass counting statistics error (0.50 ± 0.12 %) as derived by the analysis tool SQUIRREL (see section 2.4) was negligible. The ratio of *Mams* and *Mcpc* plus $E^+_{trans}$ yields the uppermost boundary and the ratio minus $E^-_{trans}$ the lowermost boundary.

$$E^+_{trans} = \frac{Mams}{Mcpc - E_{mass\_cpc}} - \frac{Mams}{Mcpc} \quad \textbf{Eq. 16}$$

$$E^-_{trans} = \frac{Mams}{Mcpc} - \frac{Mams}{Mcpc + E_{mass\_cpc}} \quad \textbf{Eq. 17}$$

In the following one example is given for the PCI POLARCAT at 72 nm $d_{mob}$ (~ 100 nm $d_{va}$, see Figure 17).

Eq. 13: $$Mcpc_{sdev1} = 2.15 * 10^{-3} = 1.86 * 10^{-1} * 1.15 * 10^{-2}$$ (µg m$^{-3}$)

Eq. 14: $$Mcpc_{sdev2} = 5.17 * 10^{-2} = 1.86 * 10^{-1} * \frac{3.12 * 10^{-2}}{1.12 * 10^{-1}}$$ (µg m$^{-3}$)

Eq. 15: $$E_{mass\_cpc} = 5.17 * 10^{-2} = \sqrt{2.15 * 10^{-3^2} + 5.17 * 10^{-2^2}}$$ (µg m$^{-3}$)

Eq. 16: $$E^{+}_{trans} = 1.05 * 10^{-1} = \frac{5.06 * 10^{-2}}{1.86 * 10^{-1} - 5.17 * 10^{-2}} - \frac{5.06 * 10^{-2}}{1.86 * 10^{-1}}$$

Eq. 17: $$E^{-}_{trans} = 5.91 * 10^{-2} = \frac{5.06 * 10^{-2}}{1.86 * 10^{-1}} - \frac{5.06 * 10^{-2}}{1.86 * 10^{-1} + 5.17 * 10^{-2}}$$

**LSP counting method**

The error bars in Figure 17 denote the standard deviation from the transmission efficiency defined as the ratio of the one minute average counts of the LSP ($Cavg_{lsp}$) and the one minute average counts of the CPC ($Cavg_{cpc}$) for the 20 minutes measurement interval. This standard deviation is for example 1.27*10$^{-1}$ for 630 nm $d_{va}$.

The counting statistics error was calculated by Gaussian error propagation. However, it is negligible compared to the standard deviation and was hence not included in Figure 17. The uncertainty of the counts for both instruments is given by the inverse of the square root of the total counts.

$$E_{count} = \sqrt{\left(\frac{1}{Cavg_{cpc}} * \frac{1}{\sqrt{Ctotal_{lsp}}}\right)^2 + \left(\frac{Cavg_{lsp}}{Cavg_{cpc}^2} * \frac{1}{\sqrt{Ctotal_{cpc}}}\right)^2}$$

**Eq. 18**

with $Ctotal_{lsp}$: total counts by the LSP, $Ctotal_{cpc}$: total counts by the CPC, both during the 20 minutes measurement interval.

With numbers for the 630 nm $d_{va}$ example this results in:

Eq. 18: $$E_{count}\,(630nm) = 1.92 * 10^{-4} = \sqrt{\left(\frac{1}{28.2} * \frac{1}{\sqrt{36539}}\right)^2 + \left(\frac{12.2}{28.2^2} * \frac{1}{\sqrt{102630}}\right)^2}$$

## *7.2 Appendix B – POLARCAT plumes*

**Table 19: List of all 48 identified pollution plumes. The highlighted plumes were used for the aerosol lifetime calculation.**

| Date | Time | Classification | Sub-class | mean aerosol concentration ± 1 standard deviation |
|---|---|---|---|---|
| **2008** | **UTC** | | | **(µg m$^{-3}$)** |
| 30 June | 14:14-14:24 | BB / FF no Asia | EU FF, Can BB | 1.61 ± 0.83 |
| | 15:08-15:12 | BB / FF no Asia | NA, EU FF, Can BB | 1.61 ± 1.00 |
| | 16:12-16:18 | BB / FF no Asia | NA, EU FF, Can BB | 1.62 ± 1.22 |
| 8 July | 13:14-13:32 | „pure“ BB (Plume I) | Can BB, Sib BB | 0.82 ± 0.35 |
| | 13:34-13:38 | „pure“ BB | Can BB, Sib BB | 0.47 ± 0.32 |
| | 13:46-13:56 | „pure“ BB | Can BB, Sib BB | 0.63 ± 0.42 |
| | 13:56-14:02 | BB / FF no Asia | NA BB / FF | 0.51 ± 0.20 |
| | 14:18-14:24 | BB / FF no Asia | NA BB / FF | 0.53 ± 0.27 |
| | 14:42-14:52 | BB / FF no Asia | NA BB / FF | 0.42 ± 0.20 |
| | **14:52-15:02** | **NA / EU, FF / little BB (Plume II)** | **NA FF / little BB** | **0.62 ± 0.35** |
| | **15:02-15:08** | **NA / EU, FF / little BB (outlier)** | **NA FF / little BB** | **0.35 ± 0.18** |
| | 15:24-15:32 | BB / FF no Asia | NA BB / FF | 0.40 ± 0.48 |
| | **15:40-15:50** | **NA / EU, FF / little BB (Plume III)** | **NA FF / little BB** | **0.63 ± 0.32** |
| 10 July | 14:48-14:58 | BB / FF no Asia | NA BB / FF | 0.48 ± 0.36 |
| | 15:10-15:18 | „pure“ BB | Can BB, Sib BB | 0.42 ± 0.21 |
| | **15:22-15:28** | **NA / EU, FF / little BB** | **NA FF / little BB** | **0.37 ± 0.31** |
| | **15:42-15:52** | **NA / EU, FF / little BB** | **NA FF / little BB** | **0.39 ± 0.32** |
| | 15:52-16:02 | BB / FF no Asia | NA BB / FF | 0.36 ± 0.30 |
| **12 July a** | **11:30-11:36** | **NA / EU, FF / little BB** | **NA FF / little BB** | **0.57 ± 0.28** |
| | **11:40-12:00** | **NA / EU, FF / little BB** | **NA FF / little BB** | **0.52 ± 0.26** |
| | 12:24-12:28 | BB / FF no Asia | NA FF / BB | 0.58 ± 0.28 |
| | **12:28-12:34** | **NA / EU, FF / little BB** | **NA FF / little BB** | **0.45 ± 0.21** |
| | 12:44-12:52 | BB / FF no Asia | NA FF / BB | 0.34 ± 0.16 |
| | 12:58-13:06 | BB / FF no Asia | NA FF / BB | 0.61 ± 0.36 |

| | **13:12-13:18** | **NA / EU, FF / little BB** | **NA FF / little BB** | **0.37 ± 0.37** |
|---|---|---|---|---|
| **Date** | **Time** | **Class** | **Sub-class** | **mean aerosol concentration ± 1 standard deviation** |
| | **13:30-13:36** | **NA / EU, FF / little BB** | **NA FF / little BB** | **0.32 ± 0.20** |
| | 13:44-13:54 | BB / FF no Asia | EU FF, Can BB | 0.42 ± 0.20 |
| 12 July b | 18:28-18:46 | BB / FF no Asia | NA BB / FF | 0.56 ± 0.41 |
| | 19:06-19:16 | BB / FF no Asia | NA BB / FF | 0.69 ± 0.30 |
| | 19:24-19:42 | BB / FF no Asia | NA FF / BB | 0.55 ± 0.28 |
| | 19:48-20:02 | BB / FF no Asia | NA BB / FF | 0.52 ± 0.28 |
| 13 July | 18:24-18:30 | BB / FF no Asia (Plume $V_{ref}$) | NA BB / FF | 1.24 ± 0.40 |
| | 18:34-18:40 | BB / FF no Asia | NA BB / FF | 0.96 ± 0.42 |
| | 18:42-19:06 | Asia FF / Sib BB (Plume IV) | Asia FF / Sib BB | 0.98 ± 0.40 |
| | 19:18-19:24 | NA / EU, FF / little BB | EU FF, NA FF | 1.25 ± 0.60 |
| | 19:28-19:36 | NA / EU, FF / little BB | EU FF, NA FF | 0.92 ± 0.34 |
| | 19:36-19:40 | Sib BB / Asia FF | Sib BB / Asia FF | 0.40 ± 0.26 |
| | 19:56-20:02 | Sib BB / Asia FF (Plume V) | Sib BB / Asia FF | 0.26 ± 0.26 |
| | 20:10-20:16 | Sib BB / Asia FF | Sib BB / Asia FF | 0.84 ± 0.43 |
| | 20:16-20:20 | BB / FF no Asia | NA BB / FF | 0.69 ± 0.45 |
| 14 July a | 12:18-12:26 | Sib BB / Asia FF | Sib BB / Asia FF | 0.75 ± 0.33 |
| 14 July b | 14:30-14:42 | BB / FF no Asia | EU FF, Can BB | 1.39 ± 0.57 |
| | 15:50-15:56 | Asia FF / Sib BB | Asia FF / Sib BB | 0.95 ± 0.60 |
| | 15:58-16:04 | Asia FF / Sib BB | Asia FF / Sib BB | 1.03 ± 0.65 |
| | 16:04-16:08 | Asia FF / Sib BB | Asia FF / Sib BB | 1.32 ± 0.54 |
| | 16:08-16:16 | Asia FF / Sib BB | Asia FF / Sib BB | 1.24 ± 0.50 |
| | 16:22-16:28 | BB / FF no Asia | NA BB / FF | 0.86 ± 0.63 |
| | 16:30-16:40 | BB / FF no Asia | NA BB / FF | 0.80 ± 0.43 |

BB, biomass burning; FF, fossil fuel combustion; NA, North America; EU, Europe; Sib, Siberia; Asia, East Asia; class and sub-class names are composed according to the importance of the pollution contribution

## *7.3 Appendix C – Particle settling velocity*

Calculation terminal particle settling velocities after Hinds (1999)

**Eq. 19**

$$V_{TS} = \frac{\rho_p d^2 g C_c}{18\eta}$$

**Eq. 10**

$$C_c = 1 + \frac{1}{PD_p} * \left[15.60 + 7.00 * exp\left(-0.059 PD_p\right)\right]$$

With $V_{TS}$ terminal settling velocity in m $s^{-1}$, $\rho_p$ particle density (1.7 g $cm^{-3}$), $D_p$ particle diameter in µm, $g$ gravitational acceleration m $s^{-2}$, $C_c$ Cunningham slip correction factor, $\eta$ dynamic viscositiy of air at 8000 m alitutde (literature value as close to 200 hPa and -60°C as possible) (1.321e$^{-5}$ kg $(ms)^{-1}$, (Lide, 1996)), $P$ atmospheric pressure (200 hPa). $C_c$ is 1.8.

$V_{TS}$ results in 12.8 µm $s^{-1}$.

These equations are valid for the Stokes regime which extends at these ambient conditions from nm size to 100 µm.

## *7.4 Appendix D – AMS size distribution uncertainties*

The statistical counting error for the particulate sulfate size distribution has been calculated as follows.

*m/z* 48 and 64 were chosen to represent the mass size distribution of particulate sulfate as they are the basis for calculating the total mass of particulate sulfate (see fragmentation table in Allen et al. (2004b)). The statistical counting error that is calculated by the AMS data analysis software gives the error in Hz per *m/z*, per time step and per raw size bin.

The errors were converted from *Hz* into µg $m^{-3}$. The factor of 0.000265 was determined by simply calculating the ratio of the mass concentration in µg $m^{-3}$ of the respective *m/z* and the ion counting rate signal in Hz (see section 2.1.1 and references therein for a detailed description of how the mass concentration is derived from the ion counting rate).

All errors ($E_{avg\_m/z\_t}$) per *m/z* and bin were averaged over the time steps for which the size distribution was calculated:

$$E_{avg\_m/z\_t} = \frac{\sum_{i=1}^{n} er_i}{N}$$

**Eq. 20**

with $er_i$: error per bin, time step and *m/z* , and *N*: total number of time steps

The original number of bins was 305 while the size distribution was averaged to 25 bins between 50 and 800 nm. Hence, all errors in the raw bins that were combined for one new bin were averaged as follows:

$$E_{avg\_m/z\_t\_bin} = \frac{\sqrt{\sum_{i=1}^{n} er_{rawbin\_i}^2}}{N}$$

**Eq. 21**

with $E_{avg\_m/z\_t\_bin}$: average error per *m/z* over all time steps and within one new bin, $er_{rawbin\_i}{}^2$: error per *m/z* over all time steps and per raw bin.

Subsequently, the absolute error for the sum of the mass size distributions of *m/z* 48 and *m/z* 64 was derived:

$$E_{abs\_t\_bin} = \sqrt{E_{avg\_48\_t\_bin}^2 + E_{avg\_64\_t\_bin}^2}$$

**Eq. 22**

With $E_{abs\_t\_bin}$: error over all respective *m/z* for all time steps and per new bin, $E_{avg\_m/z\_t\_bin}$: average error per *m/z* over all time steps and within one new bin. All errors are in µg $m^{-3}$.

Finally, the absolute error $E_{abs\_t\_bin}$ was scaled to the total signal of particulate sulfate. The scaling factor was derived by means of the ratio of the average mass concentration of both m/z 48 and 64 and

the average mass concentration of particulate sulfate during the time period used for the size distribution. The factor was 5.

The error bars show that for small diameters until approximately 140 nm the signal is rather noisy and ranges around zero. No size distribution can be derived for these diameters. If the errors were exact, which they are not since they were up-scaled from individual *m/z* to the total mass of particulate sulfate, they should not be located completely below the zero line. Here, this is the case for only one error bar. If the exact error bars were located below the zero line nonetheless, this would be an indication that the baseline for the size distribution was not set correctly.

For larger diameters the error bars indicated that the small scale variations in the size distribution are not real but within the statistical uncertainty of the distribution.

## *7.5Appendix E - CiTTyCAT*

### CiTTyCAT details

The following table lists all input species and their volume mixing ratios except for $SO_2$, water vapor and $O_3$ which were varied. CO corresponds to the in-situ measurement during Plume V. All other values are derived from ARCTAS-summer background conditions.

**Table 20: CiTTyCAT input data for $NO_x$, CO, and VOCs**

| Species | Volume mixing ratio |
|---|---|
| CO | $9.5*10^{-8}$ |
| NO | $1.0*10^{-12}$ |
| $NO_2$ | $17.35*10^{-12}$ |
| $H_2O_2$ | $5.71*10^{-12}$ |
| $HONO_2$ | $67.1*10^{-12}$ |
| OH | $8.37*10^{-14}$ |
| $HO_2$ | $5.69*10^{-12}$ |
| PAN | $1.73*10^{-9}$ |
| $C_2H_4$ | $6.0*10^{-11}$ |
| $C_2H_2$ | $9.7*10^{-11}$ |
| $C_4H_{10}$ | $7.0*10^{-12}$ |
| $C_6H_6$ | $8.6*10^{-14}$ |
| $CH_4$ | $1.8*10^{-6}$ |
| $C_2H_6$, $C_3H_8$, $C_3H_6$, $C_5H_{12}$, $C_6H_{14}$, Isoprene, $C_7H_8$, $C_4H_8$, MeCHO, Me2CO, EtOH | 0.0 |

**Customized model output**

Figure 83 illustrates the model output parameters over time which were checked for every run. In total CiTTyCAT was programmed to write out about 90 chemical, meteorological (pressure, humidity) and physical (date, time, location, radiation) data. This example model run for a geographically fixed box was initiated with 20 pmol $mol^{-1}$ $SO_2$ and 50 nmol $mol^{-1}$ $O_3$ at a relative humidity of 10 % at 240 K. The calculation was then repeated at the same relative humidity and temperature while iterating through the $SO_2$ mixing ratio from 20 to 800 pmol $mol^{-1}$ and through ozone from 50 to 290 nmol $mol^{-1}$. Such an ensemble of model runs was repeated for changed RH and temperature conditions (RH from 10 to 90 %, and T = 250 K).

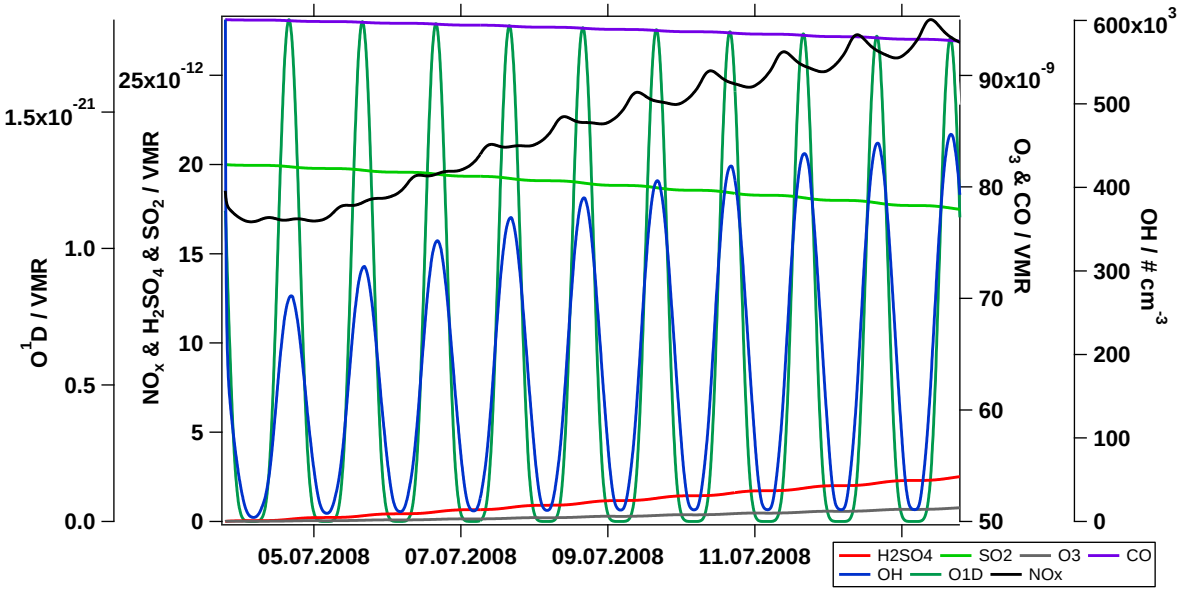


**Figure 83: Customized model output for a 10 day fixed box run. VMR stands for volume mixing ratio. The start values for $SO_2$ and $O_3$ were 20 pmol $mol^{-1}$ and 50 nmol $mol^{-1}$, respectively.**

The amount of particulate sulfate was derived as follows from the volume mixing ratio of sulfuric acid. First the volume mixing ratio (VMR) of $H_2SO_4$ was converted into µg $m^{-3}$ at STP conditions by Eq. 23.

$$MC_s = VMR_s * MW_s * \frac{1}{22.4} * 10^9$$

**Eq. 23**

With $MC_s$ mass concentration of species *s* in µg $m^{-3}$, $MW_s$ molecular weight of species *s* in g $mol^{-1}$, at STP conditions one mol of air equals 22.4 l, and $10^9$ is the conversion factor from g to µg and l to $m^3$.

Eq. 24 provides the conversion factor for sulfuric acid.

$$MC_{H_2SO_4} = VMR_{H_2SO_4} * 98_{H_2SO_4} * \frac{1}{22.4} * 10^9 = 4.375 * 10^9$$

**Eq. 24**

The mass concentration of particulate sulfate ($SO_4^{2-}$) is derived by multiplying $MC_{H_2SO_4}$ by the ratio of $MW_{SO_4^{2-}}$ and $MW_{H_2SO_4}$ (96/98=0.98).

The amount of converted $SO_2$ (in %) refers to the ratio of the input $VMR_{SO_2}$ minus the $VMR_{SO_2}$ at time *t* over the initial value time 100 %.

Figure 84 illustrates the production of OH radicals during 10 days as a function of varied ozone mixing ratios. The black horizontal lines indicate that at lower ozone abundance more OH radicals are formed with time, while at 210 nmol $mol^{-1}$ the production rate is stable and then decreases with larger mixing ratios. The data was taken from CiTTyCAT fixed box runs with 10 pmol $mol^{-1}$ $SO_2$ initial concentration. The numbers are the same for all $SO_2$ input concentrations. The sine curve form results from the photochemistry which depends on solar radiation. Figure 85 shows the same for a box run along the representative trajectory where temperature, water vapor abundance and daylight hours are varied through the pathway.

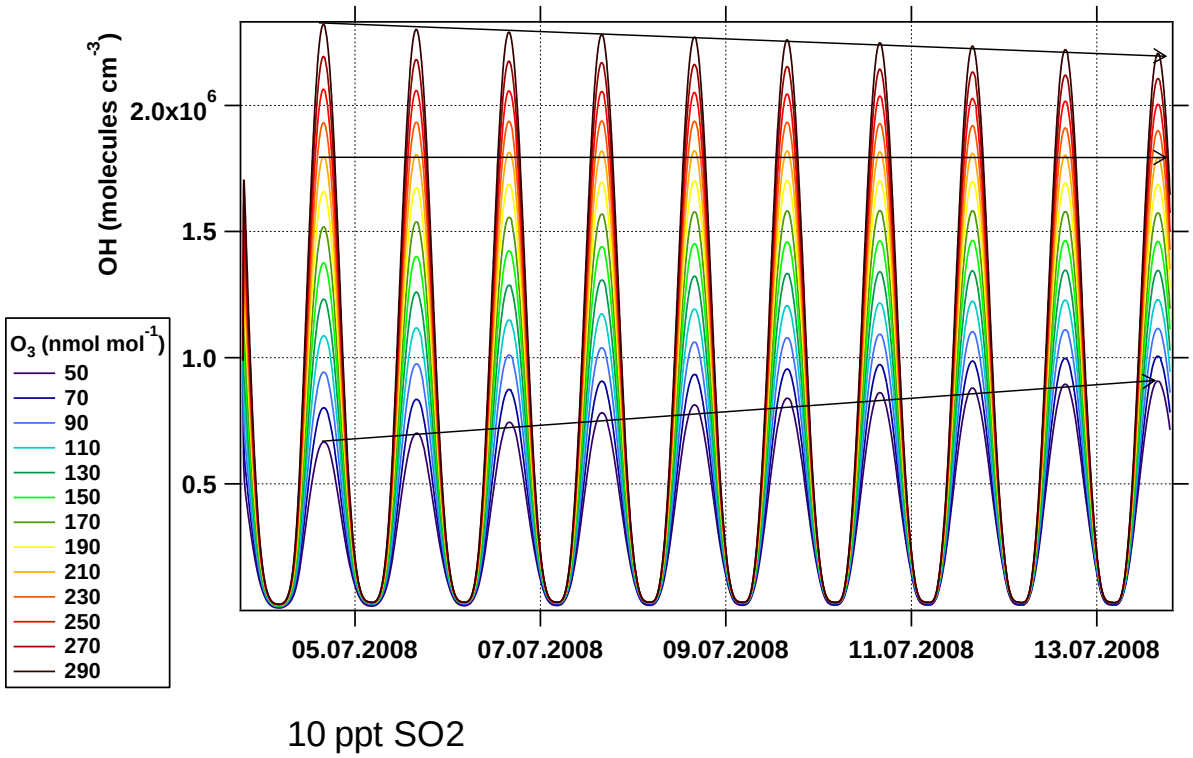


**Figure 84: OH radical production with time at different ozone mixing ratios**

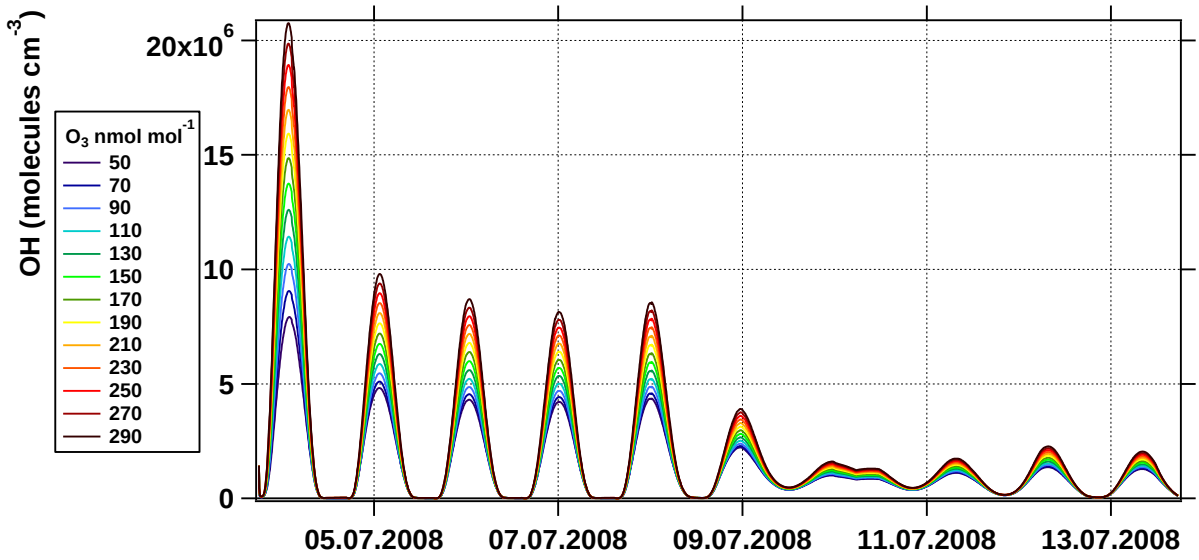


**Figure 85: OH radical concentration along the 10-day trajectory**

Figure 86 shows the dependence of OH radical production on the water vapor and ozone abundance after 10 days. Both trace gases influence the formation of OH radicals positively.

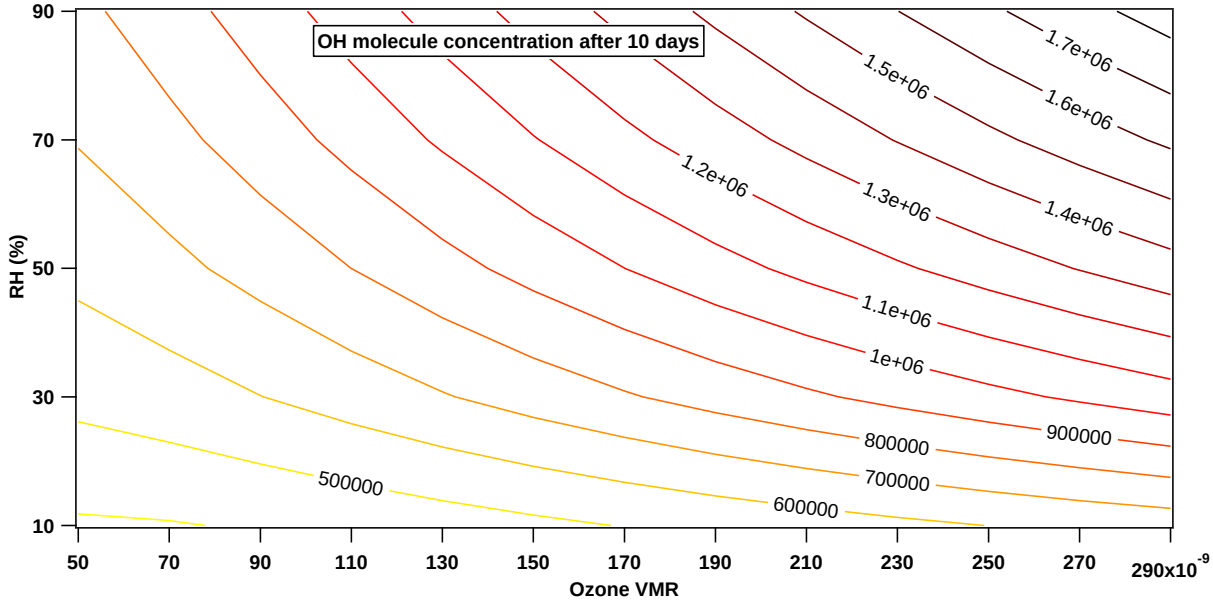


**Figure 86: OH radical concentration as a function of RH and ozone mixing ratio**

In Figure 87 the evolution of the ozone mixing ratio relative to the initial ozone concentration as a function of water vapor abundance and initial ozone mixing ratio is given. For low relative humidity values and tropospheric ozone mixing ratios there is slight ozone production after 10 days. The higher the relative humidity and the ozone concentration, the less ozone is available after 10 days.

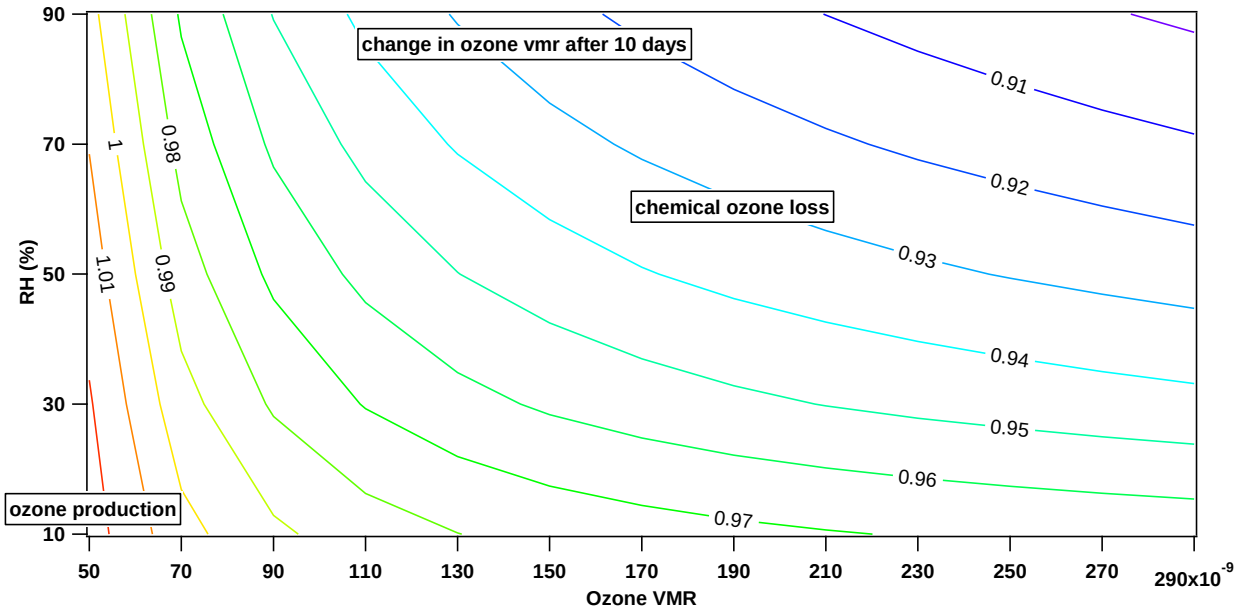


**Figure 87: Fraction relative to the initial ozone mixing ratio after 10 days as a function of relative humidity**

As shown in Figure 88, the initial ozone mixing ratio of 50 nmol mol$^{-1}$ (lowermost curve) increases slightly when running CiTTyCAT along the trajectory. Above 70 nmol mol$^{-1}$ it decreases.

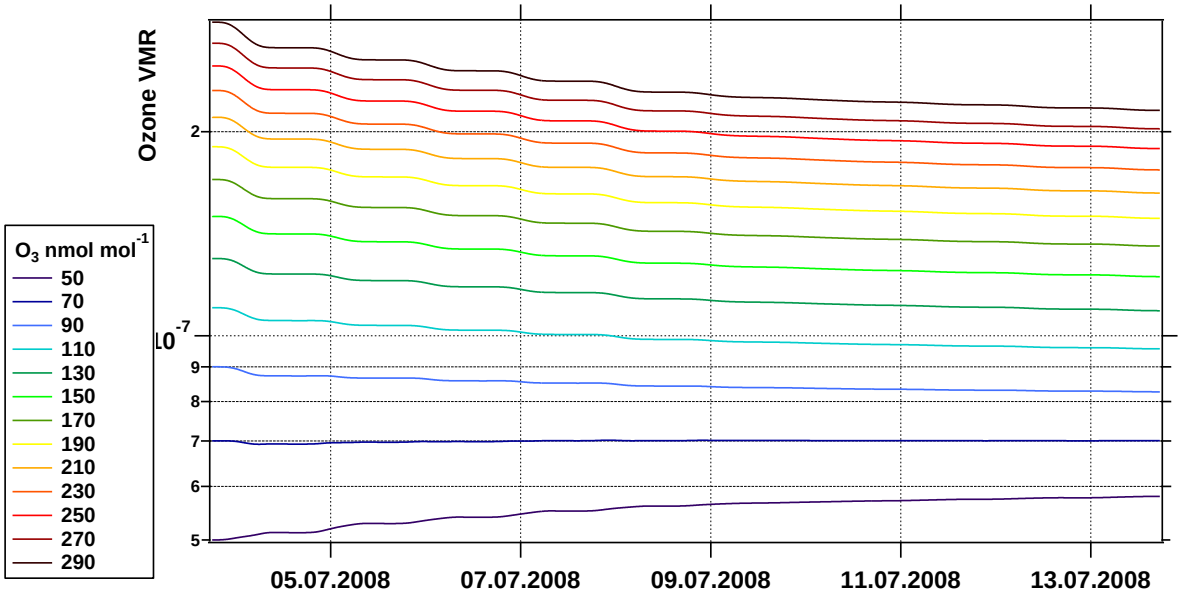


**Figure 88: Evolution of the ozone volume mixing ratio with time along the trajectory**

After 10 days more $SO_2$ is converted in the fixed box run the higher the water vapor abundance and the higher the initial ozone mixing ratio (Figure 89).

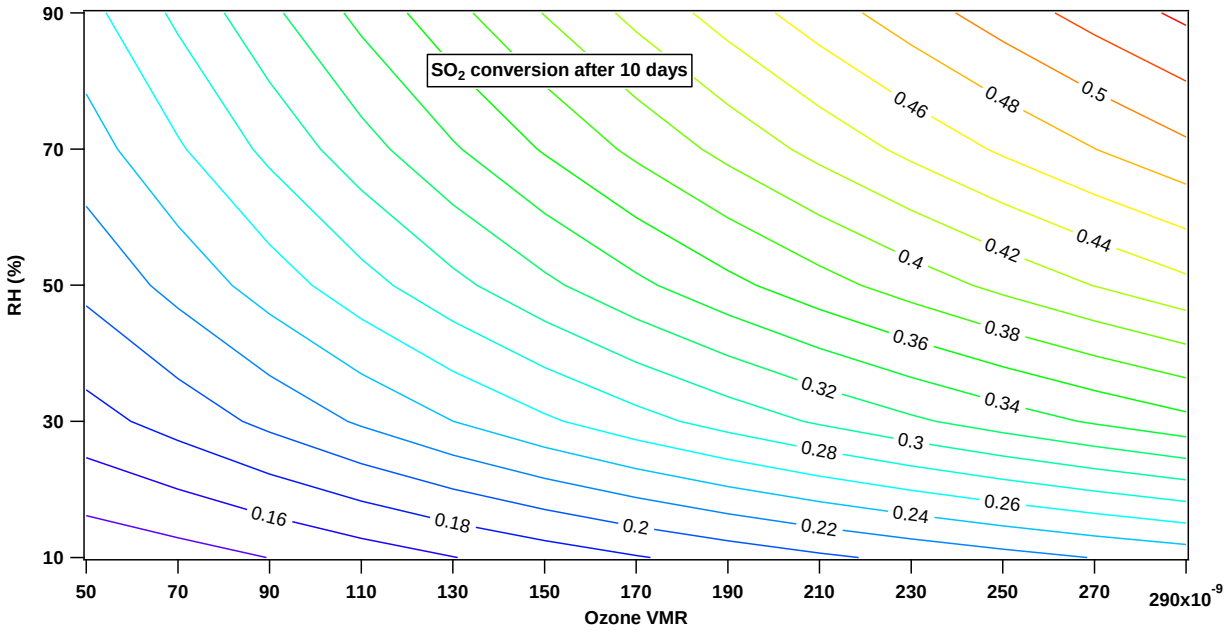


**Figure 89: Fraction of converted $SO_2$ after 10 days as a function of ozone volume mixing ratio and relative humidity**

For the runs along the trajectory, the more $SO_2$ is converted the more initial ozone is available.

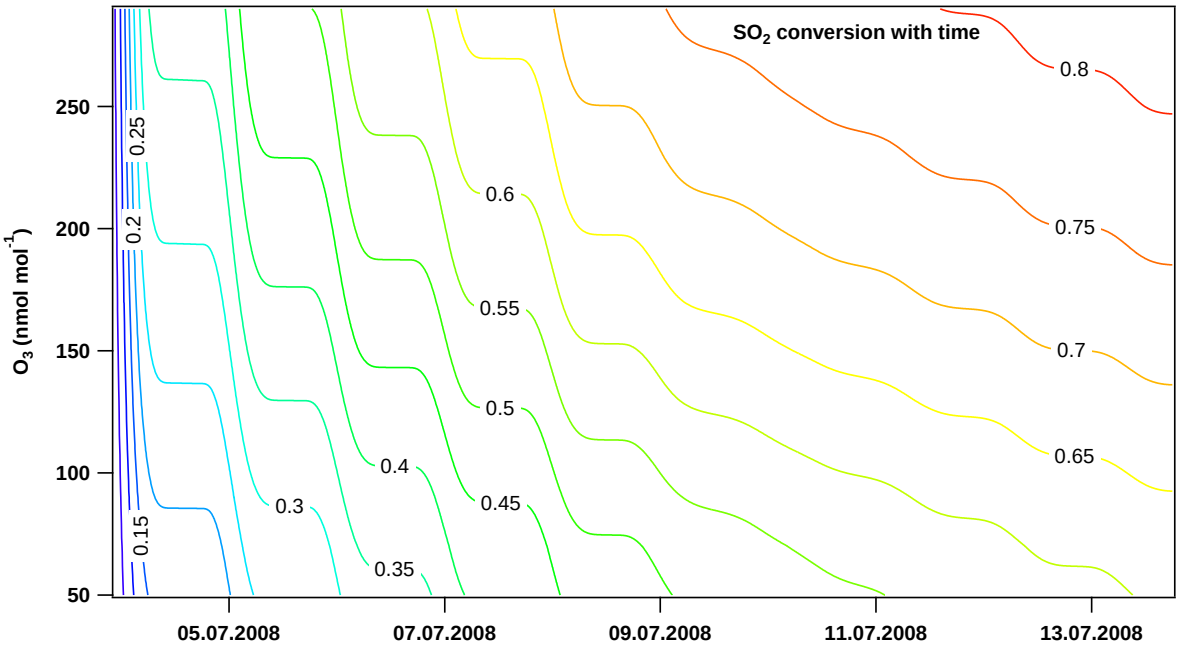


**Figure 90: SO2 conversion with time as a function of ozone mixing ratio along the trajectory**

As above figures and the results from section 3.2.3.2 show, the $SO_2$ conversion is enhanced the more water vapor and ozone are present and the warmer the ambient air. Figure 91 presents results from a sensitivity study concerning the abundance of VOCs at varied ozone concentrations. For tropospheric ozone mixing ratios, more $SO_2$ is converted the more VOCs are available. The trend reverses when ozone mixing ratios reach 150 nmol $mol^{-1}$. However, the decrease in $SO_2$ conversion is minimal. Relevant effects could only have been observed if the VOCs ratio in the model runs would have been

underestimated by more than a factor of 10 (see markers on the abscissa at 1000 %). Therefore, the estimated amount of VOCs (as shown in Table 20) did not have an important influence on the final model output.

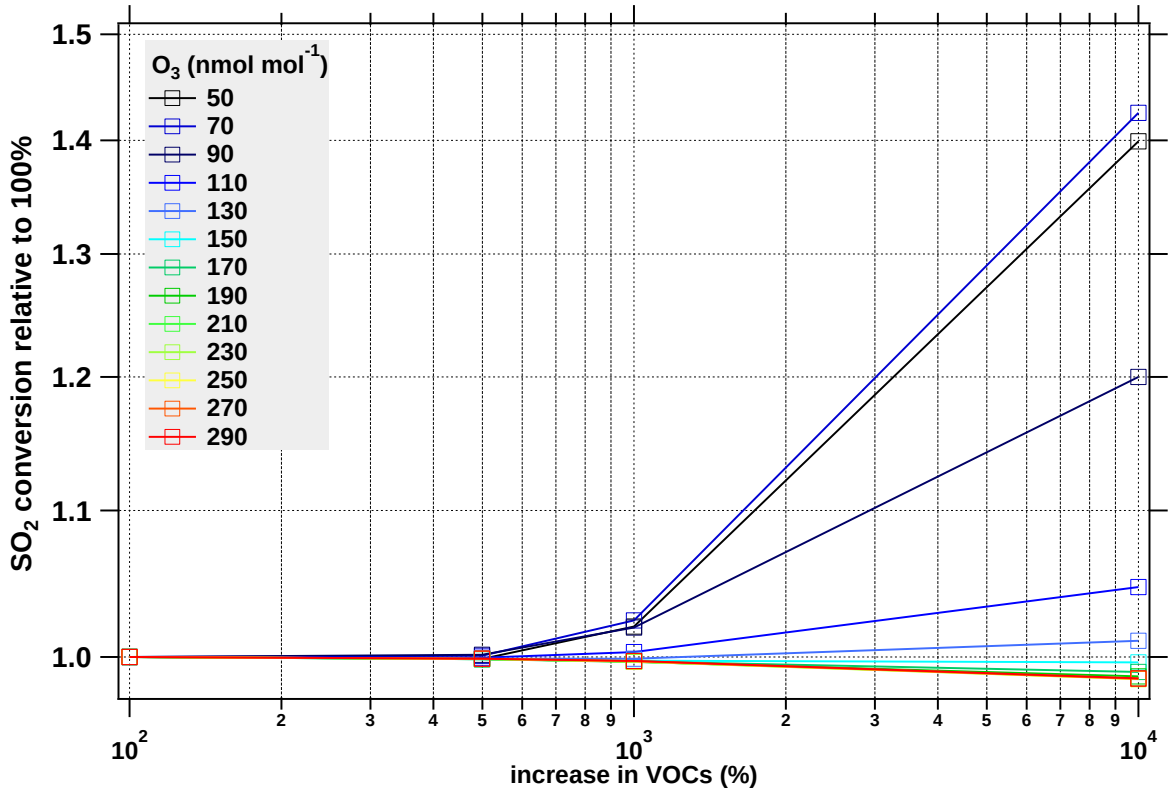


**Figure 91: Sensitivity of $SO_2$ conversion as a function of VOCs abundance after 10 days. 100 % correspond to ARCTAS-summer background mixing ratios.**

## *7.6Appendix F – POLARCAT plumes size distributions*

Number and volume size distribution fit function as programmed in the analysis software Igor 6.2 (Wavemetrics).

$$f(dp) = \sum_{i=0}^{2} A_i * exp\left\{-\left(\frac{ln\frac{dp}{x_i}}{width_i}\right)\text{^}2\right\}$$

**Eq. 25**

With $d_p$ as particle mobility diameter in µm. For the volcanic aerosol $d_p$ is the particle vacuum aerodynamic diameter in µm, $x_i$ is the mode diameter.

The above parameters compare as follows to the more commonly known monomodal log normal size distribution after Hinds (1999):

$$\frac{dN}{dlogdp} = \frac{N}{\sqrt{2\pi}log\sigma_g} * exp\left(-\frac{\left(logdp - log\bar{d}_g\right)^2}{2\left(log\sigma_g\right)^2}\right)$$

**Eq. 26**

With $\sigma_g$ the geometric standard deviation, $\bar{d}_g$ the geometric mean diameter.

For *dN*, the factor $A_i$ corresponds to $N_i/(sqrt(2\pi)*width_i)$, where $N_i$ is the total number concentration ($cm^{-3}$) and $width_i$ corresponds to $log\ \sigma_g$.

For *dV*, $A_i$ corresponds to $V_i/(sqrt(2\pi)*width_i)$, where $V_i$ is the total volume concentration ($\mu m^3 cm^{-3}$).

Futhermore $\ln(dp/x_i)$ corresponds to: $\left(logdp - log\bar{d}_g\right)$

**Table 21: Fit parameters for the log normal number and volume size distributions as shown in Figure 80.**

| Parameter* | Out-of-plume | "pure" BB | BB/FF no Asia | NA / EU, FF / little BB | Sib BB / Asia FF | Asia FF / Sib BB | Plume NA FF / BB | Plume IV Asia FF / Sib BB |
|---|---|---|---|---|---|---|---|---|
| | | | | dN | | | | |
| $A_0$ | 7680 ± 1370 | 1332 ± 51.1 | 600 ± 676 | 500 ± 309 | 514 ± 19 | 300 ± 206 | | |
| $width_0$ | 0.16 ± 0.03 | 0.53 ± 0.03 | 0.56 ± 0.21 | 0.54 ± 0.17 | 0.93 ± 0.0248 | 0.58 ± 0.13 | | |
| $x_0$ | 0.023 ± 4e-4 | 0.043 ± 0.001 | 0.045 ± 0.012 | 0.042 ± 0.003 | 0.078 ± 0.002 | 0.050 ± 0.009 | | |
| $A_1$ | 2310 ± 934 | 449 ± 24 | 374 ± 246 | 436 ± 124 | | 416 ± 106 | | |
| $width_1$ | 0.28 ± 0.10 | 0.80 ± 0.08 | 0.83 ± 0.91 | 1.01 ± 0.33 | | 0.82 ± 0.18 | | |
| $x_1$ | 0.039 ± 0.002 | 0.150 ± 0.017 | 0.110 ± 0.111 | 0.102 ± 0.048 | | 0.117 ± 0.033 | | |
| $A_2$ | 626 ± 486 | | | | | | | |
| $width_2$ | 1.21 ± 1.06 | | | | | | | |
| $x_2$ | 0.054 ± 0.083 | | | | | | | |

| Parameter* | Out-of-plume | "pure" BB | BB/FF no Asia | NA / EU, FF / little BB | Sib BB / Asia FF | Asia FF / Sib BB | Plume NA FF / BB | Plume IV Asia FF / Sib BB |
|---|---|---|---|---|---|---|---|---|
| | | | | dV | | | | |
| $A_0$ | 9e-4 ± 3e-4 | 0.0016 ± 3e-4 | 0.001 ± 2e-4 | 0.021 ± 0.004 | 0.020 ± 8e-4 | 0.011 ± 0.003 | 0.018 ± 0.004 | 0.013 ± 0.004 |
| $width_0$ | 0.16 ± 0.01 | 0.53 ± 0.20 | 0.47 ± 0.14 | 0.86 ± 8e-5 | 1.28 ± 0.07 | 0.65 ± 0.16 | 0.81 ± 0.01 | 0.36 ± 0.18 |
| $x_0$ | 0.024 ± 0.001 | 0.066 ± 0.011 | 0.062 ± 0.007 | 0.301 ± 3e-4 | 0.510 ± 0.047 | 0.180 ± 0.044 | 0.285 ± 0.080 | 0.186 ± 0.015 |
| $A_1$ | 1e-3 ± 2e-4 | 0.050 ± 0.005 | 0.028 ± 0.003 | 0.016 ± 0.003 | | 0.034 ± 0.004 | 0.020 ± 0.009 | 0.042 ± 0.006 |
| $width_1$ | 0.30 ± 0.06 | 0.80 ± 0.09 | 1.03 ± 0.10 | 0.29 ± 1e-4 | | 0.50 ± 0.08 | 0.30 ± 0.07 | 0.48 ± 0.09 |
| $x_1$ | 0.044 ± 0.002 | 0.387 ± 0.048 | 0.436 ± 0.068 | 0.362 ± 3e-4 | | 0.411 ± 0.014 | 0.400 ± 0.013 | 0.415 ± 0.015 |
| $A_2$ | 0.018 ± 2e-4 | | | | | | | |
| $width_2$ | 1.07 ± 0.03 | | | | | | | |
| $x_2$ | 0.372 ± 0.002 | | | | | | | |

## *7.7 Abbreviations and Acronyms*

| **Abbreviation / Acronym** | **Meaning** |
|---|---|
| a.s.l. | above sea level |
| ADC | analog to digital converter |
| AMS | aerosol mass spectrometer |
| amu | atomic mass unit |
| BB | biomass burning |
| BC | black carbon |
| CARIBIC | Civil Aircraft for the Regular Investigation of the atmosphere Based on the Instrument Container |
| CCN | cloud condensation nuclei |
| *CE* | collection efficiency |
| *COr* | critical orifice |
| CPC | condensation particle counter |
| C-ToF-AMS | compact time-of-flight aerosol mass spectrometer |
| DMA | differential mobility analyzer |
| EARLINET | European Aerosol Research Lidar Network |
| ECMWF | European Centre for Medium-Range Weather Forcast |
| EDGAR | Emission database for global atmospheric research |
| EMEP | European monitoring and Evaluation programme |
| eV | electron volt |
| FF | fossil fuel combustion |
| FLEXPART | Lagrangian particle dispersion model |
| *FMS mode* | fast mass spectrum mode |
| FSC | fuel sulfur content |
| FT | free troposphere |
| GDAS | Global Data Assimilation System |
| GFS | Global forecasting system |
| HALO | High Altitude Long Range Aircraft |

| Abbreviation / Acronym | Meaning |
|---|---|
| HR-ToF-AMS | high resolution time-of-flight aerosol mass spectrometer |
| HV | figh voltage |
| HYSPLIT | Hybrid Single-Particle Lagrangian Integrated Trajectory |
| ID | inner diameter |
| IE | ionization efficiency |
| IN | ice nuclei |
| JAR | Joint Aviation Requirement |
| *JMS mode* | jump mass mode |
| LAGRANTO | Lagrangian Analysis Tool |
| lidar | light detection and ranging |
| LOD | limit of detection |
| LSP | light scattering probe |
| LV-OOA | low-volatile oxygenated organic aerosol |
| *m/z* | mass to charge ratio |
| MCP | multi channel plate |
| MODIS | Moderate-resolution imaging spectrometer |
| MS | mass spectrometer |
| *MS mode* | mass spectrum mode |
| MV | manual valve |
| NCEP | National Centers for Environmental Prediction |
| NH | Northern Hemisphere |
| NMHC | non-methane hydro carbons |
| NMVOC | non-methane volatile organic compounds |
| NOAA | National Oceanic and Atmospheric Administration |
| OA | organic aerosol |
| OD | outer diameter |
| OOA | oxygenated organic aerosol |
| PCI | pressure controlled inlet |
| PDF | probability density function |

| Abbreviation / Acronym | Meaning |
|---|---|
| PID | proportional-integral-derivative controller |
| PIXE | particle induced X-ray emission |
| POA | primary organic aerosol |
| PSL | polystyrene latex sphere |
| *PToF mode* | particle time of flight mode |
| PVU | potential vorticity unit |
| pyroCb | pyro cumulo nimbus cloud |
| Q-AMS | quadrupole aerosol mass spectrometer |
| RIE | relative ionization efficiency |
| RH | relative humidity |
| SI | single Ion |
| SMPS | scanning mobility particle sizer |
| SOA | secondary organic aerosol |
| SP2 | single particle soot photometer |
| SQUIRREL | SeQUential IgoR data REtrievaL |
| STE | stratosphere-troposphere exchange |
| STP | standard temperature and pressure |
| STT | stratosphere-troposphere transport |
| SV-OO | semi-volatile oxygenated organic aerosol |
| TP | tropopause |
| TST | troposphere-stratosphere transport |
| UPS | uninterruptable power supply |
| UTLS | upper troposphere, lower stratosphere |
| VOC | volatile organic compounds |
| WCB | warm conveyor belt |
| WMO | World meteorological organization |

## *7.8 List of Field Campaign Acronyms*

| Acronym | Meaning |
|---|---|
| ACE-Asia | Aerosol Characterization Experiment |
| ADRIEX | Aerosol Direct Radiative Impact Experiment |
| ARCPAC | Aerosol, Radiation, and Cloud Processes affecting Arctic Climate |
| ARCTAS | Arctic Research of the Composition of the Troposphere from Aircraft and Satellites |
| ARCTAS-CARB | Arctic Research of the Composition of the Troposphere from Aircraft and Satellites – California Air Resource Board |
| CONCERT | CONtrail and Cirrus ExpeRimenT |
| EUCAARI-LONGREX | European integrated project on Aerosol Cloud Climate and Air Quality Interactions – LONG Range Experiment |
| ICARTT | International Consortium for Atmospheric Research on Transport and Transformation |
| ICE-L | Ice in Clouds Experiment-Layer Clouds |
| INTEX-B | Intercontinental Chemical Transport Experiment |
| ISDAC | Indirect and Semi-Direct Aerosol Campaign |
| ITOP | International Transport of Ozone and Precursors |
| MEGAPOLI | Megacities: Emissions, urban, regional and Global Atmospheric POLlution and climate effects, and Integrated tools for assessment and mitigation |
| MILAGRO / MIRAGE | Megacity Initiative: Local and Global Research Observations / Megacity Impact on Regional and Global Environment |
| NEAQS-ITCT ICARTT | New England Air Quality Study – Intercontinental Transport and Chemical Transformation |
| PAZI | Particles from Aircraft: Impact on Cirrus Clouds and Climate |
| POLARCAT | Polar Study using Aircraft, Remote Sensing, Surface Measurements and Models, of Climate, Chemistry, Aerosols, and Transport |
| TexAQS II | Texas Air Quality Field Studie II |
| YAK-AEROSIB | Airborne Extensive Regional Observations in Siberia |

## 7.9 List of Symbols

| Symbol | Description | Unit |
|---|---|---|
| $A$ | cross section | $m^2$ |
| $A_i$ | amplitude, fit parameter for the lognormal size distribution fit function | |
| $AB_{corrf}$ | air beam correction factor | |
| $b$ | slope parameter for AMS size calibration | |
| $C_{AMS}$ | AMS derived mass concentration without PCI correction | µg $m^{-3}$ |
| $C_{sAB}$ | mass concentration of species *s* including the air beam correction factor | µg $m^{-3}$ |
| $Cavg_{cpc}$ | one minute average counts of the CPC | |
| $Cavg_{lsp}$ | one minute average counts of the LSP | |
| $C_c$ | Cunningham slip correction factor | |
| $CE$ | collection efficiency | |
| $CE_{PCI}$ | collection efficiency including the transmission function of the PCI | |
| $CPC_{avg}$ | particle number concentration recorded by the CPC | |
| $C_{STP}$ | mass concentration at STP conditions | µg $m^{-3}$ |
| $Ctotal_{cpc}$ | total counts by the CPC | |
| $Ctotal_{lsp}$ | total counts by the LSP | |
| $d$ | particle diameter | m |
| $d$ | particle diameter | µm |
| $D^*$ | effective scaling diameter of AMS size calibration | nm |
| $d_1$ | diameter of $COr_1$ | µm |
| $\bar{d}_g$ | Geometric mean diameter | µm |
| $d_{mob}$ | mobility diameter | nm |
| $d_p$ | particle diameter | m |
| $d_p$ | particle vacuum aerodynamic diameter | µm |
| $D_t$ | inner diameter of PCI chamber | m |
| $d_{va}$ | vacuum aerodynamic diameter | nm |
| $d_y$ | Julian day of year | |
| $E^+_{trans}$ | positive total error in the lens transmission efficiency determined by means of the mass method | |

| Symbol | Description | Unit |
|---|---|---|
| $E_{abs\_t\_bin}$ | error over all respective *m/z* for all time steps and per new bin | µg $m^{-3}$ |
| $E_{avg\_m/z\_t}$ | error per *m/z* over all size bins during the measurement interval | µg $m^{-3}$ |
| $E_{avg\_m/z\_t\_bin}$ | average error per *m/z* over all time steps and within one new bin | µg $m^{-3}$ |
| $E_B$ | losses due to particles bouncing off the vaporizer | |
| $E_{count}$ | total counting statistics error of the counting method | |
| $E_i$ | stands for either the total number (N) or the total volume (V) of a particle size distribution | $cm^{-3}$ or $\mu m^3 cm^{-3}$ |
| $E_L$ | losses occurring in the AMS inlet and lens system | |
| $E_{mass\_cpc}$ | sum of $Mcpc_{sdev1}$ and $Mcpc_{sdev2}$ | µg $m^{-3}$ |
| $er_i$ | error per bin, time step and *m/z* | µg $m^{-3}$ |
| $er_{rawbin\_i}{}^2$ | error per *m/z* over all time steps and per raw bin | µg $m^{-3}$ |
| $E_S$ | losses due to non-focusing of irregularly shaped particles after having passed through the aerodynamic lens | |
| $E^-_{trans}$ | negative total error in the lens transmission efficiency determined by means of the mass method | |
| $g$ | gravitational acceleration | m $s^{-2}$ |
| $I_b$ | background signal of the AMS | µg $m^{-3}$ or Hz |
| $I_s$ | signal intensity of species *s* | µg $m^{-3}$ or Hz |
| $IE$ | ionization efficiency | |
| $IE_{NO3}$ | Ionization efficiency of nitrate | |
| *Mams* | AMS derived mass | µg $m^{-3}$ |
| *MC* | mass concentration | µg $m^{-3}$ |
| *Mcpc* | CPC derived mass | µg $m^{-3}$ |
| $Mcpc_{avg}$ | average mass of $NH_4NO_3$ derived by the CPC counts | µg $m^{-3}$ |
| $Mcpc_{sdev1}$ | standard deviation from the mean CPC counts leading to uncertainty in the mass of $NH_4NO_3$ | µg $m^{-3}$ |
| $Mcpc_{sdev2}$ | standard deviation found in the size distribution of the monodispers aerosol after selection by the DMA | µg $m^{-3}$ |
| *MG air* | molecular weight of air | g $mol^{-1}$ |
| $M_{NH_4NO_3}$ | mass of $NH_4NO_3$ | µg $m^{-3}$ |
| $MW_s$ | Molecular weight of species *s* | g $mol^{-1}$ |

| Symbol | Description | Unit |
|---|---|---|
| $N$ | total number of time steps | |
| $N$ | number density | # $m^{-3}$ |
| $N_A$ | Avogadro's number ($6.02*10^{23}$) | $mol^{-1}$ |
| $P$ | atmospheric pressure | hPa |
| $P_{amb}$ | ambient pressure | hPa |
| $Pcpc_{sdev}$ | standard deviation from the mean CPC counts | |
| $P_{lens}$ | pressure inside the aerodynamic lens | mbar |
| $PP$ | fraction of particles out of the entire size distribution at the selected diameter | |
| $P_{PCI}$ | pressure inside the PCI | mbar |
| $P_{STP}$ | pressure at standard temperature and pressure conditions | 1013.25 hPa |
| $q$ | specific humidity | g $kg^{-1}$ |
| $Q_0$ | volumetric flowrate upstream of $CO_{r1}$ | $m^3$ $s^{-1}$ |
| $R$ | mass resolving power | |
| $R$ | universal gas constant | J $(Kmol)^{-1}$ |
| $RIE_s$ | relative ionization efficiency of species $s$ | |
| $Re$ | Reynolds number | |
| $S$ | Jayne shape factor | |
| $SD_{sdev}$ | standard deviation from the mean of the particle number fraction of the size distribution of the monodispers aerosol at the selected diameter | |
| $St$ | Stokes number | |
| $St'$ | modified Stokes number | |
| $T$ | temperature | K |
| $U_o$ | velocity upstream of $COr_1$ | m $s^{-1}$ |
| $U_s$ | sound velocity at $Cor_1$ | m $s^{-1}$ |
| $v$ | velocity | m $s^{-1}$ |
| $V_{Cor}$ | nominal flow rate through the last critical orifice ($Cor_2$) | $cm^3$ $s^{-1}$ |
| $v_g$ | gas velocity at the exit of the aerodynamic lens | m $s^{-1}$ |
| $v_l$ | gas velocity within the aerodynamic lens | m $s^{-1}$ |

| Symbol | Description | Unit |
|---|---|---|
| $V_{meas}$ | flow rate measured by the pressure sensor in the aerodynamic lens calibrated for standard pressure and a critical orfice of 100 µm | $cm^3\ s^{-1}$ |
| *VMR* | volume mixing ratio | |
| $V_{TS}$ | terminal settling velocity | $m\ s^{-1}$ |
| *width* | width of lognormal distribution | |
| $x_i$ | modal diameter | µm |
| $\gamma$ | adiabatic index for dry air | |
| $\eta$ | dynamic viscosity | $kg\ (ms)^{-1}$ |
| $\Theta$ | potential temperature | K |
| $\mu$ | dynamic viscosity | $kg\ (ms)^{-1}$ |
| $\rho$ | density | $kg\ m^{-3}$ |
| $\rho_0$ | unit density | $1\ g\ cm^{-3}$ |
| $\rho_p$ | particle density | $g\ cm^{-3}$ |
| $\sigma$ | standard deviation | |
| $\sigma_g$ | geometric standard deviation | |
| $\tau$ | lifetime | days |

## *7.10 List of tables*

## *7.11 List of figures*

## *7.12 Publications resulting from this work*

**Peer reviewed**

Quennehen, B., Schwarzenboeck, A., **Schmale, J.**, Schneider, H. Sodemann, J., Stohl, Ancellet, G., Crummeryrolle, S., and Law, K. S.: Physical and chemical properties of pollution aerosol particles transported from North America to Greenland as measured during the POLARCAT summer campaign, *Atmos. Chem. Phys.*, 11, 10947-10963, 2011.

**Schmale, J.**, Schneider, J., Ancellet, G., Quennehen, B., Stohl, A., Sodemann, H., Burkhart, J. F., Hamburger, T., Arnold, S., Schwarzenboeck, A., Borrmann, S., and Law, K.: Source Identification and Airborne Chemical Characterisation of Aerosol Pollution from Long-range Transport over Greenland during POLARCAT Summer campaign 2008, *Atmos. Chem. Phys.*, 11, 10097-10123, 2011.

Jurkat, T., C. Voigt, F. Arnold, H. Schlager, H. Aufmhoff, **J. Schmale**, J. Schneider, M. Lichtenstern, and A. Dörnbrack, Airborne stratospheric ITCIMS measurements of SO2, HCl, and HNO3 in the aged plume of volcano Kasatochi, *J. Geophys. Res.*, 115, D00L17, doi:10.1029/2010JD013890, 2010.

Voigt, C., U. Schumann, T. Jurkat, D. Schäuble, H. Schlager, A. Petzold, J.-F. Gayet, M. Krämer, J. Schneider, S. Borrmann, **J. Schmale**, P. Jessberger, T. Hamburger, M. Lichtenstern, M. Scheibe, C. Gourbeyre, J. Meyer, M. Kübbeler, W. Frey, H. Eichler, T. Butler, M. G. Lawrence, F. Holzäpfel, F. Arnold, M. Wendisch, A. Döpelheuer, K. Gottschaldt, R. Baumann, M. Zöger, I. Sölch, M. Rautenhaus, and A. Dörnbrack, In-situ observations of young contrails – overview and selected results from the CONCERT campaign, *Atmos. Chem. Phys.*, 10, 9030-9056, 2010.

**Schmale, J.**, J. Schneider, T. Jurkat, C. Voigt, H. Kalesse, M. Rautenhaus, M. Lichtenstern, H. Schlager, G. Ancellet, F. Arnold, M. Gerding, I. Mattis, M. Wendisch, and S. Borrmann, Aerosol layers from the 2008 eruptions of Mt. Okmok and Mt. Kasatochi: In-situ UT/LS measurements of sulfate and organics over Europe, *J. Geophys. Res.*, 115, D00L07, doi:10.1029/2009JD013628, 2010.

**Conference Contributions**

**J. Schmale**, J. Schneider, G. Ancellet, B. Quennehen, A. Stohl, H. Sodemann, J. Burkhart, T. Hamburger, S.R. Arnold, A. Schwarzenböck, S. Borrmann, and K.S. Law: Source Identification and Airborne Chemical Characterisation of Aerosol Pollution from Long-range Transport over Greenland during POLARCAT Summer campaign 2008, Arctic Monitoring and Assessment Programme Conference, Copenhagen, May 4 – 6, 2011.

B. Quennehen, A. Schwarzenboeck, A. Matsuki, **J. Schmale**, H. Sodemann, J. Schneider, G. Ancellet, A. Stohl, J. Pelon, and K.S. Law, Pollution transported to the Arctic during the POLARCAT-France spring and summer campaigns: source regions and aerosol properties. EGU, Vienna, April 4-8, 2011.

T. Jurkat, C. Voigt,F. Arnold, H. Schlager, H. Aufmhoff, **J. Schmale**, J. Schneider, S. Borrmann, M. Lichtenstern, and A. Dörnbrack: Airborne ITCIMS measurements of $SO_2$, HCl and $HNO_3$ in an aged stratospheric plume of volcanic origin, International Aerosol Conference, Helsinki, Aug. 29- Sept. 3, 2010.

**J. Schmale**, J. Schneider, G. Ancellet, B. Quennehen, A. Stohl, H. Sodemann, J. Burkhart, S.R. Arnold, A. Schwarzenböck, S. Borrmann, and K.S. Law: Detection and source identification of particles pollution plumes in the Arctic summer: Results from in-situ measurements during POLARCAT-France 2008 in Greenland, International Polar Year Oslo Science Conference, Oslo, Jun 8-12, 2010.

B. Quennehen, A. Schwarzenboeck, O. Jourdan, A. Stohl, G. Ancellet, **J. Schmale**, S. Crumeyrolle, K. S. Law: Arctic Aerosol Physical and Optical Characterization During the POLARCAT campaign in Greenland, International Polar Year Oslo Science Conference, Oslo, Jun 8-12, 2010.

**J. Schmale**, J. Schneider, T. Jurkat, C. Voigt, H. Kalesse, M. Rautenhaus, M. Lichtenstern, H. Schlager, G. Ancellet, F. Arnold, M. Gerding, I. Mattis, M. Wendisch, and S. Borrmann: Measurements of particulate sulfate and organics of volcanic aerosol in the UT/LS three months after the 2008 eruptions of Mt. Okmok and Mt. Kasatochi, EGU, Vienna, May 2-8, 2010.

**J. Schmale**, J. Schneider, M. Brands, G. Ancellet, H. Schlager, M. Lichtenstern, M. Scheibe, S.R. Arnold, K.S. Law, C. Voigt, and S. Borrmann, Correlations between particulate sulfate and ozone observed in the UT/LS over Greenland and Central/Western Europe in 2008, European Aerosol Conference, Karlsruhe, Sept. 6-11, 2009.

C. Voigt, U. Schumann, T. Jurkat, D. Schäuble, H. Schlager, M. Lichtenstern, M. Scheibe, T. Hamburger, A. Petzold, A. Dörnbrack, F. Holzäpfel, J.-F. Gayet, C. Gourbeyre, M. Krämer, M. Kübbeler, J. Meyer, J. Schneider, **J. Schmale**, H. Eichler, W. Frey, S. Molleker, S. Borrmann: Detection of young contrails – selected results from the CONCERT (CONtrail and Cirrus ExpeRimenT) campaign, 2nd International Conference on Transport, Atmosphere and Climate, Aachen, Maastricht, June 22-25, 2009.

**J. Schmale**, J. Schneider, M. Brands, G. Ancellet, J. Pelon, S.R. Arnold, A. Schwarzenböck, C. Gourbeyre, S. Borrmann, and K.S. Law, Transport of North American pollution plumes towards the Arctic detected by aircraft based aerosol composition measurements in the Arctic 2008 summer season during the POLARCAT-France campaign, EGU General Assembly, Vienna, April 19-24, 2009.

K. Law, G. Ancellet, F. Ravetta, J. Pelon, S. Turquety, C. Clerbaux, M. Pommier, R. A. de Villier, J.-F. Gayet, A. Schwarzenboeck, C. Gourbeyre, F. Doussiere, P. Nedelec, J. Schneider, **J. Schmale**, M. Brands, S. Borrmann, S. Arnold, S. Monks, J.-D. Paris, POLARCAT-France Airborne Experiments: First Results, IGAC, Annecy, September 7 – 11, 2008.

# 8. Bibliography

(WMO), W. M. O.: Atmsopheric ozone 1985, WMO Global Ozone Res. and Monit. Proj. Rep. 20, Geneva, 1986.

Aiken, A. C., Decarlo, P. F., Kroll, J. H., Worsnop, D. R., Huffman, J. A., Docherty, K. S., Ulbrich, I. M., Mohr, C., Kimmel, J. R., Sueper, D., Sun, Y., Zhang, Q., Trimborn, A., Northway, M., Ziemann, P. J., Canagaratna, M. R., Onasch, T. B., Alfarra, M. R., Prevot, A. S. H., Dommen, J., Duplissy, J., Metzger, A., Baltensperger, U., and Jimenez, J. L.: O/C and OM/OC ratios of primary, secondary, and ambient organic aerosols with high-resolution time-of-flight aerosol mass spectrometry, Environ. Sci. Technol., 42, 4478-4485, 10.1021/es703009q, 2008.

Aiken, A. C., Salcedo, D., Cubison, M. J., Huffman, J. A., DeCarlo, P. F., Ulbrich, I. M., Docherty, K. S., Sueper, D., Kimmel, J. R., Worsnop, D. R., Trimborn, A., Northway, M., Stone, E. A., Schauer, J. J., Volkamer, R. M., Fortner, E., de Foy, B., Wang, J., Laskin, A., Shutthanandan, V., Zheng, J., Zhang, R., Gaffney, J., Marley, N. A., Paredes-Miranda, G., Arnott, W. P., Molina, L. T., Sosa, G., and Jimenez, J. L.: Mexico City aerosol analysis during MILAGRO using high resolution aerosol mass spectrometry at the urban supersite (T0) - Part 1: Fine particle composition and organic source apportionment, Atmos. Chem. Phys., 9, 6633-6653, 2009.

Alfarra, M. R., Coe, H., Allan, J. D., Bower, K. N., Boudries, H., Canagaratna, M. R., Jimenez, J. L., Jayne, J. T., Garforth, A. A., Li, S. M., and Worsnop, D. R.: Characterization of urban and rural organic particulate in the lower Fraser valley using two aerodyne aerosol mass spectrometers, Atmos. Environ., 38, 5745-5758, 10.1016/j.atmosenv.2004.01.054, 2004.

Alfarra, M. R., Prevot, A. S. H., Szidat, S., Sandradewi, J., Weimer, S., Lanz, V. A., Schreiber, D., Mohr, M., and Baltensperger, U.: Identification of the Mass Spectral Signature of Organic Aerosols from Wood Burning Emissions, Environ. Sci. Technol., 41, 5770-5777, 2007.

Allan, J. D., Jimenez, J. L., Williams, P. I., Alfarra, M. R., Bower, K. N., Jayne, J. T., Coe, H., and Worsnop, D. R.: Quantitative sampling using an Aerodyne aerosol mass spectrometer. 1. Techniques of data interpretation and error analysis, J. Geophys. Res., 108, AAC1-1-AAC1-AAC1-10, 10.1029/2002jd002358, 2003.

Allan, J. D., Bower, K. N., Coe, H., Boudries, H., Jayne, J. T., Canagaratna, M. R., Millet, D. B., Goldstein, A. H., Quinn, P. K., Weber, R. J., and Worsnop, D. R.: Submicron aerosol composition at Trinidad Head, California, during ITCT 2K2: Its relationship with gas phase volatile organic carbon and assessment of instrument performance, Journal of Geophysical Research-Atmospheres, 109, 16, D23s24 10.1029/2003jd004208, 2004a.

Allan, J. D., Delia, A. E., Coe, H., Bower, K. N., Alfarra, M. R., Jimenez, J. L., Middlebrook, A. M., Drewnick, F., Onasch, T. B., Canagaratna, M. R., Jayne, J. T., and Worsnopf, D. R.: A generalised method for the extraction of chemically resolved mass spectra from aerodyne aerosol mass spectrometer data, J. Aerosol. Sci., 35, 909-922, 10.1016/j.jaerosci.2004.02.007, 2004b.

AMAP: Acidifying pollutants, Arctic haze, and acidification in the Arctic, Arctic Monitoring and Assessment Programm (AMAP), Oslo, Assment Report, 2006.

Ancellet, G., Leclair de Bellevue, J., Mari, C., Nedelec, P., Kukui, A., Borbon, A., and Perros, P.: Effects of regional-scale and convective transports on tropospheric ozone chemistry revealed by aircraft observation during the wet season of the AMMA campaign, Atmos. Chem. Phys., 9, 383-411, 2009.

Andreae, M. O., and Merlet, P.: Emission of trace gases and aerosols from biomass burning, Global Biogeochemical Cycles, 15, 955-966, 2001.

Andreae, M. O., and Rosenfeld, D.: Aerosol-cloud-precipitation interactions. Part 1. The nature and sources of cloud-active aerosols, Earth-Science Reviews, 89, 13-41, 10.1016/j.earscirev.2008.03.001, 2008.

Andreae, M. O.: A New Look at Aging Aerosols, Science, 326, 1493-1494, 10.1126/science.1183158, 2009.

Appenzeller, C., Davies, H. C., and Norton, W. A.: Fragmentation of stratospheric intrusions, Journal of Geophysical Research-Atmospheres, 101, 1435-1456, 1996.

Arnold, F., Buhrke, T., and Qiu, S.: Evidence for stratospheric ozone-depleting heterogeneous chemistry on volcanic aerosols form El-Chicon, Nature, 348, 49-50, 1990.

Arnold, F., Curtius, J., Spreng, S., and Deshler, T.: Stratospheric aerosol sulfuric acid: First direct in situ measurements using a novel balloon-based mass spectrometer apparatus, J. Atmos. Chem., 30, 3-10, 1998.

Bahreini, R., Jimenez, J. L., Wang, J., Flagan, R. C., Seinfeld, J. H., Jayne, J. T., and Worsnop, D. R.: Aircraft-based aerosol size and composition measurements during ACE-Asia using an Aerodyne aerosol mass spectrometer, Journal of Geophysical Research-Atmospheres, 108, 22, 8645 10.1029/2002jd003226, 2003.

Bahreini, R., Dunlea, E. J., Matthew, B. M., Simons, C., Docherty, K. S., DeCarlo, P. F., Jimenez, J. L., Brock, C. A., and Middlebrook, A. M.: Design and operation of a pressure-controlled inlet for airborne sampling with an aerodynamic aerosol lens, Aerosol Sci. Technol., 42, 465-471, 10.1080/02786820802178514, 2008.

Bahreini, R., Ervens, B., Middlebrook, A. M., Warneke, C., de Gouw, J. A., DeCarlo, P. F., Jimenez, J. L., Brock, C. A., Neuman, J. A., Ryerson, T. B., Stark, H., Atlas, E., Brioude, J., Fried, A., Holloway, J. S., Peischl, J., Richter, D., Walega, J., Weibring, P., Wollny, A. G., and Fehsenfeld, F. C.: Organic aerosol formation in urban and industrial plumes near Houston and Dallas, Texas, Journal of Geophysical Research-Atmospheres, 114, D00f16 10.1029/2008jd011493, 2009.

Bank, A. D.: People's Republic of China: Design of the National SO2 emission trading system. , Tech. Assistance Rep. 42056, Manila. available at http://www.adb.org/Documents/TARs/PRC/42056-PRC-TAR.pdf, 2008.

Bethan, S., Vaughan, G., and Reid, S. J.: A comparison of ozone and thermal tropopause heights and the impact of tropopause definition on quantifying the ozone content of the troposphere, Q. J. R. Meteorol. Soc., 122, 929-944, 1996.

Bitar, L., Duck, T. J., Kristiansen, N. I., Stohl, A., and Beauchamp, S.: Lidar observations of Kasatochi volcano aerosols in the troposphere and stratosphere, Journal of Geophysical Research-Atmospheres, 115, D00l13 10.1029/2009jd013650, 2010.

Bond, T. C., Streets, D. G., Yarber, K. F., Nelson, S. M., Woo, J. H., and Klimont, Z.: A technology-based global inventory of black and organic carbon emissions from combustion, Journal of Geophysical Research-Atmospheres, 109, 43, D14203 10.1029/2003jd003697, 2004.

Borrmann, S., Dye, J. E., Baumgardner, D., Wilson, J. C., Jonsson, H. H., Brock, C. A., Loewenstein, M., Podolske, J. R., Ferry, G. V., and Barr, K. S.: In-situe measurements of changes in stratospheric aerosol and the $N_2O$-aerosol relationship inside and outside of the Polar Vortex, Geophysical Research Letters, 20, 2559-2562, 1993.

Borrmann, S., Dye, J. E., Baumgardner, D., Proffitt, M. H., Margitan, J. J., Wilson, J. C., Jonsson, H. H., Brock, C. A., Loewenstein, M., Podolske, J. R., and Ferry, G. V.: Aerosol as dynamical tracers in the lower stratosphere - Ozone versus aerosol correlation after the Mount-Pinatubo eruption, Journal of Geophysical Research-Atmospheres, 100, 11147-11156, 1995.

Borrmann, S., Solomon, S., Dye, J. E., and Luo, B. P.: The potential of cirrus clouds for heterogeneous chlorine activation, Geophysical Research Letters, 23, 2133-2136, 1996.

Borrmann, S., Solomon, S., Dye, J. E., Baumgardner, D., Kelly, K. K., and Chan, K. R.: Heterogeneous reactions on stratospheric background aerosols, volcanic sulfuric acid droplets, and type I polar stratospheric clouds: Effects of temperature fluctuations and differences in particle phase, Journal of Geophysical Research-Atmospheres, 102, 3639-3648, 1997.

Borrmann, S., Kunkel, D., Weigel, R., Minikin, A., Deshler, T., Wilson, J. C., Curtius, J., Volk, C. M., Homan, C. D., Ulanovsky, A., Ravegnani, F., Viciani, S., Shur, G. N., Belyaev, G. V., Law, K. S., and Cairo, F.: Aerosols in the tropical and subtropical UT/LS: in-situ measurements of submicron particle abundance and volatility, Atmos. Chem. Phys., 10, 5573-5592, 10.5194/acp-10-5573-2010, 2010.

Bourassa, A. E., Degenstein, D. A., Elash, B. J., and Llewellyn, E. J.: Evolution of the stratospheric aerosol enhancement following the eruptions of Okmok and Kasatochi: Odin-OSIRIS measurements, Journal of Geophysical Research-Atmospheres, 115, D00l03 10.1029/2009jd013274, 2010.

Box, J. E., Bai, L.-S., Benson, R., Bhattacharya, I., Bromwich, D. H., Cappelen, J., Decker, D., DiGirolamo, N., Fettweis, X., Hall, D., Hanna, E., Mote, T., Tedesco, M., van de Wal, R., and van den Broeke, M.: Greenland [in Arctic Report Card 2009], http://www.arctic.noaa.gov/reportcard., 2009.

Brands, M.: Aufbau und Characterisierung eines flugzeuggetragenen Einzelpartikel-Massenspektrometers, PhD, Fachbereich für Physik, Mathematik und Informatik, Johannes Gutenberg-Universität, Mainz, 2009.

Brands, M., Kamphus, M., Bottger, T., Schneider, J., Drewnick, F., Roth, A., Curtius, J., Voigt, C., Borbon, A., Beekmann, M., Bourdon, A., Perrin, T., and Borrmann, S.: Characterization of a Newly Developed Aircraft-Based Laser Ablation Aerosol Mass Spectrometer (ALABAMA) and First Field Deployment in Urban Pollution Plumes over Paris During MEGAPOLI 2009, Aerosol Sci. Technol., 45, 46-64, 10.1080/02786826.2010.517813, 2011.

Brock, C. A., Radke, L. F., Lyons, J. H., and Hobbs, P. V.: Arctic hazes in summer over Greenland and the North-American Arctic. 1. Incidence and origins, J. Atmos. Chem., 9, 129-148, 1989.

Brock, C. A., Radke, L. F., and Hobbs, P. V.: Sulfur in particles in Arctic hazes derived from airborne insitu and lidar measurements, Journal of Geophysical Research-Atmospheres, 95, 22369-22387, 1990.

Brock, C. A., Sullivan, A. P., Peltier, R. E., Weber, R. J., Wollny, A., Gouw, J. A., Middlebrook, A. M., Atlas, E. L., Stohl, A., Trainer, M. K., Cooper, O. R., Fehsenfeld, F. C., Frost, G. J., Holloway, J. S., Hubler, G., Neuman, J. A., Ryerson, T. B., Warneke, C., and Wilson, J. C.: Sources of particulate matter in the northeastern United States in summer: 2. Evolution of chemical and microphysical properties, Journal of Geophysical Research-Atmospheres, 113, 16, D08302 10.1029/2007jd009241, 2008.

Brock, C. A., Cozic, J., Bahreini, R., Froyd, K. D., Middlebrook, A. M., McComiskey, A., Brioude, J., Cooper, O. R., Stohl, A., Aikin, K. C., De Gouw, J. A., Fahey, D. W., Ferrare, R. A., Gao, R.-S., Gore, W., Holloway, J., Hübler, G., Jefferson, A., Lack, D. A., Lance, S., Moore, R. H., Murphy, D. M., Nenes, A., Novelli, P. C., Nowak, J. B., Ogren, J. A., Peischl, J., Pierce, R. B., Pilewskie, P., Quinn, P. K., Ryerson, T. B., Schmidt, K. S., Schwarz, J. P., Sodemann, H., Spackman, J. R., Stark, H., Thomson, D. S., Thornberry, T., Veres, P., Watts, L. A., Warneke, C., and Wollny, A. G.: Characteristics, sources, and transport of aerosols measured in spring 2008 during the aerosol, radiation, and cloud processes affecting Arctic climate (ARCPAC) project, Atmospheric Chemistry and Physics Disscussions, 10, 27361-27434, 2010.

Brooks, B. J., McQuaid, J. B., Smith, M. H., Crosier, J., Williams, P. I., Coe, H., and Osborne, S.: Intercomparison of VACC- and AMS-derived nitrate, sulphate and ammonium aerosol loadings during ADRIEX, Q. J. R. Meteorol. Soc., 133, 77-84, 10.1002/qj.90, 2007.

Brough, N., Reeves, C. E., Penkett, S. A., Stewart, D. J., Dewey, K., Kent, J., Barjat, H., Monks, P. S., Ziereis, H., Stock, P., Huntrieser, H., and Schlager, H.: Intercomparison of aircraft instruments on board the C-130 and Falcon 20 over southern Germany during EXPORT 2000, Atmos. Chem. Phys., 3, 2127-2138, 2003.

Browning, K. A., and Monk, G. A.: A simple-model for the synoptic analysis of cold fronts, Q. J. R. Meteorol. Soc., 108, 435-452, 1982.

Canagaratna, M. R., Jayne, J. T., Jimenez, J. L., Allan, J. D., Alfarra, M. R., Zhang, Q., Onasch, T. B., Drewnick, F., Coe, H., Middlebrook, A., Delia, A., Williams, L. R., Trimborn, A. M., Northway, M. J., DeCarlo, P. F., Kolb, C. E., Davidovits, P., and Worsnop, D. R.: Chemical and microphysical characterization of ambient aerosols with the aerodyne aerosol mass spectrometer, Mass Spectrom. Rev., 26, 185-222, 10.1002/mas.20115, 2007.

Cooper, O. R., Moody, J. L., Parrish, D. D., Trainer, M., Ryerson, T. B., Holloway, J. S., Hubler, G., Fehsenfeld, F. C., and Evans, M. J.: Trace gas composition of midlatitude cyclones over the western North Atlantic Ocean: A conceptual model, Journal of Geophysical Research-Atmospheres, 107, 10.1029/2001jd000901, 2002.

Crosier, J., Allan, J. D., Coe, H., Bower, K. N., Formenti, P., and Williams, P. I.: Chemical composition of summertime aerosol in the Po Valley (Italy), northern Adriatic and Black Sea, Q. J. R. Meteorol. Soc., 133, 61-75, 10.1002/qj.88, 2007.

Cross, E. S., Slowik, J. G., Davidovits, P., Allan, J. D., Worsnop, D. R., Jayne, J. T., Lewis, D. K., Canagaratna, M., and Onasch, T. B.: Laboratory and ambient particle density determinations using light scattering in conjunction with aerosol mass spectrometry, Aerosol Sci. Technol., 41, 343-359, 10.1080/02786820701199736, 2007.

Cubison, M. J., Ortega, A. M., Hayes, P. L., Farmer, D. K., Day, D. A., Lechner, M. J., Brune, W., Apel, E., Diskin, G. S., Fisher, J. A., Fuelberg, H. E., Hecobian, A., Knapp, D., Mikoviny, T., Riemer, D. D., Sachse, G., Sessions, W., Weber, R., Weinheimer, A., Wisthaler, A., and Jimenez, J.: Effects of aging on organic aerosol from open biomass burning smoke in aircraft lab studies, Atmospheric Chemistry and Physics Disscussions, 11, 12103-12140, 2011.

Cziczo, D. J., DeMott, P. J., Brooks, S. D., Prenni, A. J., Thomson, D. S., Baumgardner, D., Wilson, J. C., Kreidenweis, S. M., and Murphy, D. M.: Observations of organic species and atmospheric ice formation, Geophysical Research Letters, 31, 4, L12116 10.1029/2004gl019822, 2004.

DeCarlo, P. F., Slowik, J. G., Worsnop, D. R., Davidovits, P., and Jimenez, J. L.: Particle morphology and density characterization by combined mobility and aerodynamic diameter measurements. Part 1: Theory, Aerosol Sci. Technol., 38, 1185-1205, 10.1080/027868290903907, 2004.

DeCarlo, P. F., Kimmel, J. R., Trimborn, A., Northway, M. J., Jayne, J. T., Aiken, A. C., Gonin, M., Fuhrer, K., Horvath, T., Docherty, K. S., Worsnop, D. R., and Jimenez, J. L.: Field-deployable, high-resolution, time-of-flight aerosol mass spectrometer, Analytical Chemistry, 78, 8281-8289, 10.1021/ac061249n, 2006.

DeCarlo, P. F., Dunlea, E. J., Kimmel, J. R., Aiken, A. C., Sueper, D., Crounse, J., Wennberg, P. O., Emmons, L., Shinozuka, Y., Clarke, A., Zhou, J., Tomlinson, J., Collins, D. R., Knapp, D., Weinheimer, A. J., Montzka, D. D., Campos, T., and Jimenez, J. L.: Fast airborne aerosol size and chemistry measurements above Mexico City and Central Mexico during the MILAGRO campaign, Atmos. Chem. Phys., 8, 4027-4048, 2008.

DeCarlo, P. F., Ulbrich, I. M., Crounse, J., de Foy, B., Dunlea, E. J., Aiken, A. C., Knapp, D., Weinheimer, A. J., Campos, T., Wennberg, P. O., and Jimenez, J. L.: Investigation of the sources and processing of organic aerosol over the Central Mexican Plateau from aircraft measurements during MILAGRO, Atmos. Chem. Phys., 10, 5257-5280, 10.5194/acp-10-5257-2010, 2010.

Deshler, T.: A review of global stratospheric aerosol: Measurements, importance, life cycle, and local stratospheric aerosol, Atmos. Res., 90, 223-232, 10.1016/j.atmosres.2008.03.016, 2008.

Dickerson, R. R., Li, C., Li, Z., Marufu, L. T., Stehr, J. W., McClure, B., Krotkov, N., Chen, H., Wang, P., Xia, X., Ban, X., Gong, F., Yuan, J., and Yang, J.: Aircraft observations of dust and pollutants over northeast China: insight into the meteorological mechanisms of transport, J. Geophys. Res, D, Atmos., 112, D24S90, 10.1029/2007JD008999 2007.

Dinar, E., Mentel, T. F., and Rudich, Y.: The density of humic acids and humic like substances (HULIS) from fresh and aged wood burning and pollution aerosol particles, Atmos. Chem. Phys., 6, 5213-5224, 2006.

Doherty, S. J., Warren, S. G., Grenfell, T. C., Clarke, A. D., and Brandt, R. E.: Light-absorbing impurities in Arctic snow, Atmos. Chem. Phys., 10, 11647-11680, 10.5194/acp-10-11647-2010, 2010.

Donahue, N. M., Robinson, A. L., and Pandis, S. N.: Atmospheric organic particulate matter: From smoke to secondary organic aerosol, Atmos. Environ., 43, 94-106, 10.1016/j.atmosenv.2008.09.055, 2009.

Draxler, R. R., and Rolph, G. D.: HYSPLIT (HYbrid Single-Particle Lagrangian Integrated Trajectory) Model access via NOAA ARL READY Website (http://ready.arl.noaa.gov/HYSPLIT.php), NOAA Air Resources Laboratory, Silver Spring, MD, 2011.

Dreiling, V., and Friederich, B.: Spatial distribution of the arctic haze aerosol size distribution in western and eastern Arctic, Atmos. Res., 44, 133-152, 1997.

Drewnick, F., Schwab, J. J., Jayne, J. T., Canagaratna, M., Worsnop, D. R., and Demerjian, K. L.: Measurement of ambient aerosol composition during the PMTACS-NY 2001 using an aerosol mass spectrometer. Part I: Mass concentrations, Aerosol Sci. Technol., 38, 92-103, 10.1080/02786820390229507, 2004.

Drewnick, F., Hings, S. S., DeCarlo, P., Jayne, J. T., Gonin, M., Fuhrer, K., Weimer, S., Jimenez, J. L., Demerjian, K. L., Borrmann, S., and Worsnop, D. R.: A new time-of-flight aerosol mass spectrometer (TOF-AMS) - Instrument description and first field deployment, Aerosol Sci. Technol., 39, 637-658, 10.1080/02786820500182040, 2005.

Drewnick, F., Hings, S. S., Alfarra, M. R., Prevot, A. S. H., and Borrmann, S.: Aerosol quantification with the Aerodyne Aerosol Mass Spectrometer: detection limits and ionizer background effects, Atmospheric Measurement Techniques, 2, 33-46, 2009.

Dunlea, E. J., DeCarlo, P. F., Aiken, A. C., Kimmel, J. R., Peltier, R. E., Weber, R. J., Tomlinson, J., Collins, D. R., Shinozuka, Y., McNaughton, C. S., Howell, S. G., Clarke, A. D., Emmons, L. K., Apel, E. C., Pfister, G. G., van Donkelaar, A., Martin, R. V., Millet, D. B., Heald, C. L., and Jimenez, J. L.: Evolution of Asian aerosols during transpacific transport in INTEX-B, Atmos. Chem. Phys., 9, 7257-7287, 2009.

Dusek, U., Frank, G. P., Hildebrandt, L., Curtius, J., Schneider, J., Walter, S., Chand, D., Drewnick, F., Hings, S., Jung, D., Borrmann, S., and Andreae, M. O.: Size matters more than chemistry for cloud-nucleating ability of aerosol particles, Science, 312, 1375-1378, 10.1126/science.1125261, 2006.

Eckhardt, S., Stohl, A., Wernli, H., James, P., Forster, C., and Spichtinger, N.: A 15-year climatology of warm conveyor belts, Journal of Climate, 17, 218-237, 2004.

Ekman, A. M. L., Krejci, R., Engstrom, A., Strom, J., de Reus, M., Williams, J., and Andreae, M. O.: Do organics contribute to small particle formation in the Amazonian upper troposphere?, Geophysical Research Letters, 35, 5, L17810 10.1029/2008gl034970, 2008.

Engel, A., Bonisch, H., Brunner, D., Fischer, H., Franke, H., Gunther, G., Gurk, C., Hegglin, M., Hoor, P., Konigstedt, R., Krebsbach, M., Maser, R., Parchatka, U., Peter, T., Schell, D., Schiller, C., Schmidt, U., Spelten, N., Szabo, T., Weers, U., Wernli, H., Wetter, T., and Wirth, V.: Highly resolved observations of trace gases in the lowermost stratosphere and upper troposphere from the Spurt project: an overview, Atmos. Chem. Phys., 6, 283-301, 2006.

Esler, J. G., Tan, D. G. H., Haynes, P. H., Evans, M. J., Law, K. S., Plantevin, P. H., and Pyle, J. A.: Stratosphere-troposphere exchange: Chemical sensitivity to mixing, Journal of Geophysical Research-Atmospheres, 106, 4717-4731, 2001.

Fahey, D. W., Kawa, S. R., Woodbridge, E. L., Tin, P., Wilson, J. C., Jonsson, H. H., Dye, J. E., Baumgardner, D., Borrmann, S., Toohey, D. W., Avallone, L. M., Proffitt, M. H., Margitan, J., Loewenstein, M., Podolske, J. R., Salawitch, R. J., Wofsy, S. C., Ko, M. K. W., Anderson, D. E., Schoeberl, M. R., and Chan, K. R.: Insitu measurements constraining the role of sulfate aerosols in midlatitude ozone depletion, Nature, 363, 509-514, 1993.

Farina, S. C., Adams, P. J., and Pandis, S. N.: Modeling global secondary organic aerosol formation and processing with the volatility basis set: Implications for anthropogenic secondary organic aerosol, Journal of Geophysical Research-Atmospheres, 115, 17, D09202 10.1029/2009jd013046, 2010.

Fehsenfeld, F. C., Ancellet, G., Bates, T. S., Goldstein, A. H., Hardesty, R. M., Honrath, R., Law, K. S., Lewis, A. C., Leaitch, R., McKeen, S., Meagher, J., Parrish, D. D., Pszenny, A. A. P., Russell, P. B., Schlager, H., Seinfeld, J., Talbot, R., and Zbinden, R.: International Consortium for Atmospheric Research on Transport and Transformation (ICARTT): North America to Europe - Overview of the 2004 summer field study, Journal of Geophysical Research-Atmospheres, 111, D23s01 10.1029/2006jd007829, 2006.

Fiebig, M.: The Tropospheric Aerosol at mid-latitudes - microphysics, optics and climate forcing illustrated by the LACE 98 field study. , Ph.D., University of Munich, Munich, Germany, 2001.

Fiedler, V., Dal Maso, M., Boy, M., Aufmhoff, H., Hoffmann, J., Schuck, T., Birmili, W., Hanke, M., Uecker, J., Arnold, F., and Kulmala, M.: The contribution of sulphuric acid to atmospheric particle formation and growth: a comparison between boundary layers in Northern and Central Europe, Atmos. Chem. Phys., 5, 1773-1785, 2005.

Fiedler, V., Nau, R., Ludmann, S., Arnold, F., Schlager, H., and Stohl, A.: East Asian SO2 pollution plume over Europe - Part 1: Airborne trace gas measurements and source identification by particle dispersion model simulations, Atmos. Chem. Phys., 9, 4717-4728, 2009.

Fiedler, V., Arnold, F., Ludmann, S., Minikin, A., Hamburger, T., Pirjola, L., Dornbrack, A., and Schlager, H.: African biomass burning plumes over the Atlantic: aircraft based measurements and implications for H2SO4 and HNO3 mediated smoke particle activation, Atmos. Chem. Phys., 11, 3211-3225, 10.5194/acp-11-3211-2011, 2011.

Fischer, H., Wienhold, F. G., Hoor, P., Bujok, O., Schiller, C., Siegmund, P., Ambaum, M., Scheeren, H. A., and Lelieveld, J.: Tracer correlations in the northern high latitude lowermost stratosphere: Influence of cross-tropopause mass exchange, Geophysical Research Letters, 27, 97-100, 2000.

Fischer, H., Lawrence, M., Gurk, C., Hoor, P., Lelieveld, J., Hegglin, M. I., Brunner, D., and Schiller, C.: Model simulations and aircraft measurements of vertical, seasonal and latitudinal O-3 and CO distributions over Europe, Atmos. Chem. Phys., 6, 339-348, 2006.

Flannigan, M. D., Krawchuk, M. A., de Groot, W. J., Wotton, B. M., and Gowman, L. M.: Implications of changing climate for global wildland fire, Int. J. Wildland Fire, 18, 483-507, 10.1071/wf08187, 2009.

Foltescu, V. L., and Zahn, A.: Aerosols used as tracers for stratosphere troposphere exchange in the Arctic, Atmos. Environ., 29, 1777-1784, 1995.

Formenti, P., Elbert, W., Maenhaut, W., Haywood, J., Osborne, S., and Andreae, M. O.: Inorganic and carbonaceous aerosols during the Southern African Regional Science Initiative (SAFARI 2000) experiment: Chemical characteristics, physical properties, and emission data for smoke from African biomass burning, Journal of Geophysical Research-Atmospheres, 108, 16, 8488 10.1029/2002jd002408, 2003.

Forster, C., Stohl, A., and James, P.: The residence times of aircraft emissions in the stratosphere using a mean emission inventory and emissions along actual flight tracks, J. Geophys. Res., 108, STA9-1-STA9-STA9-9, 10.1029/2002jd002515, 2003.

Forster, P., Ramaswamy, V., Artaxo, P., Berntsen, T., Betts, R., Fahey, D. W., Haywood, J., Lean, J., Lowe, D. C., Myhre, G., Nganga, J., Prinn, R., Raga, G., Schulz, M., and Van Dorland, R.: Changes in

Atmospheric Constituents and in Radiative Forcing. In: Climate Change 2007: The Physical Science Basis. Contribution of Working Group I to the fourth Assessment Report of the Intergovernmental Panel on Climate Change. [Solomon, S., D. Qin, M. Manning, Z. Chen, M. Marquis, K.B. Averyt, M.Tignor and H.L. Miller (eds.)]. Cambridge University Press, Cambridge, United Kingdom and New York, NY, USA, 2007.

Forster, P. M. D., and Shine, K. P.: Assessing the climate impact of trends in stratospheric water vapor, Geophysical Research Letters, 29, 4, 1086 10.1029/2001gl013909, 2002.

Fountoukis, C., Nenes, A., Meskhidze, N., Bahreini, R., Conant, W. C., Jonsson, H., Murphy, S., Sorooshian, A., Varutbangkul, V., Brechtel, F., Flagan, R. C., and Seinfeld, J. H.: Aerosol-cloud drop concentration closure for clouds sampled during the International Consortium for Atmospheric Research on Transport and Transformation 2004 campaign, Journal of Geophysical Research-Atmospheres, 112, 12, D10s30 10.1029/2006jd007272, 2007.

Franke, H., Maser, R., Vinnichenko, N., Dreiling, V., Jaenicke, R., Jaeschke, W., and Leiterer, U.: Adaptation of microphysical and chemical instrumentation to the airborne measuring platform Iljushin Il-18 'Cyclone' and flight regime planning during the Arctic haze investigation 1993-95, Atmos. Res., 44, 3-16, 1997.

Fromm, M., Bevilacqua, R., Servranckx, R., Rosen, J., Thayer, J. P., Herman, J., and Larko, D.: Pyro-cumulonimbus injection of smoke to the stratosphere: Observations and impact of a super blowup in northwestern Canada on 3-4 August 1998, Journal of Geophysical Research-Atmospheres, 110, 16, D08205 10.1029/2004jd005350, 2005.

Fromm, M., Shettle, E. P., Fricke, K. H., Ritter, C., Trickl, T., Giehl, H., Gerding, M., Barnes, J. E., O'Neill, M., Massie, S. T., Blum, U., McDermid, I. S., Leblanc, T., and Deshler, T.: Stratospheric impact of the Chisholm pyrocumulonimbus eruption: 2. Vertical profile perspective, Journal of Geophysical Research-Atmospheres, 113, D08203 10.1029/2007jd009147, 2008a.

Fromm, M., Torres, O., Diner, D., Lindsey, D., Hull, B. V., Servranckx, R., Shettle, E. P., and Li, Z.: Stratospheric impact of the Chisholm pyrocumulonimbus eruption: 1. Earth-viewing satellite perspective, Journal of Geophysical Research-Atmospheres, 113, D08202 10.1029/2007jd009153, 2008b.

Fromm, M., Lindsey, D. T., Servranckx, R., Yue, G., Trickl, T., Sica, R., Doucet, P., and Godin-Beekmann, S. E.: The untold story of pyrocumulonimbus, Bull. Amer. Meteorol. Soc., 91, 1193-1209, 10.1175/2010bams3004.1, 2010.

Fromm, M. D., and Servranckx, R.: Transport of forest fire smoke above the tropopause by supercell convection, Geophysical Research Letters, 30, 1542 10.1029/2002gl016820, 2003.

Frost, G. J., McKeen, S. A., Trainer, M., Ryerson, T. B., Neuman, J. A., Roberts, J. M., Swanson, A., Holloway, J. S., Sueper, D. T., Fortin, T., Parrish, D. D., Fehsenfeld, F. C., Flocke, F., Peckham, S. E., Grell, G. A., Kowal, D., Cartwright, J., Auerbach, N., and Habermann, T.: Effects of changing power plant NOx emissions on ozone in the eastern United States: Proof of concept, Journal of Geophysical Research-Atmospheres, 111, 19, D12306 10.1029/2005jd006354, 2006.

Froyd, K. D., Murphy, D. M., Lawson, P., Baumgardner, D., and Herman, R. L.: Composition of cirrus-forming aerosols at the tropical tropopause, Atmospheric Chemistry and Physics Disscussions, 9, 20347-20369, 2009a.

Froyd, K. D., Murphy, D. M., Sanford, T. J., Thomson, D. S., Wilson, J. C., Pfister, L., and Lait, L.: Aerosol composition of the tropical upper troposphere, Atmos. Chem. Phys., 9, 4363-4385, 2009b.

Fuelberg, H. E., Harrigan, D. L., and Sessions, W.: A meteorological overview of the ARCTAS 2008 mission, Atmos. Chem. Phys., 10, 817-842, 2010.

Georgii, H. W., and Meixner, F. X.: Measurement of the tropospheric and stratospheric SO2 distribution, Journal of Geophysical Research-Oceans and Atmospheres, 85, 7433-7438, 1980.

Girardin, M. P., Ali, A. A., Carcaillet, C., Mudelsee, M., Drobyshev, I., Hely, C., and Bergeron, Y.: Heterogeneous response of circumboreal wildfire risk to climate change since the early 1900s, Glob. Change Biol., 15, 2751-2769, 10.1111/j.1365-2486.2009.01869.x, 2009.

Griffiths, P. T., Badger, C. L., Cox, R. A., Folkers, M., Henk, H. H., and Mentel, T. F.: Reactive Uptake of N2O5 by Aerosols Containing Dicarboxylic Acids. Effect of Particle Phase, Composition, and Nitrate Content, J. Phys. Chem. A, 113, 5082-5090, 10.1021/jp8096814, 2009.

Guan, H., Esswein, R., Lopez, J., Bergstrom, R., Warnock, A., Follette-Cook, M., Fromm, M., and Iraci, L. T.: A multi-decadal history of biomass burning plume heights identified using aerosol index measurements, Atmos. Chem. Phys., 10, 6461-6469, 10.5194/acp-10-6461-2010, 2010.

Hallquist, M., Wenger, J. C., Baltensperger, U., Rudich, Y., Simpson, D., Claeys, M., Dommen, J., Donahue, N. M., George, C., Goldstein, A. H., Hamilton, J. F., Herrmann, H., Hoffmann, T., Iinuma, Y., Jang, M., Jenkin, M. E., Jimenez, J. L., Kiendler-Scharr, A., Maenhaut, W., McFiggans, G., Mentel, T. F., Monod, A., Prevot, A. S. H., Seinfeld, J. H., Surratt, J. D., Szmigielski, R., and Wildt, J.: The formation, properties and impact of secondary organic aerosol: current and emerging issues, Atmos. Chem. Phys., 9, 5155-5236, 2009.

Heald, C. L., Goldstein, A. H., Allan, J. D., Aiken, A. C., Apel, E., Atlas, E. L., Baker, A. K., Bates, T. S., Beyersdorf, A. J., Blake, D. R., Campos, T., Coe, H., Crounse, J. D., DeCarlo, P. F., de Gouw, J. A., Dunlea, E. J., Flocke, F. M., Fried, A., Goldan, P., Griffin, R. J., Herndon, S. C., Holloway, J. S., Holzinger, R., Jimenez, J. L., Junkermann, W., Kuster, W. C., Lewis, A. C., Meinardi, S., Millet, D. B., Onasch, T., Polidori, A., Quinn, P. K., Riemer, D. D., Roberts, J. M., Salcedo, D., Sive, B., Swanson, A. L., Talbot, R., Warneke, C., Weber, R. J., Weibring, P., Wennberg, P. O., Worsnop, D. R., Wittig, A. E., Zhang, R., Zheng, J., and Zheng, W.: Total observed organic carbon (TOOC) in the atmosphere: a synthesis of North American observations, Atmos. Chem. Phys., 8, 2007-2025, 2008.

Heald, C. L., Kroll, J. H., Jimenez, J. L., Docherty, K. S., DeCarlo, P. F., Aiken, A. C., Chen, Q., Martin, S. T., Farmer, D. K., and Artaxo, P.: A simplified description of the evolution of organic aerosol composition in the atmosphere, Geophysical Research Letters, 37, 5, L08803 10.1029/2010gl042737, 2010.

Hegg, D. A., Warren, S. G., Grenfell, T. C., Doherty, S. J., Larson, T. V., and Clarke, A. D.: Source Attribution of Black Carbon in Arctic Snow, Environ. Sci. Technol., 43, 4016-4021, 10.1021/es803623f, 2009.

Hegg, D. A., Warren, S. G., Grenfell, T. C., Doherty, S. J., and Clarke, A. D.: Sources of light-absorbing aerosol in arctic snow and their seasonal variation, Atmos. Chem. Phys., 10, 10923-10938, 10.5194/acp-10-10923-2010, 2010.

Hegglin, M. I., Brunner, D., Peter, T., Hoor, P., Fischer, H., Staehelin, J., Krebsbach, M., Schiller, C., Parchatka, U., and Weers, U.: Measurements of NO, NOy, N2O, and O-3 during SPURT: implications for transport and chemistry in the lowermost stratosphere, Atmos. Chem. Phys., 6, 1331-1350, 2006.

Hennigan, C. J., Sullivan, A. P., Collett, J. L., and Robinson, A. L.: Levoglucosan stability in biomass burning particles exposed to hydroxyl radicals, Geophysical Research Letters, 37, L09806 10.1029/2010gl043088, 2010.

Hinds, C.: Aerosol technology: properties, behavior, and measurement of airborne particles, John Wiley & Sons, New York, 1999.

Hings, S. S.: Characterisation and Field Deployment of a Novel Quantitative Time-of-Flight Aerosol Mass Spectrometer (ToF-AMS), PhD, Fachbereich Physik, Mathematik und Informatik, Johannes Gutenberg-Universität, Mainz, 2006.

Hings, S. S., Walter, S., Schneider, J., Borrmann, S., and Drewnick, F.: Comparison of a quadrupole and a time-of-flight aerosol mass spectrometer during the Feldberg aerosol characterization experiment 2004, Aerosol Sci. Technol., 41, 679-691, 10.1080/02786820701408483, 2007.

Hirdman, D., Sodemann, H., Eckhardt, S., Burkhart, J. F., Jefferson, A., Mefford, T., Quinn, P. K., Sharma, S., Strom, J., and Stohl, A.: Source identification of short-lived air pollutants in the Arctic using statistical analysis of measurement data and particle dispersion model output, Atmos. Chem. Phys., 10, 669-693, 2010.

Hoffmann, A., Ritter, C., Stock, M., Maturilli, M., Eckhardt, S., Herber, A., and Neuber, R.: Lidar measurements of the Kasatochi aerosol plume in August and September 2008 in Ny-Alesund, Spitsbergen, Journal of Geophysical Research-Atmospheres, 115, D00l12 10.1029/2009jd013039, 2010.

Hofmann, D., Barnes, J., O'Neill, M., Trudeau, M., and Neely, R.: Increase in background stratospheric aerosol observed with lidar at Mauna Loa Observatory and Boulder, Colorado, Geophysical Research Letters, 36, 5, L15808 10.1029/2009gl039008, 2009.

Holton, J. R., Haynes, P. H., McIntyre, M. E., Douglass, A. R., Rood, R. B., and Pfister, L.: Stratosphere-troposphere exchange, Rev. Geophys., 33, 403-439, 1995.

Hoor, P., Gurk, C., Brunner, D., Hegglin, M. I., Wernli, H., and Fischer, H.: Seasonality and extent of extratropical TST derived from in-situ CO measurements during SPURT, Atmos. Chem. Phys., 4, 1427-1442, 2004.

Hoor, P., Fischer, H., and Lelieveld, J.: Tropical and extratropical tropospheric air in the lowermost stratosphere over Europe: A CO-based budget, Geophysical Research Letters, 32, 10.1029/2004gl022018, 2005.

Hoor, P.: The UTLS cookbook: Some recipes, Max Planck Institute for Chemistry, Mainz, 2007.

Hudson, P. K., Murphy, D. M., Cziczo, D. J., Thomson, D. S., de Gouw, J. A., Warneke, C., Holloway, J., Jost, J. R., and Hubler, G.: Biomass-burning particle measurements: Characteristic composition and chemical processing, Journal of Geophysical Research-Atmospheres, 109, D23s27 10.1029/2003jd004398, 2004.

Huffman, J. A., Jayne, J. T., Drewnick, F., Aiken, A. C., Onasch, T., Worsnop, D. R., and Jimenez, J. L.: Design, modeling, optimization, and experimental tests of a particle beam width probe for the aerodyne aerosol mass spectrometer, Aerosol Sci. Technol., 39, 1143-1163, 10.1080/02786820500423782, 2005.

Jacob, D. J., Crawford, J. H., Maring, H., Clarke, A. D., Dibb, J. E., Emmons, L. K., Ferrare, R. A., Hostetler, C. A., Russell, P. B., Singh, H. B., Thompson, A. M., Shaw, G. E., McCauley, E., Pederson, J. R., and Fisher, J. A.: The Arctic Research of the Composition of the Troposphere from Aircraft and Satellites (ARCTAS) mission: design, execution, and first results, Atmos. Chem. Phys., 10, 5191-5212, 10.5194/acp-10-5191-2010, 2010.

Jaenicke, R.: Atmospheric aerosols and global climate, J. Aerosol Sci., 11, 577-588, 1980.

Jaenicke, R.: Aerosol physics and chemistry, in: Landholt-Börnstein, Zahlenwerte und Funktionen aus Naturwissenschaft und Technik, edited by: Fischer, G., Springer-Verlag, Berlin, 391-457, 1988.

Jäger, H.: Long-term record of lidar observations of the stratospheric aerosol layer at Garmisch-Partenkirchen, Journal of Geophysical Research-Atmospheres, 110, D08106 10.1029/2004jd005506, 2005.

James, P., Stohl, A., Forster, C., Eckhardt, S., Seibert, P., and Frank, A.: A 15-year climatology of stratosphere-troposphere exchange with a Lagrangian particle dispersion model - 2. Mean climate and seasonal variability, Journal of Geophysical Research-Atmospheres, 108, 8522 10.1029/2002jd002639, 2003.

Jayne, J. T., Leard, D. C., Zhang, X. F., Davidovits, P., Smith, K. A., Kolb, C. E., and Worsnop, D. R.: Development of an aerosol mass spectrometer for size and composition analysis of submicron particles, Aerosol Sci. Technol., 33, 49-70, 2000.

Jimenez, J. L., Jayne, J. T., Quan, S., Kolb, C. E., Worsnop, D. R., Yourshaw, I., Seinfeld, J. H., Flagan, R. C., Xuefeng, Z., Smith, K. A., Morris, J. W., and Davidovits, P.: Ambient aerosol sampling using the aerodyne aerosol mass spectrometer, J. Geophys. Res., 108, SOS13-11-SOS13-SOS13-13, 10.1029/2001jd001213, 2003.

Jimenez, J. L., Canagaratna, M. R., Donahue, N. M., Prevot, A. S. H., Zhang, Q., Kroll, J. H., DeCarlo, P. F., Allan, J. D., Coe, H., Ng, N. L., Aiken, A. C., Docherty, K. S., Ulbrich, I. M., Grieshop, A. P., Robinson, A. L., Duplissy, J., Smith, J. D., Wilson, K. R., Lanz, V. A., Hueglin, C., Sun, Y. L., Tian, J., Laaksonen, A., Raatikainen, T., Rautiainen, J., Vaattovaara, P., Ehn, M., Kulmala, M., Tomlinson, J. M., Collins, D. R., Cubison, M. J., Dunlea, E. J., Huffman, J. A., Onasch, T. B., Alfarra, M. R., Williams, P. I., Bower, K., Kondo, Y., Schneider, J., Drewnick, F., Borrmann, S., Weimer, S., Demerjian, K., Salcedo, D., Cottrell, L., Griffin, R., Takami, A., Miyoshi, T., Hatakeyama, S., Shimono, A., Sun, J. Y., Zhang, Y. M., Dzepina, K., Kimmel, J. R., Sueper, D., Jayne, J. T., Herndon, S. C., Trimborn, A. M., Williams, L. R., Wood, E. C., Middlebrook, A. M., Kolb, C. E., Baltensperger, U., and Worsnop, D. R.: Evolution of Organic Aerosols in the Atmosphere, Science, 326, 1525-1529, 10.1126/science.1180353, 2009.

Jonsson, H. H., Wilson, J. C., Brock, C. A., Knollenberg, R. G., Newton, R., Dye, J. E., Baumgardner, D., Borrmann, S., Ferry, G. V., Pueschel, R., Woods, D. C., and Pitts, M. C.: Performance of a focused cavity aerosol spectrometer for measurements in the stratosphere of particle-size in the 0.06-2.9-mu-m-diameter range, J. Atmos. Ocean. Technol., 12, 115-129, 1995.

Jost, C., Trentmann, J., Sprung, D., Andreae, M. O., McQuaid, J. B., and Barjat, H.: Trace gas chemistry in a young biomass burning plume over Namibia: Observations and model simulations, Journal of Geophysical Research-Atmospheres, 108, 13, 8482 10.1029/2002jd002431, 2003.

Jurkat, T., Voigt, C., Arnold, F., Schlager, H., Aufmhoff, H., Schmale, J., Schneider, J., Lichtenstern, M., and Dornbrack, A.: Airborne stratospheric ITCIMS measurements of SO2, HCl, and HNO3 in the aged plume of volcano Kasatochi, Journal of Geophysical Research-Atmospheres, 115, D00l17 10.1029/2010jd013890, 2010.

Karagulian, F., Clarisse, L., Clerbaux, C., Prata, A. J., Hurtmans, D., and Coheur, P. F.: Detection of volcanic SO2, ash, and H2SO4 using the Infrared Atmospheric Sounding Interferometer (IASI), Journal of Geophysical Research-Atmospheres, 115, D00l02 10.1029/2009jd012786, 2010.

Kärcher, B., Mohler, O., DeMott, P. J., Pechtl, S., and Yu, F.: Insights into the role of soot aerosols in cirrus cloud formation, Atmos. Chem. Phys., 7, 4203-4227, 2007.

Keim, E. R., Fahey, D. W., DelNegro, L. A., Woodbridge, E. L., Gao, R. S., Wennberg, P. O., Cohen, R. C., Stimpfle, R. M., Kelly, K. K., Hintsa, E. J., Wilson, J. C., Jonsson, H. H., Dye, J. E., Baumgardner, D., Kawa, S. R., Salawitch, R. J., Proffitt, M. H., Loewenstein, M., Podolske, J. R., and Chan, K. R.: Observations of large reductions in the NO/NOy ratio near the mid-latitude tropopause and the role of heterogeneous chemistry, Geophysical Research Letters, 23, 3223-3226, 1996.

Khosrawi, F., and Konopka, P.: Enhanced particle formation and growth due to mixing processes in the tropopause region, Atmos. Environ., 37, 903-910, 10.1016/s1352-2310(02)00976-7, 2003.

Kimmel, J. R., Farmer, D. K., Sueper, D., Cubison, M. J., Tanner, C., and Jimenez, J.: Monitoring of Fast Changes in Aerosol Chemistry with a Time-of-Flight Aerosol Mass Spectrometer, 56th Annual Conference of the American Society for Mass Spectrometry, Denver, Colorado, 2008.

Kline, J., Huebert, B., Howell, S., Blomquist, B., Zhuang, J., Bertram, T., and Carrillo, J.: Aerosol composition and size versus altitude measured from the C-130 during ACE-Asia, Journal of Geophysical Research-Atmospheres, 109, D19s08 10.1029/2004jd004540, 2004.

Koch, D., and Hansen, J.: Distant origins of Arctic black carbon: a Goddard Institute for Space Studies ModelE experiment, J. Geophys. Res., 110, 14 pp.-14 pp., 10.1029/2004jd005296, 2005.

Kravitz, B., Robock, A., and Bourassa, A.: Negligible climatic effects from the 2008 Okmok and Kasatochi volcanic eruptions, Journal of Geophysical Research-Atmospheres, 115, D00l05 10.1029/2009jd013525, 2010.

Kristiansen, N. I., Stohl, A., Prata, A. J., Richter, A., Eckhardt, S., Seibert, P., Hoffmann, A., Ritter, C., Bitar, L., Duck, T. J., and Stebel, K.: Remote sensing and inverse transport modeling of the Kasatochi eruption sulfur dioxide cloud, Journal of Geophysical Research-Atmospheres, 115, D00l16 10.1029/2009jd013286, 2010.

Krueger, A., Krotkov, N., and Carn, S.: El Chichon: The genesis of volcanic sulfur dioxide monitoring from space, J. Volcanol. Geotherm. Res., 175, 408-414, 10.1016/j.jvolgeores.2008.02.026, 2008.

Lacis, A. A., Wuebbles, D. J., and Logan, J. A.: Radiative forcing of climate by changes in the vertical distribution of ozone, Journal of Geophysical Research-Atmospheres, 95, 9971-9981, 1990.

Lamarque, J. F., Bond, T. C., Eyring, V., Granier, C., Heil, A., Klimont, Z., Lee, D., Liousse, C., Mieville, A., Owen, B., Schultz, M. G., Shindell, D., Smith, S. J., Stehfest, E., Van Aardenne, J., Cooper, O. R., Kainuma, M., Mahowald, N., McConnell, J. R., Naik, V., Riahi, K., and van Vuuren, D. P.: Historical (1850-2000) gridded anthropogenic and biomass burning emissions of reactive gases and aerosols: methodology and application, Atmos. Chem. Phys., 10, 7017-7039, 10.5194/acp-10-7017-2010, 2010.

Lance, S., Shupe, M., Feingold, G., Brock, C. A., Cozic, J., Holloway, J., Moore, K., Nenes, A., Schwarz, J. P., Spackman, J. R., Froyd, K. D., Murphy, D. M., Brioude, J., Cooper, O., Stohl, A., and Burkhart, J. F.: Cloud condensation nuclei as a modulator of ice processes in Arctic mixed-phase clouds, Atmospheric Chemistry and Physics Disscussions, 11, 6737-6770, 2011.

Lanz, V. A., Alfarra, M. R., Baltensperger, U., Buchmann, B., Hueglin, C., and Prevot, A. S. H.: Source apportionment of submicron organic aerosols at an urban site by factor analytical modelling of aerosol mass spectra, Atmos. Chem. Phys., 7, 1503-1522, 2007.

Lavoue, D., Liousse, C., Cachier, H., Stocks, B. J., and Goldammer, J. G.: Modeling of carbonaceous particles emitted by boreal and temperate wildfires at northern latitudes, Journal of Geophysical Research-Atmospheres, 105, 26871-26890, 2000.

Law, K. S., and Stohl, A.: Arctic air pollution: Origins and impacts, Science, 315, 1537-1540, 10.1126/science.1137695, 2007.

Lee, C., Martin, R. V., van Donkelaar, A., Lee, H., Dickerson, R. R., Hains, J. C., Krotkov, N., Richter, A., Vinnikov, K., and Schwab, J. J.: SO2 emissions and lifetimes: Estimates from inverse modeling using in situ and global, space-based (SCIAMACHY and OMI) observations, Journal of Geophysical Research-Atmospheres, 116, 13, D06304 10.1029/2010jd014758, 2011.

Lee, Y. N., Weber, R., Ma, Y., Orsini, D., Maxwell-Meier, K., Blake, D., Meinardi, S., Sachse, G., Harward, C., Chen, T. Y., Thornton, D., Tu, F. H., and Bandy, A.: Airborne measurement of inorganic ionic components of fine aerosol particles using the particle-into-liquid sampler coupled to ion chromatography technique during ACE-Asia and TRACE-P, Journal of Geophysical Research-Atmospheres, 108, 8646 10.1029/2002jd003265, 2003.

Lee, D. S., Fahey, D. W., Forster, P. M., Newton, P. J., Wit, R. C. N., Lim, L. L., Owen, B., and Sausen, R.: Aviation and global climate change in the 21st century, Atmos. Environ., 43, 3520-3537, 10.1016/j.atmosenv.2009.04.024, 2009.

Lee, J. K., Rubow, K. L., Pui, D. Y. H., and Liu, B. Y. H.: Design and performance evaluation of a pressure-reducing device for aerosol smapling from high-purity gases, Aerosol Sci. Technol., 19, 215-226, 1993.

Lemke, P., Ren, J., Alley, R. B., Allision, I., Carrasco, J., Flato, G., Fujii, Y., Kaser, G., Mote, P., Thomas, R. H., and Zhang, T.: Observations: Changes in Snow, Ice and Frozen Ground. In: Climate Change 2007: The Physical Science Basis. Contribution of Working Group I to the fourth Assessment Report of the Intergovernmental Panel on Climate Change. [Solomon, S., D. Qin, M. Manning, Z. Chen, M. Marquis, K.B. Averyt, M.Tignor and H.L. Miller (eds.)]. Cambridge University Press, Cambridge, United Kingdom and New York, NY, USA, 2007.

Lewis, A. C., Evans, M. J., Methven, J., Watson, N., Lee, J. D., Hopkins, J. R., Purvis, R. M., Arnold, S. R., McQuaid, J. B., Whalley, L. K., Pilling, M. J., Heard, D. E., Monks, P. S., Parker, A. E., Reeves, C. E., Oram, D. E., Mills, G., Bandy, B. J., Stewart, D., Coe, H., Williams, P., and Crosier, J.: Chemical composition observed over the mid-Atlantic and the detection of pollution signatures far from source regions, Journal of Geophysical Research-Atmospheres, 112, 17, D10s39 10.1029/2006jd007584, 2007.

Li, C., Krotkov, N. A., Dickerson, R. R., Li, Z. Q., Yang, K., and Chin, M.: Transport and evolution of a pollution plume from northern China: A satellite-based case study, Journal of Geophysical Research-Atmospheres, 115, 11, D00k03 10.1029/2009jd012245, 2010.

Lide, D. R.: Handbook of Chemistry and Physics, 76th ed., edited by: Lide, D. R., CRC Press, Boca Raton, Florida, USA, 1996.

Liu, P., Ziemann, P. J., Kittelson, D. B., and McMurry, P. H.: Generating particle beams of controlled dimensions and divergence. 2. Experimental evaluation of particle motion in aerodynamic lenses and nozzle expansions, Aerosol Sci. Technol., 22, 314-324, 1995a.

Liu, P., Ziemann, P. J., Kittelson, D. B., and McMurry, P. H.: Generating particle beams of controlled dimensions and divergence. 1. Theory of particle motion in aerodynamic lenses and nozzle expansions, Aerosol Sci. Technol., 22, 293-313, 1995b.

Liu, P. S. K., Deng, R., Smith, K. A., Williams, L. R., Jayne, J. T., Canagaratna, M. R., Moore, K., Onasch, T. B., Worsnop, D. R., and Deshler, T.: Transmission efficiency of an aerodynamic focusing lens system: Comparison of model calculations and laboratory measurements for the Aerodyne Aerosol Mass Spectrometer, Aerosol Sci. Technol., 41, 721-733, 10.1080/02786820701422278, 2007.

Lu, Z., Streets, D. G., Zhang, Q., Wang, S., Carmichael, G. R., Cheng, Y. F., Wei, C., Chin, M., Diehl, T., and Tan, Q.: Sulfur dioxide emissions in China and sulfur trends in East Asia since 2000, Atmos. Chem. Phys., 10, 6311-6331, 10.5194/acp-10-6311-2010, 2010.

Maria, S. F., Russell, L. M., Gilles, M. K., and Myneni, S. C. B.: Organic aerosol growth mechanisms and their climate-forcing implications, Science, 306, 1921-1924, 10.1126/science.1103491, 2004.

Martin, R. S., Silva, P. J., Moore, K., Erupe, M., and Doshi, V. S.: Particle composition and size distributions in and around a deep-pit swine operation, Ames, IA, J. Atmos. Chem., 59, 135-150, 10.1007/s10874-008-9097-y, 2008.

Martinsson, B. G., Papaspiropoulos, G., Heintzenberg, J., and Hermann, M.: Fine mode particulate sulphur in the tropopause region measured from intercontinental flights (CARIBIC), Geophysical Research Letters, 28, 1175-1178, 2001.

Martinsson, B. G., Nguyen, H. N., Brenninkmeijer, C. A. M., Zahn, A., Heintzenberg, J., Hermann, M., and van Velthoven, P. F. J.: Characteristics and origin of lowermost stratospheric aerosol at northern midlatitudes under volcanically quiescent conditions based on CARIBIC observations, Journal of Geophysical Research-Atmospheres, 110, 12, D12201 10.1029/2004jd005644, 2005.

Martinsson, B. G., Brenninkmeijer, C. A. M., Carn, S. A., Hermann, M., Heue, K. P., van Velthoven, P. F. J., and Zahn, A.: Influence of the 2008 Kasatochi volcanic eruption on sulfurous and carbonaceous aerosol constituents in the lower stratosphere, Geophysical Research Letters, 36, 5, L12813 10.1029/2009gl038735, 2009.

Matsui, H., Kondo, Y., Moteki, N., Takegawa, N., Sahu, L. K., Zhao, Y., Fuelberg, H. E., Sessions, W. R., Diskin, G., Blake, D. R., Wisthaler, A., and Koike, M.: Seasonal variation of the transport of black carbon aerosol from the Asian continent to the Arctic during the ARCTAS aircraft campaign, Journal of Geophysical Research-Atmospheres, 116, D05202 10.1029/2010jd015067, 2011.

Matthew, B. M., Middlebrook, A. M., and Onasch, T. B.: Collection efficiencies in an Aerodyne Aerosol Mass Spectrometer as a function of particle phase for laboratory generated aerosols, Aerosol Sci. Technol., 42, 884-898, 10.1080/02786820802356797, 2008.

Mattis, I., Ansmann, A., Wandinger, U., and Muller, D.: Unexpectedly high aerosol load in the free troposphere over central Europe in spring/summer 2003, Geophysical Research Letters, 30, 2178 10.1029/2003gl018442, 2003.

Mattis, I., Siefert, P., Muller, D., Tesche, M., Hiebsch, A., Kanitz, T., Schmidt, J., Finger, F., Wandinger, U., and Ansmann, A.: Volcanic aerosol layers observed with multiwavelength Raman lidar over central Europe in 2008-2009, Journal of Geophysical Research-Atmospheres, 115, 9, D00l04 10.1029/2009jd013472, 2010.

Mauritsen, T., Sedlar, J., Tjernstrom, M., Leck, C., Martin, M., Shupe, M., Sjogren, S., Sierau, B., Persson, P. O. G., Brooks, I. M., and Swietlicki, E.: An Arctic CCN-limited cloud-aerosol regime, Atmos. Chem. Phys., 11, 165-173, 10.5194/acp-11-165-2011, 2011.

McConnell, J. R., Edwards, R., Kok, G. L., Flanner, M. G., Zender, C. S., Saltzman, E. S., Banta, J. R., Pasteris, D. R., Carter, M. M., and Kahl, J. D. W.: 20th-century industrial black carbon emissions altered arctic climate forcing, Science, 317, 1381-1384, 10.1126/science.1144856, 2007.

McNaughton, C., Clarke, A., Freitag, S., Kapustin, V., Kondo, Y., Moteki, N., Sahu, L., Takegawa, N., Schwarz, J. P., Spackman, J. R., Watts, L. A., Diskin, G., Podolske, J. R., Holloway, J., Wisthaler, A., Mikoviny, T., de Gouw, J., Warneke, C., Jimenez, J., Cubison, M. J., Howell, S. G., Middlebrook, A., Bahreini, R., Anderson, B., Winstead, E., Thornhill, L., Lack, D. A., Cozic, J., and Brock, C. A.: Absorbing aerosol in the troposphere of the Western Arctic during the 2008 ARCTAS/ARCPAC airborne field campaigns, Atmospheric Chemistry and Physics Disscussions, 11, 1543-1594, 2011.

McNaughton, C. S., Clarke, A. D., Howell, S. G., Pinkerton, M., Anderson, B., Thornhill, L., Hudgins, C., Winstead, E., Dibb, J. E., Scheuer, E., and Maring, H.: Results from the DC-8 Inlet Characterization Experiment (DICE): Airborne versus surface sampling of mineral dust and sea salt aerosols, Aerosol Sci. Technol., 41, 136-159, 10.1080/02786820601118406, 2007.

Methven, J.: Offline trajectories: Calculations and accuracy., Dept. of Meteorolo., Univ. of Reading, U.K., 1997.

Methven, J., Arnold, S. R., O'Connor, F. M., Barjat, H., Dewey, K., Kent, J., and Brough, N.: Estimating photochemically produced ozone throughout a domain using flight data and a Lagrangian model, Journal of Geophysical Research-Atmospheres, 108, 19, 4271 10.1029/2002jd002955, 2003.

Möhler, O., and Arnold, F.: Gaseous sulfuric-acid and sulfur-dioxie measurements in the Arctic troposphere and lower stratosphere - Implications for hydroxil radical abundances, Geophysical Research Letters, 19, 1763-1766, 1992.

Morgan, W. T., Allan, J. D., Bower, K. N., Capes, G., Croiser, J., Williams, P. I., and Coe, H.: Vertical distribution of sub-micron aerosol chemical composition from North-Western Europe and the North-East Atlantic, Atmos. Chem. Phys., 9, 5389-5401, 2009.

Morgan, W. T., Allan, J. D., Bower, K. N., Esselborn, M., Harris, B., Henzing, J. S., Highwood, E. J., Kiendler-Scharr, A., McMeeking, G. R., Mensah, A. A., Northway, M. J., Osborne, S., Williams, P. I., Krejci, R., and Coe, H.: Enhancement of the aerosol direct radiative effect by semi-volatile aerosol components: airborne measurements in North-Western Europe, Atmos. Chem. Phys., 10, 8151-8171, 10.5194/acp-10-8151-2010, 2010a.

Morgan, W. T., Allan, J. D., Bower, K. N., Highwood, E. J., Liu, D., McMeeking, G. R., Northway, M. J., Williams, P. I., Krejci, R., and Coe, H.: Airborne measurements of the spatial distribution of aerosol chemical composition across Europe and evolution of the organic fraction, Atmos. Chem. Phys., 10, 4065-4083, 10.5194/acp-10-4065-2010, 2010b.

Murphy, D. M., and Thomson, D. S.: Laser ionization mass-spectroscopy of single aerosol-particles, Aerosol Sci. Technol., 22, 237-249, 1995.

Murphy, D. M., Thomson, D. S., and Mahoney, T. M. J.: In situ measurements of organics, meteoritic material, mercury, and other elements in aerosols at 5 to 19 kilometers, Science, 282, 1664-1669, 1998.

Murphy, D. M.: Something in the air, Science, 307, 1888-1890, 10.1126/science.1108160, 2005.

Murphy, D. M., Cziczo, D. J., Froyd, K. D., Hudson, P. K., Matthew, B. M., Middlebrook, A. M., Peltier, R. E., Sullivan, A., Thomson, D. S., and Weber, R. J.: Single-particle mass spectrometry of tropospheric aerosol particles, Journal of Geophysical Research-Atmospheres, 111, D23s32 10.1029/2006jd007340, 2006.

Murphy, D. M., Cziczo, D. J., Hudson, P. K., and Thomson, D. S.: Carbonaceous material in aerosol particles in the lower stratosphere and tropopause region, Journal of Geophysical Research-Atmospheres, 112, 10, D04203 10.1029/2006jd007297, 2007.

Neto, T. G. S., Carvalho, J. A., Veras, C. A. G., Alvarado, E. C., Gielow, R., Lincoln, E. N., Christian, T. J., Yokelson, R. J., and Santos, J. C.: Biomass consumption and CO2, CO and main hydrocarbon gas emissions in an Amazonian forest clearing fire, Atmos. Environ., 43, 438-446, 10.1016/j.atmosenv.2008.07.063, 2009.

Ng, N. L., Canagaratna, M. R., Zhang, Q., Jimenez, J. L., Tian, J., Ulbrich, I. M., Kroll, J. H., Docherty, K. S., Chhabra, P. S., Bahreini, R., Murphy, S. M., Seinfeld, J. H., Hildebrandt, L., Donahue, N. M., DeCarlo, P. F., Lanz, V. A., Prevot, A. S. H., Dinar, E., Rudich, Y., and Worsnop, D. R.: Organic aerosol components observed in Northern Hemispheric datasets from Aerosol Mass Spectrometry, Atmos. Chem. Phys., 10, 4625-4641, 10.5194/acp-10-4625-2010, 2010.

Olivier, J. G., and Berdowski, J. J. M.: Global emissions sources and sinks, in: "The Climate System", edited by: Berdowski, J., Guicherit, R., and Heij, B. J., A. A. Balkema Publishers/Swets & Zeitlinger Publishers, Lisse, The Netherlands, 33-78, 2001.

Ovadnevaite, J., Ceburnis, D., Plauskaite-Sukiene, K., Modini, R., Dupuy, R., Rimselyte, I., Ramonet, M., Kvietkus, K., Ristovski, Z., Berresheim, H., and O'Dowd, C. D.: Volcanic sulphate and arctic dust plumes over the North Atlantic Ocean, Atmos. Environ., 43, 4968-4974, 10.1016/j.atmosenv.2009.07.007, 2009.

Pan, L. L., Randel, W. J., Gary, B. L., Mahoney, M. J., and Hintsa, E. J.: Definitions and sharpness of the extratropical tropopause: A trace gas perspective, Journal of Geophysical Research-Atmospheres, 109, 10.1029/2004jd004982, 2004.

Paris, J. D., Stohl, A., Nedelec, P., Arshinov, M. Y., Panchenko, M. V., Shmargunov, V. P., Law, K. S., Belan, B. D., and Ciais, P.: Wildfire smoke in the Siberian Arctic in summer: source characterization and plume evolution from airborne measurements, Atmos. Chem. Phys., 9, 9315-9327, 2009.

Park, R. J., Jacob, D. J., Palmer, P. I., Clarke, A. D., Weber, R. J., Zondlo, M. A., Eisele, F. L., Bandy, A. R., Thornton, D. C., Sachse, G. W., and Bond, T. C.: Export efficiency of black carbon aerosol in continental outflow: global implications, J. Geophys. Res, D, Atmos., 110, 7 pp.-7 pp., 10.1029/2004jd005432, 2005.

Parrish, D. D., Allen, D. T., Bates, T. S., Estes, M., Fehsenfeld, F. C., Feingold, G., Ferrare, R., Hardesty, R. M., Meagher, J. F., Nielsen-Gammon, J. W., Pierce, R. B., Ryerson, T. B., Seinfeld, J. H., and Williams, E. J.: Overview of the Second Texas Air Quality Study (TexAQS II) and the Gulf of Mexico Atmospheric Composition and Climate Study (GoMACCS), Journal of Geophysical Research-Atmospheres, 114, D00f13 10.1029/2009jd011842, 2009.

Petzold, A., Weinzierl, B., Huntrieser, H., Stohl, A., Real, E., Cozic, J., Fiebig, M., Hendricks, J., Lauer, A., Law, K., Roiger, A., Schlager, H., and Weingartner, E.: Perturbation of the European free troposphere aerosol by North American forest fire plumes during the ICARTT-ITOP experiment in summer 2004, Atmos. Chem. Phys., 7, 5105-5127, 2007.

Popp, P. J., Marcy, T. P., Watts, L. A., Gao, R. S., Fahey, D. W., Weinstock, E. M., Smith, J. B., Herman, R. L., Troy, R. F., Webster, C. R., Christensen, L. E., Baumgardner, D. G., Voigt, C., Kärcher, B., Wilson, J. C., Mahoney, M. J., Jensen, E. J., and Bui, T. P.: Condensed-phase nitric acid in a tropical subvisible cirrus cloud, Geophysical Research Letters, 34, 5, L24812 10.1029/2007gl031832, 2007.

Prata, A. J., Gangale, G., Clarisse, L., and Karagulian, F.: Ash and sulfur dioxide in the 2008 eruptions of Okmok and Kasatochi: Insights from high spectral resolution satellite measurements, Journal of Geophysical Research-Atmospheres, 115, D00l18 10.1029/2009jd013556, 2010.

Pratt, K. A., Mayer, J. E., Holecek, J. C., Moffet, R. C., Sanchez, R. O., Rebotier, T. P., Furutani, H., Gonin, M., Fuhrer, K., Su, Y. X., Guazzotti, S., and Prather, K. A.: Development and Characterization of an Aircraft Aerosol Time-of-Flight Mass Spectrometer, Analytical Chemistry, 81, 1792-1800, 10.1021/ac801942r, 2009.

Pratt, K. A., and Prather, K. A.: Aircraft measurements of vertical profiles of aerosol mixing states, Journal of Geophysical Research-Atmospheres, 115, 10, D11305 10.1029/2009jd013150, 2010.

Quennehen, B., Schwarzenboeck, A., Schmale, J., Schneider, J., Stohl, A., Jourdan, O., Ancellet, G., Crummeryrolle, S., and Law, K.: North American transported pollution plume properties during the POLARCAT summer campaign in Greenland, Atmospheric Chemistry and Physics Disscussions, 11, 11771-11808, 2011.

Quinn, P. K., Bates, T. S., Coffman, D., Onasch, T. B., Worsnop, D., Baynard, T., de Gouw, J. A., Goldan, P. D., Kuster, W. C., Williams, E., Roberts, J. M., Lerner, B., Stohl, A., Pettersson, A., and Lovejoy, E. R.: Impacts of sources and aging on submicrometer aerosol properties in the marine boundary layer across the Gulf of Maine, Journal of Geophysical Research-Atmospheres, 111, 20, D23s36 10.1029/2006jd007582, 2006.

Quinn, P. K., Shaw, G., Andrews, E., Dutton, E. G., Ruoho-Airola, T., and Gong, S. L.: Arctic haze: current trends and knowledge gaps, Tellus Ser. B-Chem. Phys. Meteorol., 59, 99-114, 10.1111/j.1600-0889.2006.00238.x, 2007.

Quinn, P. K., Bates, T. S., Baum, E., Doubleday, N., Fiore, A. M., Flanner, M., Fridlind, A., Garrett, T. J., Koch, D., Menon, S., Shindell, D., Stohl, A., and Warren, S. G.: Short-lived pollutants in the Arctic: their climate impact and possible mitigation strategies, Atmos. Chem. Phys., 8, 1723-1735, 2008.

Rahn, K. A., Borys, R. D., and Shaw, G. E.: Asian source of Arctic haze bands, Nature, 268, 713-715, 1977.

Rahn, K. A., and McCaffrey, R. J.: On the origin and transport of the winter Arctic aerosol, Ann. N. Y. Acad. Sci., 388, 486-503, 1980.

Real, E., Law, K. S., Weinzierl, B., Fiebig, M., Petzold, A., Wild, O., Methven, J., Arnold, S., Stohl, A., Huntrieser, H., Roiger, A., Schlager, H., Stewart, D., Avery, M., Sachse, G., Browell, E., Ferrare, R., and Blake, D.: Processes influencing ozone levels in Alaskan forest fire plumes during long-range transport over the North Atlantic, Journal of Geophysical Research-Atmospheres, 112, 19, D10s41 10.1029/2006jd007576, 2007.

Real, E., Law, K. S., Schlager, H., Roiger, A., Huntrieser, H., Methven, J., Cain, M., Holloway, J., Neuman, J. A., Ryerson, T., Flocke, F., de Gouw, J., Atlas, E., Donnelly, S., and Parrish, D.: Lagrangian analysis of low altitude anthropogenic plume processing across the North Atlantic, Atmos. Chem. Phys., 8, 7737-7754, 2008.

Reid, G. C., and Gage, K. S.: On the annual variation in height of the tropical tropopause, J. Atmos. Sci., 38, 1928-1938, 1981.

Reid, J. S., Koppmann, R., Eck, T. F., and Eleuterio, D. P.: A review of biomass burning emissions part II: intensive physical properties of biomass burning particles, Atmos. Chem. Phys., 5, 799-825, 2005.

Reitz, P.: Aerosol mass spectrometry on cloud condensation nuclei and ice nuclei, PhD, Fachbereich Physik, Mathematik und Informatik, Johannes Gutenberg-Universität, Mainz, 2011.

Roberts, G. C., Day, D. A., Russell, L. M., Dunlea, E. J., Jimenez, J. L., Tomlinson, J. M., Collins, D. R., Shinozuka, Y., and Clarke, A. D.: Characterization of particle cloud droplet activity and

composition in the free troposphere and the boundary layer during INTEX-B, Atmos. Chem. Phys., 10, 6627-6644, 10.5194/acp-10-6627-2010, 2010.

Roiger, A., Schlager, H., Arnold, F., Schäfler, A., Cooper, O., Lazarra, M., Stohl, A., Sodemann, H., and Schiller, C.: Airborne observation of an Asian pollution plume in the Arctic UTLS, Atmospheric Chemistry and Physics Disscussions, in prep., 2011.

Rolph, G. D.: Real-time Environmental Applications and Display sYstem (READY) Website (http://ready.arl.noaa.gov), NOAA Air Resources Laboratory, Silver Spring, MD, 2011.

Sander, R., Burrows, J., and Kaleschke, L.: Carbonate precipitation in brine - a potential trigger for tropospheric ozone depletion events, Atmos. Chem. Phys., 6, 4653-4658, 2006.

Schmale, J., Schneider, J., Jurkat, T., Voigt, C., Kalesse, H., Rautenhaus, M., Lichtenstern, M., Schlager, H., Ancellet, G., Arnold, F., Gerding, M., Mattis, I., Wendisch, M., and Borrmann, S.: Aerosol layers from the 2008 eruptions of Mount Okmok and Mount Kasatochi: In situ upper troposphere and lower stratosphere measurements of sulfate and organics over Europe, J. Geophys. Res., 115, D00L07, doi:10.1029/2009JD013628, 2010.

Schmale, J., Schneider, J., Ancellet, G., Quennehen, B., Stohl, A., Sodemann, H., Burkhart, J. F., Hamburger, T., Arnold, S., Schwarzenboeck, A., Borrmann, S., and Law, K.: Source Identification and Airborne Chemical Characterisation of Aerosol Pollution from Long-range Transport over Greenland during POLARCAT Summer campaign 2008, Atmospheric Chemistry and Physics Disscussions, 11, 7593-7658, 2011.

Schneider, J., Hings, S. S., Hock, B. N., Weimer, S., Borrmann, S., Fiebig, M., Petzold, A., Busen, R., and Kärcher, B.: Aircraft-based operation of an aerosol mass spectrometer: Measurements of tropospheric aerosol composition, J. Aerosol. Sci., 37, 839-857, 10.1016/j.jaerosci.2005.07.002, 2006a.

Schneider, J., Weimer, S., Drewnick, F., Borrmann, S., Helas, G., Gwaze, P., Schmid, O., Andreae, M. O., and Kirchner, U.: Mass spectrometric analysis and aerodynamic properties of various types of combustion-related aerosol particles, Int. J. Mass Spectrom., 258, 37-49, 10.1016/j.ijms.2006.07.008, 2006b.

Schnell, R. C.: Arctic haze and the Arctic Gas and Aerosol Sampling Program (AGASP), Geophysical Research Letters, 11, 361-364, 1984.

Schreiner, J., Voigt, C., Zink, P., Kohlmann, A., Knopf, D., Weisser, C., Budz, P., and Mauersberger, K.: A mass spectrometer system for analysis of polar stratospheric aerosols, Rev. Sci. Instrum., 73, 446-452, 10.1063/1.1430732, 2002.

Schumann, U.: On conditions for contrail formation from aircraft exhausts, Meteorol. Z., 5, 4-23, 1996.

Schumann, U., Schlager, H., Arnold, F., Baumann, R., Haschberger, P., and Klemm, O.: Dilution of aircraft exhaust plumes at cruise altitudes, Atmos. Environ., 32, 3097-3103, 1998.

Schumann, U., Weinzierl, B., Reitebuch, O., Schlager, H., Minikin, A., Forster, C., Baumann, R., Sailer, T., Graf, K., Mannstein, H., Voigt, C., Rahm, S., Simmet, R., Scheibe, M., Lichtenstern, M., Stock, P., Ruba, H., Schauble, D., Tafferner, A., Rautenhaus, M., Gerz, T., Ziereis, H., Krautstrunk, M., Mallaun, C., Gayet, J. F., Lieke, K., Kandler, K., Ebert, M., Weinbruch, S., Stohl, A., Gasteiger, J., Gross, S., Freudenthaler, V., Wiegner, M., Ansmann, A., Tesche, M., Olafsson, H., and Sturm, K.: Airborne observations of the Eyjafjalla volcano ash cloud over Europe during air space closure in April and May 2010, Atmos. Chem. Phys., 11, 2245-2279, 10.5194/acp-11-2245-2011, 2011.

Schwarz, J. P., Spackman, J. R., Fahey, D. W., Gao, R. S., Lohmann, U., Stier, P., Watts, L. A., Thomson, D. S., Lack, D. A., Pfister, L., Mahoney, M. J., Baumgardner, D., Wilson, J. C., and Reeves, J. M.: Coatings and their enhancement of black carbon light absorption in the tropical atmosphere, Journal of Geophysical Research-Atmospheres, 113, D03203 10.1029/2007jd009042, 2008.

Seinfeld, J., and Pandis, S. N.: Atmospheric chemistry and physics: From air pollution to climate change, 2nd ed., Wiley-Interscience, 2006.

Sessions, W., Fuelberg, H. E., Kahn, R. A., and Winker, D.: An investigation of methods for injecting emissions from boreal forest wildfires using WRF-Chem during ARCTAS, Atmospheric Chemistry and Physics Disscussions, 10, 26551-26606, 2010.

Shapiro, M. A.: Turbulent mixing within tropopause folds as a mechanism for the exchange of chemical-constituents between the stratosphere and troposphere, J. Atmos. Sci., 37, 994-1004, 1980.

Shaw, G. E.: The arctic haze phenomenon, Bull. Amer. Meteorol. Soc., 76, 2403-2413, 1995.

Shinozuka, Y., Redemann, J., Livingston, J. M., Russell, P. B., Clarke, A. D., Howell, S. G., Freitag, S., O'Neill, N. T., Reid, E. A., Johnson, R., Ramachadran, S., McNaughton, C. S., Kapustin, V. N., Brekhovskikh, V., Holben, B. N., and McArthur, L. J. B.: Airborne observation of aerosol optical depth during ARCTAS: vertical profiles, inter-comparison, fine-mode fraction and horizontal variability, Atmospheric Chemistry and Physics Disscussions, 10, 18315-18363, 2010.

Shiraiwa, M., Kondo, Y., Moteki, N., Takegawa, N., Miyazaki, Y., and Blake, D.: Evolution of mixing state of black carbon in polluted air from Tokyo, Geophysical Research Letters, 34, L16803, doi:10.1029/2007GL029819, 2007.

Sillman, S., and He, D. Y.: Some theoretical results concerning O-3-NOx-VOC chemistry and NOx-VOC indicators, Journal of Geophysical Research-Atmospheres, 107, 15, 4659 10.1029/2001jd001123, 2002.

Simoneit, B. R. T., Schauer, J. J., Nolte, C. G., Oros, D. R., Elias, V. O., Fraser, M. P., Rogge, W. F., and Cass, G. R.: Levoglucosan, a tracer for cellulose in biomass burning and atmospheric particles, Atmos. Environ., 33, 173-182, 1999.

Singh, H. B., Anderson, B. E., Brune, W. H., Cai, C., Cohen, R. C., Crawford, J. H., Cubison, M. J., Czech, E. P., Emmons, L., Fuelberg, H. E., Huey, G., Jacob, D. J., Jimenez, J. L., Kaduwela, A., Kondo, Y., Mao, J., Olson, J. R., Sachse, G. W., Vay, S. A., Weinheimer, A., Wennberg, P. O., and Wisthaler, A.: Pollution influences on atmospheric composition and chemistry at high northern latitudes: Boreal and California forest fire emissions, Atmos. Environ., doi: 10.1016/j.atmosenv.2010.08.026, 2010.

Smith, J. B., Hintsa, E. J., Allen, N. T., Stimpfle, R. M., and Anderson, J. G.: Mechanisms for midlatitude ozone loss: Heterogeneous chemistry in the lowermost stratophere?, J. Geophys. Res., 106(D1), 1297-1309, 2001.

Sodemann, H., Pommier, M., Arnold, S., Monks, S., Stebel, K., Burkhart, J. F., Hair, J. W., Diskin, G. S., Clerbaux, C., Coheur, P. F., Hurtmans, D., Schlager, H., Blechschmidt, A.-M., Kristjansson, J. E., and Stohl, A.: Episodes of cross-polar transport in the Arctic troposphere during July 2008 as seen from models, satellite, and observations, Atmospheric Chemistry and Physics Disscussions, 10, 26361-26410, 2010.

Solomon, S., Borrmann, S., Garcia, R. R., Portmann, R., Thomason, L., Poole, L. R., Winker, D., and McCormick, M. P.: Heterogeneous chlorine chemistry in the tropopause region, Journal of Geophysical Research-Atmospheres, 102, 21411-21429, 1997.

Solomon, S.: Stratospheric ozone depletion: A review of concepts and history, Rev. Geophys., 37, 275-316, 1999.

Solomon, S., Quin, D., Manning, M., Chen, Z., Marquis, M., Averyt, K., Tingor, M., and Miller, L.: Climate Change 2007: The Physical Science Basis. Contributions of Working Group I to the Fourth Assessment Report of the Intergovernmental Panel on Climate Change, Cambridge Univ. Press, New York, 2007.

Speidel, M., Nau, R., Arnold, F., Schlager, H., and Stohl, A.: Sulfur dioxide measurements in the lower, middle and upper troposphere: Deployment of an aircraft-based chemical ionization mass

spectrometer with permanent in-flight calibration, Atmos. Environ., 41, 2427-2437, 10.1016/j.atmosenv.2006.07.047, 2007.

Sprenger, M., and Wernli, H.: A northern hemispheric climatology of cross-tropopause exchange for the ERA15 time period (1979-1993), Journal of Geophysical Research-Atmospheres, 108, 14, 8521 10.1029/2002jd002636, 2003.

Stocks, B. J., Mason, J. A., Todd, J. B., Bosch, E. M., Wotton, B. M., Amiro, B. D., Flannigan, M. D., Hirsch, K. G., Logan, K. A., Martell, D. L., and Skinner, W. R.: Large forest fires in Canada, 1959-1997, Journal of Geophysical Research-Atmospheres, 108, 8149 10.1029/2001jd000484, 2002.

Stohl, A., Bonasoni, P., Cristofanelli, P., Collins, W., Feichter, J., Frank, A., Forster, C., Gerasopoulos, E., Gaggeler, H., James, P., Kentarchos, T., Kromp-Kolb, H., Kruger, B., Land, C., Meloen, J., Papayannis, A., Priller, A., Seibert, P., Sprenger, M., Roelofs, G. J., Scheel, H. E., Schnabel, C., Siegmund, P., Tobler, L., Trickl, T., Wernli, H., Wirth, V., Zanis, P., and Zerefos, C.: Stratosphere-troposphere exchange: A review, and what we have learned from STACCATO, Journal of Geophysical Research-Atmospheres, 108, 15, 8516 10.1029/2002jd002490, 2003a.

Stohl, A., Forster, C., Eckhardt, S., Spichtinger, N., Huntrieser, H., Heland, J., Schlager, H., Wilhelm, S., Arnold, F., and Cooper, O.: A backward modeling study of intercontinental pollution transport using aircraft measurements, Journal of Geophysical Research-Atmospheres, 108, 18, 4370 10.1029/2002jd002862, 2003b.

Stohl, A., Wernli, H., James, P., Bourqui, M., Forster, C., Liniger, M. A., Seibert, P., and Sprenger, M.: A new perspective of stratosphere-troposphere exchange, Bull. Amer. Meteorol. Soc., 84, 1565-+, 10.1175/bams-84-11-1565, 2003c.

Stohl, A., Forster, C., Frank, A., Seibert, P., and Wotawa, G.: Technical note: The Lagrangian particle dispersion model FLEXPART version 6.2, Atmos. Chem. Phys., 5, 2461-2474, 2005.

Stohl, A.: Characteristics of atmospheric transport into the Arctic troposphere, Journal of Geophysical Research-Atmospheres, 111, 17, D11306 10.1029/2005jd006888, 2006.

Stohl, A., Berg, T., Burkhart, J. F., Fjaeraa, A. M., Forster, C., Herber, A., Hov, O., Lunder, C., McMillan, W. W., Oltmans, S., Shiobara, M., Simpson, D., Solberg, S., Stebel, K., Strom, J., Torseth, K., Treffeisen, R., Virkkunen, K., and Yttri, K. E.: Arctic smoke - record high air pollution levels in the European Arctic due to agricultural fires in Eastern Europe in spring 2006, Atmos. Chem. Phys., 7, 511-534, 2007.

Strahan, S. E., Duncan, B. N., and Hoor, P.: Observationally derived transport diagnostics for the lowermost stratosphere and their application to the GMI chemistry and transport model, Atmos. Chem. Phys., 7, 2435-2445, 2007.

Streets, D. G., Bond, T. C., Carmichael, G. R., Fernandes, S. D., Fu, Q., He, D., Klimont, Z., Nelson, S. M., Tsai, N. Y., Wang, M. Q., Woo, J. H., and Yarber, K. F.: An inventory of gaseous and primary aerosol emissions in Asia in the year 2000, Journal of Geophysical Research-Atmospheres, 108, 10.1029/2002jd003093, 2003.

Swinbank, R., and Oneill, A.: A stratosphere troposphere data assimilation system, Monthly Weather Review, 122, 686-702, 1994.

Takegawa, N., Miyakawa, T., Watanabe, M., Kondo, Y., Miyazaki, Y., Han, S., Zhao, Y., van Pinxteren, D., Bruggemann, E., Gnauk, T., Herrmann, H., Xiao, R., Deng, Z., Hu, M., Zhu, T., and Zhang, Y.: Performance of an Aerodyne Aerosol Mass Spectrometer (AMS) during Intensive Campaigns in China in the Summer of 2006, Aerosol Sci. Technol., 43, 189-204, 10.1080/02786820802582251, 2009.

Talbot, R. W., Vijgen, A. S., and Harriss, R. C.: Soluble species in the Arctic summer troposphere - acid gases, aerosols, and precipitations, Journal of Geophysical Research-Atmospheres, 97, 16531-16543, 1992.

Theys, N., Van Roozendael, M., Dils, B., Hendrick, F., Hao, N., and De Maziere, M.: First satellite detection of volcanic bromine monoxide emission after the Kasatochi eruption, Geophysical Research Letters, 36, 5, L03809 10.1029/2008gl036552, 2009.

Thomas, A., Flugzeuggestützte Messungen des atmosphärischen Aerosols: Saharastaub, stratosphärisches Hintergrundaerosol und nichtsichtbare Wolken in den Tropen, Fachbereich für Physik, Mathematik und Informatik, PhD, Johannes Gutenberg-Universität, Mainz, 2003.

Thomason, L., and Peter, T.: SPARC Assessment of Stratospheric Aerosol Properties, in: WCRP-124, WMO/TD-No. 1295, SPARC Report No.4, Toronto, Canada, 2006.

Trickl, T., Giehl, H., Jäger, H., and Fromm, M.: 33 years of stratospheric aerosol measurements at Garmisch-Partenkirchen (1976-2010), 25th International Laser Radar Conference, St. Petersburg, Russia, 5 - 9 July, 2010, 2010.

Ulbrich, I. M., Canagaratna, M. R., Zhang, Q., Worsnop, D. R., and Jimenez, J. L.: Interpretation of organic components from Positive Matrix Factorization of aerosol mass spectrometric data, Atmos. Chem. Phys., 9, 2891-2918, 2009.

van der Werf, G. R., Randerson, J. T., Giglio, L., Collatz, G. J., Kasibhatla, P. S., and Arellano, A. F.: Interannual variability in global biomass burning emissions from 1997 to 2004, Atmos. Chem. Phys., 6, 3423-3441, 2006.

van Donkelaar, A., Martin, R. V., Leaitch, W. R., Macdonald, A. M., Walker, T. W., Streets, D. G., Zhang, Q., Dunlea, E. J., Jimenez, J. L., Dibb, J. E., Huey, L. G., Weber, R., and Andreae, M. O.: Analysis of aircraft and satellite measurements from the Intercontinental Chemical Transport Experiment (INTEX-B) to quantify long-range transport of East Asian sulfur to Canada, Atmos. Chem. Phys., 8, 2999-3014, 2008.

Vernier, J. P., Thomason, L., Pommereau, J. P., Bourassa, A., Pelon, J., Garnier, A., Hauchecorne, A., Blanot, L., Trepte, C., Degenstein, D. A., and Vargas, F.: Major influence of tropical volcanic eruptions on the stratospheric aerosol layer during the last decade, Geophysical Research Letters, 38, L12807, doi:10.1029/2011GL047563, 2011.

Villani, P., Picard, D., Marchand, N., and Laj, P.: Design and validation of a 6-volatility tandem differential mobility analyzer (VTDMA), Aerosol Sci. Technol., 41, 898-906, 10.1080/02786820701534593, 2007.

Virtanen, A., Joutsensaari, J., Koop, T., Kannosto, J., Yli-Pirila, P., Leskinen, J., Makela, J. M., Holopainen, J. K., Poschl, U., Kulmala, M., Worsnop, D. R., and Laaksonen, A.: An amorphous solid state of biogenic secondary organic aerosol particles, Nature, 467, 824-827, 10.1038/nature09455, 2010.

Voigt, C., Schreiner, J., Kohlmann, A., Zink, P., Mauersberger, K., Larsen, N., Deshler, T., Kroger, C., Rosen, J., Adriani, A., Cairo, F., Di Donfrancesco, G., Viterbini, M., Ovarlez, J., Ovarlez, H., David, C., and Dornbrack, A.: Nitric acid trihydrate (NAT) in polar stratospheric clouds, Science, 290, 1756-1758, 2000.

Voigt, C., Schlager, H., Ziereis, H., Kärcher, B., Luo, B. P., Schiller, C., Krämer, M., Popp, P. J., Irie, H., and Kondo, Y.: Nitric acid in cirrus clouds, Geophysical Research Letters, 33, 4, L05803 10.1029/2005gl025159, 2006.

Voigt, C., Kärcher, B., Schlager, H., Schiller, C., Krämer, M., de Reus, M., Vossing, H., Borrmann, S., and Mitev, V.: In-situ observations and modeling of small nitric acid-containing ice crystals, Atmos. Chem. Phys., 7, 3373-3383, 2007.

Voigt, C., Schumann, U., Jurkat, T., Schauble, D., Schlager, H., Petzold, A., Gayet, J. F., Krämer, M., Schneider, J., Borrmann, S., Schmale, J., Jessberger, P., Hamburger, T., Lichtenstern, M., Scheibe, M., Gourbeyre, C., Meyer, J., Kubbeler, M., Frey, W., Kalesse, H., Butler, T., Lawrence, M. G., Holzapfel, F., Arnold, F., Wendisch, M., Dopelheuer, A., Gottschaldt, K., Baumann, R., Zoger, M., Solch, I., Rautenhaus, M., and Dornbrack, A.: In-situ observations of young contrails - overview and

selected results from the CONCERT campaign, Atmos. Chem. Phys., 10, 9039-9056, 10.5194/acp-10-9039-2010, 2010.

von Glasow, R., Bobrowski, N., and Kern, C.: The effects of volcanic eruptions on atmospheric chemistry, Chemical Geology, 131-142, 2009.

von Hobe, M., Grooss, J. U., Gunther, G., Konopka, P., Gensch, I., Kramer, M., Spelten, N., Afchine, A., Schiller, C., Ulanovsky, A., Sitnikov, N., Shur, G., Yushkov, V., Ravegnani, F., Cairo, F., Roiger, A., Voigt, C., Schlager, H., Weigel, R., Frey, W., Borrmann, S., Muller, R., and Stroh, F.: Evidence for heterogeneous chlorine activation in the tropical UTLS, Atmos. Chem. Phys., 11, 241-256, 10.5194/acp-11-241-2011, 2011.

Warneke, C., de Gouw, J. A., Stohl, A., Cooper, O. R., Goldan, P. D., Kuster, W. C., Holloway, J. S., Williams, E. J., Lerner, B. M., McKeen, S. A., Trainer, M., Fehsenfeld, F. C., Atlas, E. L., Donnelly, S. G., Stroud, V., Lueb, A., and Kato, S.: Biomass burning and anthropogenic sources of CO over New England in the summer 2004, J. Geophys. Res, D, Atmos., 111, 1-13, 10.1029/2005jd006878, 2006.

Weigel, R., Borrmann, S., Kazil, J., Minikin, A., Stohl, A., Wilson, J. C. , Reeves, J. M. , Kunkel, D. , de Reus, M. , Frey, W. , Lovejoy, E. R. , Volk, C. M. , Viciani, S. , D'Amato, F. , Cairo, F. , Schlager, H. , Law, K. S. , Shur, G. N. , Belyaev, G. V. , and Curtius, J. : In situ observations of new particle formation in the tropical upper troposphere: the role of clouds and the nucleation mechanism, Atmos. Chem. Phys. Discuss., 11, 9249-9312, 2011.

Wernli, H., and Davies, H. C.: A Lagrangian-based analysis of extratropical cyclones .1. The method and some applications, Q. J. R. Meteorol. Soc., 123, 467-489, 1997.

Wiedinmyer, C., Quayle, B., Geron, C., Belote, A., McKenzie, D., Zhang, X. Y., O'Neill, S., and Wynne, K. K.: Estimating emissions from fires in North America for air quality modeling, Atmos. Environ., 40, 3419-3432, 10.1016/j.atmosenv.2006.02.010, 2006.

Wild, O.: Cambridge Tropospheric Trajectory Model - Model Description, 1996.

Wilson, J. C., Jonsson, H. H., Brock, C. A., Toohey, D. W., Avallone, L. M., Baumgardner, D., Dye, J. E., Poole, L. R., Woods, D. C., Decoursey, R. J., Osborn, M., Pitts, M. C., Kelly, K. K., Chan, K. R., Ferry, G. V., Loewenstein, M., Podolske, J. R., and Weaver, A.: In-situe observations of aerosol and chlorine monoxide after the 1991 eruption of Mount-Pinatubo - Effect of reactions on sulfate aerosol, Science, 261, 1140-1143, 1993.

WMO: Scientific Assessment of Ozone Depletion: 1998, WMO Global Ozone Observing System, Report No. 44, Geneva, Switzerland, 1999.

Wuebbles, D. J., Lei, H., and Lin, J. T.: Intercontinental transport of aerosols and photochemical oxidants from Asia and its consequences, Environmental Pollution, 150, 65-84, 10.1016/j.envpol.2007.06.066, 2007.

Yokelson, R. J., Crounse, J. D., DeCarlo, P. F., Karl, T., Urbanski, S., Atlas, E., Campos, T., Shinozuka, Y., Kapustin, V., Clarke, A. D., Weinheimer, A., Knapp, D. J., Montzka, D. D., Holloway, J., Weibring, P., Flocke, F., Zheng, W., Toohey, D., Wennberg, P. O., Wiedinmyer, C., Mauldin, L., Fried, A., Richter, D., Walega, J., Jimenez, J. L., Adachi, K., Buseck, P. R., Hall, S. R., and Shetter, R.: Emissions from biomass burning in the Yucatan, Atmos. Chem. Phys., 9, 5785-5812, 2009.

Zahardis, J., and Petrucci, G. A.: The oleic acid-ozone heterogeneous reaction system: products, kinetics, secondary chemistry, and atmospheric implications of a model system - a review, Atmos. Chem. Phys., 7, 1237-1274, 2007.

Zahn, A., Brenninkmeijer, C. A. M., Maiss, M., Scharffe, D. H., Crutzen, P. J., Hermann, M., Heintzenberg, J., Wiedensohler, A., Gusten, H., Heinrich, G., Fischer, H., Cuijpers, J. W. M., and van Velthoven, P. F. J.: Identification of extratropical two-way troposphere-stratosphere mixing based on CARIBIC measurements of O-3, CO, and ultrafine particles, Journal of Geophysical Research-Atmospheres, 105, 1527-1535, 2000.

Zahn, A., and Brenninkmeijer, C. A. M.: New directions: A chemical tropopause defined, Atmos. Environ., 37, 439-440, 2003.

Zelenyuk, A., Yang, J., Choi, E., and Imre, D.: SPLAT II: An Aircraft Compatible, Ultra-Sensitive, High Precision Instrument for In-Situ Characterization of the Size and Composition of Fine and Ultrafine Particles, Aerosol Sci. Technol., 43, 411-424, 10.1080/02786820802709243, 2009.

Zhang, Q., Alfarra, M. R., Worsnop, D. R., Allan, J. D., Coe, H., Canagaratna, M. R., and Jimenez, J. L.: Deconvolution and quantification of hydrocarbon-like and oxygenated organic aerosols based on aerosol mass spectrometry, Environ. Sci. Technol., 39, 4938-4952, 10.1021/es048568I, 2005a.

Zhang, Q., Worsnop, D. R., Canagaratna, M. R., and Jimenez, J. L.: Hydrocarbon-like and oxygenated organic aerosols in Pittsburgh: insights into sources and processes of organic aerosols, Atmos. Chem. Phys., 5, 3289-3311, 2005b.

Zhang, Q., Jimenez, J. L., Canagaratna, M. R., Allan, J. D., Coe, H., Ulbrich, I., Alfarra, M. R., Takami, A., Middlebrook, A. M., Sun, Y. L., Dzepina, K., Dunlea, E., Docherty, K., DeCarlo, P. F., Salcedo, D., Onasch, T., Jayne, J. T., Miyoshi, T., Shimono, A., Hatakeyama, S., Takegawa, N., Kondo, Y., Schneider, J., Drewnick, F., Borrmann, S., Weimer, S., Demerjian, K., Williams, P., Bower, K., Bahreini, R., Cottrell, L., Griffin, R. J., Rautiainen, J., Sun, J. Y., Zhang, Y. M., and Worsnop, D. R.: Ubiquity and dominance of oxygenated species in organic aerosols in anthropogenically-influenced Northern Hemisphere midlatitudes, Geophysical Research Letters, 34, 6, L13801 10.1029/2007gl029979, 2007a.

Zhang, R. Y., Li, G. H., Fan, J. W., Wu, D. L., and Molina, M. J.: Intensification of Pacific storm track linked to Asian pollution, Proc. Natl. Acad. Sci. U. S. A., 104, 5295-5299, 10.1073/pnas.0700618104, 2007b.

Zhao, Y., Wang, S. X., Nielsen, C. P., Li, X. H., and Hao, J. M.: Establishment of a database of emission factors for atmospheric pollutants from Chinese coal-fired power plants, Atmos. Environ., 44, 1515-1523, 10.1016/j.atmosenv.2010.01.017, 2010.

Zobrist, B., Marcolli, C., Pedernera, D. A., and Koop, T.: Do atmospheric aerosols form glasses?, Atmos. Chem. Phys., 8, 5221-5244, 2008.